RIJKSUNIVERSITEIT GRONINGEN

Polycyclic Aromatic Hydrocarbons and dust in regions of massive star formation

PROEFSCHRIFT

ter verkrijging van het doctoraat in de
Wiskunde en Natuurwetenschappen
aan de Rijksuniversiteit Groningen
op gezag van de
Rector Magnificus, dr. F. Zwarts
in het openbaar te verdedigen op
vrijdag 13 december 2002
om 11.00 uur

door

Els Peeters

geboren op 4 juni 1973
te Tienen, België

Promotor: prof. dr. A. G. G. M. Tielens
Referent: dr. P. R. Roelfsema

Beoordelingscommissie:
dr. L. J. Allamandola
dr. F. Boulanger
prof. dr. J. M. van der Hulst

Voor Jan

Cover:
The cover illustration symbolizes how PAHs and their close relatives have opened up our window on star forming regions. It represents three 2,6-dimethylpyrazine molecules, a substance used by Nobles in the Aztec court in combination with vanilla to create an aphrodisiacal drink they called *choclatl*. Grey spheres represent carbon, blue spheres nitrogen and red spheres hydrogen. Molecules with a somehow related structure are discussed in this thesis. The images are of the Trifid Nebula (top, COPYRIGHTS:GMOS, Gemini Observatory), the Cone Nebula (bottom left, COPYRIGHTS:ACS Science & Engineering Team, NASA) and the Omega Nebula (bottom right, COPYRIGHTS:ACS Science & Engineering Team, NASA). Design by Jan Cami using IDL.

Contents

1

Introduction

Polycyclic Aromatic Hydrocarbons (PAHs) are known on earth as a large family of tarry materials naturally present in for example coal and crude oil. In addition, they are also formed in the combustion of all sorts of carbonaceous fuels and hence are found in auto exhaust, cigarette smoke, candle soot and (for the less qualified cooks) in burned hamburgers. PAHs are regularly placed under the media spotlight for the persistent detrimental effect of their carcinogenic properties on the environment, due to their long-term stability.

To date, PAHs are the largest known molecules in space, and ubiquitously present with high abundances. Intimately interwoven with dust, they are formed in the outflows of evolved and dying stars. They play a vital role in the interstellar (IS) chemistry and the heating of the ISM; and can be used to probe environmental conditions within astronomical objects.

The research described in this thesis concerns the study of the infrared spectral characteristics of PAHs. In this introduction, the life cycle of stars, dust and gas is briefly discussed (Sect. 1.1). Subsequently, we focus on the molecular structure of PAHs and their relatives (Sect. 1.2), and the way we can observe them, i.e. by IR spectroscopy (Sect. 1.3). Section 1.4 fully discusses the link between the Unidentified Infrared (UIR) bands and the PAHs. The relevance of PAHs and the remaining questions are highlighted in Sect. 1.5. Finally, we outline the content of this thesis.

1.1 Life cycle of stars, dust and gas

In a truly cosmic life cycle (see Fig. 1.1), stars are born from the remnants of earlier generations of stars. Their lives are a continuous fight against gravity, a fight which starts by interstellar clouds which – under the influence of gravity – gather, grow in size and become dense "molecular" clouds. As (parts of) these clouds further collapse, the temperature in the inner parts increases, until the temperature is high enough to ignite hydrogen fusion in the core. At that moment, a star is born.

The radiation fields and stellar winds of the newly born stars effect the surrounding molecular gas. The larger masses involved in massive star formation cause the processes to be more violent and disruptive and to occur on much shorter time scales. Particularly important is the

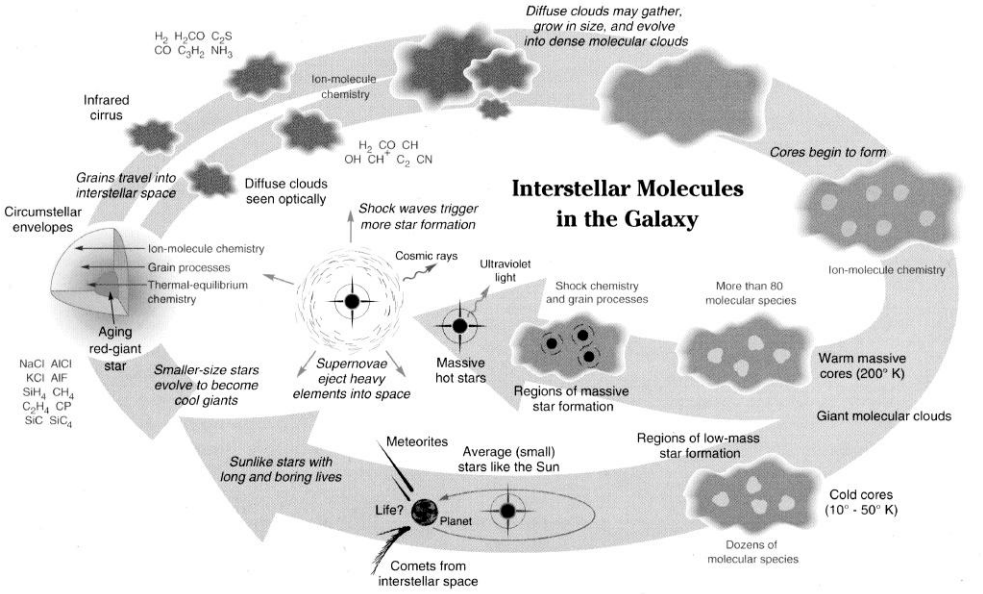

Figure 1.1 — The life cycle of stars, gas and dust in the interstellar/circumstellar medium. Illustration by Steven Simpson (Verschuur 1992), Sky & Telescope Magazine.

creation of emission nebulae known as H II regions, i.e. regions of ionised gas, primarily hydrogen. The stars that create them, of spectral type O and B, are the most massive, hot and luminous stars, with effective temperatures in the range of about 10 000 to 50 000 K.

Once a star is born, the energy produced by these nuclear processes balance the gravitational force and a stable configuration results. During stellar evolution, different nuclear reactions occur in the star inducing changes in its chemical composition. Low-mass stars convert elements upto C, O and N. Nuclear burning in high-mass stars progresses through the production of heavy elements up to those in the mass range around iron and hence these stars are more enriched in heavy elements as are low-mass stars.

These heavy elements are then returned to the Inter Stellar Medium (ISM) through different processes. Low- and intermediate-mass stars will eventually go through a phase called the Asymptotic Giant Branch (AGB). At this moment, the outer layers are loosely bound to the core of the star and the core material (C and O) is brought up to the stellar surface (the so-called dredge-ups). Starting at the AGB phase, the star sheds a major part of its envelope by means of a hefty, dust-driven wind. High-mass stars return their material to the ISM in two ways : (i) during their life-time, they exhibit strong winds expelling considerable parts of their mass, (ii) they end their life's by a violent explosion, called supernova (SN). Due to their much shorter life-time, massive stars are the the dominant contributors to the abundances of metals in our Galaxy and other galaxies.

These stellar ejecta eventually conglomerate in diffuse clouds; these clouds will then eventually start to contract and form the next generation of stars. This time, the stars will have a elemental composition determined by the previous stellar population. Around low-mass stars, planets may form, made of the ashes of stars that have long gone.

This life cycle of the stars is closely interlinked with chemical evolution of the elements they inject into the ISM. Much of the heavy elements are injected in the form of small solid dust particles. Such dust particles are formed in the expanding cooling outflows of evolved or dying stars. The relative importance of the different types of objects is not well known. As explained above, the surface composition of the AGB star changes during its evolution due to dredge-up events. Oxygen-rich giants with abundances of O larger than of C will typically form all kinds of silicates and oxides ("sand"), while carbon-rich giants – with C/O > 1 – will produce carbonaceous dust ("soot"). Besides these dust particles, the ejecta are also replete with many molecules : small ones such as CO, H_2O, C_2H_2, ... and much larger ones such as acetylenic chain derivatives (e.g. HC_7N, HC_9N, C_4H, ...). Supernova ejecta are also known to form dust but the amount of dust is unknown (Lucy et al. 1989, 1991; Amari et al. 1992; Anders & Zinner 1993; Wooden et al. 1993; Dalgarno et al. 1997). SNe also contain molecules (SiO, CO, H_2, e.g. Meikle et al. 1989; Liu & Dalgarno 1994; Dalgarno et al. 1997; Reynoso & Goss 2002).

Through stellar winds or explosions, these stellar masses/envelopes are ejected into the ISM. Here, the nature of the dust grains and molecules undergo dramatic changes. Molecular bonds are constantly broken and reformed by the ubiquitous UV photons in the diffuse ISM and ion-molecule reactions. Here applies the survival of the fittest : only the most stable and strongest species will survive. Similarly, dust grains can *grow* by coagulation and accretion, and heavier elements produced by stars can be incorporated. Also, the dust grains are *processed* by highly energetic irradiation, highly energetic particles and strong shocks – mainly due to massive stars – destroying the particle partly or completely.

The dust and molecules may gather in clouds which grow in size and coalesce forming dense molecular clouds. The inner part of these clouds are shielded from the aggressive attacks of the energetic photons, and shocks present in the ISM and are very cold. This facilitates the formation of ice mantles on the grain surfaces. The grain mantles grow by accretion of gas-phase species or by coagulation. UV irradiation gives rise to rich chemistry and more complex molecules can form.

Subsequently, these clouds collapse and a protostar is formed. Due the high temperature the ice mantles are evaporated and the formed molecules released. This phase is characterised by a rich gas-phase chemistry that involves complex and large molecules. Eventually, a star is born. In case of a massive star, the temperature increases tremendously and strong shocks occur inducing the destruction of all dust grains and molecules and hence leaving a dust cavity around the new born star.

1.2 MAHs, PAHs and their relatives

As a byproduct of dust formation, PAHs are formed. Before going into detail about the astronomical observations and characteristics of PAHs, we first focus on their structure.

The ability of carbon atoms to have four bonds allows them to form complex structures. Carbon atoms can be configured in a planar hexagonal ring – a benzene ring – where each carbon atom is bounded to 3 neigbouring atoms by σ bonds. These bonds are localised. The fourth electron of each carbon atom forms a delocalised π bond with similar electrons from neighbouring carbon atoms. This configuration is called aromatic. This benzene ring can be used as a basis for larger molecules consisting out of several of these rings formed together and therefore called polycyclic. If these molecules only exist out of hydrogen and

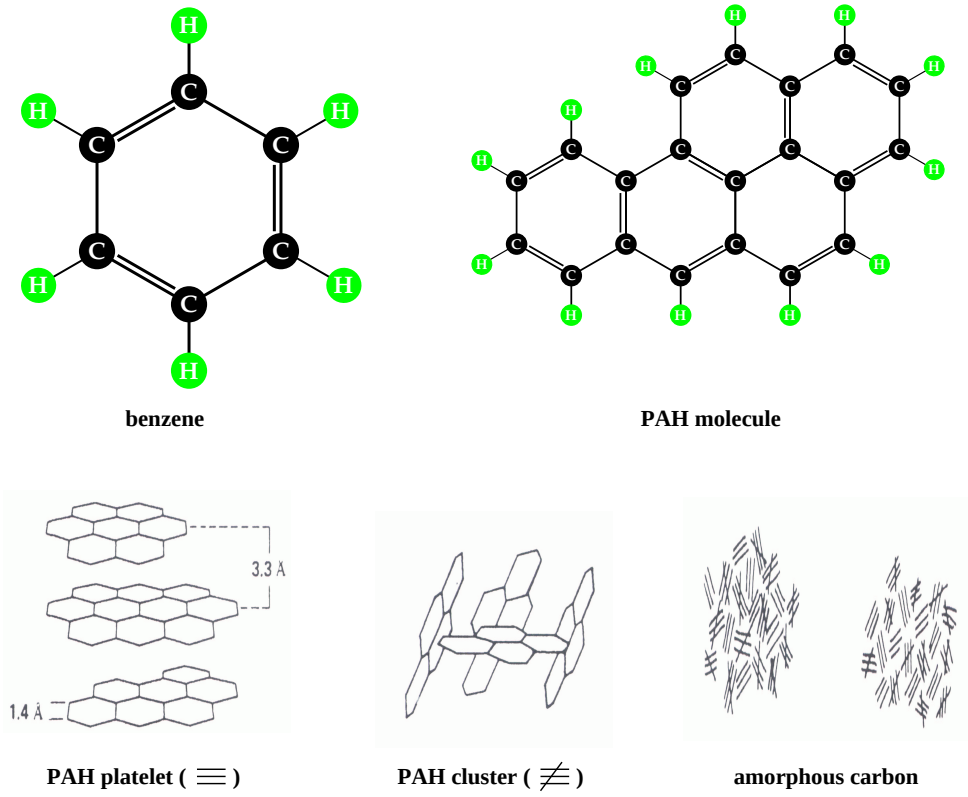

Figure 1.2 — Different structures of carbon based species.

carbon they are called Polycyclic Aromatic Hydrocarbons (PAHs). Hence, PAHs are a large family of different molecules with a similar structure. In this way, benzene can be dubbed as Monycyclic Aromatic Hydrocarbon (MAH). Hydrocarbons that are not aromatic are called aliphatic. By ordering PAH molecules in different parallel layers, PAH platelets (i.e. graphite) are formed while PAH clusters are formed by sticking PAHs in a ordered way both parallel and disordered. Amorphous carbon is then a random combination of PAH platelets and PAH clusters. All these different forms of carbon based species are shown in Fig. 1.2.

1.3 Infrared spectroscopy of PAHs and dust

IR spectroscopy is a powerful tool to study the characteristics of molecules and dust grains present in space.

The dust absorbs a large fraction of the UV radiation and re-emits the absorbed energy in the IR and sub-mm with the peak of the dust emission depending on the temperature of the dust grains. The compact H II regions (i.e. H II regions with sizes < 0.5 pc and densities $> 5\ 10^3$) studied in this thesis are all associated with relatively hot dust; therefore they are IR bright (see Fig. 1.3). Moreover, we can directly observe the dust in the IR.

In addition, the infrared holds the spectroscopic fingerprints of the dust components and

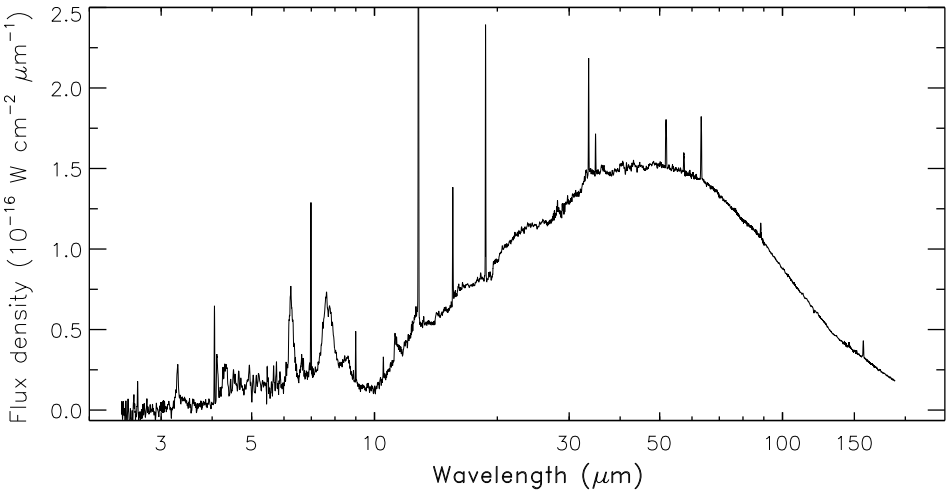

Figure 1.3 — The infrared spectrum of a typical compact H II region obtained with the spectrometers on board the Infrared Space Observatory (ISO). The bulk of emission is emitted by dust grains in thermal equilibrium with the radiation field. Other dust components are absorption by silicate grains at 9.7 μm and the Unidentified InfraRed (UIR) bands at 3.3, 6.2, 7.7, 8.6, 11.2 and 12.7 μm. The spectrum also exhibits a large number of recombination lines of hydrogen and fine-structure lines.

the molecules. Indeed, in the mid-infrared, the emission is due to vibrationally excited molecules and dust. This allows us to identify the different materials since each of them has its own set of wavelengths at which they emit. Vibrational modes involving a change in bond lengths are called stretching modes. Those involving mainly a change in bond angle are called bending modes. As an example, we illustrate in Fig. 1.4 the main vibrational modes of a PAH molecule.

1.4 The UIR bands and PAHs [1]

The UIR bands

The infrared spectra of a wide variety of objects with associated dust and gas – including H II regions, Post-AGB stars, PNe, YSOs, the diffuse ISM and galaxies – are dominated by emission bands at 3.3, 6.2, 7.7, 8.6, 11.2 and 12.7 μm (see Fig. 1.5, cf. Gillett et al. 1973; Geballe et al. 1985; Cohen et al. 1986; Cox & Kessler 1999). Often, these bands are accompanied by broad emission plateaus underneath them. Since the carriers of these bands remained unknown for almost a decade, these bands are referred to as the Unidentified InfraRed (UIR) emission bands.

Its carriers

In the early '80, it was recognised that the UIR bands coincide with C-H and C-C vibrational modes characteristic of aromatic materials (Duley & Williams 1981). While the vibrational spectrum of any (almost) exclusively aromatic material can provide a good fit to the observed

[1] See Allamandola et al. (1989b); Puget & Léger (1989); Tielens et al. (1999) for extended overviews.

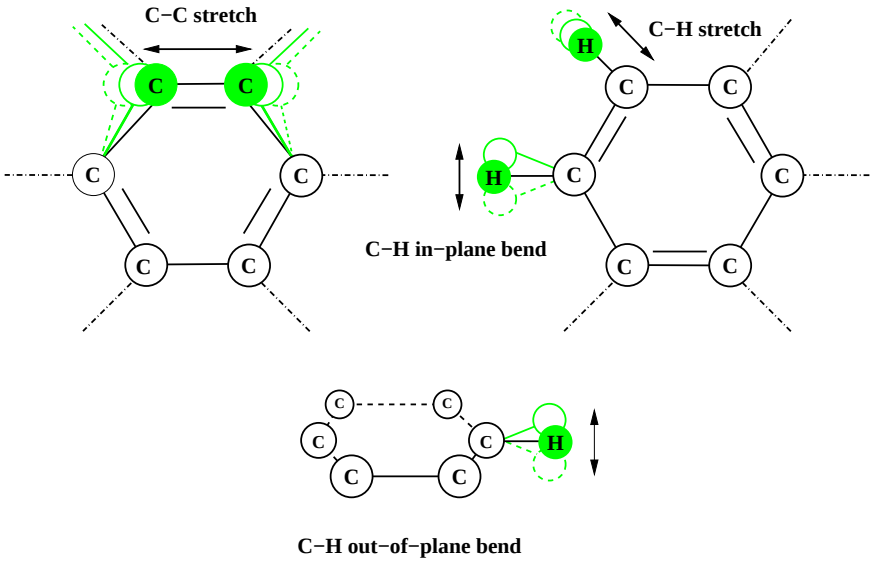

Figure 1.4 — A simplified illustration of the main vibrational modes in a PAH molecule. Possible vibrational modes can involve a change in the C-C and C-H bond length (C-C stretch and C-H stretch respectively) or bending of the C-H bond in the plane of the PAH molecule and out of the plane of the PAH molecule.

UIR bands, they are generally attributed to small PAH *molecules* rather than soot, Hydrogenated Amorphous Carbon (HAC) or Quenched Carbon Composites (QCC) dust grains. The main argument for this is the detection of the UIR bands in reflection nebulae far from an illuminating star and the independence of the color temperature with the distance from the star, indicating that the carriers of the UIR bands can be heated to very high temperatures in such cold environments upon absorption of a *single* FUV photon (Sellgren 1984). Classical grains are not hot enough to emit at mid-infrared wavelengths in these environments, hence the carrier of the UIR bands are attributed to small species containing $\sim$ 50 carbon atoms (Sellgren 1984). This point has now been reinforced by ISO (Infrared Space Observatory) observations revealing that the mid-infrared spectra of the diffuse ISM is dominated by these IR emission features (Mattila et al. 1996; Boulanger et al. 1998a; Boulanger 1999; Boulanger et al. 2000). A second argument is that an absorbed photon does not remain localised long enough in a single aromatic unit of (or loosely bound to) a solid grain so that the emission of this grain can mimic that of a single PAH molecule (Tielens 1993). Finally, larger aromatic species do not simultaneously give rise to a high feature to continuum ratio and a high aromatic to aliphatic ratio ($I_{3.3}/I_{3.4}$) as observed in space (Tielens et al. 1999).

Excitation mechanism of PAHs

The absorption of a FUV photon by a PAH molecule induces a transition to an upper electronic state. The excited molecule then makes rapid isoenergetic transitions to the ground electronic state leaving most of the initial excitation energy in the form of vibrational energy. Subsequentely, this highly vibrationaly excited molecule cools down, mainly by IR emission

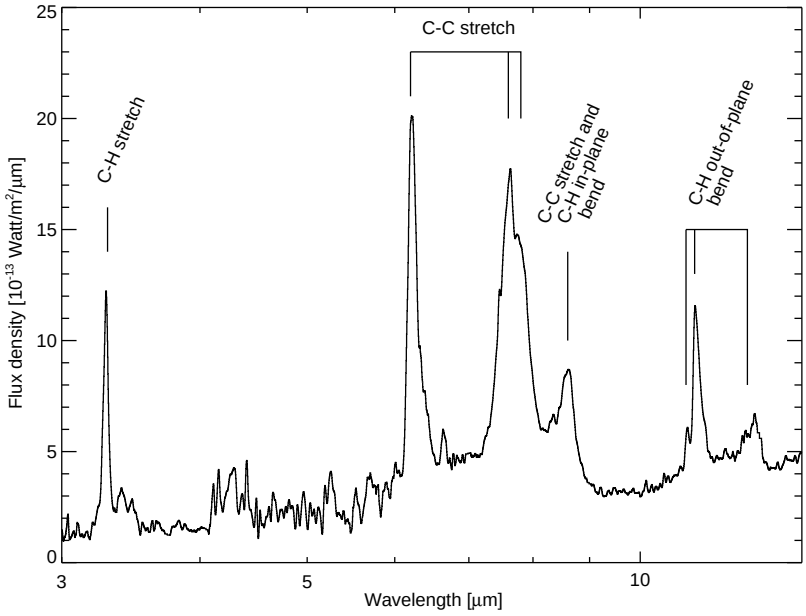

Figure 1.5 — The IR spectrum of a massive star forming regions. The UIR bands are clearly present (the atomic emission lines are removed).

in the C-C and C-H vibrational modes. In this way, the PAH molecules leave behind their signature in the form of the UIR bands.

Theoretical and experimental spectroscopy of PAHs

The interpretation of the UIR bands and their carriers is heavily based upon theoretical and experimental spectroscopy of PAHs and their relatives. Comparison of astronomical spectra with laboratory spectroscopy and theoretical calculations of the vibrational modes of well characterised materials allows to determine the specific carrier or to constrain the possible candidate carriers of the emission band under consideration as well as to determine the cause of the observed spectral variations.

One of the early pivotal results of the laboratory and theoretical studies on PAHs reported over the last decade is the remarkable effect ionisation has on the infrared spectra (Szczepanski & Vala 1993a; Joblin et al. 1994, 1995; Langhoff 1996; Kim et al. 2001; Hudgins & Allamandola 1999a, and ref. therein). While PAH characteristic frequencies are only modestly affected by ionisation, the influence on intensity is striking - particularly in the 5 to 10 μm region (see Fig. 1.6). The bands in this region grow from the smallest features in neutral PAH spectra to become the dominant bands in ionised PAH spectra. Hence, the UIR spectrum arises from both charged and neutral PAHs.

As a result of these laboratory and theoretical studies on PAHs, it also became clear that a distribution of different charge states (both positive and negative) of PAHs is present in a wide variety of astrophysical environments. The charge of a PAH molecule is set by

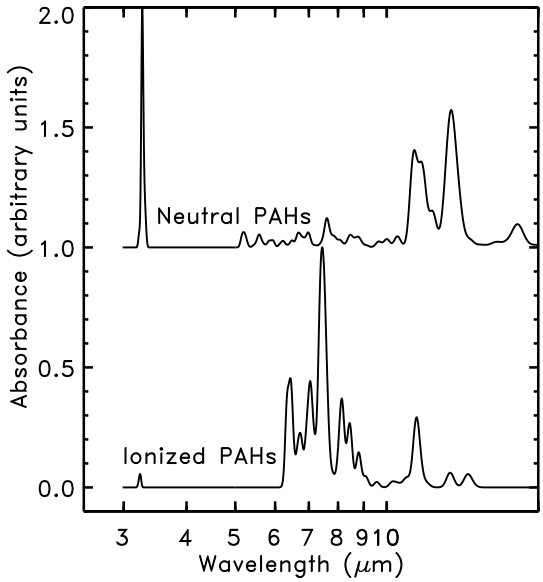

Figure 1.6 — The absorption spectrum of a mixture of neutral PAHs (a) compared to the spectrum of the same PAHs in their positive state (b). This comparison shows that, for PAH spectra, ionisation has a much greater influence on relative intensities than on peak frequencies, with the features in the 6 to 10 μm region substantially enhanced with respect to the rest of the spectrum (Figure adapted from Allamandola et al. 1999b).

the balance between photoelectrically ejected electrons and the PAH-electron recombination rate and is therefore determined by the ratio of the illuminating UV radiation field and the electron density, G_0/n_e. For example, in regions of low G_0/n_e, the PAH charge is dominated by neutral and anionic PAHs while in regions of high G_0/n_e the PAH charge is dominated by multiple ionised PAHs (Bakes et al. 2001). As mentioned above, the charge state of a PAH molecule highly influences the apparent vibrational infrared spectrum.

Laboratory measurements of a collection of different PAHs also reinforced the presence of a family of PAHs in astronomical environments rather then one specific PAH molecule (Desert et al. 1990; Schutte et al. 1993; Verstraete et al. 2001; Pech et al. 2001).

Formation and evolution

Since in many objects the IR emission originates in material recently ejected from a star, PAHs probably are the extension of the grain size distribution of circumstellar carbon grains into the molecular domain and as such may shed light on the detailed formation mechanism of carbon stardust which likely is comparable to terrestrial soot formation in flames. Indeed, PAHs are the building blocks of soot particles due to their high stability and their similar structure (see Allamandola et al. 1989b; Frenklach & Feigelson 1989; Tielens 1990, 1997a; Tielens & Charnley 1997; Cherchneff et al. 2000, for extended overviews).

Most of the carbon in the outflow from C-rich AGB stars is tied up in CO and C_2H_2. Since CO is so stable, acetylene and its radical derivatives are likely to be the dominant precursor molecules from which PAHs and soot are formed. This occurs through two distinct steps : (i) the formation of the first ring out of actylene and (ii) the growth of additional rings by repeated radical formation by abstraction of a H-atom and addition of hydrocarbons; a PAH molecule is formed. These PAHs can grow and coagulate to form PAH clusters, PAH platelets and eventually amorphous carbon particles. In this soot formation process, the most difficult step is the formation of the first aromatic ring.

This formation route does not apply to H-poor environments. Here, the formation process is based on 3 different stages : (i) the formation of small linear C-chain radicals, (ii) the subsequent formation of monocyclic ring molecules. These flexible chains can isomerise to rings upon C addition, (iii) eventually this isomerisation leads to the formation of planar, carbon hexagon structures. In contrast to the above discussed formation process, the absence of hydrogen leads to dangling bonds at the peripheries. Incorporating pentagons and curling reduces the dangling bonds which can lead to the formation of fullerene molecules (Curl & Smalley 1988; Kroto 1988). Larger species may also grow through cluster-cluster reactions.

As PAHs are closely related to dust, their evolution is very similar to that of dust. Formed mainly in the outflow of evolved stars, they are ejected by their dust-driven winds in the ISM. As the dust grains, they undergo dramatic changes. On one hand, the PAHs can *grow* by coagulation and accretion and even become part of dust grains themselves, and heavier elements as for example nitrogen, produced by stars can be incorporated. On the other hand, PAHs are *processed* and *destroyed* partly or completely by highly energetic radiation, highly energetic particles and strong shocks. However, PAHs are very stable and can survive their stay in the ISM; only the small ones ($\sim$ 20–30 C-atoms) are completely destroyed (Allain et al. 1996).

In dense molecular clouds, PAHs get frozen into the ice mantles on the grain surfaces. UV irradiation and the infall of cosmic rays give rise to rich surface chemistry and more complex molecules can form. For example, a hydrogen atom on the periphery of a PAH molecule can be replaced by different functional groups as e.g. methyl (Bernstein et al. 1999; Muñoz Caro et al. 2001; Bernstein et al. 2002).

When a protostar is formed, these newly processed PAH molecules are released into the gas-phase. However, they are less stable than the pure PAHs and hence are easily photodestoyed by UV photons. Furthermore, in the near vicinity of a newly born star, all PAHs are destroyed due to the highly energetic UV radiation of the star.

PAH abundances

Fig. 1.7 shows the infrared emission spectrum of interstellar dust heated by the interstellar radiation field (Reach & Boulanger 1998). Different components can be distinguished : the UIR bands and their underlying plateaus, the 25 and 60 μm cirrus and the far-infrared emission. Each of these spectral components is carried by a different size species/particle (Draine & Anderson 1985; Puget et al. 1985; Desert et al. 1990). The UIR bands are carried by PAHs, their underlying plateaus by PAH-clusters (Bregman et al. 1989; Buss et al. 1990), the 25 μm cirrus by very small grains (Low et al. 1984; Puget et al. 1985; Boulanger et al. 1996b), the 60 μm cirrus by small grains (Low et al. 1984) and the far-infrared emission ($\lambda > 100$ μm by classical grains (Boggess et al. 1992; Boulanger et al. 1996a). The abundance of C,

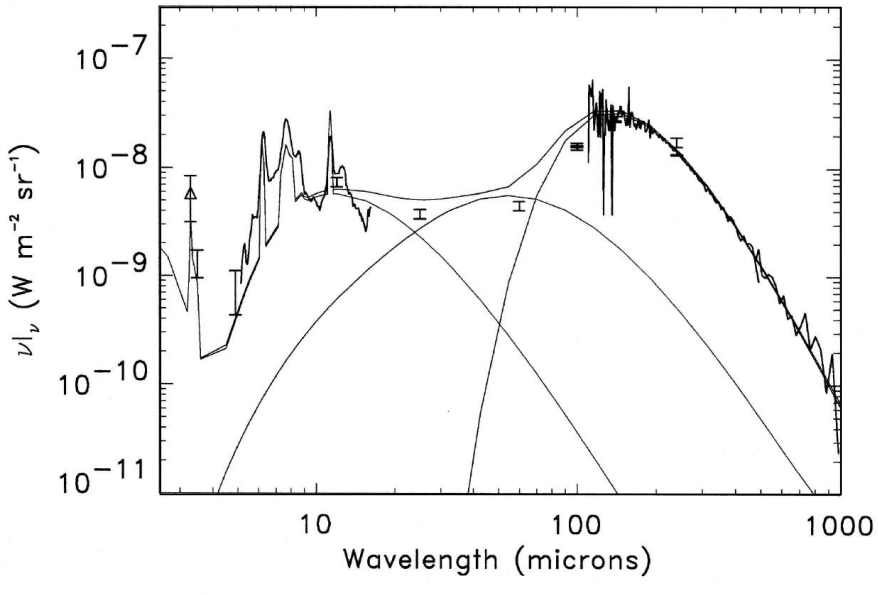

Figure 1.7 — The infrared emission spectrum of interstellar dust heated by the interstellar radiation field. The far-infrared spectrum is from COBE/FIRAS, and the mid-infrared spectrum is from ISOCAM. Points with error bars are from COBE/DIRBE broad-band observations and the Arome balloon experiment. The brightness here corresponds to an interstellar gas column density of 10^{20} cm^{-2}. The continuous thin curve is a model consisting of three dust components (PAHs and PAHs-clusters, (very) small grains and big grains), whose individual contributions are also shown. [Taken from Reach & Boulanger (1998)].

Table 1.1 — Abundance of the carriers of the different IR emission components [taken from Tielens et al. (1999)].

carrier	IR emission component	size Å	f_C^a ppm
PAHs	UIR bands	4-10 ^{b}	14
PAH-clusters	plateaus	10-20	8
very small grains	25 μm cirrus	20-30	7
small grains	60 μm cirrus	50	16
classical grains	$\lambda > 100$ μm	≥ 100	35 ^{c}

(a) Abundance of C locked up in these species in parts per million; (b) Size corresponds to disk rather than sphere; (c) The abundance of C locked up in dust grains is very uncertain.

F_C locked up in the carriers of these different IR emission components are given in Table 1.1 (Reach & Boulanger 1998; Tielens et al. 1999; Boulanger 1999). Very similar fractions of the carbon are locked up in PAH clusters which carry the plateau emission underlying the UIR bands and in the very smal grains which are responsible for the 25 μm cirrus. The abundance of PAHs and small grains responsible for the fluctuation part of the 60 μm cirrus are slightly larger. Finally, the fraction of the elemental carbon locked up in larger dust grains is very unclear because the cosmic abundance of C is uncertain. Adopting B star C-abundances leaves about 35 ppm for classical dust grains. This small fraction of the carbon available for the interstellar grains responsible for visible extinction provides problems for all current dust models.

1.5 Why do we study PAHs?

Every molecule has a niche and each niche has its molecule. As is unequivocally evident from infrared observations, the niche for PAHs is the whole universe. Hence, it may not come as a surprise that PAHs play a crucial role in several astrophysical processes.

We mention a few processes here. As described above, PAHs are the building blocks in the carbon condensation route (Frenklach & Feigelson 1989; Tielens 1990, 1997a; Tielens & Charnley 1997; Cherchneff et al. 2000). PAHs also dominate the heating and cooling of the ambient ISM via photoelectric ejection (Verstraete et al. 1990; Bakes & Tielens 1994), infrared emission and gas-grain collisional cooling (Aannestad & Kenyon 1979; Dwek 1986). In addition, PAHs influence the charge balance and in this way – through their influence on the equilibrium state of chemical reations – the gas-phase abundancies in interstellar clouds (Lepp & Dalgarno 1988; Bakes & Tielens 1998). Due to their large surface areas, PAHs also affect the on-going surface chemistry and so play a significant role in IS chemistry (Tielens & Allamandola 1987).

In addition, PAHs are mentioned as possible carriers of the Diffuse Interstellar Bands (DIBs; these are absorption bands observed in the UV and visible part of the spectrum along many lines of sight Leger & Dhendecourt 1985; van der Zwet & Allamandola 1985; Crawford et al. 1985; Salama et al. 1996). The PAHs may also be involved in the 2175Å feature (Joblin et al. 1992) which dominates the interstellar UV extinction curve (Fitzpatrick 1986).

PAHs are generally accepted to trace star formation. This is nicely illustrated in Fig 1.8 of the molecular ridge of the star formation complex NGC 6334. The PAHs emission clearly show very extended filamentary structure over the whole starforming complex, some $\sim$15 pc in size. van den Ancker et al. (2000a) distinguish shocked gas and PDRs through the presence of the PAH features. Furthermore, extra-galactic studies use the PAH features, in combination with the emission lines, qualitatively and quantitatively as diagnostics for the ultimate physical processes powering galactic nuclei (Genzel et al. 1998; Lutz et al. 1998; Rigopoulou et al. 1999; Clavel et al. 2000; Helou et al. 2000; Tran et al. 2001). For example, these authors conclude, in this way, that ULIRGs are mainly powered by starbursts. Consequentely, the strength of the PAH bands can also probe evolutionary effects. In addition, PAHs also can serve as tracers of elemental evolution in external galaxies.

Obviously, this is heavily based on the precise knowledge of the UIR bands and the PAH families present in astronomical environments. Although the presence of PAHs in space is generally accepted, presently, the specific molecular identification of the carriers remains elusive. Consequentely, the ultimate goal is the identification of the individual molecules of

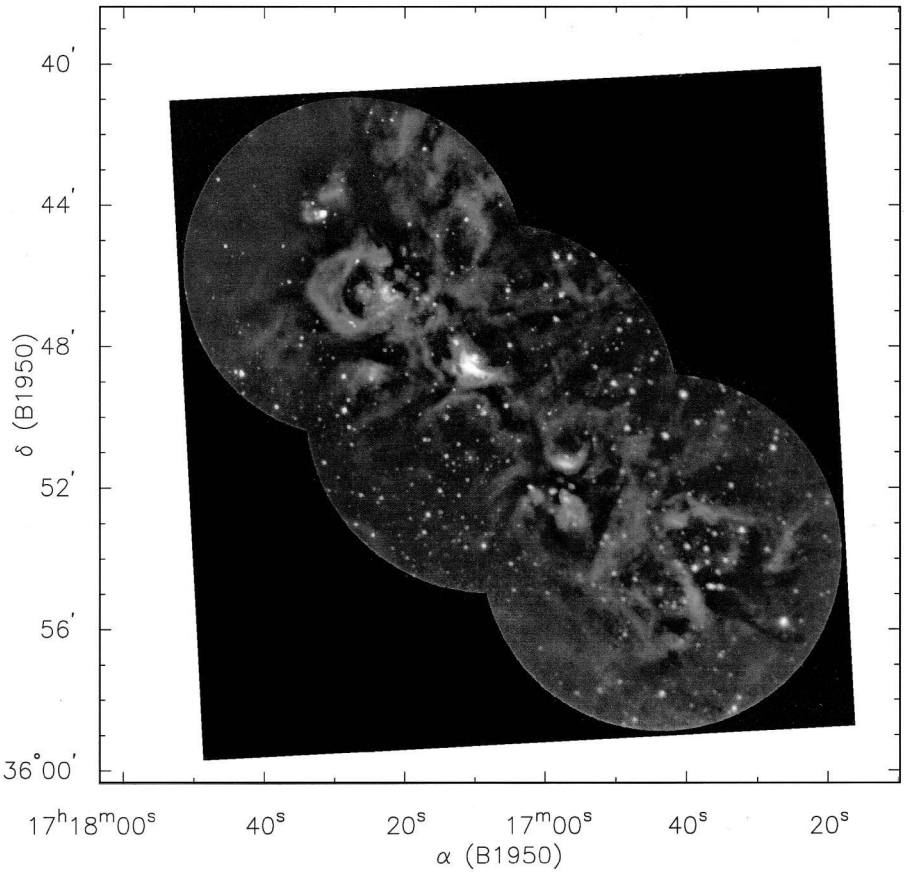

Figure 1.8 — Infrared image of the molecular ridge of NGC 6334. The white color represents star forming regions, the grey filamentary structure represents PAH molecules and dark regions symbolises dark clouds. [Taken from Burton et al. (2000)].

the PAH family. Furthermore, if we want to use PAHs and their emission bands as tools for probing the universe, for example the starburst contribution to extra-galactic spectra, then we have to understand how the local environment and/or the history influence the composition of this PAH family; and vice-versa, how the PAH molecules influence the local physical and chemical processes.

1.6 In this thesis

The research described in this thesis addresses the questions mentioned above : the composition and evolution of PAHs in space.

In this thesis, we apply the combination of astronomical observations with theoretical and experimental work on PAHs. We make use of all four instruments on board ISO in one way or another, though the work presented here is mainly based on the Short Wavelength

Spectrometer (SWS). These data are supplemented with high spatial resolution ground-based data.

1.6.1 The Infrared Space Observatory

The Infrared Space Observatory (ISO, Kessler et al. 1996) was launched in November 1995 and had an operational lifetime of over 28 months. ISO carried four instruments providing spectroscopy and imaging between 2.3 and 193 μm; the Short Wavelength Spectrometer (SWS, de Graauw et al. 1996), Long Wavelength Spectrometer (LWS, Clegg et al. 1996), a camera (ISOCAM, Cesarsky et al. 1996) and an imaging photo-polarimeter (ISOPHOT, Lemke et al. 1996).

With these instruments, offering unprecedented combinations of wavelength coverage, sensitivity, and spatial and spectral resolutions in the infrared spectral region, ISO opened the infrared Universe. Specific for the UIR bands, the complete access to the 2.3–197 μm wavelength range allowed – for the first time – the study of the PAHs in space in all their glory. ISO reinforced the ubiquitous nature of the UIR bands (Cox & Kessler 1999) and has revealed the incredible richness of the UIR spectrum and the widespread variations in the relative strength and profiles of these features from source to source and within sources (e.g. Molster et al. 1996; Roelfsema et al. 1996; Verstraete et al. 1996; Tielens et al. 1999; Maillard et al. 1999; Moutou et al. 1999a,c; Joblin et al. 2000; Van Kerckhoven et al. 2000; Hony et al. 2001; Van Kerckhoven 2002, this thesis). In addition, observations of the UIR bands in regions of low UV flux reinforced the proposed heating mechanism of PAHs (Boulanger et al. 1996b; Mattila et al. 1996; Lemke et al. 1998; Boulanger 1999; Boulanger et al. 2000).

1.6.2 Outline

Chapter 2 presents an ISO spectral catalogue of 43 compact H II regions containing the combined SWS-LWS spectra for each of the sources, the fluxes of the atomic fine-structure lines and hydrogen recombination lines, and an inventory of the spectra in terms of molecular lines, dust and ice bands.

In Chapters 3 and 4, we study the profiles and peak position of the main UIR bands (3.3, 6.2, 7.7, 8.6 and 11.2 μm) in a large sample of sources including reflection nebulae, H II regions, YSOs, evolved stars and galaxies that show strong unidentified infrared bands. We investigate the spectral characteristics of the PAHs and their dependence on the local environment. The IR emission features vary considerably and systematically with source type. Moreover, the observed pronounced contrast in the spectral variations for the CH modes versus the CC modes is striking. We conclude that a PAH family is present and is dependent on the local environment; e.g. pure carbon PAHs are present in C-rich evolved stars while substituted/complexed pahs dominate in the ISM.

In chapter 5, we present the first detection of UIR emission features at ~ 6.4 and 7.9 μm in the spectrum of the dusty WC8 Wolf-Rayet star WR 48a. We compare the observed profiles with those studied in Chapter 3. Based on the H-deficient nature of WC-stars, we attribute the emission features to large carbonaceous molecules or amorphous carbon dust grains in the circumstellar environment of WR 48a and confirm the apparent sensitivity of the UIR bands to physical conditions.

Chapter 6 reports the detection of deuterated PAHs and derives the D/H ratio of the PAH molecules present in the Orion Bar. The cosmic deuterium to hydrogen (D/H) ratio is of

key importance from a cosmological and stellar evolution perspective and traces interstellar chemical evolution. Since the PAH emission features are widespread and probe many different types of cosmic environments, observations of deuterated PAHs can provide fundamental, far reaching new insight and perspective into galactic and extragalactic processes.

In Chapter 7, a set of ISOPHOT spectra from a sample of H II regions in the Large Magellanic Cloud (LMC) is presented. The LMC spectra have been compared with ISO-SWS spectra from Galactic H II regions and with the ISOCAM observation towards a quiescent molecular cloud in the SMC (Reach et al. 2000). In this way, we can assess the influence of metallicity (direct or indirect) on the UIR bands. The relative strengths of the UIR bands vary considerably and a segregation between the sources in the different types of environment (Milky Way – LMC : others – LMC : 30 Dor – SMC) is present. Clearly, the PAHs are sensitive to the local phusical conditions.

In Chapter 8, we supplement the ISO data on two compact H II regions with high spatial resolution ground-based observations. We report the discovery of a new broad dust feature in one of the sources and compare its profile with those studied in Chapter 3. Likely, the carrier of this new emission band is related to PAH molecules. We examine the spatial variation of the PAHs and the different dust components and discuss the dependence on the local conditions. We highlight the possible heating mechanisms of the dust components and find that the dust is colocated with the ionised gas in the arcs of both H II regions while the PAH emission originates from the PDR. The carrier of this new dust feature also resides inside the H II region. Likely, the PAH molecules are destroyed inside the H II region by the energetic photons.

Finally, we will summarise the main results of this thesis and outline future research.

2

The ISO spectral catalogue of compact H II regions in the Galaxy

Based on :

E. Peeters, N.L. Martín-Hernández, F. Damour, P. Cox, P.R. Roelfsema,
J.-P. Baluteau, A.G.G.M. Tielens, E. Churchwell, M.F. Kessler,
J.S. Mathis, C. Morisset, D. Schaerer

Astronomy & Astrophysics, 381, 571, 2002

Abstract Infrared spectra between 2.3 and 196 μm were taken towards a sample of 45 compact H II regions using the two spectrometers (SWS and LWS) on board ISO. The primary goal is to determine the distribution of element abundances in the Galaxy, although there are also many other uses of this database. The spectra contain a wealth of information on the ionized gas and the associated photodissociation regions through the atomic fine-structure lines and on the dust properties via the dust emission bands and the continuum. Significant variations are found from source to source in both spectral shape and content. The sample of H II regions spans a wide range in galactocentric distance (from 0 to 22 kpc) enabling an investigation of the variations of the nebular properties across the Galactic plane. The observations and the data reduction are described in detail in the present paper. The ISO spectral catalogue of compact H II regions contains the combined SWS-LWS spectra for each of the sources, the fluxes of the atomic fine-structure lines and hydrogen recombination lines, and an inventory of the spectra in terms of molecular lines, dust and ice bands.

2.1 Introduction

H II regions are photoionized regions surrounding OB stars. When the O and B stars are newly formed, they are still deeply embedded in their parental molecular cloud and the associated regions of ionized gas are generally small (with linear sizes below $\sim 0.1\,\mathrm{pc}$) and dense ($n_\mathrm{e} \geq 10^4\,\mathrm{cm}^{-3}$). These 'ultracompact' H II regions evolve further into 'compact' H II regions when the dense, ionized gas grows in size at the expense of the molecular gas (e.g., Churchwell 1990; Garay & Lizano 1999). Ultracompact H II regions are known to be the most luminous objects in the Galaxy at far-infrared wavelengths (Churchwell 1990) and the dust in and around these regions absorbs most of the stellar luminosity which is then re-emitted in the infrared. Due to the high degree of obscuration, most ultracompact and compact H II regions can only be studied at radio and infrared wavelengths. Whereas many radio studies are available (e.g., Wood & Churchwell 1989; Garay et al. 1993; Kurtz et al. 1994; Afflerbach et al. 1996; Rudolph et al. 1996; Kurtz et al. 1999), observations of large samples of ultracompact and compact H II regions in the infrared have been done at either low spatial resolution or with poor resolving powers using the IRAS LRS data (e.g., Simpson & Rubin 1990) or ground-based observations (Faison et al. 1998). Observations of selected atomic fine-structure lines were made with the Kuiper Airborne Observatory (KAO) for ~ 40 compact H II regions (Simpson et al. 1995; Afflerbach et al. 1997; Rudolph et al. 1997, and references therein). Finally, detailed studies have been made from the ground towards a few sources (e.g., Roelfsema et al. 1989; Watarai et al. 1998; Feldt et al. 1998, 1999; Takahashi et al. 2000; Henning et al. 2001).

The two spectrometers on board the Infrared Space Observatory (ISO, Kessler et al. 1996), the Short Wavelength Spectrometer (SWS, de Graauw et al. 1996) and the Long Wavelength Spectrometer (LWS, Clegg et al. 1996), provided a unique opportunity to measure spectra from 2.5 to 196 μm with resolving powers $\frac{\lambda}{\Delta\lambda}$ between 150 and 500, towards 45 Galactic H II regions. The spectral coverage gives access to nearly all the atomic fine-structure and hydrogen recombination lines in the infrared range. In addition to the atomic emission lines, the ISO spectra reveal the shape of the strong dust continuum and several emission features. Absorption bands from molecular ice species were detected toward some sources. The observed H II regions were carefully selected to sample the Galactic disk out to 22 kpc from the center, permitting a study of Galactic abundance variations over a larger range than in previous studies. The information contained in the combined SWS-LWS grating spectra provides a basis for a broad range of studies including the properties of H II regions, the characteristics of associated dust and the abundance gradients in the Galaxy.

This Paper presents for each source the combined SWS-LWS spectrum, the measured line fluxes for all the atomic emission lines and the inventory of the detected molecular lines and the dust and ice bands. An accompanying Paper (Martín-Hernández et al. 2002a, hereafter Paper II) will discuss the first results of the properties of the compact H II regions and the element abundance as derived from the present data.

The sample of compact H II regions with their observations are discussed in Sect. 2.2. Sect. 2.3 gives a detailed description of the reduction of the SWS and LWS data; the line flux determination, the error determination and the influence of the source structure on the observed fluxes are discussed in Sect. 2.4. Sect. 2.5 compares the ISO data with corresponding KAO and IRAS observations. Characteristics of the H II regions such as the kinematic distance, the luminosity and the morphology are described in Sect. 2.6. The ISO spectra, the

line fluxes, the detected molecular lines and dust and ice bands are discussed in Sect. 2.7 for each H II region of the sample. This Sect. contains the core of the paper. A summary is given in Sect. 2.8. The tables of line fluxes and the spectra are presented in the Appendix 2.A.

2.2 Observations

In the Ultracompact H II Region (UCH II) ISO program, a total of 45 H II regions were observed using the SWS and the LWS in the grating mode yielding complete spectra from 2.3 to 196 μm. The data were obtained with two guaranteed time programs (ISM_IV01 and ISM_IV02) as well as a solicited proposal (ZZ_ISM).

2.2.1 The sample

The H II regions were selected primarily to be observable with the SWS and the LWS. First, the sources were required to be bright enough (at least a few Jy in the IRAS 12 μm band) to ensure detectability with both instruments. Second, the nebulae had to be compact with sizes smaller than the SWS and LWS beams (i.e. $\lesssim 20''$) so that all the nebular flux is within both beams. Six sources are point-like for the ISO spectrometers, i.e. with mid-infrared sizes $\leq 5''$. Third, to minimize confusion problems, isolated regions were prefered over sources lying in complexes. Finally, the sources were chosen to cover as wide a distribution as possible in galactocentric distance in order to derive the Galactic element abundance over larger scales than in previous studies. ISO was pointed at the IRAS positions of the selected IRAS sources. The sample was enlarged by DR 21 and Sgr C.

For two of the sources, IRAS 18316−0602 (also known as GL7009) and IRAS 19110+1045, the 2.3 to 196 μm spectra were found to be dominated by absorption and they are not considered in this catalogue. A detailed analysis of their spectral content can be found in Dartois et al. (1998). The sample considered for this catalogue consists therefore of 43 H II regions which are listed in Table 2.1. For each source, the name, the equatorial coordinates of the position observed with the SWS and LWS, the date of the observation, the Target Dedicated Time (TDT) of the observations (which uniquely identifies each observation) and some other common designations are given in Table 2.1. For the majority of the sources, the SWS and LWS observations were concatenated, i.e. the LWS spectrum was measured immediately after the SWS observation was completed. For Sgr C, only an SWS spectrum was taken in the UCH II ISO program and the LWS full grating spectrum was extracted from the ISO archive.

2.2.2 The SWS observations

The SWS grating spectra were taken in the so-called Astronomical Observation Templates 01 (AOT 01) full scan mode (de Graauw et al. 1996) speed 2. The SWS has two spectrometer sections. : the short wavelength section (SW) covering 2.3 to 12 μm, and the long wavelength section (LW), from 11 to 45 μm, yielding a total wavelength coverage of 2.3-45 μm. The combined spectrometer sections are composed of 12 separate grating bands, the AOT bands (see Table 2.2). Each AOT band is defined through a combination of detector array (1×12 detectors), instrument aperture and grating order. The SWS has three apertures with sizes of $14'' \times 20''$ for band 1 and 2, $14'' \times 27''$ for band 3A ,3C and 3D, $20'' \times 27''$ for band 3E and $20'' \times 33''$ for band 4.

Table 2.1 — Journal of observations. The coordinates of the positions observed with ISO are given.

Source	RA* (J2000.0)	Dec* (J2000.0)	Date	TDT$^\diamond$ SWS	TDT$^\diamond$ LWS	Galactic name	Other designations
IRAS 01045+6506	01 07 50.7	+65 21 21.7	18-Mar-98	85303602	-	G124.64+2.54	WB 380
IRAS 01420+6401	01 45 39.6	+64 16 02.1	21-Jul-97	61301076	61301075	G128.77+2.01	WB 399
IRAS 02219+6125	02 25 44.6	+62 06 11.3	23-Aug-97	64600609	-	G133.70+1.20	W3 A, RAFGL 326
			11-Jan-98	78800709	78800710		
IRAS 02383+6241	02 42 19.8	+62 53 51.8	3-Mar-98	83901404	83901403	G135.18+2.69	WB 436
IRAS 02575+6017	03 01 31.3	+60 29 13.5	27-Mar-98	86300968	86300969	G138.29+1.55	WB 463, RAFGL 4029
IRAS 04025+5313	04 06 25.5	+53 21 50.0	26-Sep-97	68100312	68100305	G149.59+0.90	WB 529
IRAS 05167+3858	05 20 11.1	+39 01 19.7	22-Aug-97	64501216	64501206	G168.68+1.08	WB 625
IRAS 05221+4139	05 25 39.8	+41 41 50.3	22-Aug-97	64501104	64501107	G167.06+3.46	WB 640
IRAS 05302+3739	05 33 40.1	+37 41 07.3	22-Aug-97	-	64501371	G171.26+2.54	WB 656
IRAS 05335+3609	05 36 52.6	+36 11 00.3	8-Oct-97	-	69201373	G172.87+2.26	WB 668
IRAS 06158+1517	06 18 44.8	+15 16 43.4	13-Mar-98	84901804	84901903	G195.65−0.10	Sh 266, WB 794
IRAS 10589−6034	11 00 59.8	−60 50 27.1	11-Aug-96	26800760	26800723	G289.88−0.79	RAFGL 4122
IRAS 11143−6113	11 16 33.8	−61 29 59.4	5-Aug-96	26200509	26200510	G291.86−0.68	RAFGL 4127
IRAS 12063−6259	12 09 01.1	−63 15 54.7	2-Aug-96	25901414	60900713	G298.19−0.78	RAFGL 4144
IRAS 12073−6233	12 10 00.3	−62 49 56.5	2-Aug-96	25901572	25901573	G298.23−0.33	
IRAS 12331−6134	12 36 01.9	−61 51 03.9	10-Sep-96	29900470	29900475	G301.11+0.97	
IRAS 15384−5348	15 42 17.1	−53 58 31.5	10-Sep-96	29900661	29900628	G326.44+0.91	
IRAS 15502−5302	15 54 06.0	−53 11 36.4	5-Aug-97	27301117	62802718	G328.31+0.43	
IRAS 16128−5109	16 16 39.3	−51 16 58.3	6-Sep-96	29402233	29402234	G332.15−0.45	
IRAS 17160−3707	17 19 26.1	−37 10 53.8	6-Oct-96	32400821	32400822	G350.10+0.09	
IRAS 17221−3619	17 25 31.7	−36 21 53.5	12-Oct-96	33100380	33100376	G351.46−0.44	
IRAS 17279−3350	17 31 18.0	−33 52 49.4	3-Oct-96	32200877	32200878	G354.20−0.05	RAFGL 5347

Table 2.1 — Continued.

Source	RA* (J2000.0)	Dec* (J2000.0)	Date	TDT$^\diamond$ SWS	TDT$^\diamond$ LWS	Galactic name	Other designations
Sgr C	17 44 35.6	−29 27 29.3	5-Mar-98	84100301	-	G359.43−0.08	
	17 44 35.9	−29 27 54.3	11-Mar-98	-	84700220		
IRAS 17455−2800	17 48 41.5	−28 01 38.3	29-Aug-96	28701327	28701328	G1.13−0.11	Sgr D
IRAS 17591−2228	18 02 13.2	−22 27 58.9	14-Apr-97	51500580	51500579	G7.47+0.06	
IRAS 18032−2032	18 06 13.9	−20 31 43.2	14-Apr-97	51500478	51500477	G9.61+0.20B	RAFGL 5436
IRAS 18116−1646	18 14 35.2	−16 45 20.6	13-Apr-96	14801733	14801732	G13.88+0.28	
IRAS 18162−2048	18 19 12.0	−20 47 31.1	13-Apr-96	14802136	14802135	G10.84−2.59	RAFGL 2121
IRAS 18317−0757	18 34 24.9	−07 54 47.9	8-Mar-97	47801040	47801041	G23.96+0.15	RAFGL 2194
IRAS 18434−0242	18 46 04.0	−02 39 20.5	17-Apr-96	15201383	15201381	G29.96−0.02	RAFGL 2245
IRAS 18469−0132	18 49 33.0	−01 29 03.7	26-Oct-97	71100888	71100887	G31.40−0.26	
IRAS 18479−0005	18 50 30.8	−00 01 59.4	17-Apr-96	15201791	15201792	G32.80+0.19	RAFGL 5536
IRAS 18502+0051	18 52 50.2	+00 55 27.6	17-Apr-96	15201645	15201645	G33.91+0.11	RAFGL 5541
IRAS 19207+1410	19 23 02.4	+14 16 40.6	15-Apr-96	15001041	15001039	G49.20−0.35	RAFGL 2379
IRAS 19442+2427	19 46 20.1	+24 35 29.4	15-Apr-96	15000444	15000443	G60.90−0.10	RAFGL 2454, Sh 87
IRAS 19598+3324	20 01 45.6	+33 32 43.7	11-Apr-96	14601350	14601348	G70.29+1.60	K3-50 A
			4-Dec-96	38402466	-		
DR 21	20 39 00.9	+42 19 41.9	17-Apr-96	15200555	15200786	G81.70+0.54	RAFGL 2624
IRAS 21190+5140	21 20 44.9	+51 53 26.5	24-Apr-96	15901853	15901854	G93.53+1.47	M1-78
IRAS 21270+5423	21 28 41.9	+54 36 51.5	13-Feb-98	82100309	82100310	G96.29+2.59	Sh 127A, WB 85A
IRAS 21306+5540	21 32 11.4	+55 53 23.9	15-Feb-98	82301012	82301011	G97.52+3.18	Sh 128, WB 91
IRAS 22308+5812	22 32 45.9	+58 28 21.0	12-May-96	17701258	17701257	G105.63−0.34	Sh 138, WB 191
			30-May-97	56101082	56101081		
IRAS 23030+5958	23 05 10.6	+60 14 40.6	24-Jun-96	22000961	22000962	G110.10+0.05	Sh 156, WB 240
IRAS 23133+6050	23 15 31.4	+61 07 08.5	24-Jun-96	22001506	22001505	G111.62+0.37	Sh 159, WB 261

(*) Units of RA are hours, minutes, and seconds; units of Dec are degrees, arcminutes, and arcseconds. ($^\diamond$) Target Dedicated Time.

Table 2.2 — The SWS AOT bands and LWS detectors.

SWS			LWS	
Band	λ * (μm)	$1\sigma^{\diamond}$ (%)	Detector	λ * (μm)
1A	2.38 – 2.61	4	SW 1	43.0 – 50.5
1B	2.60 – 3.03	4	SW 2	49.5 – 64.0
1D	3.02 – 3.53	4	SW 3	57.0 – 70.0
1E	3.52 – 4.06	4	SW 4	67.0 – 82.0
2A	4.05 – 5.31	8	SW 5	76.0 – 93.0
2B	5.30 – 7.01	8	LW 1	84.0 – 110.0
2C	7.00 – 12.1	8	LW 2	103.0 – 128.0
3A	12.0 – 16.6	16	LW 3	123.0 – 152.0
3C	16.5 – 19.6	16	LW 4	142.0 – 171.0
3D	19.5 – 27.6	16	LW 5	161.0 – 196.0
3E	27.5 – 29.0	23		
4	28.9 – 45.2	25		

* Official band ranges; $^{\diamond}$ 1σ absolute flux accuracy (R. Shipman, private communication); SW = short-wavelength section, LW = long-wavelength section.

In the AOT 01 mode, spectra are taken by scanning the grating over its full mobility range and back. Thus, for each detector of a detector array and each AOT band two independent scans are obtained; one 'up' and one 'down' scan. As a result, 24 independent measurements of the incident spectrum are obtained (i.e. 2 scans $\times$ 12 detectors). Due to the sampling strategy of the SWS AOT 01 mode, each of these independent measurements individually is under-sampled. However, because the measurements are obtained at slightly different wavelength offsets they can be combined to yield a factor of four oversampled spectrum. The spectrum nominally has a spectral resolving power of $\frac{\lambda}{\Delta\lambda} \sim 450$ and a wavelength accuracy of about 10% of a resolution element. By comparing the independently reduced up and down scans for a given source, an estimate of the instrumental uncertainty can be obtained.

For calibration purposes, the compact H II region K3-50 A has also been observed with the SWS in the AOT 01 mode speed 4 yielding a spectral resolving power of $\simeq$ 1600. The results on K3-50 A reported in the catalogue refer to the AOT 01 mode speed 4 data (TDT = 38402466).

2.2.3 The LWS observations

The LWS spectra were measured using the LWS AOT 01 mode (Clegg et al. 1996). The LWS has two spectrometer sections : the short wavelength section (SW) covering 43 to 93 μm, and the long wavelength section (LW), from 84 to 196 μm, yielding a total wavelength coverage of 43-196 μm. Each spectrum consists of ten overlapping sub-spectra, one for each of the ten detectors. The LWS field of view is restricted by an internal field mirror to provide an

approximately circular footprint on the sky with a wavelength dependent diameter of $\sim 80''$ (for the exact diameter see the ISO Handbook Volume IV: 'LWS - The Long Wavelength Spectrometer' by Gry et al. 2000). The official wavelength ranges are given in Table 2.2 for the ten LWS detectors.

In the AOT 01 mode, spectra are taken by scanning the grating 3 times over its full mobility range and back. For each target, 6 scans are obtained, 3 in 'up' and 3 in 'down' direction. Combined these scans yield a spectrum sampled at 1/4 of a spectral resolution element. The resolution element is 0.283 μm for detectors SW1–SW5 (43–93 μm) in second spectral order and for detectors LW1–LW5 (84–196 μm) in first order, it is 0.584 μm. The resolving power, $\frac{\lambda}{\Delta\lambda}$, of the LWS grating spectra varies from 140 to 330. Analoguous to SWS, an estimate of the instrumental uncertainty can be obtained by comparing the independently reduced up and down scans for a given source.

2.3 Data reduction

One of the aims of this study is to derive line ratios across the available wavelength range and to combine the spectra measured by the SWS and the LWS. This requires a detailed understanding of the calibration between: i) the two spectrometers, ii) the different bands of the SWS, and iii) the different detectors of the LWS. This knowledge will define the limits of the present dataset and constrain any conclusion one can draw from the line fluxes given in the tables of this catalogue.

The following gives a detailed account of the reduction of both the SWS and the LWS data. Since the SWS reduction requires more steps than the LWS reduction and since new methods were applied, we describe in more detail the SWS data reduction.

2.3.1 SWS data reduction

The SWS data were processed with IA^3, the SWS Interactive Analysis package (de Graauw et al. 1996) using calibration files and procedures applied in the IA^3 test version of Aug 4, 2000 (except for the flux calibration files, see Sect. 2.3.1), corresponding to a stable test-phase of OLP10 (Off-Line Processing 10).

For a general description of the SWS instrument and its reduction, we refer to the ISO Handbook Volume VI : 'SWS - The Short Wavelength Spectrometer' by Leech & the SWS Instrument Dedicated Team and the SWS Instrument Support Team (2001). The standard reduction process consists of corrections for the electronics of the system, dark current subtraction, correction for the relative spectral response of the instrument (RSRF) and wavelength and flux calibration. Finally, the wavelengths are corrected for the ISO velocity resulting in an Auto Analysis Result (AAR).

In the following Sects., the additional reduction steps applied to the data presented here, the final calibration errors and the unresolved problems are described.

Additional reduction steps

In the AOT 01 mode, the grating scanner moves within one reset interval while the detectors are integrating. Hence, during a single integration, radiation of different wavelengths is observed and thus signal from line and continuum emission is mixed. As a result the slope of the integration ramp shows a change. When the contrast between the continuum signal and line signal is large enough, this will give such a sharp slope change that it is flagged as

a glitch (i.e. a cosmic ray hit) in OLP versions earlier then OLP10. Hence, in combining the detector measurements by rebinning the data, the peak of the line is not properly reconstructed due to the missing high flux samples. Hence, the total flux of the atomic line will be underestimated. In the present analysis, automatic glitch detection and removal was only applied in wavelength regions where no line emission is expected. Afterwards, the line regions are checked manually for glitches at the AAR level. Since strong glitches left in the data will influence the average flux of the detectors, this is done for each detector separately before flat-fielding the detectors.

The Si:Ga detectors of band 2 and the Ge:Be detectors of band 4 exhibit memory effects. The detector responsivity is not constant and their response to a sudden flux change is not 'instantaneous' with respect to the time resolution of the SWS read-outs. Both effects depend on the present illumination, the detector operating parameters (bias, temperature) and the illumination history during the last hours. Generally, compact H II regions have strong increasing continuum in this wavelength region. As a result memory effects strongly affect the shape of the underlying continuum. Especially when comparing the 'up' and 'down' scans, large differences are seen due to the fact that the 'flux history' as perceived by the detectors is different for the two directions. This detector memory effect has been studied extensively by Fouks and Schubert who have proposed a model for the behaviour of the Si:Ga detectors (Fouks & Schubert 1995). For the band 4 Ge:Be detectors no satisfactory model has been established to date. For the SWS band 2 detectors, a detector memory effect correction algorithm based on the Fouks & Schubert formalism has been implemented (see Kester 2001). This algorithm was applied to all band 2 data. For the resulting corrected data generally the 'up' and 'down' scans agree within a few percent.

The flux calibration files were updated while reducing the sample sources (corresponding to the final post-mission calibration, OLP10; Shipman & Lahuis (2000)). In order to get the final line fluxes, we multiplied the spectra and the measured line fluxes by a factor corresponding to the ratio of the used to the new flux scale calibration factors.

Within filter elements or within the detector material - especially for the band 3 detectors - multiple reflections between the element front and back surfaces may occur. The resulting interference fringes appear as a high frequency modulation of the detector output signal. To some extent all detector bands suffer from fringes. Bands 1, 2 and 4 are only lightly affected, whereas the fringes are more pronounced in band 3. These fringes can be corrected by fitting cosine functions to the data in wavenumber space and dividing the observed fluxes by those functions. This procedure was applied to bands 3C, 3D and 3E, where the fringes are resolved. Only for the high resolution data of K3-50A, fringes are also resolved and hence removed in band 3A.

The final reduction steps are applied at the AAR level. Strong glitches left in the spectra are removed manually (see above). The signals of the 12 detectors of a given AOT band are then all flat-fielded to the average level. Subsequently, for each resolution bin, the median and the standard deviation are calculated. Each point whose deviation from the mean is more than 2.5 times the standard deviation is removed when situated in line-free spectral regions. Remaining bad data points are manually removed. Finally, all detector data are rebinned to a wavelength grid with a spectral resolution of ~ 450.

In case of sources with no or low flux, the reduction process is simplified. Since the deglitching method only influences the flux of strong lines, deglitching is applied to these sources. Furthermore, for each resolution bin, the median and the standard deviation are

calculated. Each point that deviates from the mean by more than 2.5 times the standard deviation is removed when situated in *all* spectral regions.

Final calibration accuracies

The final absolute flux scale accuracies for the calibrated SWS spectra are given in Table 2.2. For each AOT band the 1σ accuracy is given including the SWS absolute flux calibration error and the uncertainties in the synthetic stellar models used in establishing the absolute flux scale.

The intrinsic wavelength scale accuracy for SWS was established early on in the ISO mission to be better than $\lambda/\Delta\lambda \geq 5000$ (Valentijn et al. 1996). For the resolution of ~ 450 of the data presented here, this corresponds to $\leq 10\%$ of a resolution element. However due to the limited accuracy of the satellite pointing and the offset of the given coordinates from the source peak position in some cases, the sources are not always centred in the SWS aperture. Since the observed wavelength directly depends on the angle of incidence of the radiation on the grating, an offset position translates into a slight wavelength shift. Thus, satellite pointing errors lead to an increase in the wavelength error resulting in an overall wavelength accuracy of about 1/3 to 1/6 of a spectral resolution element.

Unsolved problems

For SWS, a few problems still remain in the calibration. These problems and their consequences for the data presented here are discussed in the following paragraphs.

- **Pointing errors** Since the SWS sensitivity (given by the beamprofiles), is not uniform across the instrument aperture (see Salama 2001), a spatial offset will generally result in a lower flux than what would have been observed at the centre of the aperture. Such an offset can be due to pointing effects of the satellite, to incorrect coordinates of the centre of the source or to the extent of sources. For extended sources, different positions corresponds to different sensitivities. Each AOT band has its own beamprofile (see Salama 2001).

- **Spurious spectral features** During the calibration process, the RSRF was fine-tuned to fit three narrow features in band 2C (9-9.3 μm, 10.1 μm and 11.0 μm) and one feature in band 3A (12.3 μm) which are believed to be instrumental since they were seen in all sources with the same strength and width. Although corrected, the shape of the RSRF in these regions is still less reliable than in the rest of the AOT band.

- **Band 2A** For most sources, the noise in band 2A dominates the spectra in this wavelength region (see Fig. 2.6). The noise level in band 2A is considerably higher than in other bands. In addition, compact H II regions have a low flux continuum in this wavelength range.

- **Band 3** Due to insufficient suppression of different grating orders, some of the radiation at wavelengths of approximately 13 μm is transmitted through the optical path corresponding to the long wavelength band 3D. As a result of this leakage, the slope of the continuum in band 3D is not certain longwards of 26 μm.

  Band 3E has a very small extent in wavelength causing difficulties in its calibration. This results in a significantly higher flux scale error of 23% (see Table 2.2) as well as

in a relatively poor quality spectral responsivity curve. Thus, the overall shape of band 3E continuum is not very reliable.

These two problems can lead to the appearances of spurious features which are sometimes mistaken for dust emission features (e.g. the 22 μm feature, Chan & Onaka 2000).

- **Incomplete removal of fringes** Although the procedure for removing fringes is generally very successful in the centre of AOT bands, in some cases at the edges of a band some residual fringing is left. However, this does not significantly affect the measured line intensities. Some fringes are left in the spectrum K3-50A.

- **Overlap 2C-3A** As can be seen in the spectrum of IRAS 12073, IRAS 15502, IRAS 18434, K3-50A and DR21 in Fig. 2.6, band 2C and band 3A do not show similar flux in their overlap region (between 12 and 12.7 μm). Poor matches between different AOT bands can often be understood from a combination of dark current uncertainties and a steep RSRF in the overlap region. Dividing the data by the RSRF, when the dark current subtraction was not done properly, will induce incorrect shapes in regions where the RSRF shows features or where the RSRF has a steep slope (i.e. at the ends of the bands). For band 2C, deviation of the intrinsic flux can be due to improper correction for memory effects. This should be seen when comparing the up and down scan. The resulting effect on the line flux of [Ne II] is however less severe than the aperture effect and the calibration error.

- **Band 4** As explained in Sect. 2.3.1, band 4 detectors suffer strongly from memory effects and to date no proper correction method has been devised. As a result, the continuum between 29 and 45 μm is not well reconstructed. The 'up' and 'down' scans in this wavelength range can show differences by as much as 30%. Even the signal level around some of the strong lines in this band is affected in that they show tails due to memory effects. To make things worse, the Ge:Be detectors of band 4 are much more sensitive to cosmic particle hits than the other bands. The resulting glitches are almost impossible to correct due to their tails caused by memory effects. As a consequence of these problems together, the shape of band 4 is uncertain, e.g. DR21 presents an extreme example (see Fig. 2.6) and the fluxes of lines in this band have relatively high errors (see Table 2.8).

  Apart from the difficulty in the shape of the underlying continuum due to the detector memory effects and their interplay with the cosmic particle hits, there appear to be some features within band 4 that could be related to calibration problems in the RSRF. For this wavelength range, no well understood calibration sources have been found to date. As a result, the RSRF is entirely derived from pre-flight ground based tests, which means this curve is valid only for extended sources uniformly filling the SWS beam. It is suspected that the sharp 'kink' around 33 μm as well as the plateau around the 33.47 μm [S III] line are due to errors in the RSRF.

  When corrections for band 4 detector memory effects and/or a better responsivity curve become available the data will be re-analysed and better quality line fluxes can be published.

Remarks

A sinusoidal wave is present in the reduced spectrum of K3-50A in band 3A (see Fig. 2.6), as well as in the raw data. The origin of this wave is unclear to us.

The observation with TDT number 64600609 is plotted in the SWS region for W3 since the band overlaps are slightly better in this spectrum. For IRAS 22308, the SWS spectrum with TDT number 17701257 is shown, the LWS part has TDT number 17701258. Again, for the SWS part, this spectrum has a slightly higher quality. For LWS, we took the observation obtained immediately after the SWS observation plotted here. When comparing these two observations of the same source in the SWS wavelength regime, differences can be found because the orientation of the aperture is not the same and the source is extended. For the LWS regime, the aperture position and orientation is the same for both observations.

2.3.2 LWS data reduction

The LWS observations are calibrated using the pipeline version 8.7. For a detailed description of the instrument and its reduction we refer to Swinyard et al. (1998) and the ISO Handbook Volume IV: LWS - The Long Wavelength Spectrometer by Gry et al. (2000).

LWS data was calibrated following the standard reduction steps, which basically include: first-level deglitching, responsity drift and absolute response correction, dark current subtraction and finally, wavelength and flux calibration. These processes yield the Auto Analysis Result (AAR).

Additional reduction steps

The dark signal subtraction is a crucial step for very faint sources because a wrong subtraction can lead to negative photocurrent values and to large differences in the flux levels between the sub-spectra. Therefore, the faint sources were reprocessed with the LWS Interactive Analysis Software (LIA) in order to refine this process. LIA also allows us to redo the drift and absolute responsivity corrections, but these tools were not used as their improvement over the pipeline was found to be small.

The post-pipeline analysis of the AAR was performed with the ISO Spectroscopy Analysis Package (ISAP). First of all, the deglitching done in the pipeline removes a large part of the glitches, but some of them or their tails can remain in the data. Furthermore, some glitches may cause latency effects on the detector response which may cause part of a scan for one detector to be higher than the others for some period of time. ISAP permits the removal of these bad data. This step is followed by taking the average of all the 6 scans for every detector and the correction for fringes.

Fringes are caused by the interference of two beams (one beam arising from the normal reflection from the LWS field mirror and another from the support structure holding this mirror) which propagate along the instrument with a time delay between them. All detectors are in principle influenced, but the long wavelength detectors are most affected. Fringes occur in the spectra when the source is extended (i.e. $> 20''$) and/or structured, or when a point-like source is mispointed or when a point-like source is observed against a strong background. The latter is common for sources that lie in the Galactic plane, such as H II regions. The fringes are then expected at the longer wavelengths where the intrinsic emission of the source decreases and becomes comparable to the Galactic background emission. These fringes affect

the continuum as well as the [O I] and [C II] lines at 145 and 158 μm. They are corrected for in ISAP by dividing out a sinusoidal function with a wavelength dependent amplitude.

Final calibration accuracies

The intrinsic wavelength calibration accuracy achieved in the grating mode is better than 1/4 of a resolution element of the grating, i.e. 0.07 μm for the SW detectors and 0.15 μm for the LW detectors.

A 10% absolute flux uncertainty is a "reasonable" value for the majority of the LWS observations for all but the SW1 detector. The calibration of the SW1 detector is worse compared to the other detectors, yielding a higher absolute flux uncertainty. In case of very faint sources ($<$ 100 Jy at 100 μm), very bright sources ($>$ 50000 Jy at 100 μm), extended sources with a complex morphology, sources not centred in the beam or sources observed against a strong background, the absolute flux uncertainty can be higher. An indicator for the latter is the scatter between adjacent detectors in the defringed and aperture corrected spectrum.

Unsolved problems

- **Differences between overlapping sub-spectra** The continuum flux in the SW1 detector is on average $\sim$ 20% higher than the continuum flux in the adjacent detector, varying from about 50% for IRAS 05335 to a good agreement in the case of IRAS 18116. For the other detectors, the differences in flux in the overlapping regions are much lower, ranging from a few % up to 20% in a few cases.

- **Incomplete removal of fringes** The routine in ISAP used to remove fringes worked successfully except in the case of some very strong sources (for instance IRAS 18434 and IRAS 19598) where a spurious broad feature centred at 127 μm with a FWHM of $\sim$2 μm is found in detector LW3. This broad feature causes an insufficient removal of fringes resulting in a poor determination of the continuum for the [O I] 145 μm line observed in this detector.

- **Spurious features** Spurious features are found in most of the spectra at 112.0 μm (in detector LW2), at 141.8 μm and at 146.5 μm (the latter two in detector LW3). The former is identified as HD R(0); the emission at 146.5 μm almost blends with the [O I] emission line at 145 μm. These are probably absorption features of Uranus which appear as emission lines in the output product. In addition, there is a spurious broad feature centred at 127 μm, as discussed above.

- **Memory effects** Memory effects, which appear as slope differences between both scan directions, are due to the different response of the detectors depending on whether the signal increases or decreases with time. SW1 is always affected by this problem. The other detectors are only troubled in the case of strong and intermediate sources. Detector SW2 is specially affected in strong sources, influencing the [O III] line at 51.8 μm. For intermediate sources, memory effects are mainly present, although in a much lower degree, in detectors LW2, LW3 and LW4. To date, no correction tool is available. Hence, both scan directions are reduced separately in order to quantify this effect.

- **Non-linear detector behaviour** For very strong sources (of the order of 10000 Jy), the long wavelength detectors (especially LW3) can have a non-linear response and saturate. As a result, the shape of the sub-spectra sags in the middle. Only detector LW3 in the strongest sources (e.g. IRAS 02219, IRAS 18434 and IRAS 19598) seems to be affected by this problem. A test on IRAS 19598 was made by reprocessing the data with 1/4 second ramps. However, the overall shape of the LW3 detector, dominated by the spurious broad feature mentioned earlier, did not improve.

2.3.3 Extended source calibration

The SWS calibration (except the flux calibration of band 4) and LWS calibration are entirely based on point sources. To correct for source structure within the instrument beam at any given wavelength, the beam profile has to be convolved with the source brightness distribution. This correction can only be applied when the source structure is known *at all wavelengths in the spectrum, both for the continuum emitting regions and for the line emitting regions*. Such a detailed knowledge of the source structure is not available for any of the H II regions discussed in this paper.

In addition, for the LWS detectors, a substantial fraction of the flux from an on-axis point source is diffracted out of the aperture. Because the calibration is applied to point sources observed on axis, these losses are automatically corrected for. However, these diffraction losses do not occur in the case of extended sources and so the flux of these sources is overestimated.

The spectra have therefore been derived assuming that the sources are point-like for both SWS and LWS and on axis for LWS. The jumps occuring at the SWS band edges and/or at the junction of the SWS and the LWS spectra and/or at the overlap of two LWS detectors can be caused by this effect. The line fluxes listed in Tables 2.8, 2.7 and 2.9 , also assume that the sources are point-like and on axis. For extended sources, conversion factors (depending on the wavelength) should be applied to convert the fluxes from Jy to MJy/sr. The conversion factors for an *infinitely extended and homogeneously distributed* source at the key wavelength of each AOT band and LWS detector are given in Salama (2001) and can be applied, if desired, for both the spectra and the presented fluxes. These extended source correction factors are illustrative so caution should be taken when applying them.

2.4 Line fluxes

2.4.1 Gaussian fits

The fluxes of the lines in the SWS and LWS spectra are measured by fitting a Gaussian with the interactive line-fitting routine in ISAP. For the lines in the LWS spectrum, the FWHM of the Gaussian fits was kept fixed with a value equal to the spectral resolution element of the data ($0.283\,\mu\mathrm{m}$ for lines in detectors SW1-5, and $0.584\,\mu\mathrm{m}$ for detectors LW1-5). The FWHM in the fit of the SWS lines was kept as a free parameter as it changes with wavelength. The line fluxes were measured in the independently reduced ‘up’ and ‘down’ scans and in the combined spectrum. The latter measurement gives an estimate of the statistical error of the line flux through the error in the fit. The difference in the line fluxes measured in the ‘up’ and ‘down’ scans, on the other hand, provides an estimate of the systematic error coming from memory effects and the uncertainty in the choice of the local continuum. The error listed in Tables 2.8, 2.7 and 2.9 is the square root of the quadratic sum of these two errors (the calibration uncertainties are *not* included in these listed errors).

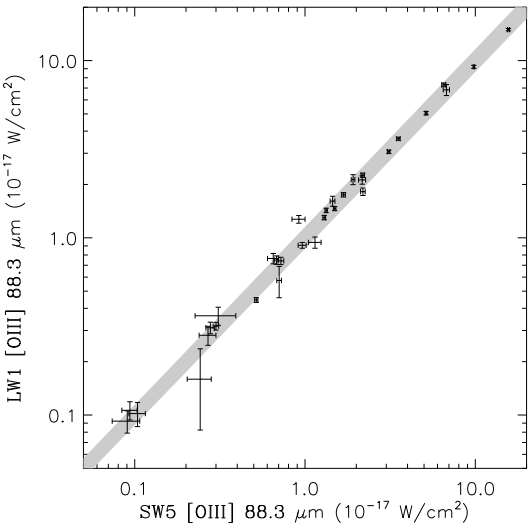

Figure 2.1 — Comparison of the [O III] 88.3 μm fine-structure line present in both the SW5 and the LW1 detector. The error bars correspond to the maximum of the fit error and the up-down error (see text). The grey band corresponds to the 10% calibration uncertainty expected for both detectors.

A line is defined as being detected if it is present in both the up and the down scan, its peak intensity is two or more times higher than the rms noise of the local continuum and when the line has a FWHM of the spectral resolution element. For any line which does not fulfil all these criteria, an upper limit for the flux is derived. The upper limits are defined as the flux of a feature with a peak flux three times the continuum rms noise and a width equal to the instrumental resolution element.

A few lines occur in the overlap region of SWS AOT bands. Usually, one of each pair of lines is incompletely covered or falls outside the 'official' wavelength range of the band, where the sensitivity of the detector has dropped dramatically and the line in the other band is used. The lines in these overlap regions listed in Tables 2.8 and 2.9 are Brβ in 1B, H I (10-5) and H I (9-5) in 1D, H I (8-5) in 1E, H I (14-6) and Brα in 1E and [Ar II] 7 μm in 2C.

For the LWS observations, some of the fine-structure lines were measured simultaneously by two adjacent detectors, e.g. the [O III] 88 μm line by the SW5 and LW1 detectors, and the [O I] 145 μm line by LW3 and LW4. For the sample of H II regions, the fluxes for the [O III] 88 μm line agree very well as shown in Fig. 2.1. Judging from Fig. 2.1, the 10% calibration uncertainty associated with these detectors is a conservative estimate. The value quoted in Table 2.7 is the weighted mean flux of both lines. This has not been applied to the [O I] 145 μm line, for which only the line flux measured in detector LW4 is listed, as the line in detector LW3 is heavily affected by fringes and its local continuum is very difficult to determine (see Sect. 2.3.2).

2.4.2 Error budget

In order to calculate the final error on the line fluxes, a description of the errors that are involved, is given. First, by fitting the observed line with a Gaussian, a statistical error of the line flux is obtained through the error in the fit. Second, an additional error is obtained by the difference in the line fluxes measured in both the - independently reduced - up and down scans. Third, all SWS AOT bands and LWS detectors have an absolute flux uncertainty.

This absolute flux uncertainty is discussed in Sect. 2.3.1 for SWS and in Sect. 2.3.2 for LWS. Fourth, all steps in the reduction process involve additional errors. Recently, a full error propagation is done for each detector flux for the applied SWS reduction process (implemented in the test version of IA by fall 2000). Since, this was not included in the pipeline at the time the reduction was done, this error estimate is not available. The total error on the line flux is generally dominated by the absolute flux uncertainty.

Errors on line ratios

For two lines in the same AOT band (for SWS) or in the same detector (for LWS), the uncertainty in the absolute flux will cancel out when taking a ratio of them. Hence, in this case, the final error on the line flux, used to calculate the error on the considered line ratio, will be the square root of the quadratic sum of the statistical error coming from the Gaussian fit and the error derived from the difference between the up and down scan measurements (i.e. the error listed in Tables 2.8, 2.7 and 2.9).

When the lines of a line ratio are observed in different SWS AOT bands or LWS detectors, the total error on each individual line flux must include the absolute flux uncertainty of the SWS AOT band or LWS detector in which the line is observed. In this case, the error, ϵ, on each individual line is based on the following formalism :

$$\epsilon = \sqrt{\epsilon_{\rm gauss}^2 + \epsilon_{\rm mem}^2 + \epsilon_{\rm absflux}^2}$$

where $\epsilon_{\rm gauss}$ is the statistical error coming from the Gaussian fit, $\epsilon_{\rm mem}$ is the error coming from the difference between the up and down scan measurements and $\epsilon_{\rm absflux}$ is the absolute flux uncertainty of the AOT band / detector that observed the considered line. In most cases, the error is dominated by the absolute flux uncertainty.

2.4.3 Influence of source morphology and size on the observed line fluxes

The extent and structure of some sources (see Sect. 2.6.2) influence the observed line fluxes in two ways. First, the aperture size changes with wavelength (see Sect. 2.2.2 and Sect. 2.2.3). Second, the morphology, the size of the source, the offset from the source peak position and the pointing error of the satellite are important for the observed flux due to the instrumental beam profiles (see Sect. 2.3.1, Sect. 2.3.2 and Sect. 2.3.3). Several sources, flagged in Tables 2.8 and 2.9, show offsets between the SWS pointing and the radio source peak position of more than 10 $''$. Other sources (e.g. IRAS 17279) show complex structure. Hence, care should be taken in the interpretation and analysis of the data.

2.5 Comparison with other instruments

2.5.1 Comparison with KAO

For a number of H II regions in the present sample, fine-structure lines were measured with the KAO (see Table 2.3 for references). For the [O III] 51.8 and 88.3 μm and the [N III] 57.3 μm lines, the LWS line fluxes are systematically higher compared to the KAO fluxes (see Fig. 2.2, top panel). However, their ratio is smaller than the aperture ratio suggesting that the sources are more extended than the KAO beam but smaller than the LWS beam at these wavelengths. Analogous, for the [S III] 18.7 and 33.5 μm and [Ne III] 36.0 μm lines,

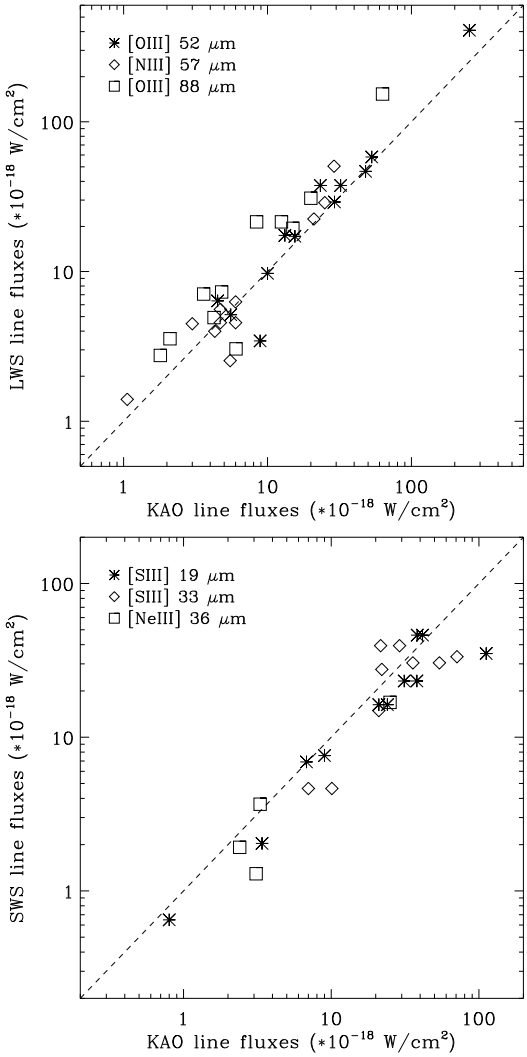

Figure 2.2 — Comparison of the LWS and KAO line fluxes for [S III] 18.7 μm, [S III] 33.5 μm and [Ne III] 36.0 μm fine-structure line (top panel) and for [O III] 51.8 μm, [N III] 57.3 μm and [O III] 88.3 μm fine-structure line (bottom panel). Beam size differences are *not* taken into account.

the fluxes obtained by the KAO are higher compared to SWS suggesting that the sources are more extended than the SWS beam at those wavelengths (see Fig. 2.2, bottom panel).

2.5.2 Comparison with IRAS

Analogously, the [S IV] 10.5 μm, [Ne II] 12.8 μm, [Ne III] 15.5 μm and [S III] 18.7 μm fine-structure lines are compared with IRAS observations (see Fig. 2.3, top panel). The observed IRAS line fluxes are systematically higher compared to the ISO fluxes due to its

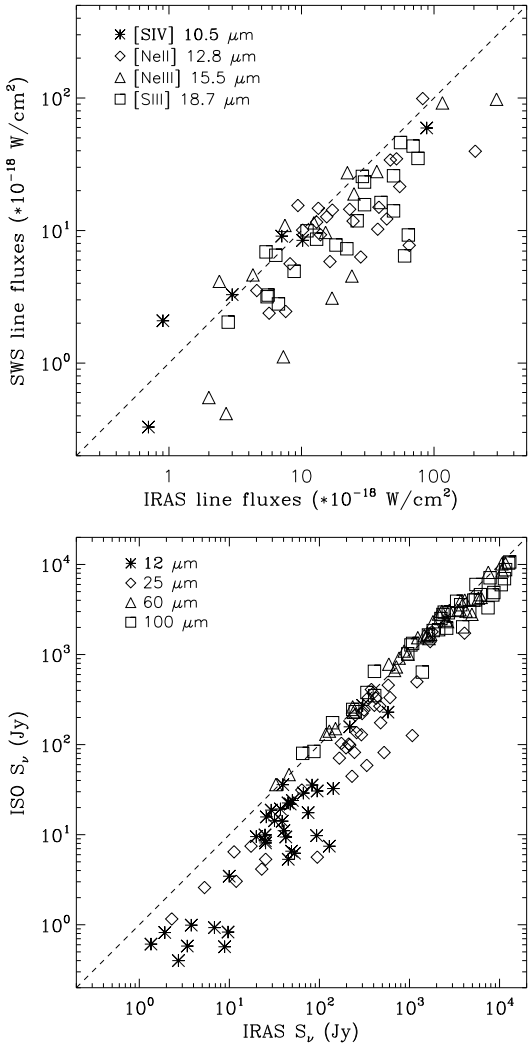

Figure 2.3 — Comparison of the SWS and IRAS line fluxes for [S IV] 10.5 μm, [Ne II] 12.8 μm, [Ne III] 15.5 μm and [S III] 18.7 μm fine-structure lines (top panel). The IRAS fluxes are taken from Simpson & Rubin (1990). Comparison of the IRAS PSC fluxes and the flux seen by ISO within the IRAS filters centred at 12, 25, 60 and 100 μm (bottom panel). Beam size differences are *not* taken into account.

larger aperture. However, their ratio is smaller than the aperture ratio suggesting that the sources are more extended than the SWS beam but smaller than the IRAS beam at these wavelengths.

In addition, we compared the flux seen by ISO in the four IRAS bands at 12, 25, 60 and 100 μm with the corresponding IRAS PSC fluxes. The combined ISO SWS-LWS spectra are therefore used as they are observed. Hence, no correction is applied to the spectra. Fig.

Table 2.3 — References for the KAO observations.

Source	References
IRAS 01045	Rudolph et al. (1997)
IRAS 12073	Simpson et al. (1995)
IRAS 17455	Megeath et al. (1990)
	Simpson et al. (1995)
IRAS 17591	Afflerbach et al. (1997)
IRAS 18032	Afflerbach et al. (1997)
IRAS 18317	Simpson et al. (1995)
IRAS 18434	Herter et al. (1981)
	Megeath et al. (1990)
	Simpson et al. (1995)
IRAS 18479	Afflerbach et al. (1997)
IRAS 19110	Herter et al. (1981)
IRAS 19598	Megeath et al. (1990)
	Colgan et al. (1991)
IRAS 21270	Rudolph et al. (1997)
IRAS 21306	Rudolph et al. (1997)
IRAS 23030	Herter et al. (1982)
	Simpson et al. (1995)

2.3 (bottom panel) shows clearly that the 60 and 100 μm filters give similar results for the IRAS PSC and ISO. For the 12 and 25 μm band filters, large differences are noted implying that the corresponding emission regions are larger then the ISO-SWS aperture.

2.6 Properties of the H II regions

2.6.1 Kinematic distances

Kinematic distances to the program H II regions were derived from velocities taken from the literature as detailed in Table 2.4. A flat Galactic rotation curve and the IAU standard Galactic constants ($R_\odot$=8.5 kpc and $\theta_\odot$=220 $\mathrm{km\,s^{-1}}$) were adopted. The kinematic distance to an H II region is best determined using velocities of radio hydrogen recombination lines. Where such data are available, they have been used. Where no recombination line data were available, the velocity information derived from molecular studies was used. In case of different molecular observations and/or various velocity components observed for one molecular species, we selected the velocity from a high density tracer with the following order of preference: CS, NH_3, H_2CO and CO.

In the case of IRAS 17591, the observed radio recombination line has a very complex profile and the derived distance is very sensitive to the exact peak velocity. Hence, we have followed Bronfman et al. (1996) and assigned a distance of 5.5 kpc derived from CS observations.

Table 2.4 gives the selected tracer (column 2), its velocity (column 3), the derived Galactocentric distance (column 4), the distance from the Sun, including the near and far distance for the sources in the inner solar circle, the latter one in brackets (column 5) and the list of references for the observed velocity (column 6). For sources within the solar circle there is always an ambiguity in determining the distance to the Sun due to the fact that there is a 'near'

and a 'far' intersection of the line of sight with the orbit of the source around the Galactic Centre giving the same radial velocity. The distance ambiguity of some of the sources located within the solar circle can be resolved using additional information:

(a) For IRAS 12331, IRAS 18502 and IRAS 19207, the Galactic rotation model is not giving the measured V_{lsr}, indicating that these H II regions deviate from the model. Here, the most probable estimate of the solar distances is given, i.e. the distance of the tangent point providing the closest V_{lsr} to the observed one.

(b) IRAS 15384 is located in the vicinity of the RCW 94–95 H II region complex (McClure-Griffiths et al. 2001), which is part of a large star-forming complex in the Scutum-Crux arm. The radial velocity of -39 km/s for IRAS 15384 (c.f. Table 2.4) confirms its association to this complex, for which radio recombination line velocities between -42 and -45 km/s (Caswell & Haynes 1987) have been measured. The near distance to RCW 94–95 is favoured due to the identification of stars of spectral type O to B3 located at similar distances in the vicinity of the complex (Georgelin et al. 1994). We will, therefore, consider IRAS 15384 to be located at the near distance, i.e 2.7 kpc.

(c) The radial velocity of IRAS 15502 (-97 km/s, Table 2.4) places this source at 4.6 kpc from the Galactic Center and at either 6.0 or 8.4 kpc from the Sun. However, the line-of-sight towards this source is near the tangent to the orbit where the radial velocity reaches a maximum (~ -105 km/s). There is no ambiguity for an object at this maximum velocity, which is located at 4.5 kpc from the Galactic Center and 7 kpc from the Sun. We will adopt these values for IRAS 15502, a compromise between the near and far distances.

(d) In the cases of Sgr C and IRAS 17455, the heliocentric far distance is disregarded because it would place the source just behind the Galactic Center.

(e) The near and far distances to IRAS 18032 derived from its CS radial velocity ($+4.6$ km s^{-1}, Bronfman et al. 1996) are 1.0 and 15.8 kpc. However, an H I absorption profile obtained by Hofner et al. (1994) indicates that this source is closer than the tangent point and further than the near kinematic distance. Moreover, they find the absorption profile to be consistent with the location of the source in the 3 kpc expanding arm. Assuming a Galactocentric distance of 3 kpc, the implied heliocentric distance is 5.7 kpc.

(f) In the cases of IRAS 18116 and IRAS 18317, Solomon et al. (1987) resolved the near-far distance ambiguity towards the associated molecular cloud choosing the distance with the better fit to the size-CO line width relation. For both sources, the near distance (4.5 and 4.9 kpc, respectively) provided a better fit than the far distance.

(g) Martí et al. (1993) favoured the near distance towards IRAS 18162 based on the proximity of this source to several reflection nebulae and an H II region, apparently embedded in the same molecular cloud, and whose distances are known.

(h) For IRAS 18434, arguments based on extinction and the spectral type of the ionizing star proposed by Pratap et al. (1999) favour the heliocentric near distance (5.7 kpc) instead of the far distance of 9 kpc.

(i) IRAS 18479 is located at either 1.3 or 13 kpc from the Sun. The H I absorption spectrum obtained towards this source was used by Kuchar & Bania (1994) to resolve this kinematic distance ambiguity. The fact that the H I absorption profile shows velocities higher than that of the recombination line verified the location of IRAS 18479 at the far distance, i.e. 13.0 kpc.

(j) IRAS 19442 is associated with the faint, optical H II region S87. An exciting star in this nebula, BD$+24^\circ 3880$, has been identified (Crampton et al. 1978) as a B0.5V star at a dis-

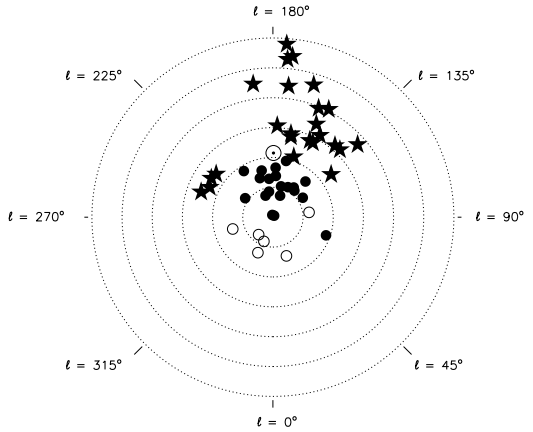

Figure 2.4 — Distribution over the Galactic plane of the H II regions. Distances to the Galactic Centre are indicated by concentric circles from 4 to 24 kpc by steps of 4 kpc. The position of the Sun (at 8.5 kpc) is shown by the $\odot$ symbol. $\star$: sources beyond the solar circle; $\bullet$: sources in the solar circle using the near distance; $\circ$: sources in the solar circle using the far distance.

tance of 2.3 kpc, which is in fair agreement with the near kinematic distance to IRAS 19442, 2.0 kpc. The far distance is, therefore, disregarded.

Figs. 2.4 and 2.5 shows the distribution of the H II regions in Table 2.1 as a function of Galactocentric distance ($R_{\rm gal}$), using the distances from Table 2.4. The nebulae are distributed in the Galactic plane from the centre out to 22 kpc. Whereas the Galactic disk is well sampled between 3 and 12 kpc, fewer sources were observed in the inner regions and in the outer Galaxy.

2.6.2 Morphology

Despite the selection criterion that program sources should be point-like, many sources were found to be extended during follow-up studies. In part, this is due to the fact that the selection was often only based on IRAS data which has a limited spatial resolution. Recent radio observations show that the morphology of the selected H II regions is more complex than originally suspected and that some of the sources show structure at the size scale of the SWS apertures. The fact that some of the nebulae are extended and structured makes the interpretation of the ISO spectral data less straightforward than in the case of a point-like source. The main reason is that in the combined SWS-LWS spectrum the aperture size changes over the entire wavelength range from $14'' \times 20''$ for SWS band 1A to $\sim 86''$ diameter for LWS detector SW3. As a result the region of the extended nebula seen by ISO will be a function of wavelength. In addition, the morphology, size of the sources, the offset from the source peak position and the pointing error of the satellite are important for the observed flux, as mentioned in Sects. 2.3.1 and 2.3.2. Table 2.4 gives an overview of these characteristics for each source in order to estimate whether these effects may be important. The source morphology and size derived from radio data are given in columns 7 and 8, respectively. The morphology classification is based on the work by Wood & Churchwell (1989). The sources with offsets between the ISO pointing and the peak of the radio source of more than $10''$ are flagged in column 8.

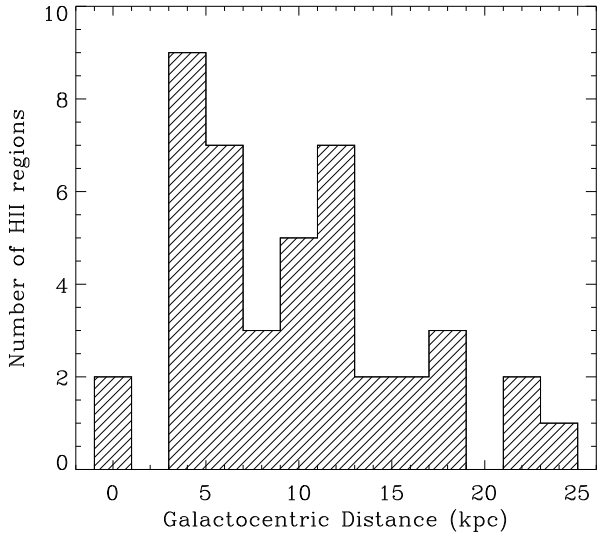

Figure 2.5 — Distribution of the H II regions as a function of Galactocentric distance (R_{gal}).

2.6.3 Luminosity

The FIR luminosities are determined by fitting a blackbody through the IRAS fluxes at 25, 60 and 100 μm taken from the Point Source Catalogue. The applied IRAS colour corrections are those for a source radiating like a blackbody. The derived luminosities are given in Table 2.4.

We choose to derive the luminosities in this way for the following reasons. First, one could consider integrating the full ISO SWS-LWS spectrum. However, due to the combination of the different aperture sizes within SWS/LWS respectively and between SWS and LWS on one hand and the extend of our sources on the other hand, different regions are looked at within different aperture sizes. Hence, only for point-like sources, do the full ISO SWS-LWS spectrum reflect the SED of the source over the total wavelength range, i.e. from 2.3 to 196 μm. For extended sources, one can not compare straightforwardly the obtained spectra in different aperture sizes. When integrating the LWS spectrum only, the short wavelength contribution (< 45 μm), which is a significant fraction of the total luminosity, is ignored. By fitting a (modified) blackbody to the LWS spectrum, the peak of the blackbody is not well defined causing large uncertainties in the derived luminosities. Finally, the IRAS flux at 12 μm is ignored since many features beside the dust continuum attribute to this filter.

Depending on which IRAS ratio (i.e. $f_\nu(25)/f_\nu(60)$, $f_\nu(25)/f_\nu(100)$ or $f_\nu(60)/f_\nu(100)$) is taken, a different temperature is derived for this blackbody and hence different colour corrections. This influences the derived luminosity by less than 4%. In general, the FIR spectra of H II regions are not perfect blackbodies but rather a combination of (modified) blackbodies at different temperatures. Derivation of the luminosity assuming that the source radiates like a single temperature modified blackbody gives a difference of less then 7% with those derived by assuming a blackbody. The error on the derived luminosities is dominated by the absolute flux calibration of IRAS, i.e. 30%.

Table 2.4 — Properties of the H II regions.

Source	Distance					Morphology	Size[b]	Ref.	Luminosity	
	Tracer	V_{LSR} (km/s)	D_{Gal} (kpc)	$D_{\odot}$ [b] (kpc)	Ref.				$L/L_{\odot}$ [c] (10^4)	
IRAS 01045	H42α	-69.3	13.8	7.0	1	spherical	5	1,12,22,23	4.10	
IRAS 01420	CO	$-81.9^{\dagger}$	16.3	9.5	2,3	spherical	21	22	2.86	
IRAS 02219	H66α	-36.5	11.0	3.3	1	shell	35	1,24,25	52.9 $\natural$	
IRAS 02383	CO	$-71.5^{\dagger}$	15.8	8.6	2,3	cometary	28	22	2.67	
IRAS 02575	CS	-38.0	11.5	3.6	4	complex	< 7	26	2.96	
IRAS 04025	CO	$-60.2^{\dagger}$	18.5	10.7	2,3	–	–	–	1.27	
IRAS 05167	CO	-26.3	21.7	13.3	3	–	–	–	1.64	
IRAS 05221	CS	-25.5	17.7	9.3	4	–	–	–	2.51	
IRAS 05302	CO°	-20.0	21.2	12.8	3	–	–	–	0.36	
	CO°	-10.3	12.3	3.8	3				0.03	
IRAS 05335	CO	-17.3	23.2	14.8	3	–	–	–	1.53	
IRAS 06158	CO	$+31.3^{\dagger}$	18.0	9.7	2,3,5	shell	60	27	5.29	
IRAS 10589	H109(110)α	$+22.0$	9.5	8.0	6	cometary	13	23	29.4	
IRAS 11143	H109(110)α	$+25.0$	9.7	8.8	6	complex	66	23	17.1 $\natural$	
IRAS 12063	H109(110)α	$+16.0$	9.3	9.5	6	complex	26	23	45.0	
IRAS 12073	H109(110)α	$+31.0$	10.1	10.8	6	double	45	23	400	
IRAS 12331	H109(110)α	-42.0	6.9	4.5 ‡	6	complex	67$\bigstar$	23	8.45	
IRAS 15384	H109(110)α	-39.0	6.4	2.7 ‡	6	cometary	40	23	10.1	
IRAS 15502	H109(110)α	-97.0	4.5	7.0 ‡	6	double	30	23	131	
IRAS 16128	H109(110)α	-55.0	5.5	3.7 (11.4)	6	complex	18$\bigstar$	23	22.8	(216)
IRAS 17160	H109(110)α	-69.0	3.0	5.7 (11.0)	6	complex	$\triangle$.$\bigstar$	23	35.6	(133)
IRAS 17221	H109(110)α	-21.0	5.2	3.4 (13.4)	6	complex	67	23	7.52	(117)
IRAS 17279	H109(110)α	-33.0	3.4	5.1 (11.8)	6	complex	$\triangle$	23	10.4	(55.9)
Sgr C	H70α	-65.5	0.3	8.2 ‡	7	complex	120	7	$\triangleleft$	

Table 2.4 — Continued.

Source	Distance					Morphology	Size[b]	Ref.	Luminosity	
	Tracer	V_{LSR} (km/s)	D_{Gal} (kpc)	$D_\odot$ [a] (kpc)	Ref.				$L/L_\odot$ [c] (10^4)	
IRAS 17455	H70α	$-19.6^\diamond$	0.2	8.3 ‡	8	core-halo	22	28,29,30	49.2	
IRAS 17591	CS	+15.4	5.5	3.0 (13.8)	4	complex	14	1,28,29	2.04	(43.2)
IRAS 18032	–	–	3.0	5.7 ‡	9	complex	35	23,28,29,31	32.3	
IRAS 18116	H92α	+51.9	4.3	4.5 ‡	10	cometary	20	28,29	18.6	
IRAS 18162	CO	$+11.9^\dagger$	6.6	1.9 ‡	11,12,13	core-halo	5	12	2.43 ↯	
IRAS 18317	H76α	+80.0	4.5	4.9 ‡	14	complex	13	28	14.7	
IRAS 18434	H76α	+95.3	4.6	5.7 ‡	14	cometary	7	28,31,32	70.9	
IRAS 18469	CS	$+87.2^\dagger$	4.8	5.3 (9.2)	4,15	core-halo	13	28	11.1	(33.4)
IRAS 18479	H110α	+16.9	7.4	13.0 ‡	16	complex	11	1,23,28,29	147	
IRAS 18502	H76α	+100.0	4.7	7.1 ‡	14	core-halo	6	28,29	19.6	
IRAS 19207	H109α	+67.2	6.1	5.7 ‡	17	shell	140	33	38.4	
IRAS 19442	H110α	+19.0	7.7	2.0 ‡	16	core-halo	9	23,34	3.39	
IRAS 19598	H110α	−24.2	9.6	8.2	16	spherical	6	1,23,35,36	187	
DR 21	H76α	−1.4	8.6	2.8	18	complex	30	18,23	◁	
IRAS 21190	H76α	−72.1	12.7	8.9	19	shell	7	37	21.4	
IRAS 21270	CO	$-93.4^\dagger$	14.8	11.3	3,20	complex	♭,★	22,27	7.60	
IRAS 21306	CS	−71.1	12.6	8.3	4	complex	♭,★	38,39	12.1	
IRAS 22308	CS	−52.1	11.3	5.5	4	cometary	90	27	7.00	
IRAS 23030	CS	−52.1	11.4	5.2	4	cometary	40	39	10.5	
IRAS 23133	H92α	−66.7	12.6	6.7	21	spherical	9	23,39,40	27.5	

([a]) Number in brackets is the far solar distance. ([b]) Approximate source size in arcsec. ([c]) Luminosity corresponding with the far solar distance is given in brackets. (†) Velocity averaged from the different references. ($^\circ$) 2 CO components found. No other molecular tracer is available. (‡) See Sect. 2.6.1. ($^\diamond$) Velocity forbidden in the sense of Galactic rotation. A distance of 0.2 kpc is assumed (Lis 1991; Mehringer et al. 1998). ($^\triangle$) The object extends over several arcminutes. (↯) Upper limit. (◁) No IRAS fluxes available. (♭) See Sect. 2.6.4. (★) The offset between the ISO pointing and the radio source peak is more than $10''$.

IRAS 12063 It has three components embedded in a low brightness region (Martín-Hernández et al. 2002b).

IRAS 12073 It contains two main compact components A and B. The ISO observations include component A but the apertures center is offset from the peak emission of component A (Martín-Hernández et al. 2002b).

IRAS 12331 It appears as a quasi-spherical and multi-peaked object (Martín-Hernández et al. 2002b).

IRAS 15384 This source appears as a cometary-like source exhibiting a compact core which contains 50% of the flux. The ISO observations are centered on this compact core (Martín-Hernández et al. 2002b).

IRAS 15502 It contains two compact objects A and B. The ISO observations are centered in between these two compact sources (Martín-Hernández et al. 2002b).

IRAS 16128 It appears as a compact object embedded in a low brightness region. The compact object contains 4 embedded cores. The ISO pointing is at the edge of the source (Martín-Hernández et al. 2002b).

IRAS 17160 It is a complex source which spreads over a region of $\sim 2.5'$. The ISO pointing is at the edge of the main component (Martín-Hernández et al. 2002b).

IRAS 17221 It is a quasi-spherical, complex source (Martín-Hernández et al. 2002b).

IRAS 17279 It has three components, A, B and C. The main component A is complex, formed by a core and embedded in a large, low brightnes region. The ISO observations are centered on component A (Martín-Hernández et al. 2002b).

Sgr C It is part of the Sagittarius source complex located near the Galactic Center. It is a shell-like H II region, adjacent and possibly connected to a nonthermal filament like that seen in Sgr A (e.g. Liszt & Spiker 1995).

IRAS 17455 It is a well known star forming region, part of the Sagittarius source complex located near the Galactic Center. It is a compact H II region superposed on a much larger, diffuse emission (e.g. Liszt 1992; Mehringer et al. 1998).

IRAS 17591 Garay et al. (1993) showed that this radio source consists of a main bright component of 14 $''$ (labeled C) and two weaker components west of the main source (labeled A and B). The ISO pointing is centred on component C.

IRAS 18032 This complex consits out of a bright unresolved source and lower brightness extended sources (Kurtz et al. 1994; Garay et al. 1993; Cesaroni et al. 1994). ISO is centred on the extended component B (Martín-Hernández et al. 2002b).

Table 2.4 — Continued.

REFERENCES : (1) Afflerbach et al. (1996); (2) Brand & Wouterloot (1994); (3) Wouterloot & Brand (1989); (4) Bronfman et al. (1996); (5) Fich & Blitz (1984); (6) Caswell & Haynes (1987); (7) Liszt & Spiker (1995); (8) Liszt (1992); (9) Hofner et al. (1994); (10) Garay et al. (1994); (11) de Vries et al. (1984); (12) Martí et al. (1993); (13) Shepherd & Churchwell (1996); (14) Wood & Churchwell (1989); (15) Plume et al. (1992); (16) Araya et al. (2002); (17) Reifenstein et al. (1970); (18) Roelfsema et al. (1989); (19) Walmsley et al. (1981); (20) Blitz et al. (1982); (21) Lebrón et al. (2001); (22) Rudolph et al. (1996); (23) Martín-Hernández et al. (2002b); (24) Roelfsema & Goss (1991); (25) Tieftrunk et al. (1997); (26) Carpenter et al. (1990); (27) Fich (1993); (28) Becker et al. (1994); (29) Garay et al. (1993); (30) Mehringer et al. (1998); (31) Cesaroni et al. (1994); (32) Fey et al. (1995); (33) Mehringer (1994); (34) Barsony (1989); (35) Roelfsema et al. (1988); (36) De Pree et al. (1994); (37) Zijlstra et al. (1990); (38) Ho et al. (1981); (39) Fich (1986); (40) Kurtz et al. (1999)

The IRAS fluxes $f_\nu(60)$ for IRAS 21190 and $f_\nu(100)$ for IRAS 11143 and IRAS 18116 are upper limits. Hence, the derived luminosities for those sources are also upper limits.

2.6.4 Notes on individual sources

IRAS 01045 It exhibits a shell-like morphology (Rudolph et al. 1996). The ISO apertures are overlayed on the radio continuum emission in Martín-Hernández et al. (2002b).

IRAS 01420 It is an optically visible H II which has been observed at radio wavelengths by Rudolph et al. (1996).

IRAS 02219 It is part of the large H II region/molecular cloud complex W3 (Dickel et al. 1980). It is a shell-like and assymmetrically edge-brightened H II region which appears to be in a late stage of its expansion (e.g. Tieftrunk et al. 1997).

IRAS 02383 It exhibits a bright, arc-like leading edge towards the west and a long tail trailing to the east (Rudolph et al. 1996).

IRAS 02575 Kurtz et al. (1994) found 2 components with sizes of $3.8''$ (core-halo) and $1.1''$ (unresolved). The ISO observations are centred on the first component. The ISO apertures contain also a young stellar object (AFGL 4029).

IRAS 06158 It corresponds with an optically visible nebula denominated S266. It is thought to contain a Herbig Ae/Be star (di Francesco et al. 1998).

IRAS 10589 It exhibits a bright, arc-like leading edge towards the west and a long tail trailing to the east (Martín-Hernández et al. 2002b).

IRAS 11143 This large complex H II region contains multiple components (Martín-Hernández et al. 2002b).

IRAS 18116 It exhibits a bright, arc-like leading edge towards the south-west and a long tail trailing to the north-east (Garay et al. 1993).

IRAS 18162 This radio continuum source is associated with a highly active star formation site (e.g. Martí et al. 1993; Stecklum et al. 1997).

IRAS 18317 The radio continuum observations by Wood & Churchwell (1989) reveal a multiple peaked source elongated along the north-south axis.

IRAS 18434 Fey et al. (1995) found extended emission ($\sim 22''$) at 1.3 cm. Observations at 21 cm by Kim & Koo (2001) found two strong components embedded in an extended emission ($\sim 6'$). See Chapter 8 and Martín-Hernández et al. (2003) for a detailed description.

IRAS 18469 Kurtz et al. (1994) found two unresolved radio components. Diffuse emission extended over $\sim 60''$ has been observed by Kurtz et al. (1999).

IRAS 18479 Kurtz et al. (1994) found 4 components. Extended emission ($\sim 20''$) is found by Kurtz et al. (1999). The ISO apertures are overlayed on the radio continuum emission in (Martín-Hernández et al. 2002b).

IRAS 18502 The radio continuum observations by Wood & Churchwell (1989) and Garay et al. (1993) reveal a core-halo H II region.

IRAS 19207 It is part of the W51 complex. It is a shell-like structure and displays edge-brightening towards the north-west and a low-level emission components which extends to the south-east (Mehringer 1994).

IRAS 19442 The radio continuum sourse consists of a compac core of $1''$ and a fan-shaped tail to the south (Barsony 1989; Kurtz et al. 1994, 1999). The ISO apertures are overlayed on the radio continuum emission in (Martín-Hernández et al. 2002b).

IRAS 19598 The object is not isolated (Kurtz et al. 1994). De Pree et al. (1994) found extended emission ($\sim 17''$). The ISO observations are pointed towards component A (Martín-Hernández et al. 2002b).

DR 21 This object contain multiple components (Kurtz et al. 1994). Both component A and B are on the edge of the SWS apertures (Martín-Hernández et al. 2002b).

IRAS 21190 The nature of this source was controversial; it has been classified as both an H II region and a planetary nebula. Now, it is generally accepted as an H II region. See Chapter 8 for a detailed description.

IRAS 21270 Rudolph et al. (1996) observed two radio components, A and B, of $30''$ and $9''$, respectively. The ISO apertures are centered in between the two sources. The offset between component B and the ISO pointing is $25''$.

IRAS 21306 Ho et al. (1981) observed a extended radio component associated with the optical H II region S128 and a compact ($\sim 3''$) H II region located at approximately $60''$ north. The ISO apertures are centred in between these two components.

IRAS 22308 It corresponds with an optically visible nebula denominated S138. It exhibits a bright, arc-like leading edge towards the south-east and a long tail trailing to the north-west (Fich 1993).

IRAS 23030 It corresponds with an optically visible nebula denominated S156. It exhibits a bright, arc-like leading edge towards the north and a long tail trailing to the south (Fich 1986).

IRAS 23133 It exhibits a shell-like morphology (Kurtz et al. 1994). The ISO apertures are overlayed on the radio continuum emission in Martín-Hernández et al. (2002b).

2.7 The catalogue of combined SWS-LWS spectra

We present in Figure 2.6, the combined SWS-LWS spectra from 2.5 to 196 μm of all the H II regions observed in the survey (see Table 2.1). The spectral properties of each H II region are detailed in a series of tables which give the fluxes of the atomic fine-structure lines in the SWS (Tables 2.8) and in the LWS (Table 2.7), the fluxes of the hydrogen recombination lines (Tables 2.9) and information on the presence of dust bands (Table 2.5) and molecular ices (Table 2.6).

The combined SWS–LWS spectra (Figure 2.6) show that compact H II regions display a great diversity in their spectral properties. Generally, the infrared spectrum of an H II region is dominated by a strong dust continuum that peaks at $\sim 40\,\mu$m. On top of this continuum, there is a series of fine-structure lines and hydrogen recombination lines. In addition, a family of prominent dust bands (most notably the emission features present at mid-infrared wavelengths and attributed to small aromatic carbon species such as Polycyclic Aromatic Hydrocarbons or PAHs; Allamandola et al. (1989b)) and in some cases bands from molecular ice species (CO_2, H_2O). Finally, in a few cases, molecular lines of H_2 and OH are detected.

Detailed discussions of the atomic fine-structure from the ionised gas and the photo-dissociation regions (PDRs) are left to later publications (Paper II; Morisset et al. 2002; Martín-Hernández 2002, Damour et al. in prep.).

The first studies of the dust properties in compact H II regions have been given in a series of papers (Roelfsema et al. 1996; Cox & Roelfsema 1999; Peeters et al. 1999; Van Kerckhoven et al. 2000; Hony et al. 2001, Chapters 3, 4 and 7). The study of the dust continuum will be presented by Jones et al. (in prep.). The ice content in compact H II regions is discussed in Boogert (1999), Boogert et al. (in prep.). Hereafter we briefly describe the content of the infrared spectra of compact H II regions and outline the potential use of the present catalogue in future studies.

2.7.1 Atomic emission lines

In the spectra presented in Figure 2.6, the main atoms (O, N, Ne, Ar, S, C and Si) are detected via their fine-structure lines. The lines of [C II], [O I] and [Si II], which originate in the photo-dissociation regions (PDRs) associated with the H II regions, are seen in almost every

source. They provide an important diagnostic of the physical conditions of the dense warm gas located just outside the ionised nebula. A detailed analysis will be given in Damour et al. (in prep.) where the present data will be compared to PDR model predictions. The strongest lines in the combined SWS–LWS spectra are emitted by atoms in the ionised nebula which, in rough order of importance, are the fine-structure lines of O^{++}, S^{++} and S^{+++}, Ne^{+} and Ne^{++}, Ar^{+} and Ar^{++} and N^{++} and N^{+} (see Figure 2.6 and Tables 2.8 & 2.7). Except for oxygen, the species are present in different stages of ionisation and the range of ionisation potential sampled by these lines extends to ~ 41 eV. This information allows us to describe the ionisation state of each H II region and to derive the properties of the exciting star(s). The H II regions studied in this paper form a prime sample to examine the variations of the nebular properties with galactocentric distance and to investigate the distribution of the relative and absolute element abundances in the Milky Way. The study of the ionisation state and the element abundance based on the present sample of compact H II regions is the major aim of this ISO program and the subject of an accompanying paper (Martín-Hernández et al. 2001, i.e. Paper II).

In addition to the fine-structure lines, H I recombination lines are present in the spectra (see Fig. 2.6 and Tables 2.9). These H I recombination lines are used to derive the extinction law at these wavelengths by comparing the observed line strengths to the predictions of recombination theory (see Paper II).

Some sources exhibit unusual lines. IRAS 12073 has an emission line at 4.3 μm ([KIV] ?), IRAS 12331 at 21.8 and 27.1 μm (HI or [ArIII]; [SV]) and K3-50 A at 4.295, 4.377 and 4.617 (?, HI, [KIII]?). The SWS AOT06 of IRAS 18434 shows also the 4.617 μm [KIII] line.

2.7.2 Molecular emission lines

In a few sources, molecular lines of H_2 are detected. In one case, IRAS 21190+5140 (M1-78), six emission lines of molecular hydrogen are present in the SWS spectrum, i.e. 1-0 O(3) to O(5) and 0-0 S(3) to S(5). IRAS 12063 shows the 0-0 S(5) H_2 line and K3-50 A exhibits the 1-0 O(3) and 0-0 S(1) H_2 lines.

The molecular absorption line of OH at 119.2 μm is present in the following sources : IRAS 17221, IRAS 17279, IRAS 17455, IRAS 17591, IRAS 18032, IRAS 18317, IRAS 18434, IRAS 18469, IRAS 18479, IRAS 18502 and Sgr C. The latter sources also show an OH absorption line at 79.3 μm. W3 A, IRAS 19442 and DR 21 exhibit CO emission lines (162.9, 173.6 and 185.9 μm). The H_2O emission line at 179.7 μm is clearly present in Sgr C.

2.7.3 Dust content

The infrared spectra of compact H II regions are dominated by a strong continuum due to the thermal emission of dust. As mentioned in Sect. 2.6.3, it is not straightforward to compare the obtained spectrum of an extended source over different aperture sizes. So, caution should be taken when studying the SED of a specific source when this source is not a point source. For most of the sources, the dust continuum seems to peak in the range 40-60 μm when plotted in μm versus W/cm^2/ μm corresponding to dust temperatures of $\sim$ 60-70 K. In some cases (IRAS 11143, IRAS 12073, IRAS 21190 and perhaps IRAS 17455), the spectrum peaks at shorter wavelengths $\sim$ 30 μm, indicating that warmer dust is present in these nebulae. The H II regions in this sample appear to be substantially hotter than UC H II regions, with dust

temperatures of $\sim$ 30 K. Probably, the nebulae in this sample are somewhat more evolved and emerging from their dust envelopes. In the case of IRAS 02575, a strong continuum is present shortwards of 5 μm, indicating temperatures in excess of $\sim$ 800 K. This unusual temperature for an H II region can be explained by the fact that, for this source, the SWS aperture encloses both the compact H II region and an Herbig AeBe star (see Sect. 2.6.2). Finally, many H II regions show continuum emission at $\lambda < 12$ μm, indicative of a high colour temperature. Yet, it cannot be due to small molecules ($\sim$ 50 C-atoms) since those would give rise only to a weak quasi-continuum in this wavelength region (Allamandola et al. 1989b). This continuum could be due to a small fraction of dust in the H II region heated to high temperatures by resonantly scattered Lyman-alpha radiation. The complete wavelength coverage from 2.3 to 196 μm provides in principle important information on the dust spectrum at mid-infrared wavelengths dominated by the PAH emission bands and the far-infrared continuum which is dominated by the bigger dust grains. Improvement in the SWS calibration will be crucial to further study this part of the spectrum.

The IR emission features at 3.3, 6.2, '7.7', 8.6 and 11.2 μm - commonly attributed to PAHs - are present in most of the spectra of the H II regions together with many weaker features e.g. the 12.7 μm band (see Table 2.5). The shape and strength of these dust bands exhibit considerable variations from source to source. At the spectral resolution of the present data, the bands are found to form complex emission patterns with a variety of sub-peaks and spectral detail. For instance, the '7.7' μm band consists of two bands peaking at 7.6 and 7.8 μm. The variations in the relative intensities of the bands are thought to be primarily due to variations in the physical conditions of the emitting region (radiation field, density etc.) that determines the physical (ionisation) and/or chemical processing of the interstellar PAH family (e.g. Roelfsema et al. 1996; Cox & Roelfsema 1999; Peeters et al. 1999). A complete analysis of the near- and mid-infrared dust bands in the spectra of compact H II regions, together with a study of the variation of their shapes and relative intensities as a function of the ionisation state (as measured by the atomic lines), will be presented in Peeters et al. (in prep.). In addition to these emission bands, a large number of the H II regions show in their infrared spectra the broad absorption band at 9.7 μm due to the stretching mode of amorphous silicate. The corresponding bending mode at 18 μm might be present in the spectra of some sources but is not always clearly visible. A summary of the dust content in the sample of H II regions of this catalogue is given in Table 2.5, where the presence of the dust emission bands and of the silicate absorption bands is indicated for each source. Sources which are not included in Table 2.5 do not show any emission/absorption features. Given the low continuum of some sources, it is not possible to assess the presence of absorption.

2.7.4 Ice content

Since compact H II regions are embedded sources, they are potential targets for absorption studies of molecular ices. As mentioned earlier, two of the sources are dominated by absorption, displaying a very rich set of molecular ice bands (see Dartois et al. 1998, and references therein).

For three of the sources presented in this paper, broad absorption bands of amorphous H_2O ice are clearly detected at 3 and 6 μm (the stretching and bending modes, respectively). These bands might be present in some other sources but the low flux density levels (<5 Jy) in the 3 μm wavelength region results in noisy spectra from which firm conclusions cannot be drawn. In addition, the strong 3.3 and 6.2 μm dust emission bands are located in the

Table 2.5 — The dust and silicate features present in the sources.

Source	PAHs [b]						Silicate [b]
	3.3	6.2	7.7	8.6	11.2	12.7	9.7
IR 01045*	??	√	√	√	√	–	–
IR 02219	√	√	√	√	√	?	√
IR 02575	√	√	√	√	√	√	√
IR 06158*	??	??	??	–	–	–	–
IR 10589	√	√	√	√	√	–	?
IR 12063	√	√	√	√	√	–	√
IR 12073	√	√	√	√	√	√	√
IR 12331	?	√	√	√	√	√	–
IR 15384	√	√	√	√	√	√	√
IR 15502	√	√	√	√	√	–	√
IR 16128	√	√	√	√	√	√	√
IR 17160	√	√	√	√	√	√	√
IR 17221	√	√	√	√	√	√	√
IR 17279	√	√	√	√	√	√	?
Sgr C	√	√	√	√	√	√	√
IR 17455	√	√	√	√	√	?	√
IR 17591	–	√	√	√	√	√	–
IR 18032	√	√	√	√	√	√	√
IR 18116	√	√	√	√	√	√	?
IR 18162	√	√	√	√	√	√	√
IR 18317	√	√	√	√	√	√	√
IR 18434	√	√	√	√	√	–	√
IR 18469	√	√	√	√	√	√	√
IR 18479	?	√	√	?	√	–	√
IR 18502	√	√	√	√	√	√	√
IR 19207	√	√	√	√	√	√	√
IR 19442	√	√	√	√	√	√	√
IR 19598	√	√	√	√	√	–	√
DR 21	–	√	√	√	√	–	√
IR 21190	√	√	√	√	√	√	√
IR 21270*	–	√	√	√	?	–	–
IR 22308	√	√	√	√	√	√	–
IR 23030	√	√	√	√	√	√	–
IR 23133	√	√	√	√	√	√	–

([b]) The central wavelength given in μm. (*) Very low flux spectra. The feature is present (√), not present (–). The presence of the feature is dubious (?), *very* dubious (??).

Table 2.6 — Ice features present in the sources.

Source	H_2O Ices [♭]		CO_2 Ices [♭]		Ice [♭,†]
	3	6	4.27	15.2	6.85
IR 02575	√	√	√	√	-
IR 17160	-	-	-	?	-
IR 18162	√	√	√	√	-
IR 18479	-	-	?	√	-
IR 19442	-	?	?	√	-
IR 19598	√	√	√	√	√
DR 21	-	-	-	√	-

([♭]) Central wavelength is given in μm. ([†]) The ice nature of this feature is not clear. (√) The feature is present. (?) The presence of the feature is dubious. (–) The feature is not present.

red wing of both H_2O bands resp. making the situation difficult for sources with moderate amounts of extinction.

At longer wavelengths, the continuum becomes stronger making the situation more favourable to detect ice bands in absorption. The CO_2 bending mode at 15 μm is detected in 6 sources (listed in Table 2.6). Small variations in the substructure of the absorption band show that the ices have only been partially thermally processed ($45 < T < 90$ K) by the central heating source, in contrast to some highly processed regions around hot cores such as Sh 140 (Gerakines et al. 1999). Furthermore, extensive laboratory studies of the band profile show that interstellar CO_2 must be mixed with H_2O and CH_3OH ices (see Boogert 1999, Boogert et al. in prep.). The intrinsically stronger CO_2 stretching mode (4.27 μm) is present in the spectra of 3 sources (Table 2.6), but the data are of much lower quality due to the lower level of the continuum at these wavelengths. Furthermore, it is located in AOT Band 2A, which tends to be very noisy. It is thus not excluded that the CO_2 stretching mode could be present in other compact H II regions than those listed in Table 2.6.

Finally, K3-50A is the only source in the present sample that shows an absorption band around 6.85 μm (Table 2.6). The analysis of this band is difficult since it is located in a complex spectral region that includes the 6.0 μm H_2O ice absorption band, the 6.2 μm PAH emission feature, the 6.8 μm absorption feature and the emission plateau between the 6.2 and '7.7' μm PAH bands. The derived profile is similar in appearance to absorption features seen toward dense molecular clouds exhibiting signs of warmer ice (Keane et al. 2001).

2.8 Conclusions

The ISO spectral catalogue of compact H II regions presents grating spectra from 2.5 to 196 μm of 43 compact H II regions that were taken with the two spectrometers (the SWS and the LWS) on board ISO. The infrared spectra of compact H II regions show a great diversity in the dust and ice content, the dust continuum, the hydrogen recombination lines and in the relative intensities of the atomic fine-structure lines. This set of data will be a useful source

of information to study the properties of the ionised gas, the dust and the photodissociation regions associated with compact H II regions and to investigate their variations across the Galactic plane. The spectra and the line fluxes, which form the core of this paper, were derived using the latest knowledge available on the calibration on the ISO spectra.

Acknowledgements

The authors wish to thank the referee for usefull comments. EP thanks especially J. Cami, R. Shipman, D. Kester, F. Lahuis, S. Hony, A. Boogert, L. Decin and B. Vandenbussche for the support concerning the SWS data reduction. NLMH acknowledges the support of S. Sidher for the LWS data reduction. IA^3 is a joint development of the SWS consortium. Contributing institutes are SRON, MPE, KUL and the ESA Astrophysics Division. The SWS work was supported by the Dutch ISO Data Analysis Centre (DIDAC) at the Space Research Organisation Netherlands (SRON) in Groningen, the Netherlands. The ISO Spectral Analysis Package (ISAP) is a joint development by the LWS and SWS Instrument Teams and Data Centers. Contributing institutes are CESR, IAS, IPAC, MPE, RAL and SRON. LIA is a joint development of the LWS consortium. Contributing institutes are CESR, DRAL, IPAC and the ESA Astrophysics Division.

2.A Line fluxes and combined SWS-LWS spectra

In this appendix, the fluxes of the fine-structure lines and H recombination lines are given in Tables 2.7, 2.8 and 2.9. Subsequentely, Figure 2.6 shows the combined SWS-LWS spectra from 2.5 to 196 μm of all the H II regions. For details, see Sect. 2.4 and 2.7. In each panel of these figures, the combined SWS–LWS spectra of three H II regions are presented. Each spectrum is labelled with the name of the source and the position of the atomic fine-structure lines, the hydrogen recombination lines and the dust bands are indicated at the bottom of each panel together with those wavelengths at which an aperture jump occurs. Note that in order to show the general shape of the dust emission bands and the continuum, the (strong) atomic lines have been cut off at the top in some of the spectra. As explained in § 2.3, the spectra presented in Figure 2.6 are not corrected for jumps occurring at the SWS band edges, at the limit between the SWS and the LWS or between the LWS detectors. The parts of the spectra corresponding to the poorly calibrated SWS Band 3E and 4, the leak in band 3D and LWS SW1 detector are shown in grey tones.

Table 2.8 — The fluxes of the SWS fine-structure lines.

Source	Line fluxes[a,b] (10^{-18} W/cm^2)								
	Ar II 7.0 μm (8%)[c]	Ar III 9.0 μm (8%)[c]	S IV 10.5 μm (8%)[c]	Ne II 12.8 μm (16%)[c]	Ne III 15.5 μm (16%)[c]	S III 18.7 μm (16%)[c]	S III 33.5 μm (25%)[c]	Si II 34.8 μm (25%)[c]	Ne III 36.0 μm (25%)[c]
IRAS 01045	< 0.2	< 0.1	< 0.2	1.0 ± 0.2	0.6 ± 0.1	0.5 ± 0.2	< 0.3	< 0.3	< 0.3
IRAS 01420	< 0.2	< 0.1	< 0.2	< 0.2	< 0.2	< 0.1	< 0.3	< 0.3	< 0.3
IRAS 02219*	2.5 ± 0.2	12.5 ± 0.5	26 ± 1	36 ± 2	94 ± 2	59 ± 2	64 ± 5	18 ± 1	22 ± 2
IRAS 02219◇	2.6 ± 0.1	13.7 ± 0.3	28 ± 1	39 ± 2	97 ± 3	43 ± 1	54 ± 5	15.1 ± 0.8	21 ± 5
IRAS 02383	< 0.1	< 0.1	< 0.1	< 0.2	< 0.2	< 0.2	< 0.2	< 0.2	< 0.2
IRAS 02575	< 0.1	< 0.1	< 0.1	< 0.2	< 0.2	< 0.1	< 0.3	0.5 ± 0.2	< 0.3
IRAS 04025	< 0.1	< 0.1	< 0.1	< 0.1	< 0.1	< 0.1	< 0.1	< 0.1	< 0.1
IRAS 05167	< 0.2	< 0.1	< 0.1	< 0.2	< 0.1	< 0.1	< 0.1	< 0.1	< 0.1
IRAS 05221	< 0.2	< 0.1	< 0.1	< 0.1	< 0.1	< 0.1	< 0.2	< 0.2	< 0.2
IRAS 06158	< 0.2	< 0.2	< 0.2	< 0.2	< 0.2	< 0.2	< 0.3	1.3 ± 0.3	< 0.4
IRAS 10589	3.1 ± 0.1	2.5 ± 0.1	1.5 ± 0.2	14 ± 1	4.1 ± 0.2	15.7 ± 0.4	14.8 ± 0.8	4.8 ± 0.5	< 0.5
IRAS 11143	< 0.1	1.38 ± 0.07	8.4 ± 0.3	2.5 ± 0.2	11.4 ± 0.5	7.8 ± 0.2	19 ± 1	1.4 ± 0.3	2.26 ± 0.10
IRAS 12063	0.99 ± 0.09	4.0 ± 0.2	9.1 ± 0.3	9.3 ± 0.6	18.9 ± 0.5	11.8 ± 0.2	10.5 ± 0.3	4.5 ± 0.7	2.8 ± 0.2
IRAS 12073	0.9 ± 0.3	11.9 ± 0.4	59 ± 2	14 ± 1	91 ± 7	35 ± 1	33 ± 2	8.8 ± 0.8	16.8 ± 0.8
IRAS 12331♮	0.87 ± 0.08	1.6 ± 0.1	1.28 ± 0.06	6.3 ± 0.3	4.63 ± 0.09	9.3 ± 0.3	23.7 ± 0.7	2.8 ± 0.3	1.4 ± 0.1
IRAS 15384	8.2 ± 0.5	5.0 ± 0.6	2.6 ± 0.1	34 ± 2	10 ± 1	25.9 ± 0.6	28 ± 1	8 ± 1	2.3 ± 0.3
IRAS 15502	4.4 ± 0.4	0.9 ± 0.1	0.23 ± 0.03	12 ± 1	3.1 ± 0.4	4.9 ± 0.4	9.5 ± 0.2	4.1 ± 0.9	< 1.7
IRAS 16128♮	2.39 ± 0.09	1.0 ± 0.2	0.82 ± 0.03	7.7 ± 0.3	4.5 ± 0.1	6.4 ± 0.3	22 ± 2	6.1 ± 0.2	1.5 ± 0.3
IRAS 17160♮	1.6 ± 0.1	0.18 ± 0.03	< 0.1	4.4 ± 0.4	0.9 ± 0.2	2.7 ± 0.1	12.3 ± 0.7	5.1 ± 0.2	< 0.3
IRAS 17221	3.1 ± 0.1	0.76 ± 0.10	0.13 ± 0.03	10.2 ± 0.4	0.42 ± 0.09	7.3 ± 0.2	18 ± 2	3.9 ± 0.8	< 0.3
IRAS 17279	2.4 ± 0.1	0.21 ± 0.04	< 0.1	5.8 ± 0.3	0.4 ± 0.2	3.17 ± 0.08	13 ± 1	5.1 ± 0.2	< 0.3
Sgr C	2.8 ± 0.2	< 0.1	< 0.09	4.7 ± 0.3	< 0.2	1.6 ± 0.1	11 ± 1	10.1 ± 0.2	< 0.4
IRAS 17455	5.9 ± 0.2	3.4 ± 0.1	1.9 ± 0.2	21 ± 1	9.7 ± 0.3	23.2 ± 0.4	30 ± 3	5.0 ± 0.5	1.3 ± 0.2
IRAS 17591	< 0.2	< 0.1	< 0.1	0.9 ± 0.1	2.3 ± 0.3	0.93 ± 0.07	3.9 ± 0.2	1.5 ± 0.2	0.9 ± 0.2

Table 2.7 — Fluxes of the LWS fine-structure lines.

Source	Line fluxes[a,b,c] (10^{-18} W/cm^2)						
	[O III] 51.8 μm	[N III] 57.3 μm	[O I] 63.1 μm	[O III] 88.3 μm	[N II] 121.8 μm	[O I] 145.5 μm	[C II] 157.7 μm
IRAS 01420	< 0.5	< 0.3	4.04 ± 0.08	< 0.2	< 0.1	0.24 ± 0.02	3.1 ± 0.3
IRAS 02219	336 ± 13	37 ± 7	126 ± 2	69 ± 1	< 3.5	13.8 ± 0.7	23.5 ± 0.7
IRAS 02383	< 0.6	< 0.4	3.1 ± 0.4	< 0.2	< 0.2	0.09 ± 0.03	2.7 ± 0.4
IRAS 02575	< 1.2	< 0.6	8.5 ± 0.3	< 0.4	< 0.3	0.87 ± 0.05	4.9 ± 0.4
IRAS 04025	< 0.5	< 0.4	1.3 ± 0.2	< 0.2	< 0.1	0.076 ± 0.01	1.1 ± 0.1
IRAS 05167	< 0.5	< 0.3	1.7 ± 0.1	< 0.1	< 0.1	0.06 ± 0.01	2.0 ± 0.2
IRAS 05221	< 0.6	< 0.4	1.53 ± 0.07	< 0.1	< 0.1	0.24 ± 0.04	1.42 ± 0.07
IRAS 05302	< 0.4	< 0.3	< 0.1	< 0.1	< 0.1	0.06 ± 0.04	0.44 ± 0.02
IRAS 05335	< 0.5	< 0.4	0.22 ± 0.06	< 0.1	< 0.04	< 0.05	0.21 ± 0.05
IRAS 06158	< 0.9	< 0.8	30 ± 2	< 0.4	< 0.3	1.1 ± 0.1	6.9 ± 0.6
IRAS 10589	19.2 ± 0.8	5.0 ± 0.3	17.9 ± 0.7	9.2 ± 0.3	1.17 ± 0.09	2.06 ± 0.03	14.3 ± 0.8
IRAS 11143	88 ± 4	17.6 ± 0.7	5.9 ± 0.2	67 ± 2	0.7 ± 0.1	0.38 ± 0.04	5.7 ± 0.4
IRAS 12063	43 ± 2	6.5 ± 0.5	27.0 ± 0.8	13.5 ± 0.2	< 0.5	2.76 ± 0.08	9.6 ± 0.6
IRAS 12073	408 ± 20	50 ± 2	121 ± 3	153 ± 1	< 1.1	5.9 ± 0.2	24.3 ± 0.8
IRAS 12331	73 ± 2	23 ± 1	11.4 ± 0.4	35.8 ± 0.5	2.7 ± 0.1	2.29 ± 0.08	9.8 ± 0.5
IRAS 15384	68 ± 3	24.2 ± 0.8	56 ± 1	22.1 ± 0.4	3.9 ± 0.2	7.2 ± 0.2	25 ± 1
IRAS 15502	34 ± 3	19 ± 1	20 ± 3	20.5 ± 0.5	4.3 ± 0.1	4.1 ± 0.2	13.7 ± 0.5
IRAS 16128	129 ± 6	47 ± 1	39.0 ± 0.7	51.2 ± 0.6	5.3 ± 0.2	4.4 ± 0.3	19.4 ± 0.7
IRAS 17160	25.6 ± 0.8	15.0 ± 0.5	22.8 ± 0.6	14.8 ± 0.4	4.8 ± 0.5	3.3 ± 0.3	16.3 ± 0.6
IRAS 17221	13.7 ± 0.7	10.6 ± 0.5	8.8 ± 0.3	6.9 ± 0.2	6.0 ± 0.3	3.8 ± 0.2	11.4 ± 0.5
IRAS 17279	11.7 ± 0.6	13.4 ± 0.7	2.6 ± 0.2	13.0 ± 0.2	8.3 ± 0.4	1.66 ± 0.07	10.6 ± 0.7
Sgr C	8.6 ± 0.7	10.3 ± 0.3	14.8 ± 0.4	10.1 ± 0.6	15.8 ± 0.6	1.6 ± 0.2	31.6 ± 0.8
IRAS 17455	58 ± 4	28.8 ± 0.9	10.1 ± 0.3	30.9 ± 0.4	4.7 ± 0.2	2.3 ± 0.1	12.8 ± 0.4
IRAS 17591	29 ± 1	4.0 ± 0.3	6.2 ± 0.2	17.1 ± 0.3	1.10 ± 0.04	1.7 ± 0.2	9.3 ± 0.6
IRAS 18032	6.4 ± 0.9	4.5 ± 0.4	11.4 ± 0.5	3.5 ± 0.4	2.3 ± 0.4	2.8 ± 0.4	9.5 ± 0.3
IRAS 18116	16.0 ± 0.6	8.1 ± 0.7	57 ± 1	7.0 ± 0.2	3.1 ± 0.2	4.9 ± 0.1	19.0 ± 1.0
IRAS 18162	< 1.5	< 1.6	8.6 ± 0.2	< 0.8	< 0.5	1.37 ± 0.10	3.8 ± 0.3
IRAS 18317	9.7 ± 1.0	6.3 ± 0.4	16.0 ± 0.4	2.7 ± 0.2	4.7 ± 0.3	4.1 ± 0.2	18.4 ± 1.0
IRAS 18434	46 ± 2	22 ± 1	4.4 ± 0.4	19.4 ± 0.4	4.6 ± 0.2	3.2 ± 0.2	10.4 ± 0.7
IRAS 18469	14.1 ± 0.6	10.1 ± 0.5	2.34 ± 0.09	14.8 ± 0.2	3.6 ± 0.4	0.8 ± 0.1	8.6 ± 0.4
IRAS 18479	17.2 ± 0.8	2.5 ± 0.6	3.2 ± 0.3	7.0 ± 0.4	< 1.1	2.4 ± 0.1	5.5 ± 0.2
IRAS 18502	8.7 ± 0.6	3.0 ± 0.4	12.1 ± 0.4	2.9 ± 0.1	< 0.6	1.9 ± 0.2	7.1 ± 0.3
IRAS 19207	169 ± 9	47 ± 1	30.9 ± 0.6	96.7 ± 0.9	3.7 ± 0.2	4.0 ± 0.2	17.1 ± 0.9
IRAS 19442	< 2.6	< 1.7	54.7 ± 0.8	< 1.0	< 0.6	5.07 ± 0.08	17.9 ± 0.7
IRAS 19598	37 ± 1	4.6 ± 1.0	39.3 ± 0.9	21.5 ± 0.8	< 1.1	4.4 ± 0.5	14.2 ± 0.9
DR 21	15 ± 1	< 4.5	73 ± 1	11.4 ± 0.5	< 2.3	9.9 ± 0.3	12.8 ± 0.2
IRAS 21190	4.5 ± 0.4	< 1.0	30 ± 1	0.9 ± 0.1	< 0.2	1.9 ± 0.2	4.0 ± 0.3
IRAS 21270	5.1 ± 0.2	1.4 ± 0.2	8.3 ± 0.2	4.89 ± 0.09	< 0.3	0.43 ± 0.06	4.4 ± 0.7
IRAS 21306	3.4 ± 0.4	< 0.7	5.4 ± 0.2	3.06 ± 0.09	< 0.3	0.52 ± 0.06	3.4 ± 0.3
IRAS 22308*	2.4 ± 0.3	< 0.6	15.8 ± 0.5	0.98 ± 0.08	< 0.3	1.9 ± 0.1	8.1 ± 0.4
IRAS 22308†	2.4 ± 0.3	0.6 ± 0.2	15.4 ± 0.3	1.03 ± 0.09	< 0.3	2.00 ± 0.04	8.6 ± 0.4
IRAS 23030	17.4 ± 0.8	5.6 ± 0.5	31.3 ± 0.4	7.3 ± 0.2	0.9 ± 0.1	3.23 ± 0.09	12 ± 1
IRAS 23133	1.4 ± 0.5	< 1.1	43 ± 1	< 0.8	0.8 ± 0.3	4.06 ± 0.09	12.9 ± 0.7

([a]) The listed errors are the square root of the quadratic sum of the difference between the up and down scan measurements and the statistical error of the line fitting (see § 2.4). Hence, *no* calibration uncertainties are included. To obtain the final error, see § 2.4.2. ([b]) At these wavelengths, the calibration uncertainty is 10%. ([c]) Note that these lines are seen through different apertures. ($\star$) TDT = 17701257; † TDT = 56101081; see § 2.3.1.

Table 2.8 — Continued.

Source	Line fluxes[a,b] (10^{-18} W/cm^2)								
	Ar II 7.0 μm (8%) [c]	Ar III 9.0 μm (8%) [c]	S IV 10.5 μm (8%) [c]	Ne II 12.8 μm (16%) [c]	Ne III 15.5 μm (16%) [c]	S III 18.7 μm (16%) [c]	S III 33.5 μm (25%) [c]	Si II 34.8 μm (25%) [c]	Ne III 36.0 μm (25%) [c]
IRAS 18032	5.1 ± 0.4	0.61 ± 0.04	< 0.1	11.8 ± 0.7	< 0.3	6.9 ± 0.3	11.8 ± 0.8	5.9 ± 0.4	< 0.3
IRAS 18116	7.5 ± 0.4	0.79 ± 0.06	< 0.2	14 ± 1	1.1 ± 0.2	14.1 ± 0.5	28 ± 2	7.2 ± 0.4	< 0.4
IRAS 18162	< 0.2	< 0.1	< 0.1	< 0.3	< 0.1	< 0.2	< 0.9	< 1.0	< 1.1
IRAS 18317	10.9 ± 0.3	2.1 ± 0.1	0.33 ± 0.08	34 ± 1	2.4 ± 0.2	25.6 ± 0.4	27.6 ± 1.0	9.0 ± 0.5	< 0.5
IRAS 18434	22 ± 2	11.0 ± 0.7	4.2 ± 0.4	99 ± 7	27 ± 1	46 ± 1	39 ± 3	7 ± 1	3 ± 1
IRAS 18469	1.0 ± 0.3	0.2 ± 0.1	< 0.10	2.4 ± 0.1	0.55 ± 0.02	2.8 ± 0.1	8.4 ± 0.9	2.4 ± 0.3	< 0.4
IRAS 18479	1.06 ± 0.10	< 0.1	< 0.1	5.6 ± 0.4	2.7 ± 0.3	2.0 ± 0.1	2 ± 1	1.7 ± 0.2	< 0.6
IRAS 18502	2.8 ± 0.3	0.93 ± 0.06	0.49 ± 0.07	15.5 ± 0.7	3.6 ± 0.2	8.6 ± 0.2	8.1 ± 0.6	2.8 ± 0.4	< 0.4
IRAS 19207	1.0 ± 0.1	1.1 ± 0.1	1.41 ± 0.07	5.0 ± 0.4	5.7 ± 0.1	7.4 ± 0.3	27 ± 1	6.4 ± 0.7	1.6 ± 0.3
IRAS 19442	1.3 ± 0.1	< 0.1	< 0.1	2.8 ± 0.2	< 0.1	0.8 ± 0.1	1.9 ± 0.3	3.8 ± 0.6	< 0.6
IRAS 19598	2.2 ± 0.1	2.8 ± 0.1	3.3 ± 0.1	11.6 ± 0.4	27.9 ± 0.5	7.6 ± 0.2	4.6 ± 0.8	4.5 ± 0.7	1.9 ± 0.3
DR 21	2.8 ± 0.3	0.29 ± 0.05	< 0.1	5.1 ± 0.2	1.5 ± 0.6	2.2 ± 0.2	5 ± 1	4 ± 1	< 1.5
IRAS 21190	1.2 ± 0.1	3.11 ± 0.07	2.09 ± 0.08	10.1 ± 0.5	10.0 ± 0.3	6.51 ± 0.10	1.71 ± 0.09	2.8 ± 0.7	< 0.44
IRAS 21270[♮]	< 0.2	< 0.1	< 0.1	0.4 ± 0.1	< 0.1	0.6 ± 0.2	1.2 ± 0.4	0.5 ± 0.2	< 0.2
IRAS 21306[♮]	< 0.2	< 0.1	< 0.1	< 0.1	< 0.2	< 0.1	< 0.2	< 0.2	< 0.1
IRAS 22308[⋆]	1.9 ± 0.1	0.45 ± 0.04	< 0.1	3.9 ± 0.2	< 0.1	4.0 ± 0.8	4.3 ± 0.4	2.9 ± 0.2	< 0.3
IRAS 22308[†]	1.9 ± 0.3	0.4 ± 0.1	< 0.1	3.5 ± 0.3	< 0.2	3.3 ± 0.2	3.6 ± 0.3	2.6 ± 0.1	< 0.3
IRAS 23030	1.8 ± 0.2	3.1 ± 0.2	1.3 ± 0.1	14.7 ± 0.5	2.12 ± 0.09	16.3 ± 0.4	14 ± 2	4.0 ± 0.5	< 0.3
IRAS 23133	5.6 ± 0.3	1.22 ± 0.04	0.20 ± 0.05	12.7 ± 0.5	< 0.3	10.0 ± 0.2	4.6 ± 0.8	8.3 ± 0.4	< 0.9

([a]) The listed errors are the square root of the quadratic sum of the difference between the up and down scan measurements and the statistical error of the line fitting (see § 2.4). Hence, *no* calibration uncertainties are included. To obtain the final error, see § 2.4.2. ([b]) Note that these lines are seen through different apertures (see Table 2.2). ([c]) 1σ absolute flux accuracy at this wavelength (see Table 2.2). ([♮]) The approximate offset between the source peak and the ISO pointing is $\geq 10''$. This data should be used with caution (see § 2.4.3 and § 2.6.2). ([°]) TDT = 64600609; ([◇]) TDT = 78800709; ([⋆]) TDT = 17701258; ([†]) TDT = 56101082; see § 2.3.1.

Table 2.9 — The fluxes of the H I recombination lines.

Source	Line fluxes[a,b] (10^{-18} W/cm^2)											
	H I (6–4) 2.625 μm (4%)[c]	H I (13–5) 2.675 μm (4%)[c]	H I (12–5) 2.757 μm (4%)[c]	H I (11–5) 2.872 μm (4%)[c]	H I (10–5) 3.038 μm (4%)[c]	H I (9–5) 3.296 μm (4%)[c]	H I (8–5) 3.739 μm (4%)[c]	H I (5–4) 4.051 μm (4%)[c]	H I (7–5) 4.652 μm (8%)[c]	H I (6–5) 7.458 μm (8%)[c]	H I (8–6) 7.500 μm (8%)[c]	H I (9–7) 11.309 μm (8%)[c]
IRAS 01045								0.2 ± 0.1				
IRAS 02219*	2.23 ± 0.09			0.25 ± 0.02	0.29 ± 0.08	0.6 ± 0.1	0.87 ± 0.04	6.6 ± 0.2	1.4 ± 0.2	3.0 ± 0.2		
IRAS 02219◇	2.2 ± 0.2		0.2 ± 0.1	0.20 ± 0.02	0.28 ± 0.03	0.41 ± 0.10	0.76 ± 0.07	6.7 ± 0.1	1.9 ± 0.2	3.1 ± 0.4	0.9 ± 0.4	
IRAS 02575								0.23 ± 0.02				
IRAS 10589	0.6 ± 0.1					0.10 ± 0.01		1.71 ± 0.04	0.34 ± 0.06	0.52 ± 0.07		
IRAS 11143	0.35 ± 0.05							0.68 ± 0.04		0.19 ± 0.07		
IRAS 12063	0.9 ± 0.2			0.10 ± 0.04	0.15 ± 0.03	0.23 ± 0.08	0.33 ± 0.04	2.08 ± 0.08		0.7 ± 0.2	0.29 ± 0.08	
IRAS 12073	2.8 ± 0.1	0.15 ± 0.05	0.16 ± 0.02	0.24 ± 0.04	0.36 ± 0.03	0.50 ± 0.04	0.86 ± 0.07	6.6 ± 0.3	1.7 ± 0.4	2.8 ± 0.2	0.8 ± 0.1	
IRAS 12331♮								0.51 ± 0.02				
IRAS 15384	1.0 ± 0.1			0.16 ± 0.06		0.21 ± 0.02	0.38 ± 0.05	2.86 ± 0.07	0.7 ± 0.2	0.85 ± 0.07		
IRAS 15502	0.32 ± 0.06					0.11 ± 0.05		1.5 ± 0.1		0.6 ± 0.2		
IRAS 16128♮	0.42 ± 0.04							0.63 ± 0.04		0.25 ± 0.03		
IRAS 17160♮								0.30 ± 0.02		0.3 ± 0.2		
IRAS 17221	0.19 ± 0.02							0.64 ± 0.07		0.43 ± 0.07		
IRAS 17279								0.30 ± 0.03				
Sgr C								0.23 ± 0.03				
IRAS 17455	0.59 ± 0.03					0.16 ± 0.03	0.32 ± 0.04	2.0 ± 0.1		0.7 ± 0.1		
IRAS 17591								0.15 ± 0.03		0.19 ± 0.04		
IRAS 18032						0.19 ± 0.03	0.15 ± 0.02	0.89 ± 0.07				
IRAS 18116	0.34 ± 0.03							0.93 ± 0.03				
IRAS 18317	0.56 ± 0.05					0.13 ± 0.01	0.22 ± 0.03	2.0 ± 0.1		0.81 ± 0.07	0.21 ± 0.04	
IRAS 18434	2.16 ± 0.05		0.26 ± 0.07	0.17 ± 0.07	0.35 ± 0.04	0.45 ± 0.02	0.88 ± 0.06	6.8 ± 0.3	1.9 ± 0.5	2.5 ± 0.2	0.75 ± 0.06	0.3 ± 0.1
IRAS 18469								0.25 ± 0.02				
IRAS 18479								0.57 ± 0.04				

Table 2.9 — Continued.

Source	Line fluxes[a,b] (10^{-18} W/cm^2)											
	H I (6–4) 2.625 μm (4%)[c]	H I (13–5) 2.675 μm (4%)[c]	H I (12–5) 2.757 μm (4%)[c]	H I (11–5) 2.872 μm (4%)[c]	H I (10–5) 3.038 μm (4%)[c]	H I (9–5) 3.296 μm (4%)[c]	H I (8–5) 3.739 μm (4%)[c]	H I (5–4) 4.051 μm (4%)[c]	H I (7–5) 4.652 μm (8%)[c]	H I (6–5) 7.458 μm (8%)[c]	H I (8–6) 7.500 μm (8%)[c]	H I (9–7) 11.309 μm (8%)[c]
IRAS 18502	0.23 ± 0.01							0.89 ± 0.04				
IRAS 19207								0.67 ± 0.05				
IRAS 19442								0.21 ± 0.09				
IRAS 19598[b]	1.50 ± 0.08	0.05 ± 0.02	0.08 ± 0.02	0.125 ± 0.01	0.18 ± 0.02	0.28 ± 0.02	0.62 ± 0.03	4.7 ± 0.1	0.95 ± 0.08	1.96 ± 0.06	0.75 ± 0.07	
DR 21								0.88 ± 0.08		0.55 ± 0.03		
IRAS 21190	1.3 ± 0.1				0.13 ± 0.03	0.25 ± 0.02	0.27 ± 0.03	2.25 ± 0.08		0.76 ± 0.09		
IRAS 22308*	0.5 ± 0.1							0.62 ± 0.03				
IRAS 22308†								0.61 ± 0.03				
IRAS 23030	1.0 ± 0.2				0.12 ± 0.04	0.11 ± 0.05	0.15 ± 0.03	1.60 ± 0.06		0.6 ± 0.1	0.11 ± 0.04	
IRAS 23133	1.0 ± 0.1						0.31 ± 0.03	1.74 ± 0.10		0.5 ± 0.2		

Fluxes of extra H I recombination lines observed in IRAS 19598

Source	Line fluxes[a,b] (10^{-18} W/cm^2)								
	H I (14–5) 2.613 μm (4%)[c]	H I (16–6) 3.812 μm (4%)[c]	H I (15–6) 3.906 μm (4%)[c]	H I (14–6) 4.020 μm (4%)[c]	H I (12–6) 4.376 μm (4%)[c]	H I (11–6) 4.673 μm (8%)[c]	H I (10–6) 5.127 μm (8%)[c]	H I (9–6) 5.907 μm (8%)[c]	H I (10–7) 8.760 μm (8%)[c]
IRAS 19598	0.05 ± 0.01	0.03 ± 0.02	0.07 ± 0.01	0.09 ± 0.04	0.3 ± 0.2	0.12 ± 0.06	0.2 ± 0.1	0.24 ± 0.06	0.12 ± 0.01

([a]) The listed errors are the square root of the quadratic sum of the difference between the up and down scan measurements and the statistical error of the line fitting (see § 2.4). Hence *no* calibration uncertainties are included. To obtain the final error, see § 2.4.2. ([b]) Note that these lines are seen through different apertures (see Table 2.2). ([c]) 1σ absolute flux accuracy at this wavelength (see Table 2.2). ([♮]) The approximate offset between the source peak and the ISO pointing is $\geq 10''$. This data should be used with caution (see § 2.4.3 and § 2.6.2). ([°]) TDT = 64600609; ([⋄]) TDT = 78800709; ([⋆]) TDT = 17701258; ([†]) TDT = 56101082; see § 2.3.1. ([b]) Fluxes of extra H I recombination lines observed for this source are listed at the end of the table.

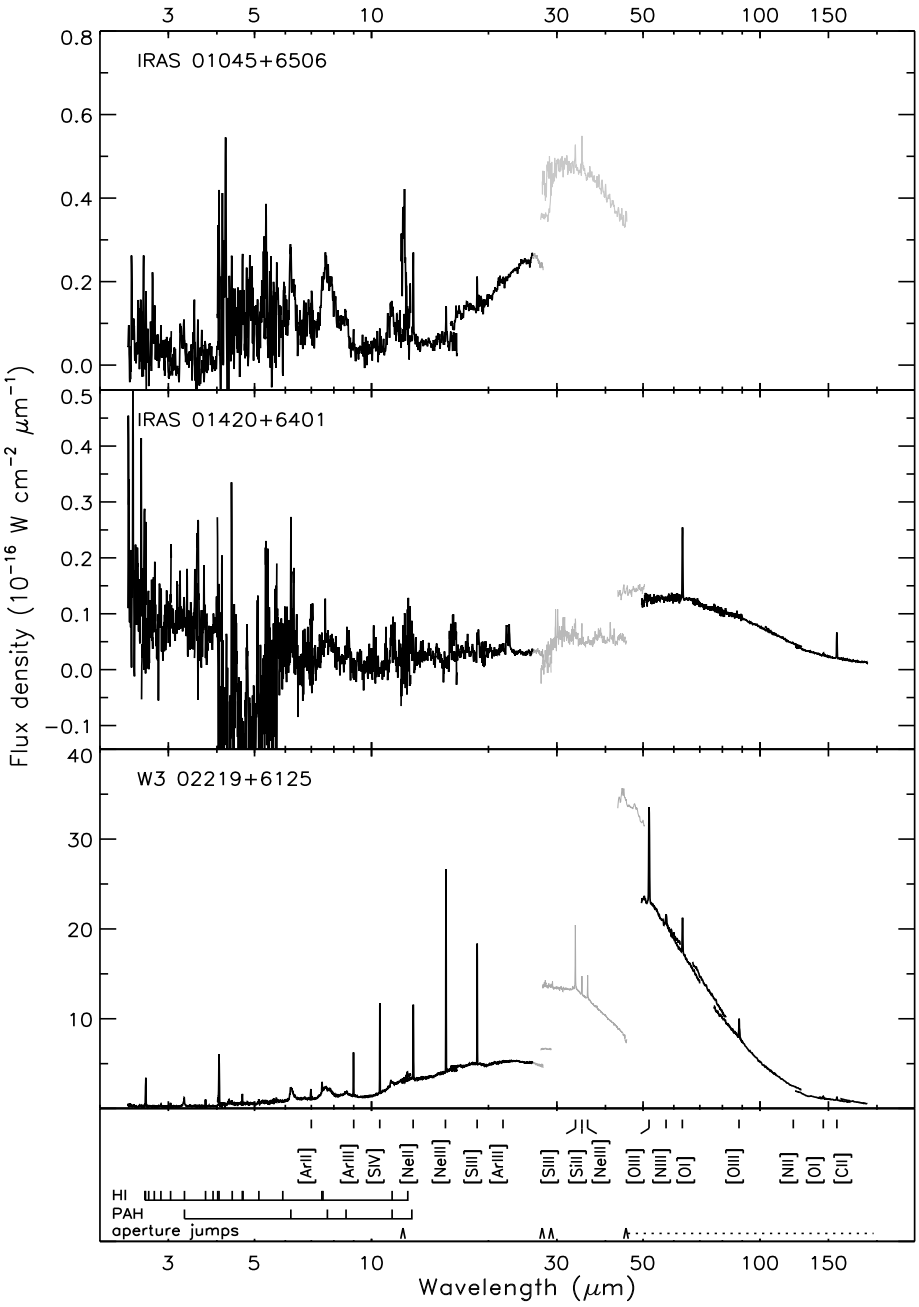

Figure 2.6 — The combined SWS-LWS spectra. The fine-structure lines, the hydrogen recombination lines and the main PAH features are identified. The wavelengths at which an aperture jump occurs within the SWS wavelength region and the wavelength between SWS and LWS, are indicated by flags. The diameter of the LWS beam smoothly changes, ranging from 67″–85″, indicated by the dotted line.

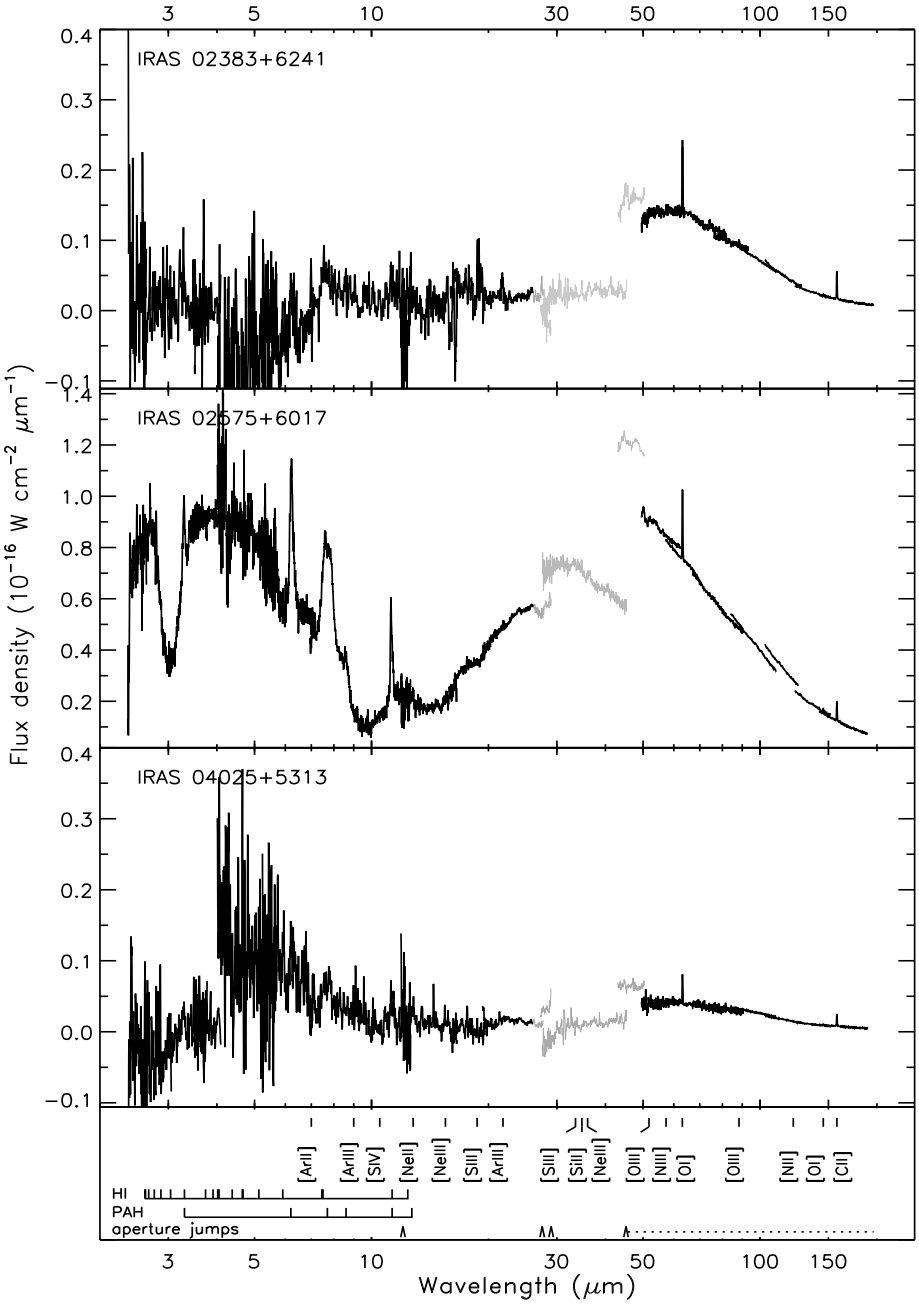

Figure 2.6 — continued.

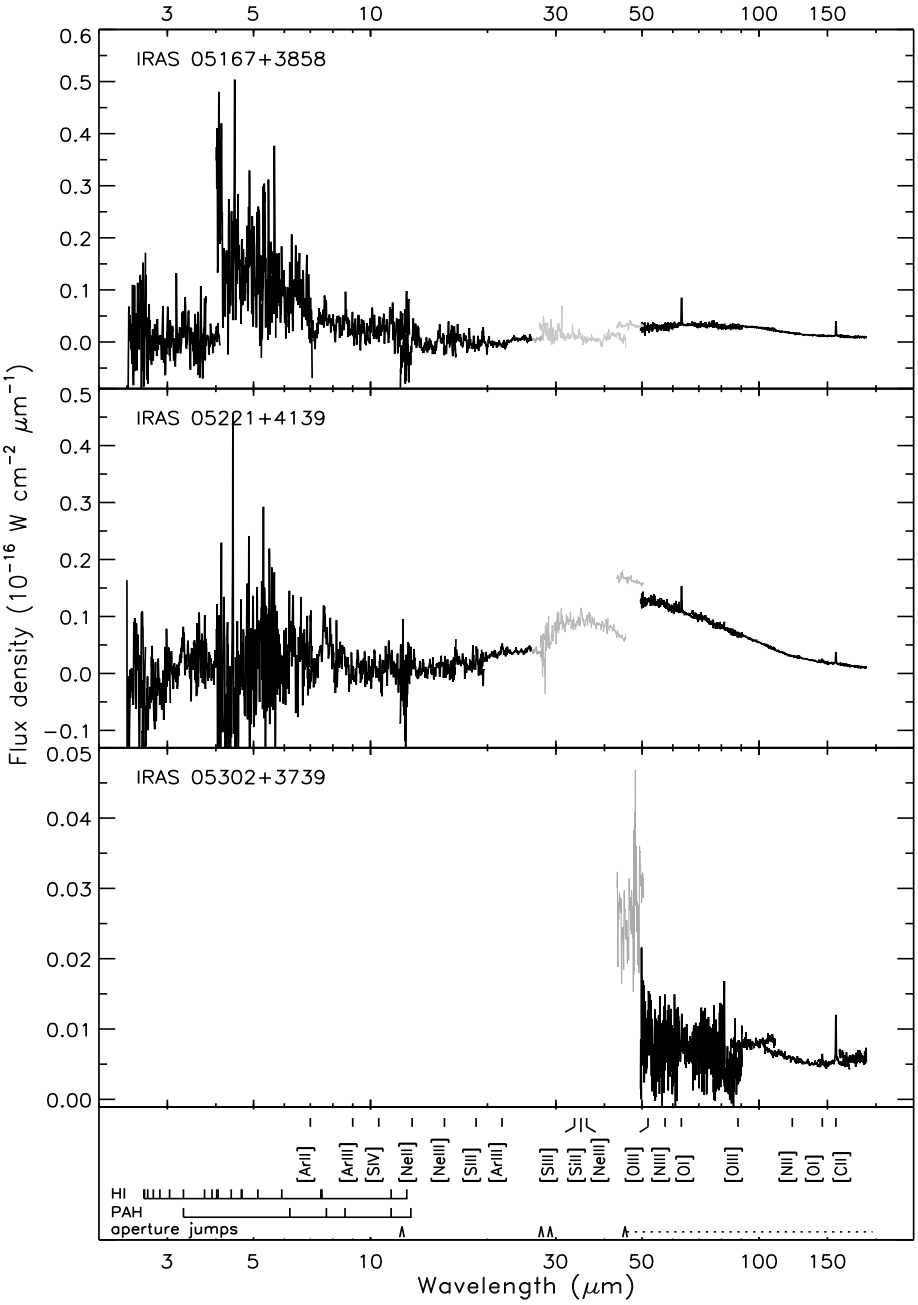

Figure 2.6 — continued.

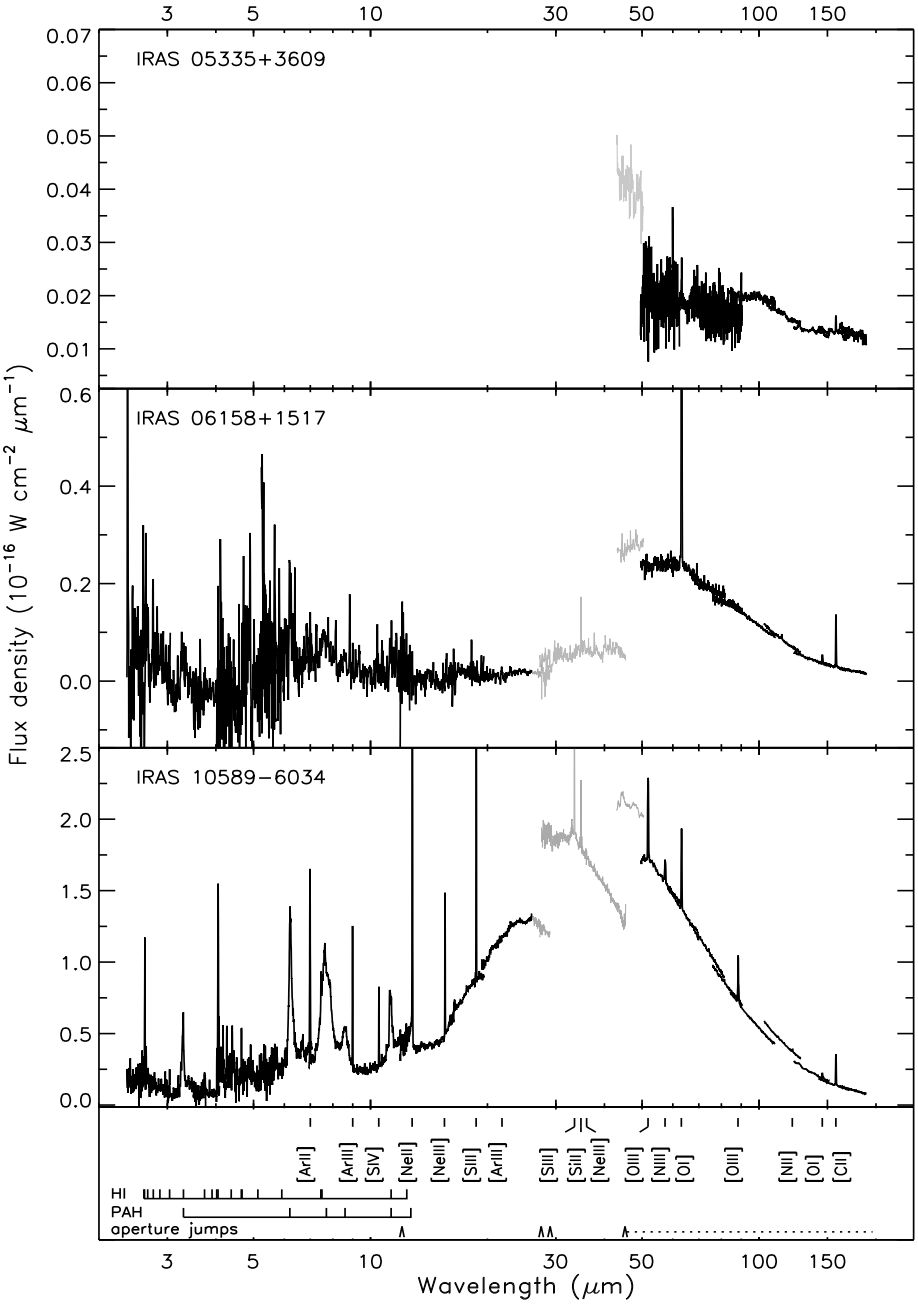

Figure 2.6 — continued.

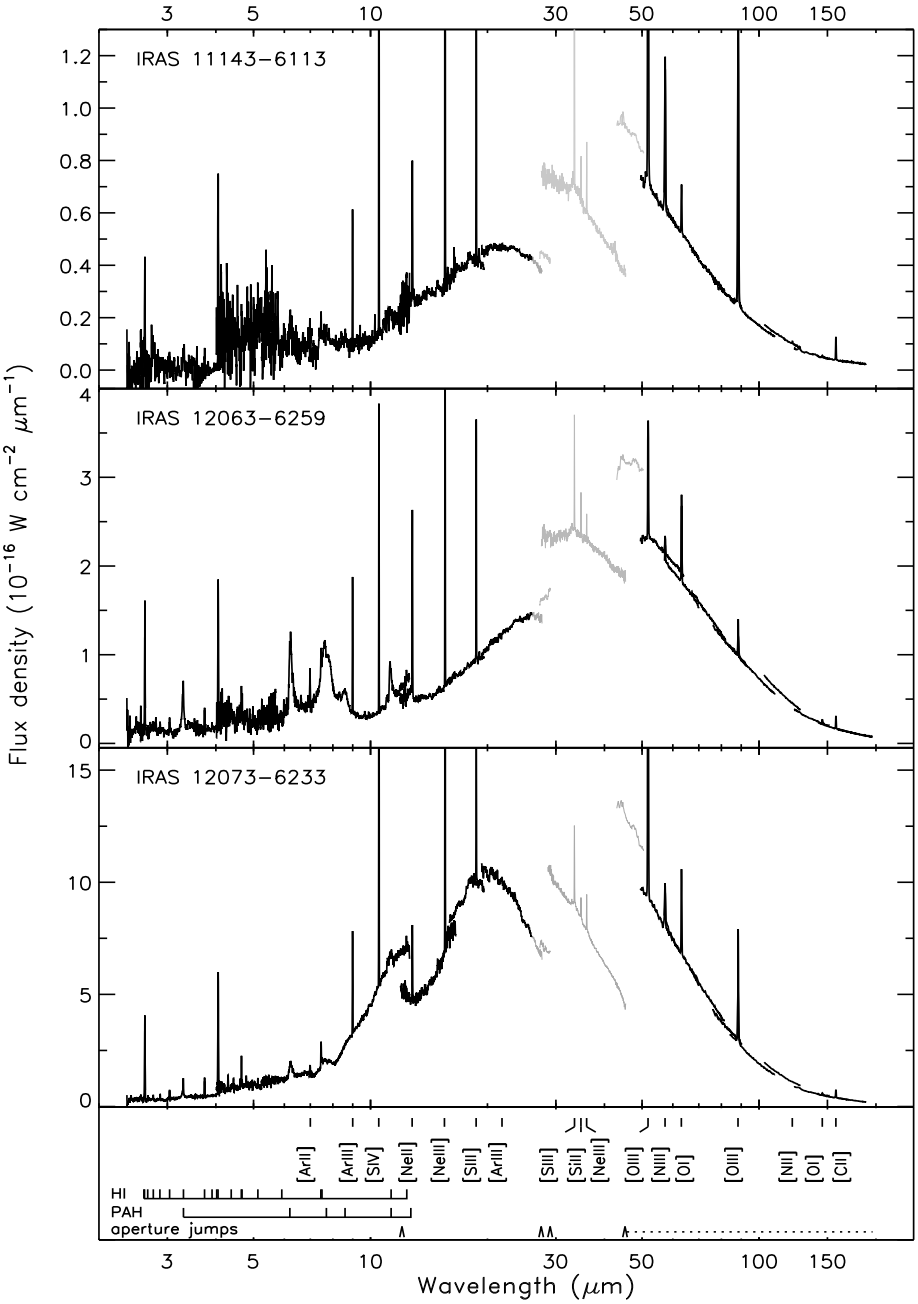

Figure 2.6 — continued.

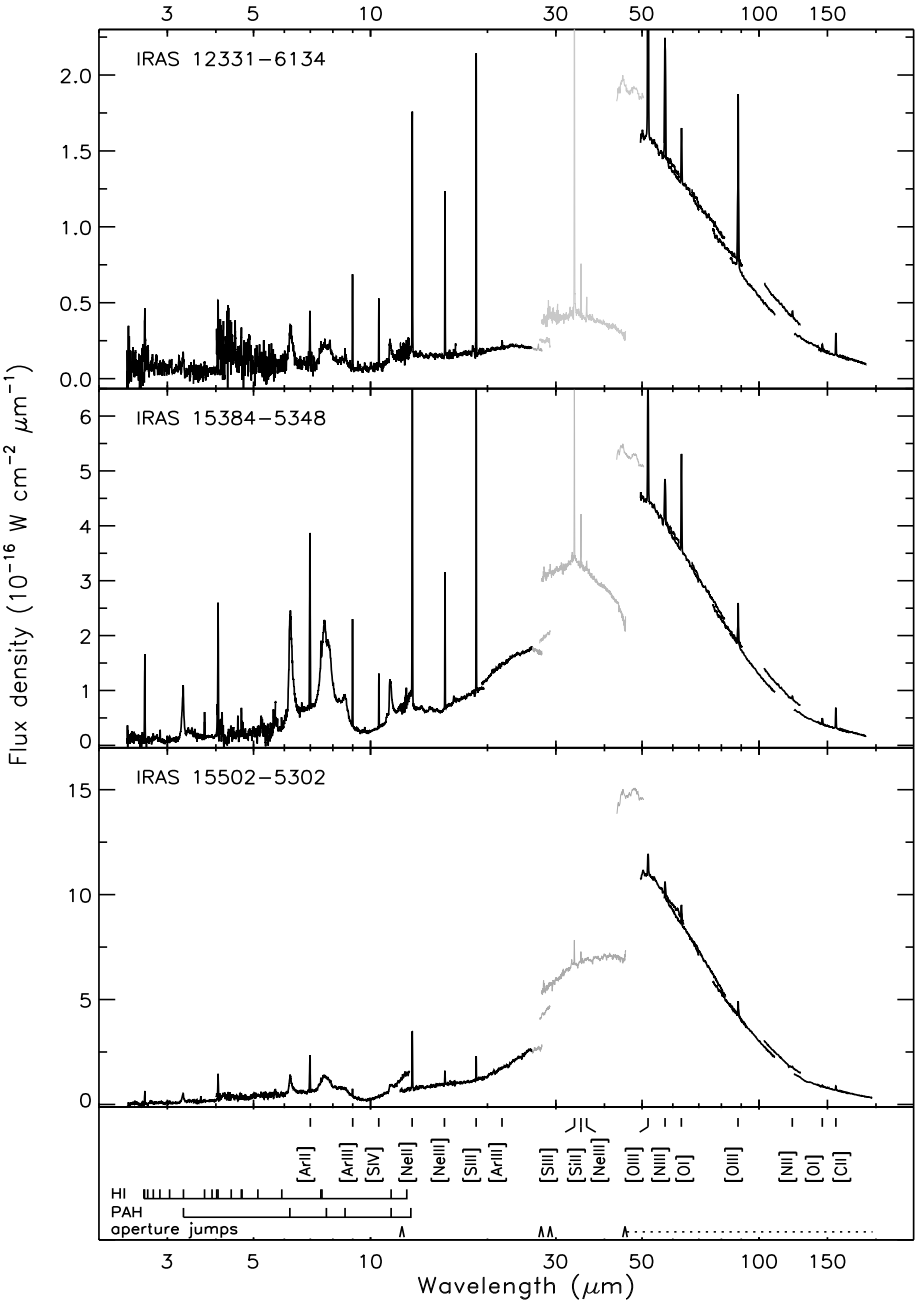

Figure 2.6 — continued.

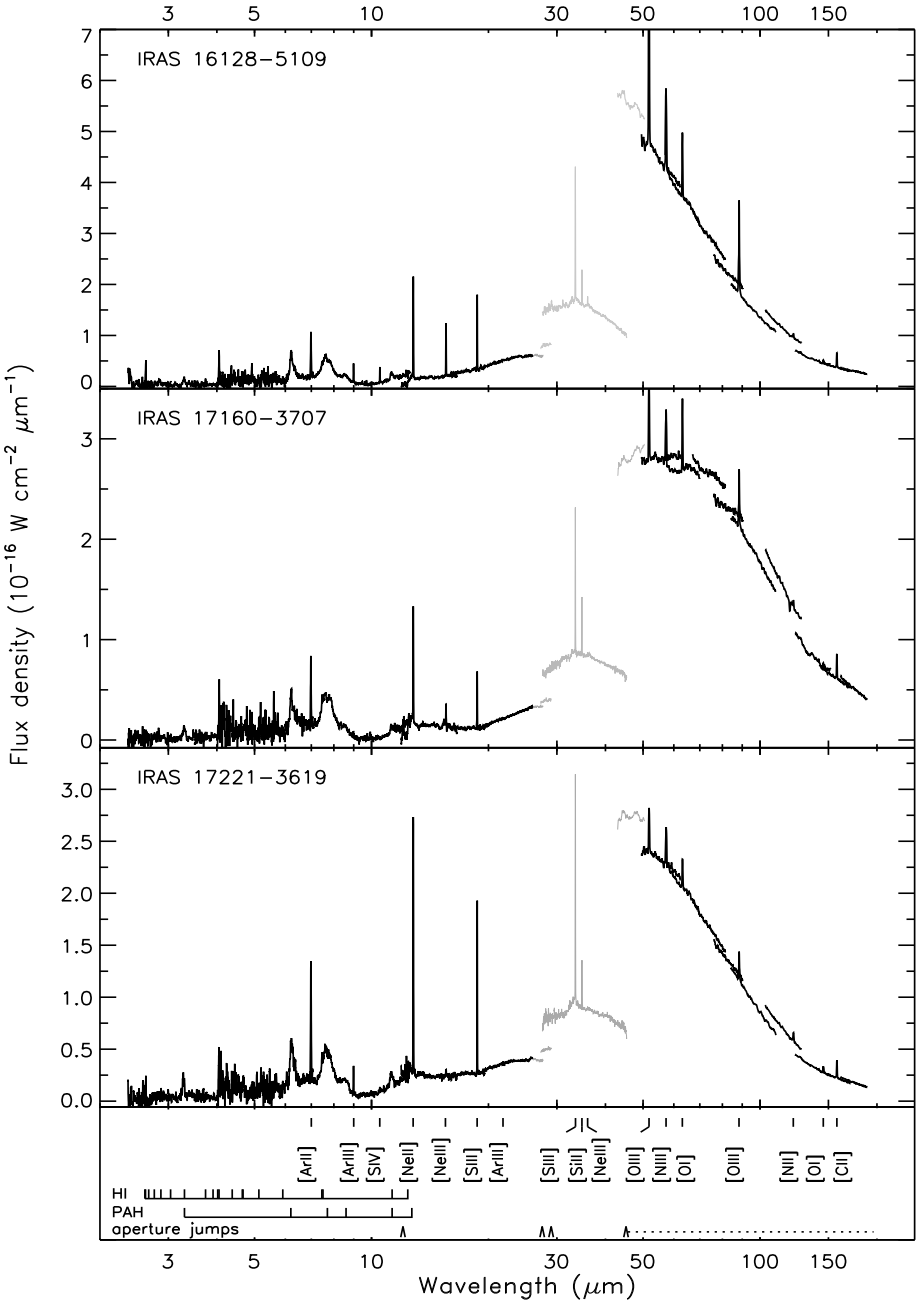

Figure 2.6 — continued.

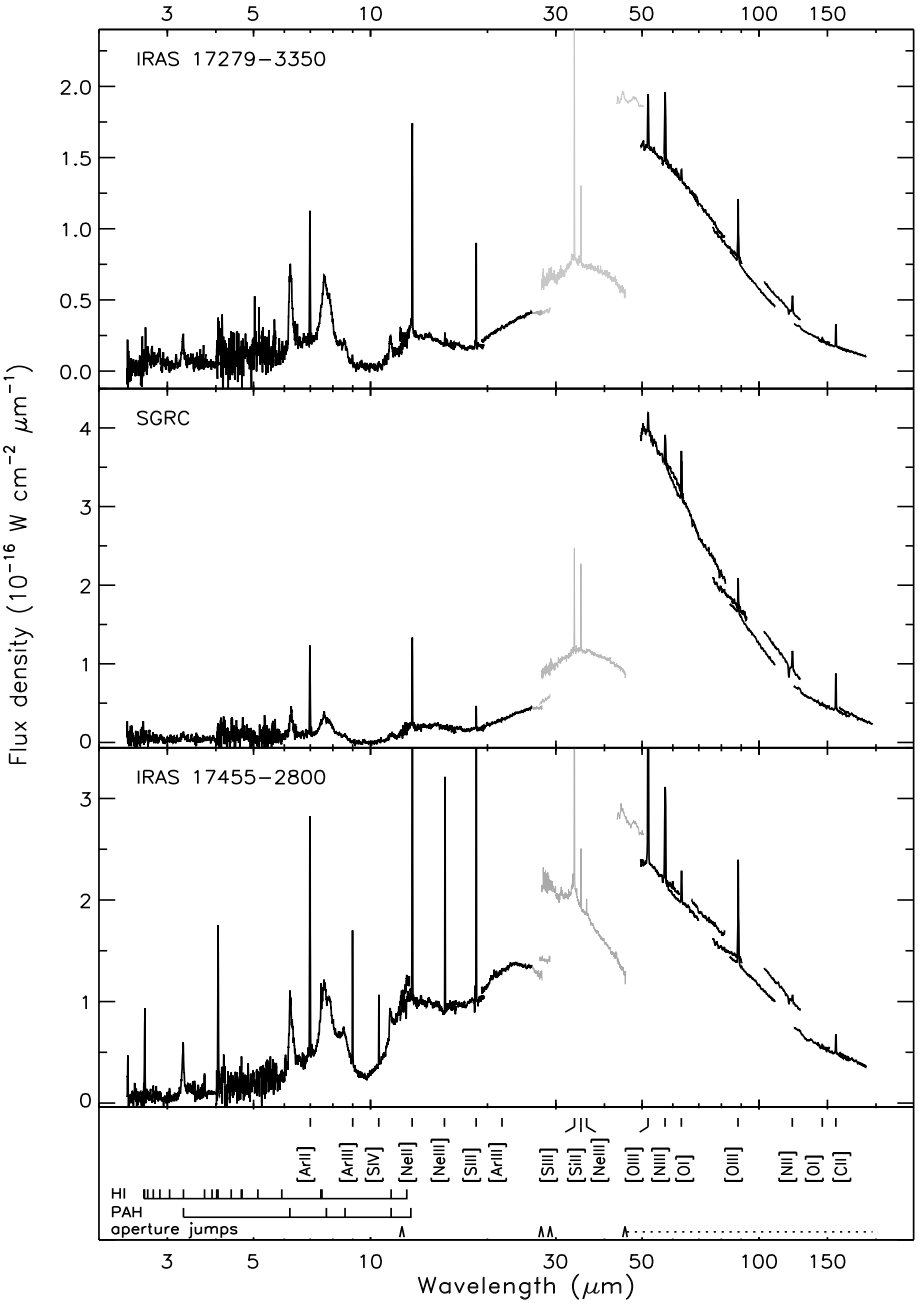

Figure 2.6 — continued.

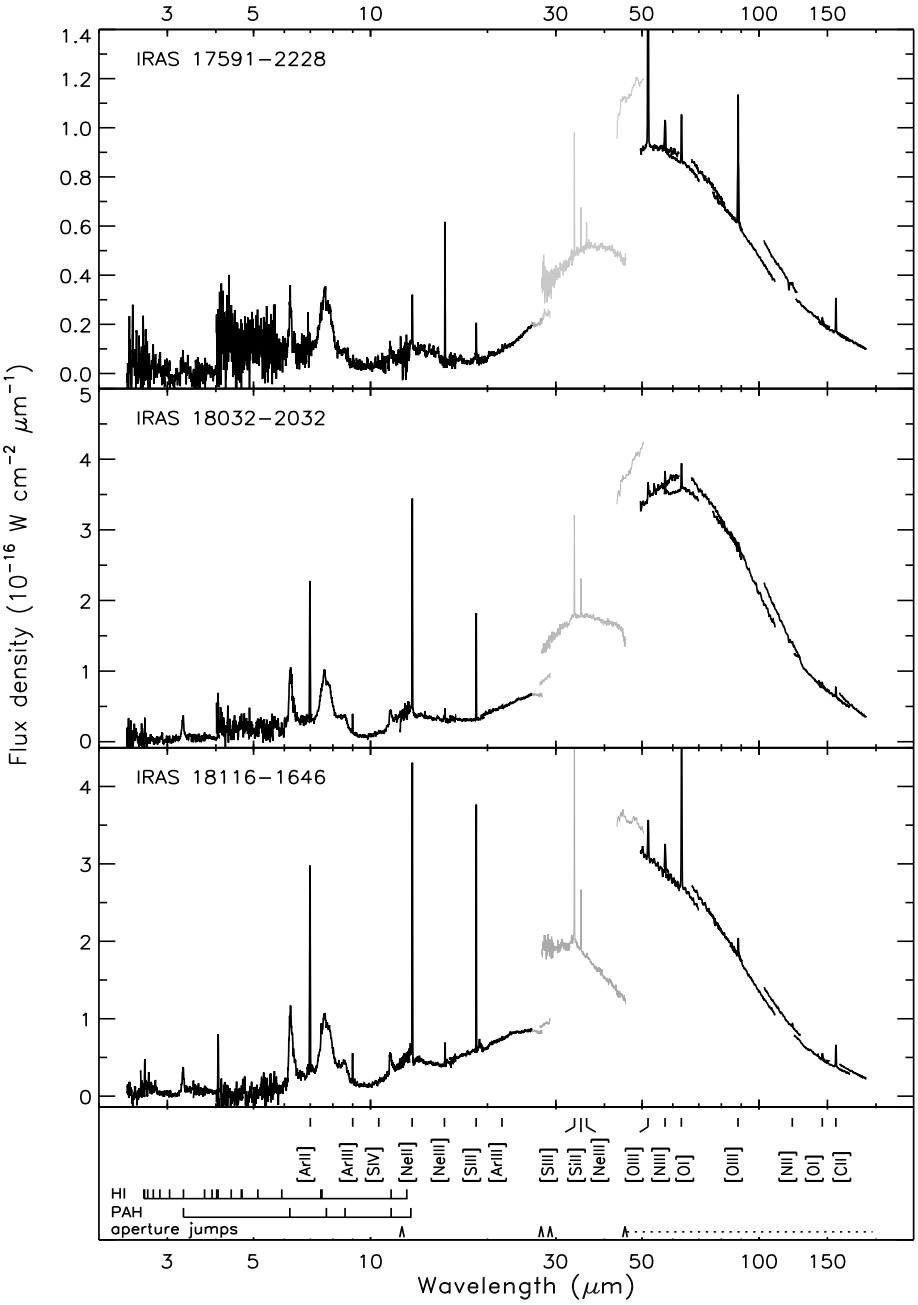

Figure 2.6 — continued.

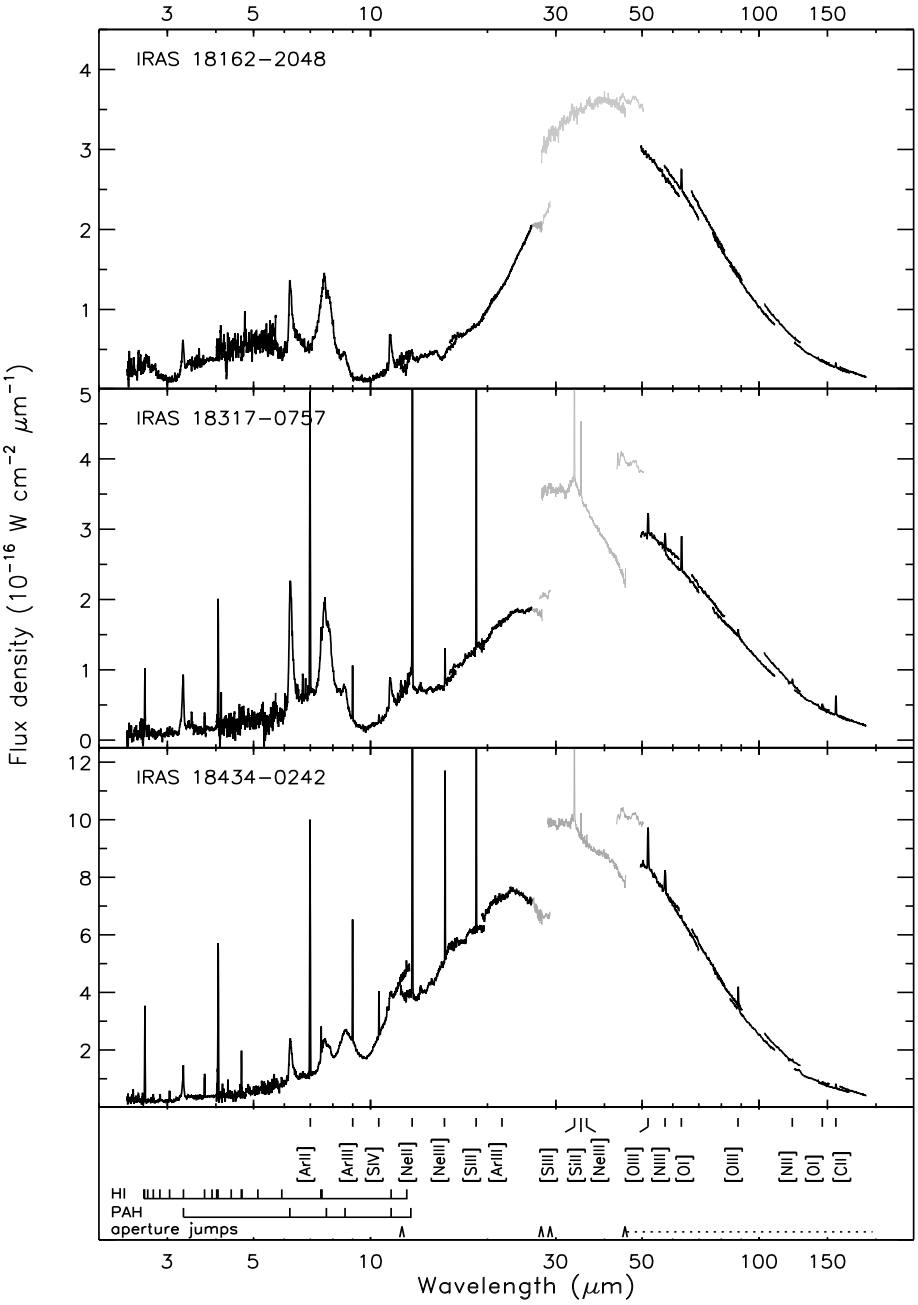

Figure 2.6 — continued.

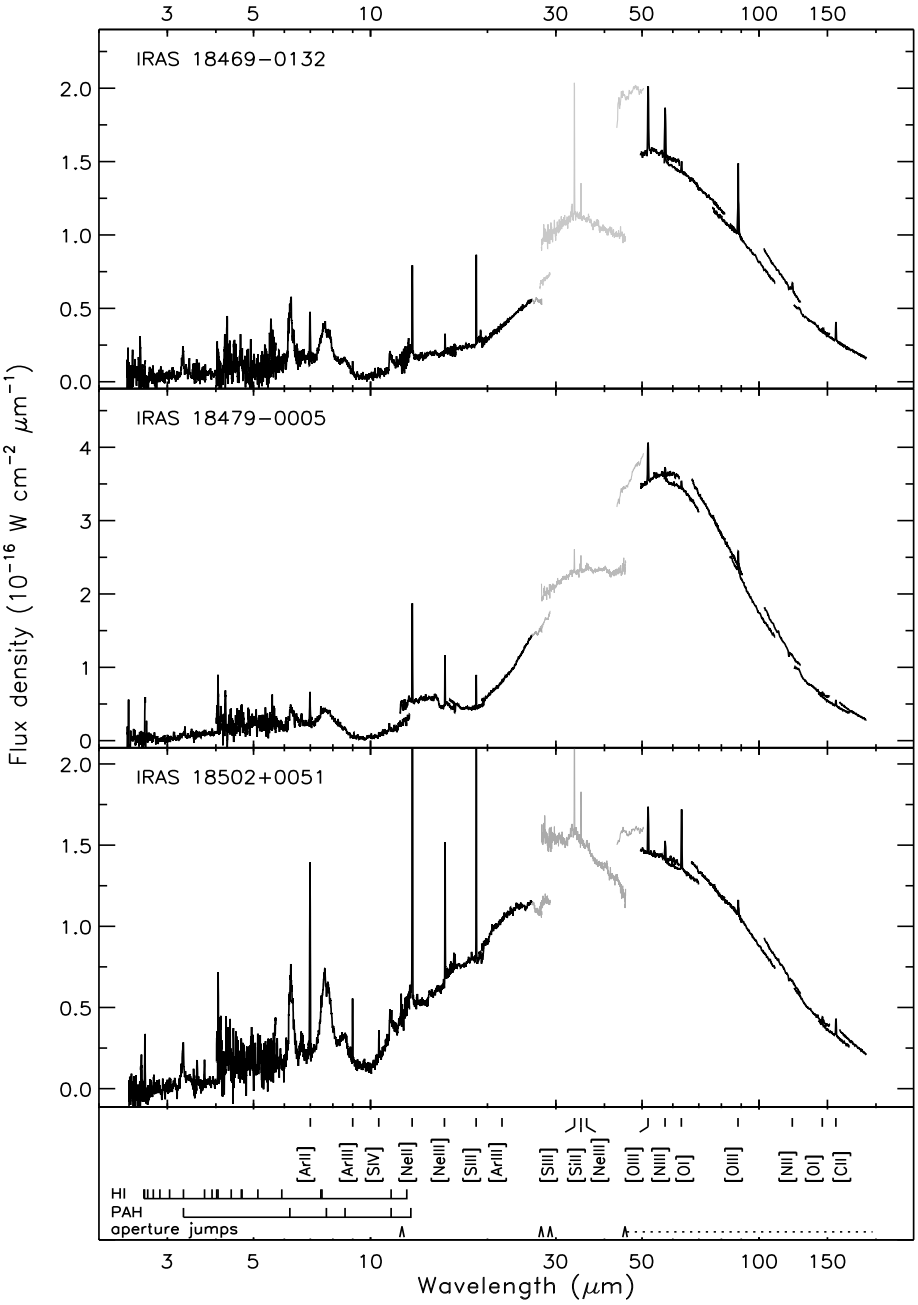

Figure 2.6 — continued.

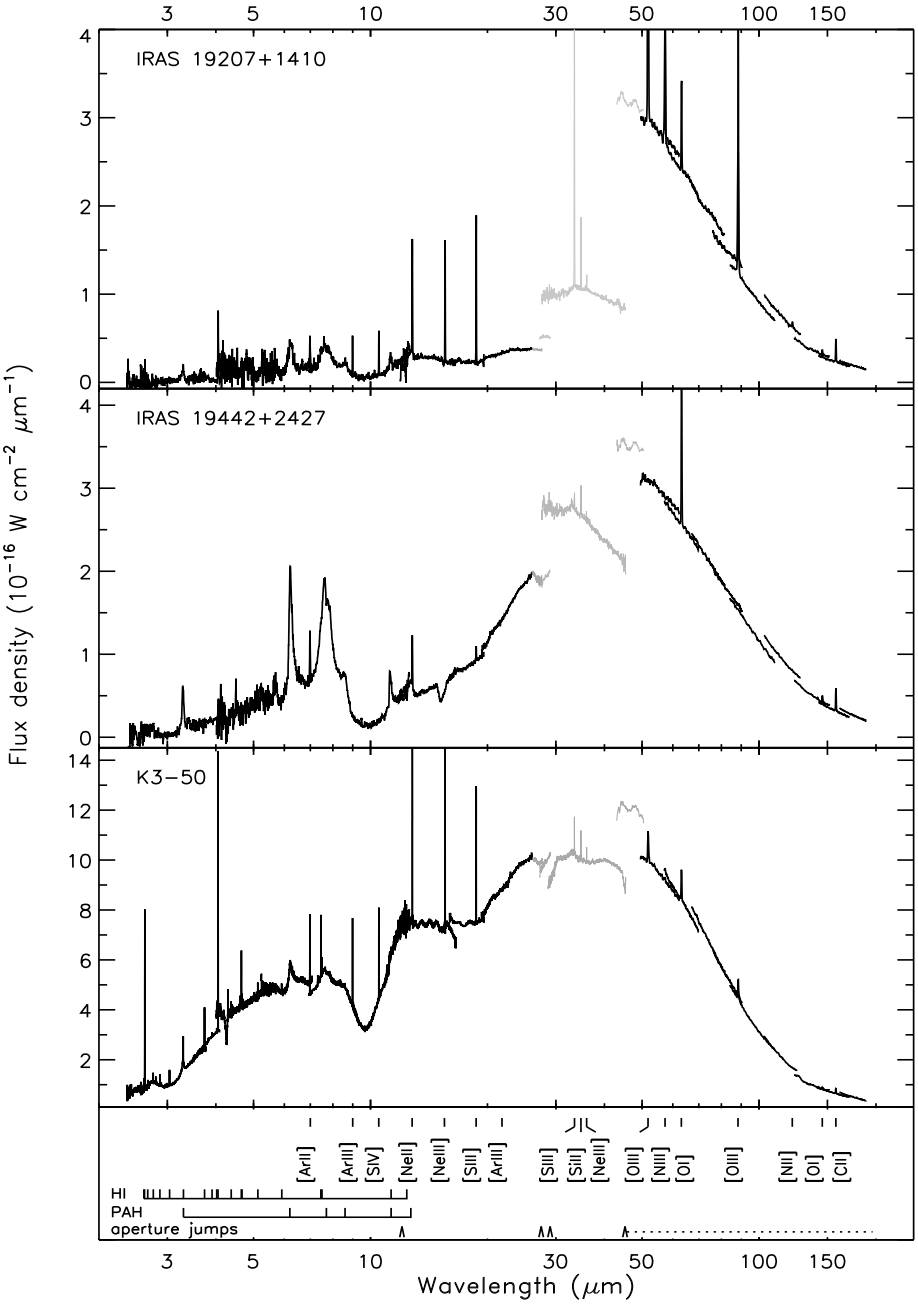

Figure 2.6 — continued.

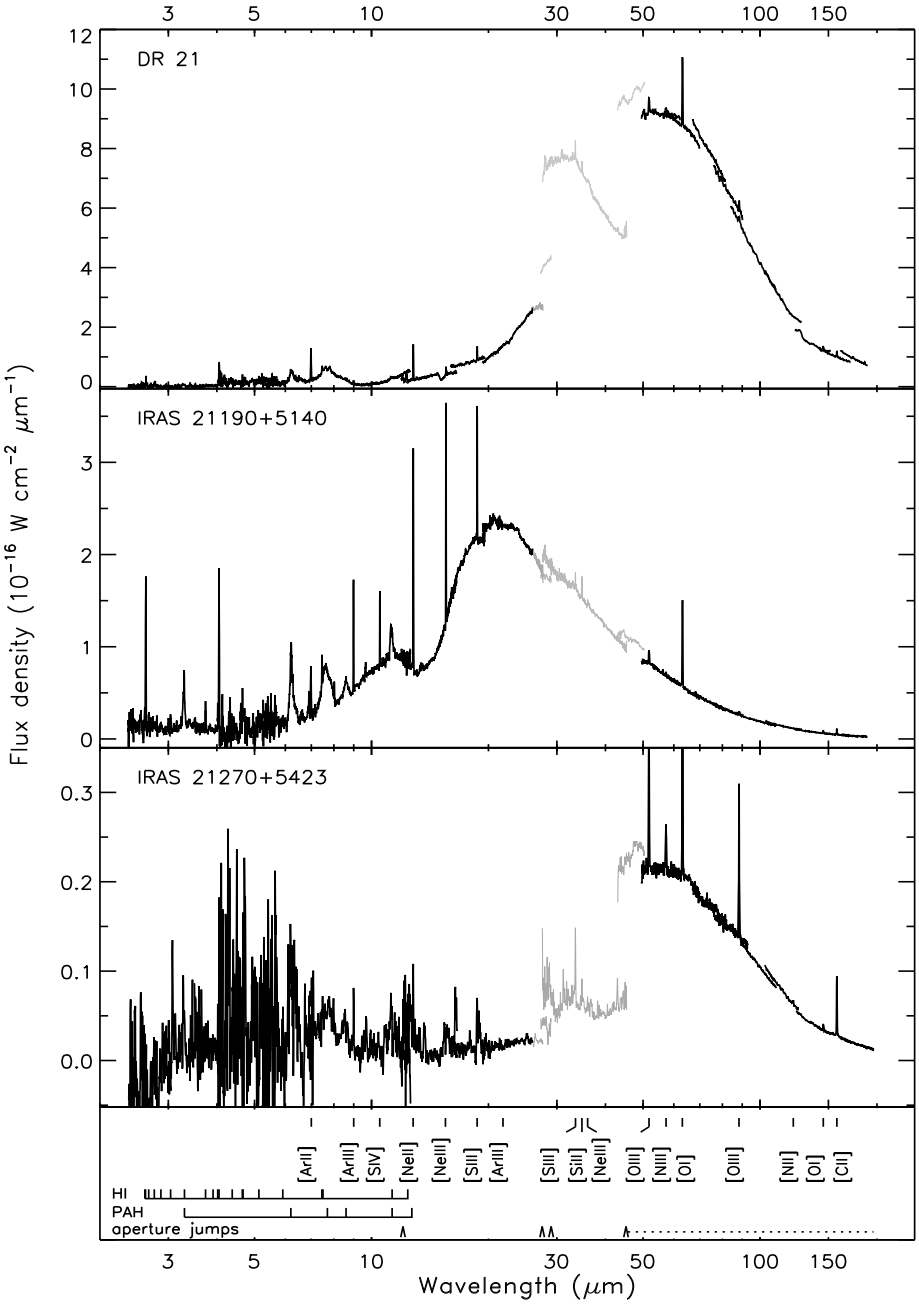

Figure 2.6 — continued.

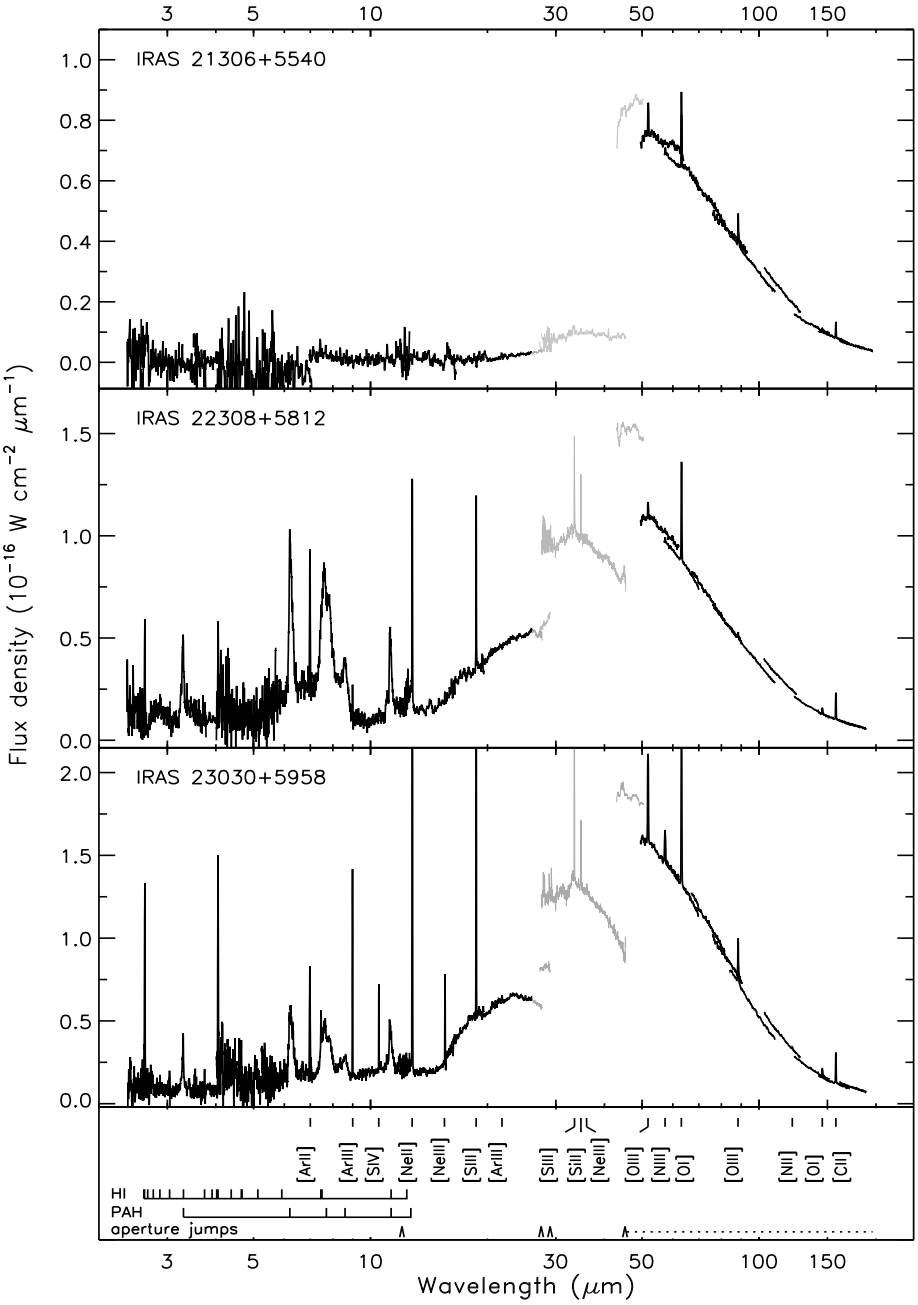

Figure 2.6 — continued.

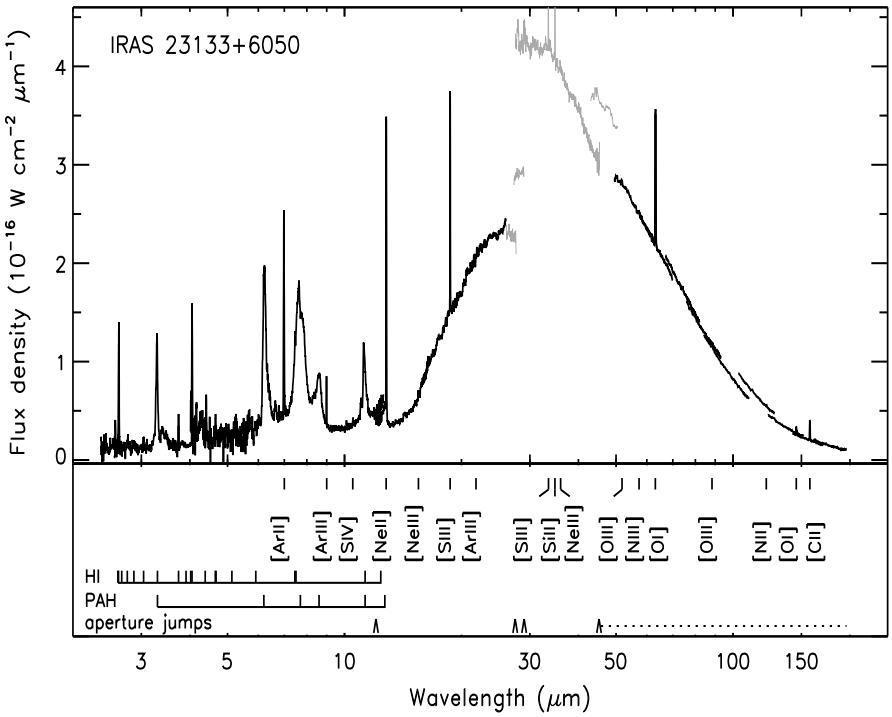

Figure 2.6 — continued.

3

The rich 6 to 9 μm spectrum of interstellar PAHs

Appeared as :

E. Peeters, S. Hony, C. Van Kerckhoven, A.G.G.M. Tielens, L.J. Allamandola, D.M. Hudgins, C.W. Bauschlicher

Astronomy & Astrophysics, 2002, 390,1089

Abstract

IR spectroscopy provides a valuable tool for the characterisation and identification of interstellar molecular species. Here, we present 6–9 μm spectra of a sample of reflection nebulae, HII regions, YSOs, evolved stars and galaxies that show strong unidentified infrared bands, obtained with the SWS spectrograph on board ISO. The IR emission features in this wavelength region show pronounced variations. 1) The 6.2 μm feature shifts from 6.22 to 6.3 μm and clearly shows profile variations. 2) The 7.7 μm complex is comprised of at least two subpeaks peaking at 7.6 and one longwards of 7.7 μm. In some cases the main peak can apparently shift up to 8 μm. Two sources do not exhibit a 7.7 μm complex but instead show a broad emission feature at 8.22 μm. 3) The 8.6 μm feature has a symmetric profile in all sources and some sources exhibit this band at slightly longer wavelengths. For the 6.2, 7.7 and 8.6 μm features, the sources have been classified independently based on their profile and peak position. The classes derived for these features are directly linked with each other. Sources with a 6.2 μm feature peaking at $\sim$ 6.22 μm exhibit a 7.7 μm complex dominated by the

7.6 μm component. In contrast, sources with a 6.2 μm profile peaking longwards of 6.24 μm show a 7.7 μm complex with a dominant peak longwards of 7.7 μm and a 8.6 μm feature shifted toward the red. Furthermore, the observed 6–9 μm spectrum depends on the type of object. All ISM-like sources and a few PNe and Post-AGB stars belong to the first group while isolated Herbig AeBe stars, a few Post-AGB stars and most PNe belong to the second group. We summarise existing laboratory data and theoretical quantum chemical calculations of the modes emitting in this wavelength region of PAH molecules. We discuss the variations in peak position and profile in view of the exact nature of the carrier. We attribute the observed 6.2 μm profile and peak position to the combined effect of a PAH family and anharmonicity with pure PAHs representing the 6.3 μm component and substituted/complexed PAHs representing the 6.2 μm component. The 7.6 μm component is well reproduced by both pure and substituted/complexed PAHs but the 7.8 μm component remains an enigma. In addition, the exact identification of the 8.22 μm feature remains unknown. The observed variations in the characteristics of the IR emission bands are linked to the local physical conditions. Possible formation and evolution processes that may influence the interstellar PAH class are highlighted.

3.1 Introduction

Mid-infrared spectra of many sources are dominated by the well-known emission features at 3.3, 6.2, 7.7 and 11.2 μm, commonly called the unidentified infrared (UIR) bands (cf. Gillett et al. 1973; Geballe et al. 1985; Cohen et al. 1986). These UIR bands are associated with a wide variety of objects - including HII regions, Post-AGB stars, PNe, YSOs, the diffuse ISM and galaxies - and are generally attributed to Polycyclic Aromatic Hydrocarbon (PAH) molecules (Léger & Puget 1984; Allamandola et al. 1985; Puget & Léger 1989; Allamandola et al. 1989b), although the exact molecular identification of the carriers remains unknown. Beyond serving as simple PAH indicators, they can serve as red-shift indicators, as tracers of elemental evolution in external galaxies, as tracers of chemical evolution and can be used to probe environmental conditions within the objects (Genzel et al. 1998; Lutz et al. 1998; Helou 1999; Serabyn 1999; Genzel & Cesarsky 2000; Helou et al. 2000; Joblin et al. 2000; Hony et al. 2001; Vermeij et al. 2002a; Verstraete et al. 2001).

The region from 6 to 9 μm reveals a number of emission features with bands at 5.2, 5.7, 6.0, 6.2, 6.8, 7.7 and 8.6 μm. The 7.7 μm feature is particularly important as it is the strongest of the interstellar UIR bands and, as such, can be used to probe objects in which the other features are weak.

Until quite recently, most of the interstellar emission bands were considered to be more-or-less invariant in position and profile. Although some minor variations were noted, by and large the 6.2 μm feature was considered fixed at 6.2 μm, regardless of the reported shift in peak position by Molster et al. (1996). The 7.7 μm band was generally treated similarly in spite of earlier papers showing this band is comprised of at least two variable components (e.g. Bregman 1989; Cohen et al. 1989; Beintema et al. 1996; Molster et al. 1996; Roelfsema et al. 1996; Moutou et al. 1999a,c; Peeters et al. 1999). It was recognised some time ago that

the 7.7 μm complex appears either with a dominant 7.6 μm component or with the dominant component peaking at 7.8–8 μm (Bregman 1989; Cohen et al. 1989). In addition, it was found that the former profile is associated with HII regions and the one peaking near 7.8 μm is associated with planetary nebulae (Bregman 1989; Cohen et al. 1989). Recently, thanks to the high resolution spectra obtained with ISO, more subpeaks of the 7.7 μm complex were reported near 7.2 to 7.4 and 8.2 μm (Moutou et al. 1999a,b).

In Sect. 3.2, our sample and the observations are presented; the data reduction, the influence of extinction and the decomposition of the spectra are discussed. Section 3.3 analyses the 6.2, 7.7 and 8.6 μm features. The link between the observed variations in the 6.2, 7.7 and 8.6 μm features and the connection with the type of object is highlighted in Sect. 3.4. Section 3.5 presents the observed trends. The spectral characteristics of PAHs in this wavelength range as measured in the laboratory and calculated by quantum chemical theories are summarised in Sect. 3.6. Section 3.7 highlights the astronomical implications. Finally, in Sect. 3.8 our main results are summarised.

3.2 The data

3.2.1 Sample

The sample includes 57 sources from a wide variety of objects, ranging from Reflection Nebulae (RNe), HII regions, Young Stellar Objects (YSOs), Post-AGB stars, Planetary Nebulae (PNe) to galaxies. We give in Table 3.1 characteristics of the sources; i.e. the extinction in the K-band, A_K, the spectral type of the illuminating source, and an estimate of the incident UV flux density at 1000Å, G_0, at the location where the PAH emission originates in units of the average interstellar radiation field (λu_λ=1.6 10^{-6} W/m^2, Habing 1968).

For the compact HII regions (CHII) present in our sample, Martín-Hernández et al. (2002a) estimated A_K based upon HI recombination lines to be between 0 and 2.7 magn. A_K is taken from Cidale et al. (2001) for CD -42 11721, from Miroshnichenko et al. (1999) for HD 179218, from Everett et al. (1995) for Orion Peak1 and from van den Ancker (1999) for IRAS 03260, GGD -27 ILL, S 106, HD 97048, BD +40 4124 and HD 100546.

For most sources, the spectral types are taken from Simbad. The spectral type of IRAS 12073 and IRAS 18434 are taken from Kaper et al. (2002a,b, and private communication) and that of IRAS 16594-4656 is from Su et al. (2001). The effective temperatures for Hb 5, NGC7027, IRAS 18576 and G 327 are taken from Gesicki & Zijlstra (2000), Latter et al. (2000), Ueta et al. (2001) and Ehrenfreund et al. (1997) respectively.

For the CHII regions and GGD -27 ILL, we have derived G_0 values from the observed IR flux and the angular size of the PAH emission region (cf. Hony et al. 2001). This estimate is based on the assumption that all the UV light is absorbed in a spherical shell with the angular diameter of the HII region and re-emitted in the IR. We have used for the size of the HII regions the measured radio sizes. This is reasonable since the PAHs are expected to be destroyed inside the HII region. The IR flux was derived from the L_{IR} given by Peeters et al. (2002b) and the radio sizes used are taken from Peeters et al. (2002b) and Martín-Hernández et al. (2002b). The G_0 values are similar to those derived by Hony et al. (2001) for the sources present in both samples. For the Orion bar, we refer to Tielens et al. (1993) and Joblin et al. (1996a) for the given G_0 values. We have taken G_0 values for the Herbig Ae Be stars from Van Kerckhoven (2002) who derived G_0 from the UV flux between 6 and 13.6 eV, F_{UV}, and the spatial distribution of the PAHs in the sources. F_{UV} is derived from the observed stellar

Table 3.1 — Journal of observations. The coordinates of the SWS pointing are given.

Source	α (J2000)[a]	δ (J2000)[a]	TDT[b]	Obs. mode[c]	Ref.	A_K^d	Sp. Type[d]	G_0^d	Object Type
NGC 253	00 47 33.19	−25 17 17.20	24701422	01(4)	1		-	-	Seyfert Galaxy
W 3A 02219+6125	02 25 44.59	+62 06 11.20	64600609	01(2)	2	1.5	O6	1E4	CHII
IRAS 02575+6017	03 01 31.28	+60 29 13.49	15200555	01(2)	2	2		1E5	CHII+YSO
IRAS 03260+3111	03 29 10.37	+31 21 58.28	65902719	01(3)	3		B9	2E4	non-iso. HAeBe star♭
Orion PK1	05 35 13.67	−05 22 08.51	68701515	01(4)	4	0.15	O6		HII
Orion PK2	05 35 15.79	−05 24 40.69	83301701	01(4)	-		O6		HII
OrionBar D8	05 35 18.22	−05 24 39.89	69501409	01(2)	5		O6		HII
OrionBar BRGA	05 35 19.31	−05 24 59.90	69502108	01(2)	-		O6		HII
OrionBar D5	05 35 19.81	−05 25 09.98	83101507	01(2)	-		O6	5E4	HII
OrionBar H2S1	05 35 20.31	−05 25 19.99	69501806	01(4)	6		O6	7E3	HII
OrionBar D2	05 35 21.40	−05 25 40.12	69502005	01(2)	-		O6		HII
NGC 2023	05 41 38.29	−02 16 32.59	65602309	01(3)	7		B1.5V	3E2	RN
HD 44179	06 19 58.20	−10 38 15.22	70201801	01(4)	8		B8V	5E6	Post-AGB star
IRAS 07027-7934	06 59 26.29	−79 38 48.01	73501035	01(2)	9		WC10	2E7	PN
M 82	09 55 50.70	+69 40 44.40	11600319	01(4)	1		-	-	starburst galaxy
HR 4049	10 16 07.56	−28 59 31.31	17100101	01(2)	8,10		B9.5Ib-II		Post-AGB star
IRAS 10589-6034	11 00 59.78	−60 50 27.10	26800760	01(2)	2	1.5		1E5	CHII
HD 97048	11 08 04.61	−77 39 18.88	61801318	01(4)	11	0.12	A0	1.7E4	non-iso. HAeBe star♭
HD 100546	11 33 25.51	−70 11 41.78	27601036	01(1)	12	0.03	B9Vne	9E3	iso. HAeBe star
IRAS 12063-6259	12 09 01.15	−63 15 54.68	25901414	01(2)	2	1.5		1E5	CHII
IRAS 12073-6233	12 10 00.32	−62 49 56.50	25901572	01(2)	2	1.5	O6-O7.5	1E6	starforming region
IRAS 13416-6243	13 46 07.61	−62 58 19.98	62803904	01(3)	-				Post-AGB star
circinus	14 13 09.70	−65 20 21.52	07902231	01(4)	13		-	-	Seyfert 2 galaxy
HE 2-113	14 59 53.49	−54 18 07.70	43400768	01(2)	14		WC10	6E4	PN

Table 3.1 — Continued.

Source	α (J2000)[a]	δ (J2000)[a]	TDT[b]	Obs. mode[c]	Ref.	A_K^d	Sp. Type[d]	G_0^d	Object Type
IRAS 15384-5348	15 42 17.16	−53 58 31.51	29900661	01(2)	2	1.5		5E4	CHII
G 327.3-0.5	15 53 05.89	−54 35 21.08	11702216	01(1)	-		38,000		HII
IRAS 15502-5302	15 54 05.99	−53 11 36.38	27301117	01(2)	2	3.1		3E6	CHII
IRAS 16279-4757	16 31 38.20	−48 04 06.38	64402513	01(3)	15				Post-AGB star
CD -42 11721 (off)	16 59 05.82	−42 42 14.80	28900461	01(2)	16,17	0.7	B0		non-iso. HAeBe star♭
CD -42 11721	16 59 06.79	−42 42 07.99	64701904	01(2)	3,16,17	0.4-0.7	B0		non-iso. HAeBe star♭
IRAS 17047-5650	17 00 00.91	−56 54 47.20	13602083	01(3)	9		WC10	5E6	PN
IRAS 16594-4656	17 03 09.67	−47 00 47.90	45800441	01(1)	18		B7		Post-AGB star
IRAS 17279-3350	17 31 17.96	−33 52 49.30	32200877	01(2)	2	2.2		5E3	CHII
IRAS 17347-3139	17 36 00.61	−31 40 54.19	87000939	01(3)	19			8E5	PN
XX-OPH	17 43 56.42	−06 16 08.00	46000601	01(4)	-		Ape		variable star
Hb 5	17 47 56.11	−29 59 39.70	49400104	01(3)	17		120,000		PN
IRAS 18032-2032	18 06 13.93	−20 31 43.28	51500478	01(2)	2	1.1		2E5	CHII
IRAS 18116-1646	18 14 35.29	−16 45 20.99	70300302	06	2			8E4	CHII
GGD -27 ILL	18 19 12.03	−20 47 30.59	14900323	01(2)		2	B1	1E6	star forming region
	18 19 12.00	−20 47 31.10	14802136	01(2)	2,20				
MWC 922	18 21 16.00	−13 01 30.00	70301807	01(2)	-		Be	6E6	emission-line star
IRAS 18317-0757	18 34 24.94	−07 54 47.92	47801040	01(2)	2	2.0	O8	1E5	CHII
IRAS 18434-0242	18 46 04.09	−02 39 20.02	51300704	06	21	1.6	O3-O5	2E6	CHII
IRAS 18502+0051	18 52 50.21	+00 55 27.59	15201645	01(2)	2		O7	1E6	CHII
HD 179218	19 11 11.16	+15 47 18.58	32301321	01(3)	11	0.37	B9	>2E4	iso. HAeBe star♭
IRAS 18576+0341	19 00 10.50	+03 45 47.99	32401203	01(1)	22		15,000	4E3	LBV
BD +30 3639	19 34 45.19	+30 30 58.79	86500540	01(3)	14		WC9	1E5	PN
IRAS 19442+2427	19 46 20.09	+24 35 29.40	15000444	01(2)	2,20		O7	7E6	CHII

Table 3.1 — Continued.

Source	α (J2000)[a]	δ (J2000)[a]	TDT[b]	Obs. mode[c]	Ref.	A_K^d	Sp. Type[d]	G_0^d	Object Type
BD +40 4124	20 20 28.31	+41 21 51.41	35500693	01(3)	23	0.3	B2V	1E4	non-iso. HAeBe star♭
S 106 (IRS4)	20 27 26.68	+37 22 47.89	33504295	01(2)	24	1.4	O8	2E5	YSO
NGC 7023 I	21 01 31.90	+68 10 22.12	20700801	01(4)	7		B3	5E2	RN
CRL 2688	21 02 18.79	+36 41 37.79	35102563	01(3)	-		F5Iae	5E3	Post-AGB star
NGC 7027	21 07 01.70	+42 14 09.10	55800537	01(4)	8		200,000	2E5	PN
IRAS 21190+5140	21 20 44.89	+51 53 26.99	74501203	06	21	0.0		6E5	CHII
IRAS 21282+5050	21 29 58.42	+51 03 59.80	05602477	01(2)	8		O9	1E5	Post-AGB star
IRAS 22308+5812	22 32 45.95	+58 28 21.00	17701258	01(2)	2,20		O7.5	1E3	CHII
IRAS 23030+5958	23 05 10.60	+60 14 40.99	75101204	06	-	0.0	O6.5	8E3	CHII
IRAS 23133+6050	23 15 31.39	+61 07 08.00	56801906	01(2)	2	0.4	O9.5	3E5	CHII

[a] : Units of α are hours, minutes, and seconds, and units of δ are degrees, arc minutes, and arc seconds.

[b] : each ISO observation is given a unique TDT (Target Dedicated Time) number.

[c] : SWS observing mode used (see de Graauw et al. 1996). Numbers in brackets correspond to the scanning speed.

[d] : see text for details (Sect. 3.2.1).

♭ : (non)-isolated Herbig Ae Be star.

References : 1 : Sturm et al. (2000); 2 : Peeters et al. (2002b); 3 : Van Kerckhoven et al. (2000); 4 : Rosenthal et al. (1999); 5 : Cesarsky et al. (2000); 6 : Verstraete et al. (2001); 7 : Moutou et al. (1999a); 8 : Beintema et al. (1996); 9 : Szczerba et al. (2001); 10 : Molster et al. (1996); 11 : Van Kerckhoven et al. (1999); 12 : Waelkens et al. (1996); 13 : Moorwood et al. (1996); 14 : Waters et al. (1998); 15 : Tielens et al. (1999); 16 : Benedettini et al. (1998); 17 : Hony et al. (2001); 18 : García-Lario et al. (1999); 19 : Cohen et al. (1999); 20 : Roelfsema et al. (1996); 21 : Peeters et al. (1999); 22 : Hrivnak et al. (2000); 23 : van den Ancker et al. (2000b); 24 : van den Ancker et al. (2000a)

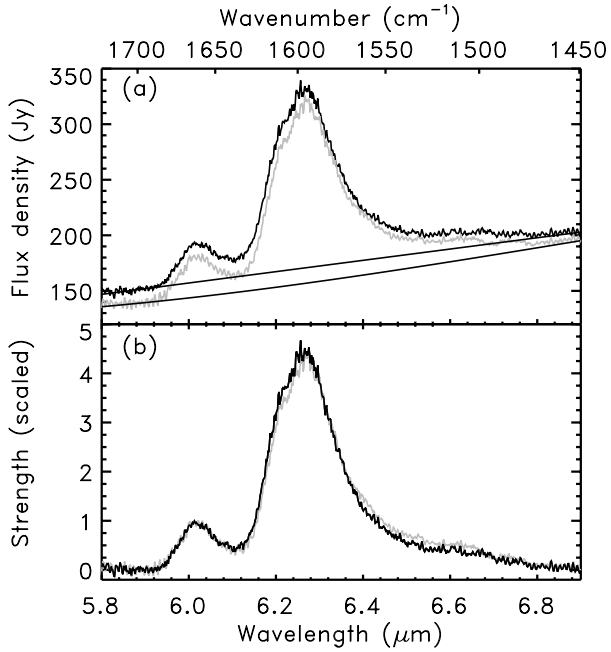

Figure 3.1 — Both the - independently reduced - up and down scans of HD 44179 are shown with their respective continua in panel a. Panel b shows the normalised profiles of the up and down scan.

flux and the known spectral type. CRL 2688 has an effective temperature of $\sim$6400K. Hence, the FUV luminosity is 0.04% of the total luminosity of the star. The star's luminosity and the NIR size are taken from Goto et al. (2002). The FIR flux of IRAS 17347 and IRAS 18576 are obtained by integrating the modified blackbody that is fitted to the SWS spectra. The size of IRAS 17347 and IRAS 18576 are taken from Meixner et al. (1999) and Ueta et al. (2001) respectively. For MWC 922, the diameter is taken from Meixner et al. (1999) and its FIR flux is derived by integrating the combined SWS and LWS spectrum longwards of 20 μm. For the RNe, PNe and Post-AGB stars not mentioned in this paragraph, the G_0 values are taken from Hony et al. (2001).

3.2.2 Observations

All spectra presented here were obtained with the Short Wavelength Spectrometer (SWS, de Graauw et al. 1996) on board the Infrared Space Observatory (ISO, Kessler et al. 1996). The spectra were taken using the AOT 01 scanning mode at various speeds or the AOT 06 mode, with resolving power ($\lambda/\Delta\lambda$) ranging from 500 to 1600. See Table 3.1 for details of the observations.

3.2.3 Reduction

The data were processed with the SWS Interactive Analysis package IA^3 (de Graauw et al. 1996) using calibration files and procedures equivalent with pipeline version 7.0 or later. Fur-

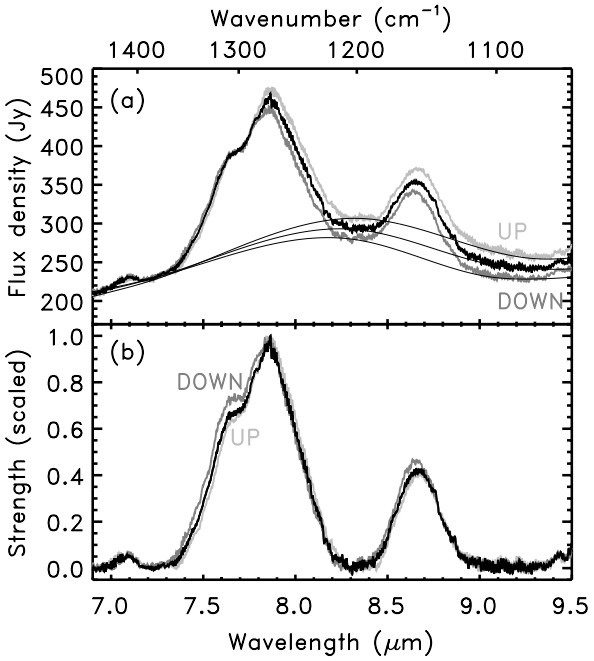

Figure 3.2 — The combined spectrum of HD 44179 (black line) together with the - independently reduced - up and down scans are shown with their respective continua in panel a. The continuum subtracted profiles are shown in panel b normalised to the peak intensity.

ther data processing consisted of bad data removal and rebinning with a constant resolution. The (sub-)features discussed here are present in all available scans.

In case of high fluxes, the obtained spectra can suffer from memory effects. These memory effects can influence the general shape of the continuum as well as the profile of broad features. The sources in our sample for which memory effects are present, are indicated in Table 3.2. At the time the data reduction was done, no memory correction tool was available. Hence, in case of memory effects, the average of the up and down scans is taken. In order to investigate the influence of memory effects on this study, we analyse the source that suffers the most from memory effects in our sample, i.e. HD 44179, by comparing the up and down scans in the region of interest, i.e. 5.5-9 μm. Fig. 3.1 shows the influence on the 6.2 μm profile. The differences are small, even in this most extreme case. The influence is more severe for the 7.7 μm complex (Fig. 3.2). The blue wing of the feature is affected, as well as the relative strength of the 7.6 component. However, the error due to detector memory effects (< 5 %) is less than the uncertainty on the integrated band intensity. It will not hamper the spectral analysis and source classification performed in this paper. Hence, it will not hamper the analysis done in this paper. Recently, a memory correction tool has become available (OLP10) and, as a check, the sources suffering from memory effects have been re-reduced. We found that that memory effects do not alter significantly the band profiles. In order to be consistent with the analysis of the other sources, we did not apply this memory correction.

Two sources in this sample (Orion peak 1 and Orion peak 2) have strong atomic emission

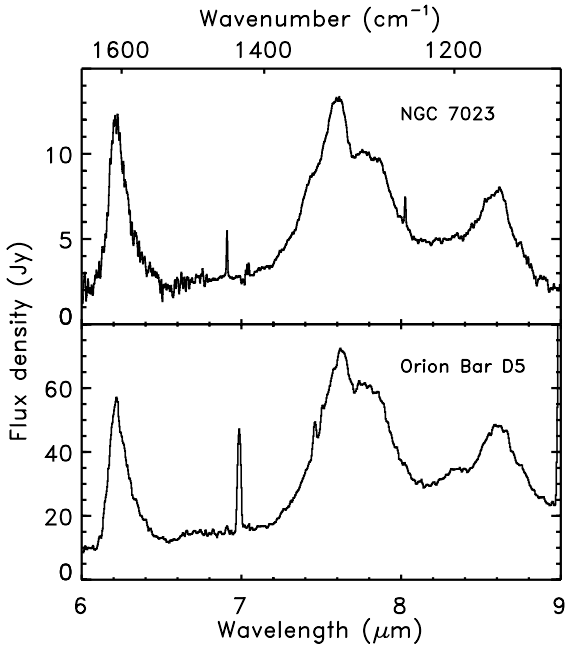

Figure 3.3 — Two examples to show the richness of the 6–9 μm region. We recognise the 6.2 and 8.6 μm features. The 7.7 μm feature breaks up in three components; two clear bands at 7.6 and 7.8 μm and a shoulder at 7.4 μm. Furthermore, weak features are present at 6.6 and 8.2 μm.

lines perched on top of the 6.2 μm PAH feature. These lines and the PAH feature are easily separated at the resolution of the SWS instrument. The contribution from any line is removed prior to the analysis of the profiles.

3.2.4 The spectra

Fig. 3.3 shows spectra of two typical sources to illustrate the spectral detail present. The complete 6–9 μm spectrum reveals an extremely rich collection of emission features with bands at 6.0, 6.2, 6.6, 7.0, 7.7, 8.3 and 8.6 μm (Beintema et al. 1996; Molster et al. 1996; Roelfsema et al. 1996; Verstraete et al. 1996; Moutou et al. 1999a,c; Peeters et al. 1999; Verstraete et al. 2001). In particular, upon close inspection, some of these features are perched on top of an emission plateau of variable strength. The beginning of this emission plateau seems to be variable and falls longwards of 6 μm while it extends until ~ 9 μm.

From the richness of the region, it is clear that several components are present. The well known 7.7 μm feature consists of two main features at 7.6 and 7.8 μm plus shoulders at 7.3-7.4, 7.45 and 8.2 μm. For example, Verstraete et al. (2001) fit the total region with several Lorentzian profiles and Van Kerckhoven (2002) fit the 7.7 μm complex with 4 Gaussians peaking at 7.5, 7.6, 7.8 and 8.0 μm.

The 7.7 μm complex

As discussed in the spectroscopy section (Sect. 3.6.2), the observed 7.7 μm profiles of class A′ can be remarkably well reproduced by either pure-C or N substituted PAHs. The dominance of the 7.8 μm band in class B′ profiles, however, remains an enigma.

When investigating other possible carriers for the 7.8 μm component, one should bear in mind the following observational facts. First, the 7.7 μm complex is always observed together with the other UIR bands. Second, the position of the 7.8 μm component correlates with the observed intensity ratio $I_{7.6}/I_{7.8}$. Third, the strength of the 7.8 μm component is correlated with the strength of the 6.2 μm feature. In addition, the different classes of the 6.2 and 7.7 μm features are directly linked with each other. Hence, the carrier of the 7.7 μm complex and in particular of the 7.8 μm component should be related to the carrier of the other UIR bands.

Other carriers have been proposed to explain the UIR bands. Proposed solid state carriers are QCC (Sakata et al. 1984), soot (Allamandola et al. 1985), coal (Papoular et al. 1989), HAC (Colangeli et al. 1995; Scott et al. 1997) and nano-sized carbon grains (Herlin et al. 1998; Schnaiter et al. 1999). Laboratory measured spectra of the solid state materials all resemble the global appearance of the observed UIR spectrum. Looking in detail, however, they do not match the observed peak positions, the observed widths and the observed profiles. In addition, these grains would be generally too cool to emit efficiently in the mid-IR. In summary, to date the molecular carrier of the so-called 7.8 μm component remains unidentified albeit that it likely has a highly aromatic character.

The 8.22 μm feature

Two Post-AGB stars (CRL 2688 and IRAS 13416) in our sample show a peculiar IR spectrum. Instead of a 7.7 μm and 8.6 μm feature, they exhibit a broad 8.22 μm feature. The other UIR bands are also slightly different. The 3.3 μm feature has a similar peak position as HD 44179 (type 2 in Tokunaga et al. 1991). But, it is broader than in HD 44179 or in HII regions. In addition, these objects emit a symmetric 6.3 μm feature. Unfortunately, the 11.2 μm feature is too weak to define its profile and peak position. Both sources show a 3.4 μm band.

There are several ways to interpret these spectra. First, the observed spectra could be a combination of emission by PAHs, giving rise to a (slightly modified) UIR spectrum, and by an unknown carrier which produce exclusively the 8.22 μm feature. In this interpretation, the 7.7 and 8.6 μm bands would be hidden in the strong 8.22 μm feature. Second, the carriers of the features in these sources might have similar CH modes as PAHs but their CC modes are different. Since dust is formed in the outflows of Post-AGB objects, the spectra of these sources might then reflect that of freshly synthesised PAHs, dust and intermediate compounds.

This broad 8.22 μm band may well be present in some other sources as an underlying plateau (Sect. 3.4). Studies of the spatial distribution of this plateau have shown that it is carried by a component which is independent of that of the 6.2 and 7.7 μm bands (Bregman 1989; Cohen et al. 1989). Energetic arguments suggests that the carrier of this plateau contains $\sim$400 C-atoms and, hence, the carrier may be in the form of PAH clusters (Bregman 1989).

In these two Post-AGB objects, the carrier of the 8.22 μm band may also be in the

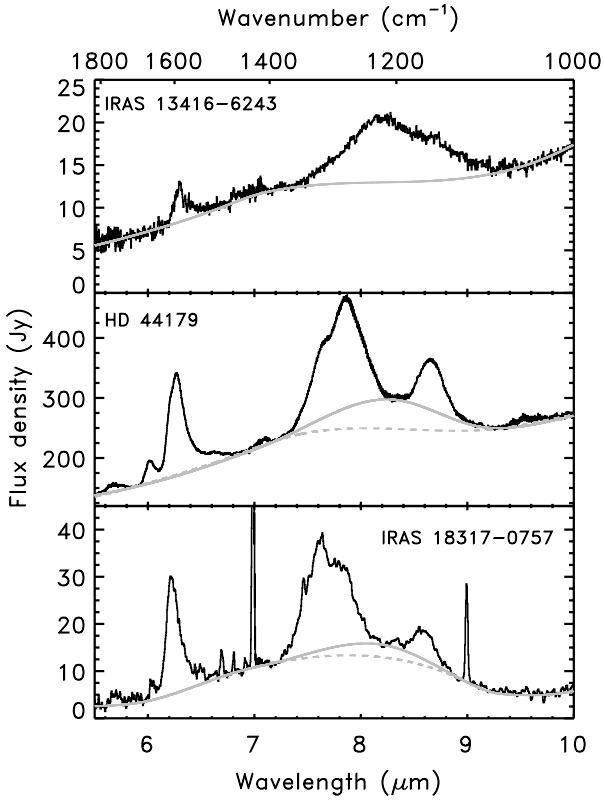

Figure 3.4 — Illustrative examples of the continua underneath the 7.7 and 8.6 μm features. The dashed line represents the general continuum, the full line the second (local) continuum. See text for details (Sect. 3.2.5).

3.2.5 Decomposition of the spectra

The continuum

The profile of the 6.2 μm feature in the spectra of all sources is determined by subtracting a local spline continuum or a straight line. To assess the sensitivity of the resulting profiles to the continuum choice, two extreme baselines have been defined and subtracted. In general, the influence of the continuum determination on the profile is very small and hence does not change significantly the band profiles nor the source classification performed hereafter. In some sources however, the continuum determination is subject to some freedom. These sources are indicated in Table 3.2.

The continuum determination around the 7.7 and 8.6 μm features is quite arbitrary. We choose to draw first a general continuum splined through points from 5-6 and 9-10 μm and through points near 7 μm, excluding possible small features in those regions (see Fig. 3.4, dashed line). In this way, the influence of a silicate absorption feature in some sources (see Table 3.2) is completely ignored. In addition, to separate and study the individual 7.7 and

8.6 μm contributions, we have also drawn a continuum under the 7.7 and 8.6 μm features themselves. This second (local) continuum is determined by taking additional continuum points near 8.3 μm - between the 7.7 and 8.6 μm features (see Fig. 3.4, full line). In this way, an underlying plateau component is defined.

Other ways of decomposing the broad, blended bands and determining the underlying continuum will yield other results. In particular, for different bandshapes (Gaussian, Lorentzian, etc.), different continua and profile parameters (central wavelength and FWHM) are obtained (Boulanger et al. 1998b; Uchida et al. 2000). However, these differences will affect all sources in a systematic way and while this will influence the profiles of the derived features, this will not affect the source-to-source variations we find.

Extinction

Extinction can have a serious effect on the apparent PAH spectrum (Spoon et al. 2002, see also Fig. 3.5). In particular, with increasing optical depth of the silicate absorption feature, the 8.6 μm feature is decreased tremendously (see Fig. 3.5). To asses the influence of extinction on the band profiles and their intensities, the "standard" extinction law (Draine 1985; Mathis 1990; Martin & Whittet 1990) is applied to a template PAH spectrum. This template spectrum is obtained by a continuum divided spectrum of a source suffering no extinction. From the resulting spectrum, the band profiles and band intensities were derived in the same way as for the sources considered in this paper (see Fig. 3.5). Although the full PAH spectrum changes significantly with increasing A_K, the normalised 6.2, 7.7 and 8.6 μm band profiles derived with the above discussed continuum determination are hardly affected by the applied extinction, largely because the extinction is quite grey over this wavelength region. But, the derived intensities and hence their ratios are certainly influenced. For this work, no extinction correction has been applied.

Five sources show water ice absorption at 6.0 μm (see Table 3.2) and hence the profile of the 6.2 μm feature can be influenced. In view of the profile of the water ice band, its influence would be expected to be strongest on the blue side of the 6.2 μm feature. However, the ice absorption is very small in our sources and the 6.2 μm band is situated in the red non-steep wing of the water band. Therefore, its influence on the 6.2 μm band profile (FWHM and peak position) is negligible (see Spoon et al. 2002).

Normalisation of the profiles

For comparison, the 6.2 μm profiles shown in Figs. 3.6, 3.7, 3.8, 3.9, 3.10 and 3.11 are scaled in such a way that the integrated flux within the profile is equal to 1. In this normalisation procedure, the lower limit (6.1 μm) is chosen so as to exclude the 6.0 μm emission feature, while the upper limit is determined by the most extreme end of the feature (i.e. 6.6 μm). Analogously, the 7.7 μm band profiles shown in Figs. 3.13, 3.14, 3.15 and 3.16 were normalised so that the total flux from 7.2 to 8.2 μm equals one. For the sources IRAS 17347, IRAS 07027, He2-113 and HD 100546, we normalised the spectra so that the total flux from 7.2 to 8.35 μm equals one in order to cover the 7.7 μm complex completely. The 8.6 μm band profiles were normalised so that the total flux from 8.2 to 8.9 equals one.

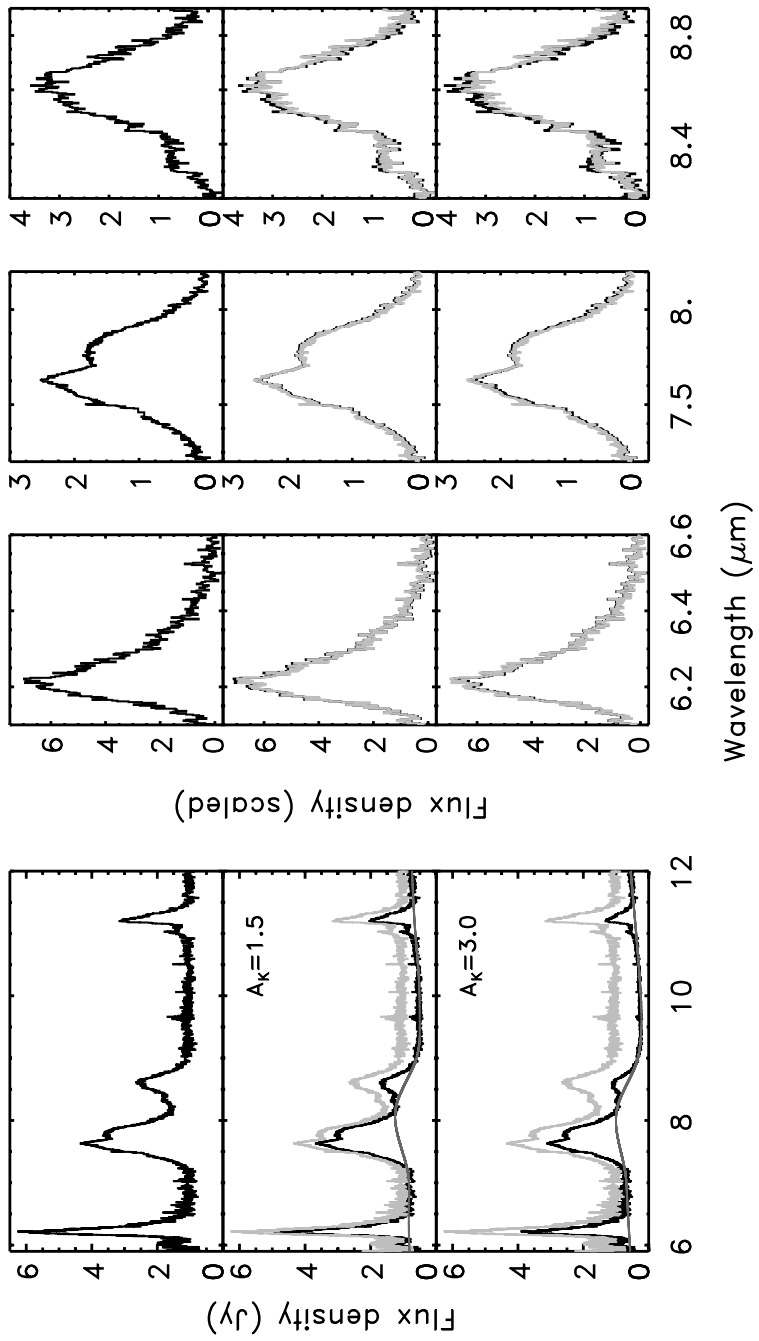

Figure 3.5 — The influence of extinction on a template PAH spectrum. The top left panel shows the template, a PAH spectrum on top of a continuum of 1. The "standard" extinction law is applied to this template spectrum for an A_K of 1.5 and 3.0 (middle and lower left panels respectively). As a reference, the template spectrum is plotted in grey. In addition, the derived continuum is shown for the extincted spectra. The derived profiles are shown in the right panels. As a reference, the profiles of the template spectrum are plotted in grey on top of the derived profiles of the extincted spectra.

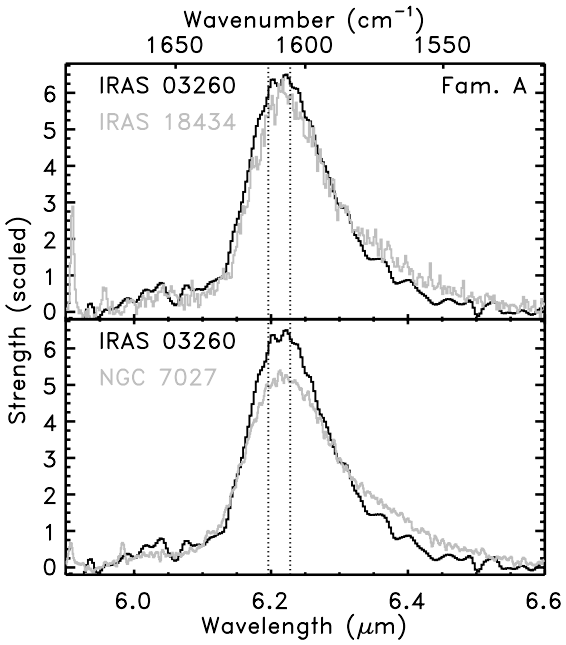

Figure 3.6 — The normalised PAH CC stretching features of class A. The spectra shown exemplify the variations inherent in this class. The dotted lines show the range in peak positions in class A.

3.3 The band profiles

In this section, we show how the various types of PAH emission spectra found in our sample can be seperated into spectral classes which correspond to different band profiles. This is done independently for the three main features in the 6–9 μm region : the 6.2, 7.7 and 8.6 μm bands. Note however that there is some variability of the band shapes within a single class.

3.3.1 The 6.2 μm feature

In this section, we classify the 6.2 μm bands present in our sample. In addition, a decomposition of the band profile into two symmetric components is discussed.

The profile of the 6.2 μm feature

The sources show a pronounced 6.2 μm feature, sometimes preceded by a weak feature at about 6.0 μm. The emission profiles of the 6.2 μm feature are distinctly asymmetric with a steep blue rise and a red tail (see Fig. 3.6). Although the profile of the 6.2 μm feature is similar for all the sources, when examined in detail significant differences become apparent. A definite range in peak positions is present in our sample, varying between 6.19 and 6.29 μm (see Fig. 3.7). The width also varies. The peak positions and FWHM values for all sources are given in Table 3.2. Perusing the derived profiles, we recognise three main classes, which we will designate by A, B, and C.

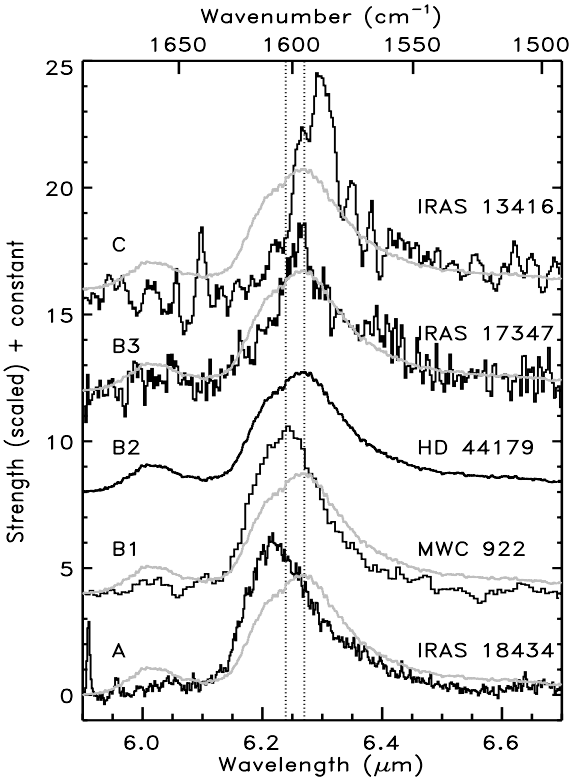

Figure 3.7 — The normalised PAH CC stretching features of class B. For ease of comparison, class A and C are represented by IRAS 18434 and IRAS 13416. As a reference, the profile of HD 44179 is plotted on top of each profile in grey. The dotted lines show the range in peak positions for class B.

First, the majority of the 6.2 μm bands peak between 6.19 and 6.23 μm. This group will be referred to as class A. Note that the strength of the red tail relative to the peak strength, and hence the FWHM, varies within this class (see bottom panel of Fig. 3.6). Furthermore, the top of the profile can be peaked or rounded off (see top panel of Fig. 3.6).

Second, the remaining sources have peak positions that range up to 6.29 μm. We define members of class B as those having profiles with a peak position between 6.235 and 6.28 μm (see Table 3.2 and Fig. 3.7 and 3.8). In general, the profiles of class B have a larger FWHM compared to those of class A.

Class B can be further subdivided. In particular, the peak position of MWC 922 is shifted toward longer wavelengths compared to class A but it has a similar profile. Other members in this group (B1) contain profiles which show a more pronounced red tail than MWC 922 (see Fig. 3.8). These variations parallel those in class A. Class B2 is represented by HD 44179 in Fig. 3.7. Their profile is clearly less red-shaded compared to class B1 (and class A). Note that the profile of HD 44179 shows substructure: one can distinguish a blue shoulder. As can

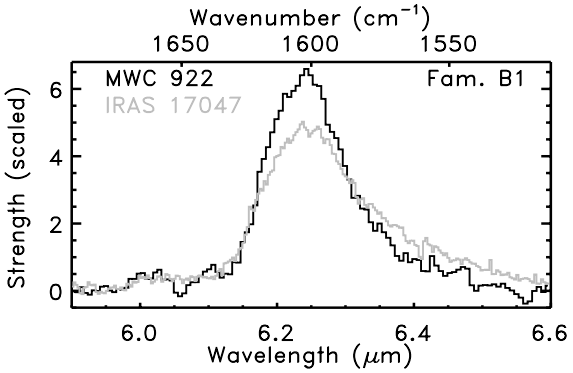

Figure 3.8 — The normalised PAH CC stretching features of class B1. These spectra show the variations inherent in this grouping.

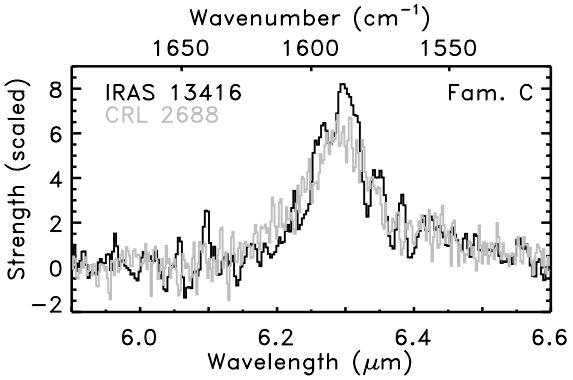

Figure 3.9 — The normalised PAH CC stretching features of class C.

be seen from Fig. 3.7, the first 'component' occurs at the peak position of class A. This is the only source where substructure is revealed so clearly. In contrast to the previous classes (B1 and A), no variations occur in the relative strength of the red tail within this group. Class B3 (exemplified by IRAS 17347 in Fig. 3.7) clearly lacks emission before 6.23 μm and has a somewhat higher peak-to-red-tail ratio than B2 sources. This subdivision of group B is somewhat arbitrary. Examining Fig. 3.7, there seems to be a gradual progression of the peak position to the red from bottom to top.

Third, IRAS 13416 shows a different profile peaking at 6.29 μm. We classify objects with this last profile as belonging to class C. Although the emission band in this source is very weak and noisy, it is clear that the profile is more symmetric than in other classes and its FWHM is the smallest found in our sample. The 6.2 μm band in CRL 2688 peaks at 6.29 μm and exhibits the same profile as IRAS 13416. Hence, this source is classified as a member of class C (see Fig. 3.9).

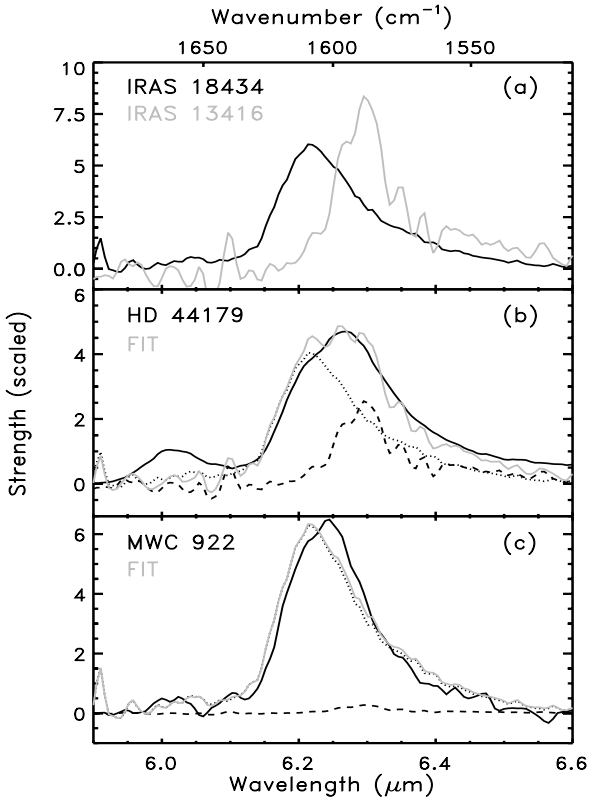

Figure 3.10 — Panel a shows the two components used for fitting the normalised profiles in class B. Panel b shows the normalised profile of HD 44179, the fit and the two components, reflecting their respective contributions. The spectra are interpolated to the same wavelength grid of resolution 500.

We did not detect in our sample the 6.35 μm band reported by Verstraete et al. (1996) in the HII region of M17-SW. In fact, a closer inspection of this data suggests that the 6.35 μm feature is the result of a cosmic ray hit on the SWS detectors. Therefore, we do not include the 6.35 μm band in our analysis.

Variations are also seen in the strength of the weak 6.0 μm feature. It seems to be uncorrelated with the 6.2 μm band in both strength and peak position (contrast e.g. HD 44179 and He 2-113, cf. Figs 3.7 and 3.10).

Decomposing the 6.2 μm feature

Because the peak position seems to gradually and smoothly increase, we hypothesise that all profiles of class B consist of a combination of two components with extreme peak position; one profile of class A and one profile with the other extreme peak position at 6.29 μm, class C. For this two component analysis, we have adopted IRAS 18434 as component 1 and

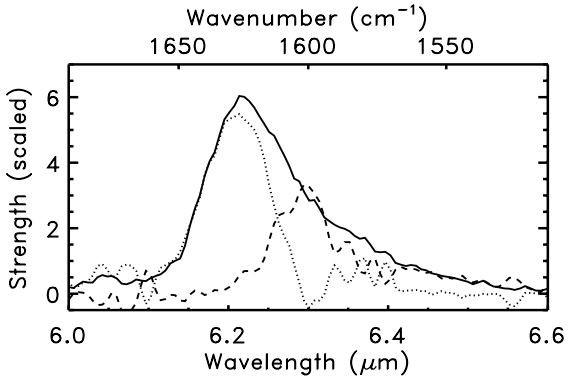

Figure 3.11 — The normalised 6.2 μm profile of IRAS 18434 (solid line) with the possible fraction of component 2, i.e. class C (dashed line). The dotted line represents the Gaussian profile derived through subtraction. The spectra are interpolated to the same wavelength grid of resolution 500.

IRAS 13416 as component 2. In order to fit a combination of these two components, we interpolated all spectra on the same wavelength grid of resolution 500. All profiles of class B are in general well fit by this procedure (see Fig. 3.10). However, we note that for B2/3 spectra, the fit starts slightly shortwards of the observed profile. The only exceptions are MWC 922 and IRAS 17347 which show some subtle differences (see Fig. 3.7). Longwards of 6.3 μm, MWC 922 is fit well by component 1 and component 2 seems to be absent. However, the peak of MWC 922 is shifted towards the red with respect to component 1. IRAS 17347 exhibits a similar profile as component 2 with slightly more emission on the blue wing. However, the profile of IRAS 17347 is shifted to the blue compared to component 2.

In fact, the component 1 profile we defined above (IRAS 18434) may already include some contribution of component 2 (IRAS 13416). To investigate this case, we have subtracted a scaled component 2 from the profile of IRAS 18434 (the adopted component 1); a symmetrical profile remains peaking at 6.21 and with a FWHM of 0.09 μm (see Fig. 3.11). Applying this method to all sources, the same symmetrical profile remains for all sources. Hence, it is possible that the two intrinsic profiles are this derived symmetric component and the intrinsically symmetric profile of component 2. The fraction of component 2 varies from source to source (see Table 3.2) covering the full range from 20 to 100 %. The systematic uncertainty due to the imperfect template spectra can be estimated by degrading the resolution of the template and the fitted sources from 500 to 100 and is found to be 5%. Based upon independent analysis of the up and down scans, we have also estimate the uncertainty in the fitting procedure associated with statistical noise. In Table 3.2, we quote the statistical uncertainty, unless it is less than this estimated systematic uncertainty. Obviously, a strong correlation is present between the fraction of component 2 and the peak position of the profile (see Fig. 3.12). The two sources whose detailed profile deviates the most in this procedure (MWC 922 and IRAS 17347), still agree well with the observed trend. It is noteworthy that no source in our sample shows this "derived" symmetric profile. One source, which we excluded because of its strong ice and silicate absorption features, does exhibit a 6.22 μm profile which closely resembles this derived symmetric profile. It will be discussed in a forthcoming paper (Peeters

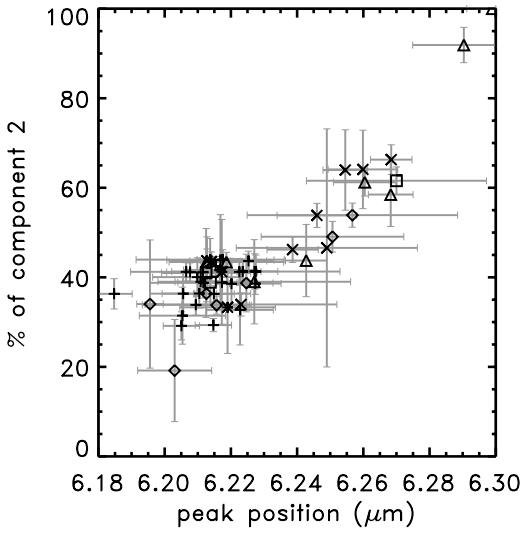

Figure 3.12 — The peak position of the 6.2 μm band plotted against the fraction of component 2 in the profile (see text). The symbols are : H II regions +, Herbig AeBe stars $\diamond$, RNe/Be/sym $\square$, Post-AGB stars $\triangle$, PNe $\times$ and galaxies $*$.

et al. 2002, in prep.). Furthermore, BD+40 4124 does exhibit a symmetric profile but slightly redshifted with respect to the profile derived through the present decomposition procedure.

3.3.2 The 7.7 μm band

Although the profile of the 7.7 μm complex seems similar for most sources, as with the 6.2 μm band, significant differences become apparent when this complex is examined in detail. Typically, this band shows major subfeatures at $\sim$ 7.6 and $\sim$ 7.8 μm (cf. Figs. 3.3 and 3.13) with possible minor subfeatures near 7.3 to 7.4, 8.0 and 8.2 μm. A definite range in relative strength of the 7.6 versus 7.8 μm component is present in our sample, going from a dominant 7.6 μm component toward a dominant component peaking longwards of 7.7 μm. Furthermore, the 7.7 μm complex shifts as a whole. In particular, when the 7.6 μm component is not dominant, the peak position of the whole complex varies from 7.79 to 7.97 μm. Whether the peak position of the minor 7.6 μm component also varies in the latter case, cannot be determined from the present dataset since it is then situated in the wing of the dominant component. In this paper, we will make a distinction between those 7.7 μm complexes with peak position shortwards of 7.7 μm, referred to as dominated by *the so-called 7.6 μm component* and those 7.7 μm complexes with peak position longwards of 7.7 μm referred to as dominated by *the so-called 7.8 μm component*. This does not necessarily imply that the apparent shift in peak position is due to a shift of the component itself but can also be due to different relative strengths of the various components giving rise to the total 7.7 μm complex. The derived peak positions of the 7.7 μm complex are given in Table 3.2.

Table 3.2 — Spectral classification of the sources, description of the band profiles and the band strength ratios.

Source	6.2 μm feature			7.7 μm complex		8.6 μm feature		$I_{7.6}/I_{7.8}$[c]	$I_{7.6}/I_{6.2}$[c]	R[e]
	fam.	peak pos. [μm]	FWHM [10^{-2} μm]	I_2[a] %	fam.	peak pos. [μm]	fam.	peak pos.[b] [μm]			
NGC 253[‡]	A	6.212±0.010	13.4±0.5	41±12	A′	7.611±0.013	A″	8.59	1.02±0.14	0.89±0.13	0.58
W 3A[†]	A	6.223±0.017	11.1±0.3	36±4	A′	7.626±0.005	A″	8.60	1.84±0.37	1.50±0.21	0.34
IRAS 02575[†,‡]	A	6.227±0.008	13.3±2.2	39±2	A′	7.696±0.108	A″	8.60	0.85±0.12	0.96±0.14	0.34
IRAS 03260	A	6.216±0.010	13.2±0.2	34±2	A′	7.622±0.027	A″	8.60	1.56±0.22	0.98±0.14	0.78
Orion PK1[†,♯]	A	6.207±0.006	12.5±0.5	41±2	A′	7.637±0.015	A″	8.60	1.43±0.20	1.15±0.16	0.37
Orion PK2[♯]	A	6.215±0.006	12.4±0.6	36±2	A′	7.632±0.006	A″	8.60	1.35±0.20	1.10±0.16	0.33
Or.Bar D8	A	6.206±0.017	15.2±0.2	41±2	A′	7.627±0.010	A″	8.61	1.32±0.42	0.93±0.20	0.56
Or.Bar BRGA	A	6.222±0.016	12.2±0.3	39±3	A′	7.635±0.007	A″	8.62	1.32±0.19	0.93±0.13	0.67
Or.Bar D5	A	6.225±0.006	12.4±0.2	44±2	A′	7.634±0.007	A″	8.61	1.35±0.38	0.93±0.18	0.80
Or.Bar H2S1	A	6.212±0.011	12.2±0.1	41±2	A′	7.627±0.010	A″	8.61	1.47±0.29	0.94±0.13	0.70
Or.Bar D2	A	6.217±0.016	11.7±1.6	44±10	A′	7.619±0.027	A″	8.62	1.15±0.34	0.73±0.14	0.52
NGC 2023	A	6.214±0.010	11.0±1.0	39±5	A′	7.609±0.069	A″	8.59	1.56±0.30	0.83±0.12	1.14
HD 44179[⋆,♭]	B2	6.268±0.007	17.6±0.4	59±7	B′	7.859±0.012	B″	8.67	0.42±0.10	0.44±0.10	0.28
IRAS 07027	B2/3	6.268±0.006	16.0±1.4	66±3	B′	7.921±0.041	B″	8.67	0.30±0.13	0.36±0.15	0.30
M 82[†?,‡]	A	6.210±0.001	13.3±0.7	44±2	A′	7.626±0.008	A″	8.61	1.08±0.15	0.90±0.13	0.74
HR 4049[○,♭]	B2	6.260±0.009	15.2±0.6	61±3	B′	7.869±0.037	B″	8.67	0.17±0.05	0.22±0.07	0.11
IRAS 10589[†?]	A	6.223±0.010	9.4±0.3	33±8	A′	7.630±0.008	A″	8.62	1.30±0.18	1.20±0.17	0.60
HD 97048	A	6.221±0.010	13.8±0.3	34±14	AB′	◇	A″	8.62	0.75±0.11	0.75±0.11	0.32
HD 100546	B	6.251±0.022	13.1±1.0	49±3	B′	7.903±0.136	B″	8.66	0.36±0.10	0.41±0.11	0.27
IRAS 12063[†]	A	6.217±0.011	11.5±0.1	42±2	A′	7.626±0.024	A″	8.59	1.20±0.17	1.22±0.17	0.43
IRAS 12073	A	6.205±0.005	10.7±1.6	30±3	A′	7.626±0.040	d	-	1.56±0.26	1.77±0.25	0.07
IRAS 13416[○]	C	6.299±0.015	8.7±1.3	100	C′	8.199±0.059	C″	-	-	-	0.21
circinus[†,‡]	A	6.210±0.014	10.0±2.5	33±10	A′	7.616±0.014	A″	8.60	0.88±0.12	1.03±0.15	0.22

Table 3.2 — Continued.

Source	6.2 μm feature				7.7 μm complex		8.6 μm feature		$I_{7.6}/I_{7.8}$[c]	$I_{7.6}/I_{6.2}$[c]	R[e]
	fam.	peak pos. [μm]	FWHM [10^{-2} μm]	I_2[a] %	fam.	peak pos. [μm]	fam.	peak pos.[b] [μm]			
HE 2-113	B2	6.255±0.007	16.7±0.4	64±9	B′	7.913±0.043	B″	8.63	0.35±0.13	0.31±0.12	0.29
IRAS 15384[†]	A	6.222±0.005	13.6±0.1	41±3	A′	7.618±0.015	A″	8.61	1.40±0.22	1.21±0.17	0.71
G 327[†]	A/B1	6.228±0.025	14.6±1.0	41±4	A′	7.619±0.028	A″	8.59	1.31±0.19	1.14±0.16	0.70
IRAS 15502[†]	A	6.211±0.008	10.2±0.8	39±2	A′	7.589±0.027	d	-	1.50±0.22	1.14±0.16	0.54
IRAS 16279	A	6.219±0.017	19.0±0.3	43±2	A′	7.633±0.031	A″	8.60	0.85±0.13	0.77±0.11	0.33
IRAS 16594	A	6.227±0.029	14.3±2.2	39±9	A′	7.621±0.035	A″	8.59	1.32±0.20	0.65±0.09	0.26
CD -42 11721(off)[†?]	A	6.224±0.008	12.5±0.4	39±6	A′	7.612±0.020	A″	8.60	1.51±0.21	0.93±0.13	0.84
CD -42 11721[†?]	A	6.212±0.014	13.0±0.2	36±2	A′	7.609±0.016	A″	8.60	1.63±0.23	1.12±0.16	0.26
IRAS 17047[⋆,♭]	B1	6.246±0.012	17.1±0.8	54±3	B′	7.830±0.026	B″	8.64	0.52±0.10	0.42±0.08	0.16
IRAS 17279[†]	A	6.215±0.005	12.2±0.4	30±2	A′	7.622±0.023	A″	8.60	1.12±0.16	0.89±0.13	0.89
IRAS 17347	B3	6.259±0.011	11.0±4.7	64±8	B′	7.972±0.033	B″	8.70	0.16±0.08	0.25±0.12	0.45
XX-OPH[○]	B3	6.270±0.027	14.5±4.7	62±3	B′	7.848±0.052	B″	8.66	0.27±0.07	0.23±0.06	0.11
Hb 5[◁]	A	6.223±0.029	13.0±2.7	34±2	-	-	A″	8.61	0.90±0.13	0.62±0.09	0.39
IRAS 18032[†]	A	6.209±0.016	11.8±0.2	34±3	A′	7.613±0.016	A″	8.60	1.19±0.17	1.25±0.18	0.82
IRAS 18116[†?]	A	6.227±0.007	11.3±1.4	41±4	A′	7.630±0.009	A″	8.60	1.17±0.17	0.88±0.12	0.73
GGD-27 ILL[†,♯]	A	6.205±0.009	13.1±0.8	38±6	A′	7.603±0.010	A″	8.60	1.15±0.16	1.51±0.21	0.57
MWC 922[♭]	B1	6.243±0.006	13.3±0.2	44±8	A′	7.665±0.030	[♮]	8.62	0.73±0.10	0.67±0.09	0.17
IRAS 18317[†]	A	6.224±0.006	13.3±0.6	41±2	A′	7.634±0.007	A″	8.59	1.29±0.19	1.04±0.15	0.62
IRAS 18434[†]	A	6.215±0.003	12.1±0.4	43±2	A′	7.637±0.010	[♮]	-	1.51±0.21	0.77±0.11	0.34
IRAS 18502[†]	A	6.214±0.022	16.0±0.6	44±5	A′	7.623±0.020	A″	8.59	1.02±0.15	1.07±0.15	0.85
HD 179218	B1/2	6.257±0.032	18.6±3.0	54±3	B′	7.786±0.126	B″	8.65	0.27±0.04	0.25±0.04	0.20
IRAS 18576[○]	B1	6.249±0.027	12.2±0.3	47±8	A′	7.653±0.084	A″	8.58	0.86±0.12	0.74±0.10	0.59
BD +30 3639[♭]	B1	6.239±0.008	14.0±0.6	46±3	B′	7.842±0.009	B″	8.64	0.34±0.05	0.38±0.05	0.32

Table 3.2 — Continued.

Source	6.2 μm feature				7.7 μm complex		8.6 μm feature		$I_{7.6}/I_{7.8}$[c]	$I_{7.6}/I_{6.2}$[c]	R[e]
	fam.	peak pos. [μm]	FWHM [10^{-2} μm]	I_2[a] %	fam.	peak pos. [μm]	fam.	peak pos.[b] [μm]			
IRAS 19442[†,♯?]	A	6.218±0.008	13.6±0.3	44±2	A′	7.614±0.019	A″	8.61	1.30±0.18	1.04±0.15	0.64
BD +40 4124	A	6.203±0.011	9.8±0.5	20±1	A′	7.603±0.034	A″	8.60	1.80±0.31	1.13±0.16	0.16
S 106 (IRS4)[†]	A	6.210±0.014	13.9±0.3	41±4	A′	7.621±0.016	A″	8.61	1.43±0.20	1.05±0.15	0.30
NGC 7023I	A	6.213±0.013	13.4±1.4	41±10	A′	7.598±0.022	A″	8.60	1.88±0.35	0.83±0.12	1.11
CRL 2688[♭]	C	6.290±0.015	11.1±1.2	98±5	C′	8.202±0.062	C″	-	-	-	0.12
NGC 7027[⋆,♭]	A	6.213±0.002	15.6±0.2	44±3	B′	7.814±0.001	B″	8.64	0.64±0.09	0.42±0.06	0.33
IRAS 21190	A	6.210±0.001	11.6±1.6	36±3	A′	7.612±0.024	A″	8.61	1.56±0.23	0.77±0.11	0.41
IRAS 21282	A	6.213±0.005	14.6±0.2	44±5	AB′	◇	A″	8.62	0.64±0.09	0.61±0.09	0.41
IRAS 22308	A	6.205±0.010	13.4±0.2	37±5	A′	7.614±0.023	A″	8.61	1.40±0.20	1.12±0.16	0.93
IRAS 23030	A	6.205±0.014	11.0±2.1	32±6	A′	7.625±0.054	A″	8.60	1.21±0.20	1.02±0.14	0.55
IRAS 23133	A	6.217±0.004	11.9±0.5	39±2	A′	7.631±0.011	A″	8.60	1.20±0.17	0.93±0.13	0.84

[a]: intensity fraction of component 2 (see Sect. 3.3.1);

[b] : peak position derived by fitting a Gaussian to the profile. The error on the position is dominated by the error on the continuum and is <0.015;

[c] : based upon the Gaussian fit to the 7.7 μm complex (see Sect. 3.3.2);

[e] : ΣPAH/cont [6-9 μm] (see Sect. 3.5)

d : feature detected;

◁ : strong [NeVI] present on top of the 7.6 μm feature, and hampers the determination of the position;

◇ : the peak intensity of the 7.6 and 7.8 μm features are equal within the estimated error;

♮ : sources with an unusual 8.6 μm feature (see Sect. 3.3.3);

⋆ and ♭ : sources suffering from memory effects at respectively 6 and 7-9 μm;

♯ : water ice absorption (6 μm) present; † : silicate absorption (9.7 μm) present;

○ : freedom in continuum determination at 6 μm;

‡ : redshifted corrected. Redshifts are taken from the NASA/IPAC Extragalactic Database.

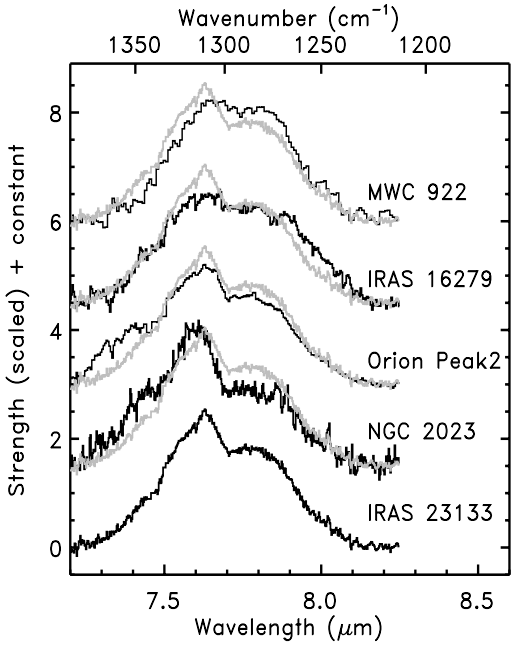

Figure 3.13 — The typical - normalised - profile of the 7.7 μm complex of class A′ represented by IRAS 23133, shown together with the particular cases within this class. As a reference, the typical A′ profile of IRAS 23133 is plotted on top of each profile in grey.

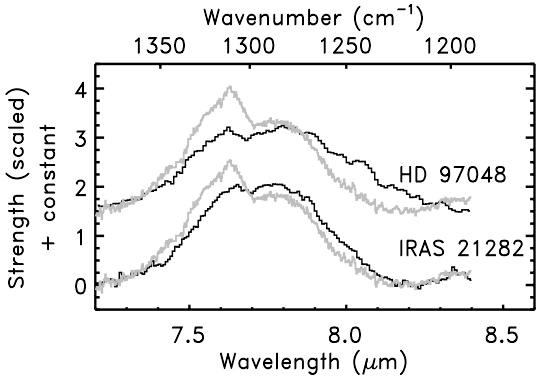

Figure 3.14 — The normalised 7.7 μm complex of class AB′. As a reference, the typical profile of class A′ (represented by IRAS 23133) is plotted on top of each profile in grey.

Perusing the derived profiles, we recognise four main spectral classes, which we will designate by A′, B′, AB′ and C′. This classification is based upon the relative strength of the 7.6 and 7.8 μm components. Sources where the 7.6 μm component is dominant, group

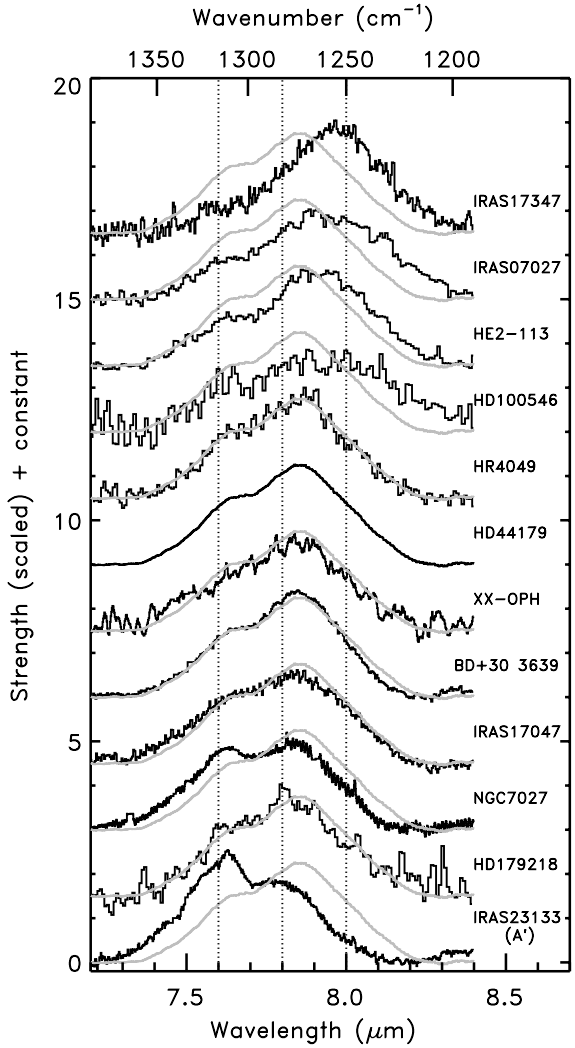

Figure 3.15 — The normalised 7.7 μm complex of class B′. These spectra show the variations inherent in this grouping. As a reference, the bottom profile represents the typical profile of class A′ and the 7.7 μm profile of HD 44179 (a member of class B′), is plotted on top of each profile in grey. The vertical dotted lines represent the nominal 7.6, 7.8 and 8 μm positions. Clear shifts in peak position of the 7.7 μm complex are present.

in class A′; class B′ contains sources which show a stronger 7.8 μm component; class AB′ groups those sources where the 7.6 and 7.8 have equal strength. Two sources do not show a 7.7 μm complex and hence form class C′.

When looking in detail at the normalised profiles of class A′, it is clear that almost all

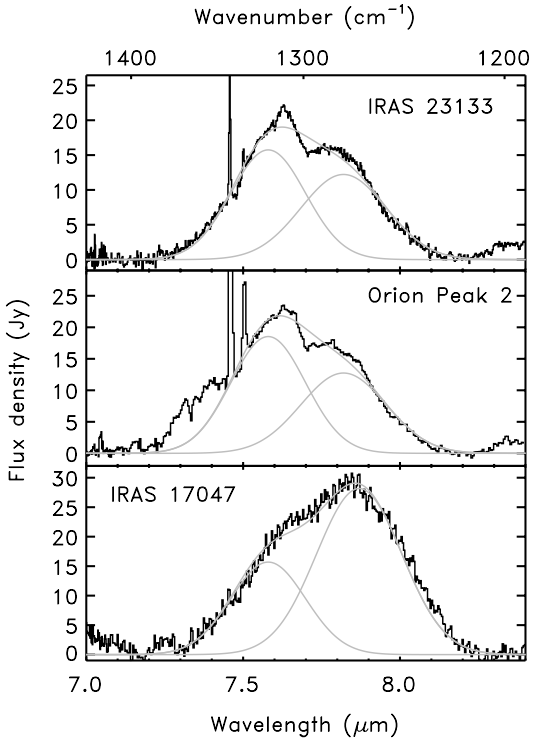

Figure 3.16 — An illustrative example of the two Gaussians fitted to the 7.7 μm complex.

sources have the same profile. Fig. 3.13 shows the possible variations within this class. Orion Peak1, Orion Peak2, NGC 7023 and NGC 2023 show extra emission between 7.2 and 7.4 μm. NGC 2023 has also a more pronounced $I_{p\,7.6}/I_{p\,7.8}$ ratio. IRAS 16279 shows extra emission on the red wing compared to the typical profile of class A$'$, indicating a contributor near 8.0 μm. MWC 922 is slightly redshifted as well. The latter two sources also show a less pronounced ratio of the peak intensities of the 7.6 and 7.8 μm components.

Two sources, HD 97048 and IRAS 21282, have an equally strong 7.6 and 7.8 μm component (see Fig. 3.14) and form class AB$'$. IRAS 21282 is also redshifted compared to the typical profile of class A$'$, while HD 97048 has extra emission at the red wing near 8.0 μm compared to class A$'$.

Class B$'$ contains a collection of many different profiles (see Fig. 3.15). All of them are redshifted by different amounts compared to the typical profile of class A$'$. The so-called 7.8 μm component moves from 7.72 towards 7.97 μm. The strength of the 7.6 μm feature shows large variations (cf. NGC 7027 versus IRAS 17347). Whether the 7.6 μm component behaves in a similar way as the so-called 7.8 μm component concerning peak position, is difficult to say since it is situated in the wing of the 7.8 μm component.

Two sources, CRL 2688 and IRAS 13416, show no 7.7 μm complex and no 8.6 μm feature (see § 3.3.3) but instead exhibit a similar broad emission feature peaking at 8.22 μm (see Fig. 3.17). These two form group C$'$.

A detailed fit to the profile can be obtained by fitting the total region with, for example, several Lorentzian profiles (Verstraete et al. 2001). Here we want to obtain an estimate of the relative flux contributions of the 2 main components rather than to fit the profile. In order to quantify these variations in the relative strength of the 7.6 and the so-called 7.8 μm features, two Gaussians are fit to the 7.6 and the 7.8 μm features respectively. In a first attempt, the position and the width of these Gaussians are fixed to λ_0(7.6) = 7.58 μm, FWHM(7.6) = 0.28 μm and λ_0(7.8) = 7.82 μm, FWHM(7.8) = 0.32 μm. For most sources, this works quite well (see Fig. 3.16). The peak intensity of the 7.6 μm band for class A$'$ and the sharpness of the top of the 7.7 μm complex is however not well reproduced in all cases (see top panel of Fig. 3.16). With this method, the extra emission present in four sources (Orion Peak 1, Orion Peak 2, NGC 2023 and NGC 7023) on the blue side of the 7.7 μm complex is ignored (see middle panel of Fig. 3.16). In the cases of a few shifted 7.7 μm complexes, no good fit is obtained (i.e. for HD 100546, HD 44179, He 2-113, BD +30, IRAS 17047, IRAS 07027, IRAS 17347). For these sources, a new fit is made in which the position of the 7.8 μm Gaussian is treated as a free parameter. The FWHM of the two Gaussians is kept fixed although - for a single source - it might give a better fit if the FWHM were a free parameter. However, to make a consistent comparison between sources, we kept the bandwidths constant. The relative strength of the 7.6 versus 7.8 μm feature as well as the intensity ratio of the 7.6 to the 6.2 μm feature are summarised in Table 3.2. Class C$'$ is excluded since it has no 7.7 μm complex. Based upon independent analysis of the up and down scans, we estimate the uncertainty in the fitting procedure associated with statistical noise to be generally less then 10%. An estimate of the systematic uncertainty on the integrated fluxes can be obtained by applying a different fit procedure and comparing this to our present 2-component decomposition. For that reason, we fitted the 7.7 μm complex with 4 Gaussians peaking at 7.5, 7.6, 7.8 and 8.0 μm (Van Kerckhoven 2002). The strength of the combined 7.5 and 7.6 μm Gaussians in this method can be compared to that of the 7.6 μm component applied here. Likewise, the combined 7.8 and 8.0 μm Gaussians in this method can be compared to the 7.8 μm component applied here. This 4-component method provide better fits to the spectra with obvious 7.5 μm components (cf. Fig. 3.16, middle panel). However, in general, the differences between the two methods are small. Hence, these intensity ratios are affected by systematic and statistical uncertainties. In Table 3.2, we quote the larger of these two.

Sources dominated by the 7.6 μm feature, always exhibit a 7.8 μm feature. In contrast, sources with a dominant 7.8 μm feature, do not always have a clear and distinctive 7.6 μm component. Especially, for sources where the 7.8 μm feature peaks at the longer wavelength end, the 7.6 μm feature is extremely weak - if present (e.g. IRAS 17347). Sources exhibiting the broad emission feature at 8.22 μm do not show a 7.7 μm complex at all (see Fig. 3.17).

3.3.3 The 8.6 μm feature

The 8.6 μm profile derived with the chosen continuum is clearly symmetric for all sources (see Fig. 3.17) and all of them have the same FWHM. Analogous to the 6.2 and 7.7 μm, a definite range in peak positions is present in our sample (see Fig. 3.17). Perusing the derived profiles, we define 3 main spectral classes A$''$, B$''$ and C$''$. Sources with peak position ranging from 8.58 to 8.62 μm group in class A$''$, sources with peak position longwards of 8.62 μm group in class B$''$. CRL 2688 does not exhibit a 8.6 μm feature and forms group

C$''$. IRAS 13416 shows a weak feature near 8.6 μm (see Fig. 3.17). Careful examination of the independently reduced up and down scans show that this feature is only present in one of the two scans. Hence, we classify this source in group C$''$. Table 3.2 gives the class and the peak position derived by fitting a Gaussian to the profile. This classification relies heavily on the adopted continuum. When taking the general continuum (see Fig. 3.4, dashed line) instead of the local continuum (see Fig. 3.4, full line) to derive the profiles, the peak position of the 8.6 μm feature shifts for all sources slightly toward the blue. As a result, the definition of the three classes changes slightly. Two sources previously classified in class B$''$ now belong to class A$''$ (i.e. NGC 7027, HD 100546). However, most sources remain in their distinct classes. Since the presence of a silicate absorption feature has no major influence on the 8.6 μm profile (see Fig. 3.5 and Sect. 3.2.5), the results discussed here are valid for all sources.

MWC 922 shows an exceptionally strong 8.6 μm feature. One HII region, IRAS 18434, has a similarly strong 8.6 μm feature. The latter source has a strong silicate absorption band but correction for the silicate absorption will make this band even stronger (see Fig. 3.5). A detailed study of these sources will be presented in Hony et al. (2002, in prep.) and Peeters et al. (2002, in prep.) respectively.

3.4 The classes

In the previous sections, an independent study of the 6.2, 7.7 and 8.6 μm features was made for our sample. For each of the features, different classes were determined. Comparing those classes, an interesting finding is made. The class classification of the different bands correlate. This is illustrated in Fig. 3.17. Sources with a 6.2 μm feature belonging to class A, have a 7.7 μm complex peaking at 7.6 μm (class A$'$) together with a class A$''$ 8.6 μm feature and are referred to as class $\mathcal{A}$ sources; while for those with a class B 6.2 μm feature, the 7.7 μm complex is dominated by the so-called 7.8 μm component (class B$'$) and their 8.6 μm feature is shifted toward the red (class B$''$). The latter sources are referred to as class $\mathcal{B}$ sources. The two sources showing a single 6.3 μm feature (class C) exhibit neither a 7.7 μm complex nor an 8.6 μm feature (class $\mathcal{C}$). Instead, both sources show a broad emission feature at 8.22 μm. The two sources with an equally strong 7.6 and 7.8 μm subfeature (i.e. class AB$'$), IRAS 21282 and HD 97048, exhibit a class A 6.2 μm feature and a class A$''$ 8.6 μm feature. Note, however, that their 8.6 μm feature peaks at the extreme end of class A$''$. Possibly, these two sources form an intermediate state between the spectrum corresponding to class $\mathcal{A}$ and the spectrum corresponding to class $\mathcal{B}$. Another example of this type is NGC 7027. Its 7.8 μm subfeature is slightly stronger in peak strength than its 7.6 μm subfeature, although by a small amount. However, this source belongs to class A when considering the 6.2 μm feature and class B$''$ concerning the 8.6 μm feature. Possibly, this is another intermediate state. IRAS 18576 and MWC 922 exhibit a B1 6.2 μm profile while their 7.7 and 8.6 μm features both belong to classes A$'$ and A$''$, respectively. Fig. 3.17 and Table 3.3 provide an overview of the PAH spectrum for each of the three main categories. Although the classification of the 7.7 μm complex was based on the dominant subfeature, i.e. the 7.6 or 7.8 μm subfeature, it is clear from Fig. 3.17 that the whole spectrum corresponding with class $\mathcal{B}$ is shifted compared to that corresponding to class $\mathcal{A}$.

The two sources with the 6.3 μm feature (IRAS 13416 and CRL 2688; class C), show a similar spectrum composed of a rather weak 6.3 μm feature, a 8.22 μm feature, an ex-

tremely weak 11.2 μm feature and a 3.3 μm band (see Hony et al. 2002, in prep.). The profiles of the 8.22 μm emission feature are identical, as are the 6.3 μm profiles. The intensity ratio $I_{6.3}/I_{8.22}$ is however not the same. Hence, the 6.3 and 8.22 μm features occur in similar conditions (object type, T, G_0, n_e, etc.). But, based on these two sources, it seems that no tight correlation, in terms of intensities, exist between them. The 8.22 μm feature in CRL 2688 and IRAS 13416 is remarkably similar in peak position and width to the plateau underneath the 7.7 and 8.6 μm features subtracted from the observed spectra (see Fig.3.4 and Sect. 3.2.5). This similarity is of course hard to prove. Here we do note that spatial studies have shown that this plateau is an independent emission component (cf. Bregman 1989; Cohen et al. 1989). Two sources which are not in our sample, IRAS 22272+5435 and IRAS 07134+1004, both show a very broad feature at ~ 8 μm, somewhat shortwards of the 8.22 μm feature. This 8 μm profile is much broader then the 8.22 μm feature and may be the result of fortuitous convolution of a 7.7 μm complex peaking at 7.6 μm and the 8.22 μm feature.

Considering the classification from an astronomical point of view, this analysis shows that the PAH spectrum in the 6 to 9 μm region, correlates with the type of source considered. All HII regions, reflection nebulae and all the extragalactic sources in this sample have a class A 6.2 μm feature, a 7.7 μm complex peaking at $\sim$ 7.6 μm (class A$'$) and a class A$''$ 8.6 μm feature. All Herbig AeBe stars that are still embedded in their molecular cloud and have an HII region associated with them behave like the ISM sources. The isolated Herbig AeBe stars, HD 179218 and HD 100546, belongs to class $\mathcal{B}$. These two sources also show crystalline silicates (Malfait et al. 1998; Malfait 1999) indicating that disk chemistry may well influence the PAH population. The evolved stars are spread over the different classes. Since their outflow is/was the place of birth of the dust, they likely show the evolution of the PAH population in the early phases of life. However, they do not reflect - at first sight - a clear link between the PAH spectrum and the source evolutionary state. The two Post-AGB stars IRAS 13416 and CRL 2688, exhibit the 6.3 and 8.22 μm features (class $\mathcal{C}$). The two extremely metal-poor sources HD 44179 and HR 4049 both exhibit a class $\mathcal{B}$ spectrum while the Post-AGB stars IRAS 16279 and IRAS 16594 display a class $\mathcal{A}$ spectrum. IRAS 21282 is similar to the latter two sources except that it has an equally strong 7.6 and 7.8 μm subfeature. The PNe show similar variability in their spectra. Hb 5 is the only PN in our sample showing a class $\mathcal{A}$ spectrum. IRAS 07027, He 2-113, IRAS 17047, IRAS 17347 and BD +30 3639 all show a class $\mathcal{B}$ spectrum. In this class, sources with mixed PAH classes are also present : IRAS 18576 and NGC 7027.

The PAH spectrum in the 6 to 9 μm region apparently reflects local physical conditions (object type, T, G_0, n_e, etc.) or the accumulated effect of processing from the formation sites in the AGB or post-AGB phases to the ISM or the influence of disk chemistry (Table 3.3).

A detailed study on the variations in the PAH spectrum of Herbig AeBe stars and the link with the local physical conditions will be given in Van Kerckhoven (2002). Hony et al. (2002, in prep.) concentrates on the PAH spectra of evolved stars and thus on the evolution of the PAH population in the early phases while Peeters et al. (2002, in prep.) focuses on the HII regions.

Table 3.3 — An overview of the classification of the 6.2, 7.7 and 8.6 μm features. The 6.2 and 8.6 μm bands are classified by their peak position (λ_p) while the 7.7 μm complex is classified by its dominant component, i.e. the 7.6 μm component and/or the so-called 7.8 μm component. See text for more details (Sects. 3.3.1, 3.3.2 and 3.3.3). For each spectral class, the range in the local radiation field G_0 and the spectral types within the class is given.

Class	Characteristics						type of object	range in G_0	Sp. types
	6.2 μm band		7.7 μm band		8.6 μm band				
		λ_p		comp.		λ_p			
$\mathcal{A}$	A	$\sim$ 6.22	A$'$	7.6	A$''$	$\sim$8.6	HII, RN, galaxies, non-isolated Herbig Ae Be stars, PN : Hb5, 2 Post-AGB stars : IRAS 16279, IRAS 16594	3E2 to 7E6	O,B
			AB$'$	equal			IRAS 21282, HD97048	1.7E4 &1E5	O9 &A0
$\mathcal{B}$	B	6.24–6.28	B$'$	”7.8”	B$''$	$>$8.62	isolated Herbig Ae Be stars, PNe, 2 Post-AGB stars : HR4049, HD44179	6E4 to 2E7	B,A, WC9-10
$\mathcal{C}$	C	$\sim$ 6.3	C$'$	8.22	C$''$	none	2 Post-AGB stars : IRAS 13416, CRL 2688	5E3	F5

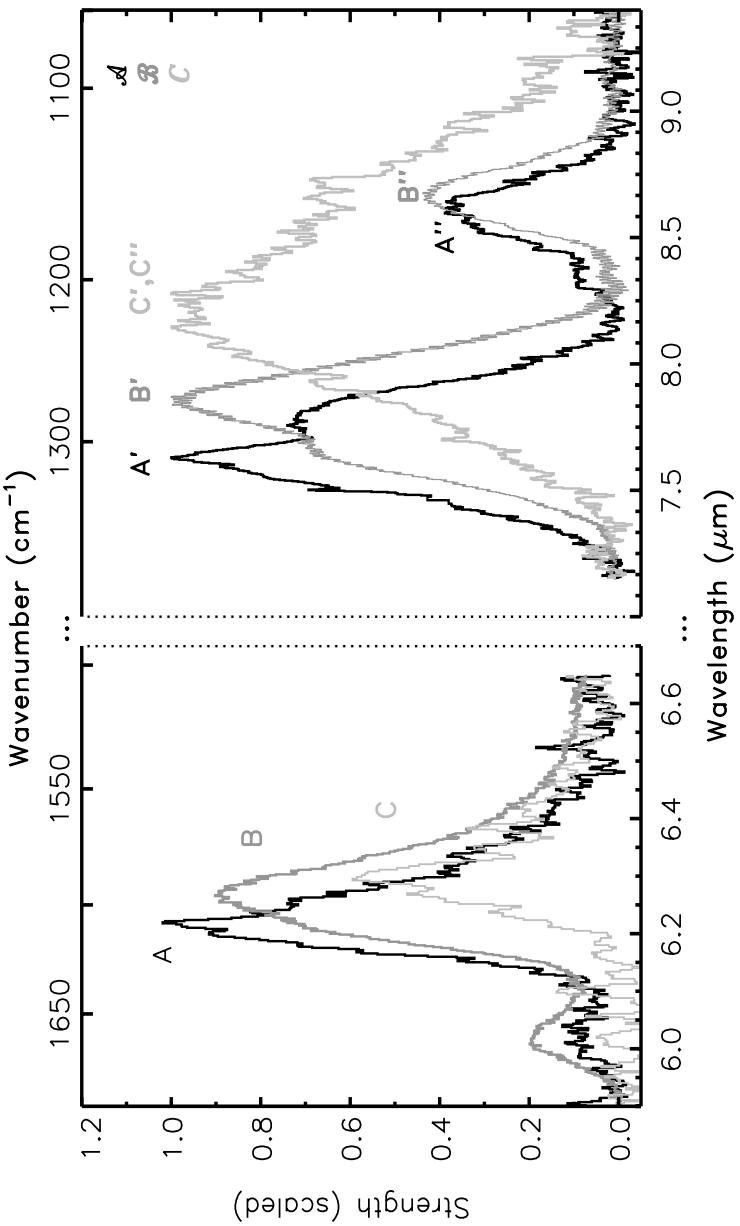

Figure 3.17 — An overview of the possible variations of the main PAH features in the 5-9 μm region, i.e. the 6.2, 7.7 and 8.6 μm features. The spectra are normalised so that the peak intensity of the strongest feature in the 8 μm region equals one. Shown is (i) the CHII region IRAS 23133 illustrative of class $\mathcal{A}$ (i.e. A, A$'$ and A$''$) with a dominant 7.6 peak (black line), (ii) the Post-AGB star HD 44179 illustrative of class $\mathcal{B}$ (i.e. B, B$'$ and B$''$), peaking at $\sim$ 7.9 μm (dark grey line) and (iii) the Post-AGB star IRAS 13416 representing class $\mathcal{C}$ (i.e. C, C$'$ and C$''$), with a broad emission feature at 8.22 μm (light grey line). A clear shift in the 7.7 μm complex is present between IRAS 23133 and HD 44179.

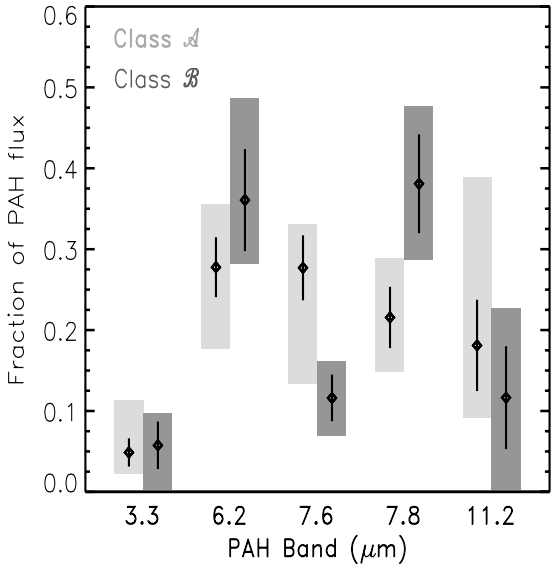

Figure 3.18 — An overview of the fraction of the PAH flux emitted in each feature for class $\mathcal{A}$ and class $\mathcal{B}$. The diamonds crossed by solid vertical lines represent the average fraction of the total PAH flux emitted in each PAH band over a given class and its standard deviation. The filled boxes represents the observed ranges of the fraction of PAH flux emitted in each PAH band within a class. Light grey represents class $\mathcal{A}$ and dark grey class $\mathcal{B}$. For the total PAH flux, we considered the 3.3, 6.2, 7.7 and 11.2 μm features.

3.5 Correlation studies

Given the close relation between the main features in the 6 to 9 μm region, it is of interest to investigate whether the strength of these features can shed more light on the origin of the observed relations and variations. Since the absolute intensities are influenced by the intrinsic luminosity and distance of the source, we study the variations in the relative strength of the PAH bands. The intensity of the 7.6 and 7.8 μm components used here are integrated intensities of the Gaussian fits, while the intensities of the other PAH features are integrated intensities of the profile. The observed intensity ratios can be influenced by extinction (see § 3.2.5). Since extinction strongly influences the intensity of the 8.6 μm feature, we do not consider this feature here.

When checking for connections between intensity ratios and object type, we do detect a relation but there are always some exceptions present. Nevertheless, when plotted against object class (classes $\mathcal{A}$ and $\mathcal{B}$), these exceptions disappear and clear segregations between the two classes become apparent.

For each class, the *average* fraction of the total PAH flux, emitted in each feature, its standard deviation and the total range present in our sample are shown in Fig. 3.18. For the

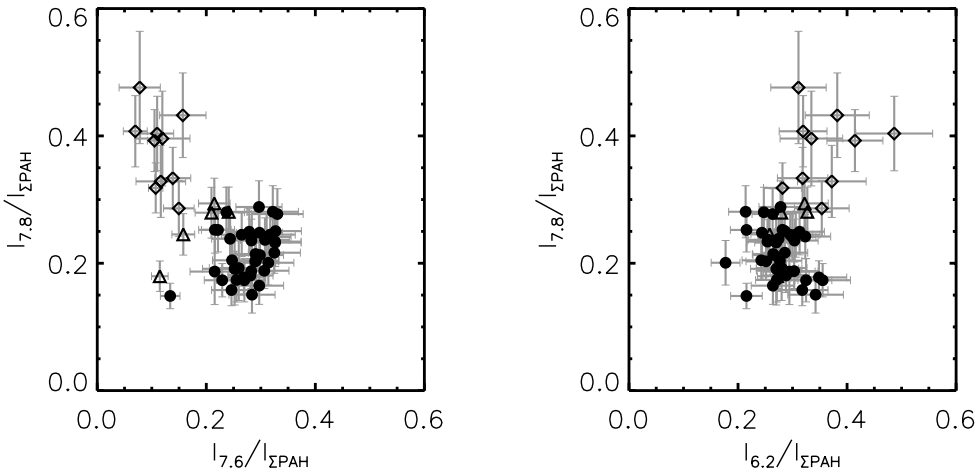

Figure 3.19 — Shown is the integrated strength of the 7.8 μm feature versus the 7.6 and 6.2 μm features, normalised on the total flux emitted in the 3.3, 6.2, 7.7 and 11.2 μm features. Class $\mathcal{A}$ is represented by $\bullet$, class $\mathcal{B}$ by $\diamond$ and sources not belonging to these two classes by $\triangle$.

total PAH flux, we only considered the 3.3, 6.2, 7.7 and 11.2 μm features. The fraction of the total PAH flux emitted in the 7.6 and the so-called 7.8 μm components clearly depends on the class of the source (see Fig. 3.18 and Fig. 3.19, left panel). In contrast, the fraction of the total PAH flux emitted in the 7.7 μm complex does not differ significantly for the two classes. Furthermore, the fraction of the total PAH flux emitted in the 6.2 and 11.2 μm feature differ for the classes $\mathcal{A}$ and $\mathcal{B}$ while a similar fraction is emitted in the 3.3 μm feature for both classes (see Fig. 3.18 and Fig. 3.19, right panel). Therefore, it seems that the increase in $I_{6.2}/I_{\Sigma PAH}$ for class $\mathcal{B}$ compared to class $\mathcal{A}$ is opposite to the behaviour of the 11.2 μm feature. However, there is no indication of this when plotting $I_{6.2}/I_{\Sigma PAH}$ versus $I_{11.2}/I_{\Sigma PAH}$. In addition, the fraction of flux emitted in the 3.3 or 11.2 μm feature does not correlate with the fraction emitted in the 6.2 μm feature. So, this difference in $I_{6.2}/I_{\Sigma PAH}$ for the two classes cannot be directly linked to *only one* band (the 3.3, 7.7 or 11.2 μm feature). Furthermore, sources with an increased emission in the 6.2 μm feature (class $\mathcal{B}$) also have an increased emission in the 7.8 μm feature and hence a decreased emission in the 7.6 μm component compared to class $\mathcal{A}$ (see Fig. 3.19, right panel).

In Fig. 3.20, the intensity ratio of the 7.6 to 7.8 μm subfeatures, i.e. $I_{7.6}/I_{7.8}$, is plotted versus the peak position of the 6.2 μm feature and of the 7.8 μm component respectively. The peak position of the 7.8 μm component is determined from the position of this subpeak in the 7.7 μm complex itself and not from the applied Gaussian fits. The error in this position is given in Table 3.2 for entrees in which the 7.7 μm complex peaks longwards of 7.7 μm. For sources with a dominant 7.6 μm component, we estimate the error to be less then 0.05 μm. It is clear that the sources reflect a gradual variation. In contrast, no clear correlation between the $I_{7.6}/I_{7.8}$ intensity ratio and the FWHM of the 6.2 μm band is present.

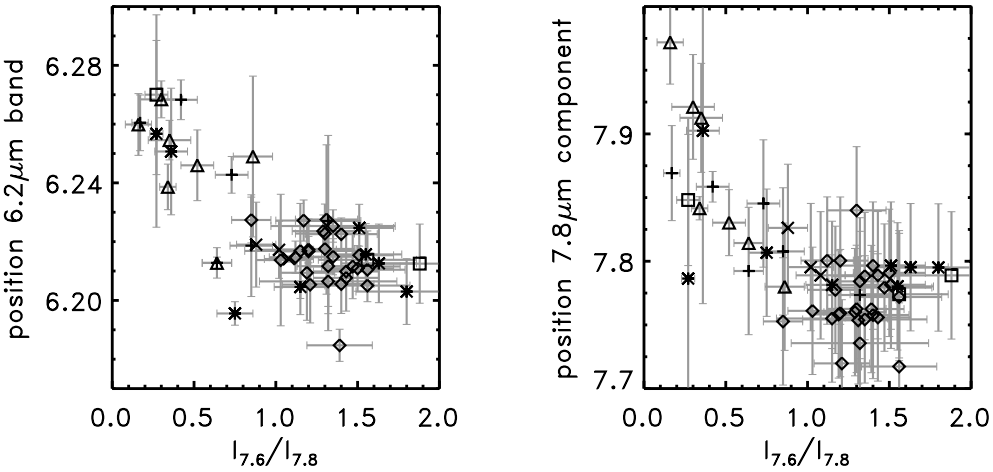

Figure 3.20 — The relation between the intensity ratio $I_{7.6}/I_{7.8}$ and the peak position of the 6.2 μm band and the 7.8 μm component respectively. Extinction is unimportant for this intensity ratio. The symbols are : HII regions +, Herbig AeBe stars $\diamond$, RNe/Be/sym $\square$, Post-AGB stars $\triangle$, PNe $\times$ and galaxies $*$.

We also checked for correlations between band strength ratios and the local radiation field G_0, however we do not detect any correlations. Furthermore, the local radiation field of the sample sources do not show differences between the two classes. In addition, we checked for correlations between band strength ratios and the integrated band-to-continuum ratio, ΣPAH/cont, in the 6–9 μm region. This ratio traces excitation conditions and/or abundance variations. The error on this ratio is dominated by the continuum determination and is less then 10%. We took the continuum described in Sect. 3.4; hence, the plateau contributes to the continuum. This ratio is given in Table 3.2. Here also, we do not detect any correlation. But, sources with the intensity ratio $I_{7.6}/I_{7.8} < 1$ do not have a high ΣPAH/cont ratio ($<$ 0.45) whereas sources where $I_{7.6}/I_{7.8} > 1$ span a range in ΣPAH/cont from 0 to 1.2.

3.6 The Infrared Emission Features and PAHs

The IR emission features at 3.3, 6.2, 7.7, 8.6, and 11.3 μm are now generally thought to arise from vibrationally excited PAHs due to their similarity with the spectra of PAHs taken under conditions which match the salient characteristics of the interstellar environment. One of the early pivotal results of the laboratory and theoretical studies on PAHs reported over the last decade is the remarkable effect ionisation has on the infrared spectra (Szczepanski & Vala 1993a; Langhoff 1996; Kim et al. 2001; Hudgins & Allamandola 1999a, and ref. therein). While PAH characteristic frequencies are only modestly affected by ionisation, the influence on intensity is striking - particularly in the 5 to 10 μm region (Fig. 3.21). The bands grow from the smallest features in neutral PAH spectra to become the dominant bands in ionised

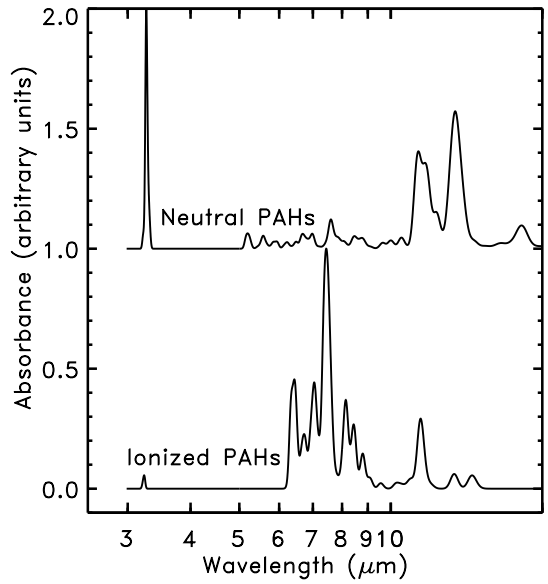

Figure 3.21 — The absorption spectrum of a mixture of neutral PAHs (a) compared to the spectrum of the same PAHs in their positive state (b). This comparison shows that, for PAH spectra, ionisation has a much greater influence on relative intensities than on peak frequencies, with the features in the 6 to 10 μm region substantially enhanced with respect to the rest of the spectrum (Figure adapted from Allamandola et al. 1999b).

PAH spectra. The CC stretching vibrations grow in intensity because, upon ionisation, the charge distribution changes significantly with the CC skeletal vibration, creating a strong oscillating dipole whereas the oscillating dipole for the CH motions and their corresponding bands are reduced. Fig. 3.21 illustrates this effect, which has been found for all PAHs measured in the laboratory to date. However, this is mostly limited to PAHs with less than 48 C-atoms. Larger PAHs are only now being studied in the laboratory. Preliminary laboratory results for PAHs containing up to 60 C-atoms also show this behaviour upon ionisation. Theoretical studies of large species support this enhancement to much larger sized PAHs. For example, Bauschlicher (2002) has shown that this holds for $C_{96}H_{24}$. Astronomically, the observation that the 6.2 and 7.7 μm features, the focus of this paper, are the most intense of the interstellar emission bands, is a clear indication that ionisation is an intrinsic characteristic of interstellar PAHs. The 3.3 μm feature on the other hand is characteristic for neutral PAHs. Hence, both ionised and neutral PAHs contribute to the interstellar IR emission spectrum.

There have been many comparisons between PAH spectra and the interstellar spectra over the years. As the observational tools have become more sensitive and the laboratory techniques more appropriate to the interstellar case, the fits have become more revealing about the different PAH populations in different regions and this, in turn, has yielded further insight into conditions in the emitting regions. Fig. 3.22 shows a fit to the emis-

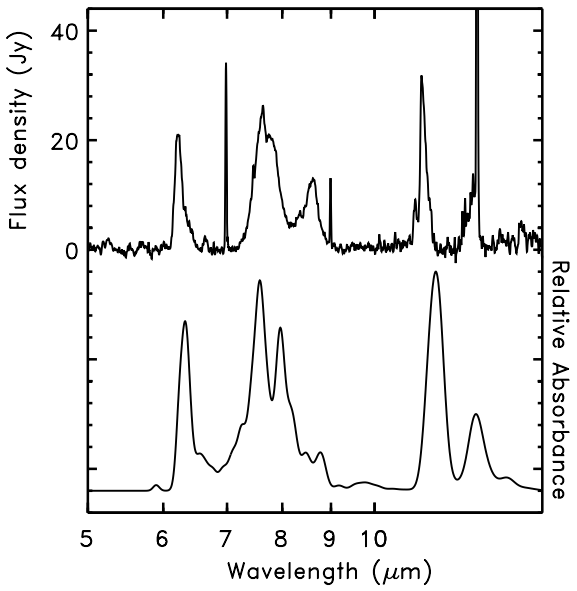

Figure 3.22 — Comparison of a typical ISM infrared emission spectrum (a) with a composite absorption spectrum generated by co-adding the individual spectra of 11 PAHs (b). The interstellar spectrum is that of IRAS 23133. The individual spectra were calculated using experimentally measured frequencies and intensities and assigning a 30 cm^{-1} FWHM Gaussian band profile, consistent with that expected from the interstellar emitters (e.g. Hudgins & Allamandola 1999b).

sion from IRAS 23133 measured with ISO by spectra now available in the Ames PAH IR spectral database (`http://web99.arc.nasa.gov/~astrochem/pahdata/index.html`). Although the fit is striking, thanks to the quality of the new ISO spectra, important differences become apparent which shed further light on the interstellar PAH population. The following differences can be seen in going from shorter to longer wavelengths. The laboratory band near 6.2 μm falls slightly to the red of the interstellar feature, laboratory components centred near 7.7 μm do not precisely match the interstellar profile at this position, the 8.6 μm laboratory band is weaker with respect to the other features in the spectrum than is the case for IRAS 23133, and the laboratory component near 11.2 μm lies to the red of the interstellar feature. The differences in the 8.6 and the 11.2 μm regions are discussed elsewhere (Hony et al. 2001, Janssen, Janssens and Swansen 2002, in prep.). Here we focus on the interstellar features near 6.2 and 7.7 μm.

Feature assignments in the 5 to 10 μm region

The 5 to 10 μm region encompasses frequencies which originate from a variety of PAH molecular vibrations. Pure CC stretching motions generally fall between about 6.1 μm and 6.5 μm, vibrations involving combinations of CC stretching and CH in-plane bending modes lie slightly longward, between roughly 6.5 μm and 8.5 μm, and CH in-plane wagging

vibrations give rise to bands in the 8.3 μm to 8.9 μm range. While the well-known interstellar features at 6.2, 7.7, and 8.6 μm dominate this range, there are at least four weak interstellar bands in this region as well, centred near 5.2, 5.6, 6.0 and 6.8 μm. Their correlation with the major features indicates that they too originate from the interstellar PAH family. The 5.2 and 5.6 μm features most likely correspond to combinations and overtones involving the CH out-of-plane fundamental vibrations which fall between 11 and 13 μm; the 6.0 μm feature likely indicates a carbonyl (>C=O) stretch of an oxygenated PAH (a quinone); and the 6.8 μm band probably corresponds to a weak aromatic CC stretching - CH in-plane bending combination mode of PAHs as for example in the fluoranthenes, or the aliphatic -CH_2- or -CH_3 deformation in a methyl or ethyl side-group attached to a PAH.

There are also other plausible interstellar PAH-related species that are likely to be important in the emission zones and which should be considered. Some examples include PAH clusters and PAH complexes with metals such as iron (metallocenes). Furthermore, one can question whether PAHs remains planar as they grow. And, if not, how does the 3-dimensional shape influence the IR spectrum? It is noteworthy in this regard that simple fullerenes do not have IR characteristics which coincide with any prominent structure in the interstellar emission spectra discussed here (Moutou et al. 1999b). Further, and in spite of much effort, there has not been any report of IR active transitions in carbon nanotubes, very large curled aromatic networks. If such curled aromatic networks (very, very large PAHs) do possess infrared activity, it appears to be very weak. Thus here we focus on the PAH molecules measured in the laboratory or theoretically calculated.

The shifts in the profiles shown by the observations presented above (see Table 3.2) are much larger than the binsize corresponding to the obtained resolution of the data. Hence, they are chemical in nature, arise from local excitation conditions and are not due to doppler broadening and shifting. Therefore, these shifts and profile variations provide important new insight into the variations of the interstellar PAH populations in the different environments. Interpretation of these new spectral aspects require probing deeper into the details of PAH spectroscopic properties in this region than heretofore. Here we consider this new information as it affects first the 6.2 μm region and then the 7.7 μm region.

3.6.1 The position of the PAH CC stretching band near 6.2 μm: experiment and theory

There are several properties which determine the precise peak positions of the infrared active bands which correspond to pure CC stretching vibrations in any given PAH. These include molecular size, molecular symmetry, and molecular heterogeneity. The roles each of these play in determining the position are discussed below. The charge of the PAH molecules also shifts the band position; but this trend is not systematic (Bakes et al. 2001, Bakes E., private communication). In addition, dehydrogenation influences the band position (Pauzat et al. 1997). However, based upon the CH out-of-plane bending modes, Hony et al. (2001) conclude that dehydrogenation has little influence on the observed interstellar PAH spectrum.

Molecular size

At the small end of the PAH size distribution (C_{10} to $\sim C_{30}$), the peak wavelength of the dominant CC stretching feature decreases steadily with molecular size (Hudgins and Alla-

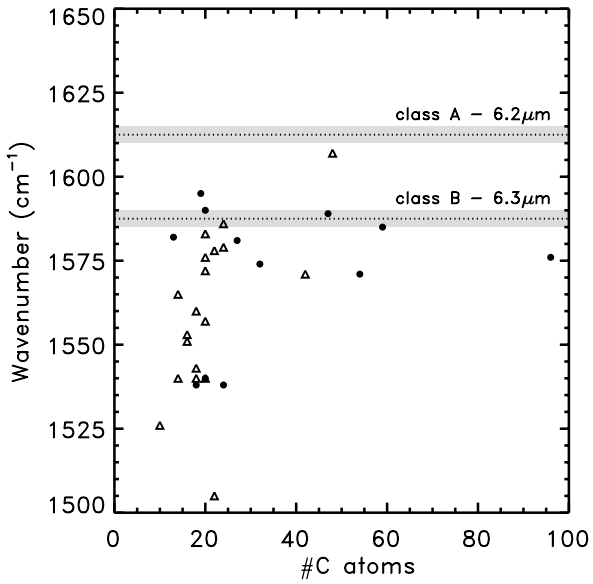

Figure 3.23 — A plot of the dominant feature position in the PAH CC stretching region as a function of molecular size. The positions and typical FWHM of the interstellar 6.2 and 6.3 μm components discussed in Sect. 3.3.1 are indicated by the horizontal shaded bands. Open symbols correspond to experimentally measured positions. Solid symbols are frequencies computed using B3LYP quantum calculations (Hudgins et al. 2001; Bauschlicher 2002, Bauschlicher, Hudgins, and Allamandola 2002 (in prep.)). Theoretical positions typically have uncertainties of 5-10 wavenumbers, with a few bands showing shifts of 15 to 20 wavenumbers.

mandola, 1999). The data shown in Fig. 3.23, which has been updated to include more PAHs than available in the original study, shows this trend.

However, Fig. 3.23 shows that the trend does not continue ad-infinitum but seems to die out for molecules with more than about 30 to 40 carbon atoms, falling slightly longwards of 6.3 μm. This behaviour is consistent with the limit of graphite which shows an emission mode at 6.3 μm (Draine 1984). Thus, as the size grows, the influence of boundary conditions on these pure CC stretching vibrations within the PAH carbon skeleton vanishes when the peak wavelength of this mode in graphite is reached. Indeed, it is a general chemical rule that within any molecule, the further a given bond or chemical subgroup is from the site of a modification, the smaller the effect exerted by that change on the properties of the specific bond or subgroup. This goes for a molecule's fundamental vibrational frequencies as well as its chemical properties. For the smallest PAHs, addition of even a single ring constitutes a significant modification to the carbon skeleton and strongly influences its pure CC stretching vibrational frequencies. However, as PAH size increases, an ever-increasing fraction of the molecule's carbon skeleton lies "far" from the site of any particular modification and is thus increasingly insensitive to that modification. As a result, the corresponding fundamental CC

stretching modes that arise within that skeleton are progressively less perturbed resulting in a levelling off of their frequencies above a certain size ($\sim$30 C atoms as estimated from Fig. 3.23).

Importantly from the astrophysical perspective, Fig. 3.23 shows that the maximum wavenumber falls some 20 cm^{-1} short of 6.2 μm, the peak position of the class A interstellar bands discussed in Sect. 3.3.1. This mismatch between PAH band position and the interstellar feature is only worsened by the approximately 10 cm^{-1} red shift which occurs for emission from a vibrationally excited PAH (Cherchneff & Barker 1989; Flickinger & Wdowiak 1990; Brenner & Barker 1992; Colangeli et al. 1992; Joblin et al. 1995; Cook & Saykally 1998). Thus, while the correlation between molecular size with band position is confirmed by new experimental and theoretical data, for the highly symmetric pure PAHs considered here, the strongest, infrared active, pure CC stretching mode cannot reproduce the position of the 6.2 μm interstellar feature and other factors which can slightly shift this frequency must be considered.

Molecular symmetry

Another property which can influence IR activity is molecular symmetry. In large, symmetric molecules there are many vibrations which correspond to very weak or infrared forbidden transitions. These vibrations are weak or IR inactive in highly symmetric species because the oscillating dipoles arising from atomic motions at one position in the molecule are cancelled by identical, but oppositely oriented dipoles arising from identical, oppositely phased motions occurring elsewhere in the molecule. Reducing molecular symmetry eliminates some of this oscillating dipole cancellation and once IR forbidden modes can become IR active. This behaviour is expected independent of the means by which symmetry is broken. For large, highly symmetric molecules such as circumcoronene ($C_{54}H_{18}^{+}$, symmetry = D_{6h}) and circumcircumcoronene ($C_{96}H_{24}^{+}$, symmetry = D_{6h}) included in Fig. 3.23, the calculations indicate that there are several infrared inactive CC stretching vibrations that fall between about 6.15 and 6.25 μm, (1626 and 1600 cm^{-1}) positions which overlap the interstellar position. Since there is no reason to expect that interstellar PAHs would be so highly symmetric, we have explored the influence of symmetry breaking on the IR spectrum to assess the possibility that asymmetric PAHs would show strong IR activity at shorter wavelengths, closing the gap between the PAH spectra and the 6.2 μm interstellar feature. Several different cases were tested and all show only marginal effects (Bauschlicher, Hudgins, and Allamandola 2002, in prep.). For example, by reducing the symmetry of the circumcoronene cation by removing first one and then two of the peripheral rings, the peak position of the strongest pure CC vibration does not shift much if at all. It falls at 6.36 μm (1572 cm^{-1}) in both circumcoronene and circumcircumcoronene with one ring removed and only slightly shifts to 6.33 μm (1580 cm^{-1}) in circumcoronene with two rings removed. Thus, we conclude that symmetry breaking alone cannot account for the difference between the interstellar feature and the PAH spectra considered to now.

Molecular heterogeneity

Another means by which IR activity can be induced in otherwise weak or forbidden transitions is by the introduction of a hetero atom into the symmetric molecular structure. This alters the molecule in two ways: it lowers the symmetry and modifies the electronic dis-

the innermost ring it falls at 6.19 μm. Bandshift behaviour when more than one nitrogen is substituted is still to be determined. For singly substituted PAHs, this peak shift has two causes. First, the insertion of nitrogen decreases molecular symmetry, increasing IR activity in modes which are normally weak because of the higher symmetry as described above. Second, the strongly electro negative nitrogen atom modifies the fixed charge distribution on the carbon network and induces stronger IR activity for these vibrations since the magnitude of the oscillating dipole increases. This behaviour can be expected independent of the means by which the charge distribution is fixed.

Bauschlicher, Hudgins, and Allamandola (2002, in prep.) have also considered oxygen and silicon atom substitution. Nevertheless, while these too show a similar induction of IR activity close to 6.2 μm, when taking chemical considerations into account, nitrogen substitution is still the most attractive candidate. First, nitrogen can be incorporated anywhere within the ring structure without compromising the aromatic stability of the π electron network. Second, oxygen substitution does not have this advantage. Oxygen or O^+ cannot form four bonds and so oxygen is not found in the middle rings. Hence, oxygen would be most stable only at the edge positions, positions which would be more reactive and subject to chemical attack. Third, although silicon can form four bonds, the C-Si bond length is larger then the C-C bond length and hence the aromatic rings will be disturbed by silicon substitution. Moreover, silicon has a much lower cosmic abundance then does nitrogen. Thus, at this stage in our understanding, large PAHs containing some nitrogen seem most plausible to account for the 6.2 μm band position. As mentioned before, there are other plausible interstellar PAH-related species in which one might induce activity at this position and these must be investigated before a firm conclusion can be drawn. Some examples include large PAHs with uneven and irregular structure, PAH clusters and PAH complexes with metals such as iron (metallocenes).

3.6.2 The position of the PAH CC stretching/CH in-plane bending feature near 7.7 μm: experiment and theory

The CC stretching/CH in-plane bending vibrations of most singly ionised PAHs possess at least one very strong feature between about 7.2 and 8.2 μm. Fig. 3.25 shows a graph of the frequencies for the strongest of these modes plotted versus the carbon number for the same molecules considered in Fig. 3.23. In this case (Fig. 3.25), there is no clear relationship between frequency and size in contrast to the behaviour for the pure CC stretch (Fig. 3.23). While a few of the smallest molecules do have vibrations which fall at the lowest frequencies measured for these modes - suggesting such a correlation - similarly sized molecules possess some of the highest vibrational frequencies. Furthermore, one of the largest PAHs in the laboratory database, hexabenzocoronene ($C_{42}H_{24}$), has the lowest frequency determined to date. Here peak positions for small and large PAHs are intermingled.

In addition, Fig. 3.25 reveals that there is also a gap between about 7.6 and 7.8 μm (1316 and 1282 cm^{-1}), with a clustering of the data between 1320 and 1355 cm^{-1} (7.4 and 7.6 μm). The data in Fig. 3.25 suggests that the mean PAH CC stretching/CH in-plane bending frequency lies near 1335 cm^{-1} (7.5 μm). This behaviour is important in view of the results presented in Sect. 3.3.2 which show that two components dominate the interstellar emission in this region, one peaking near 7.6 μm (class A$'$) , the other longwards of 7.8 μm (class B$'$). When one takes the roughly 10 cm^{-1} red shift into account for emission, it is apparent that this family of PAHs can readily reproduce the 7.6 μm component, but not the

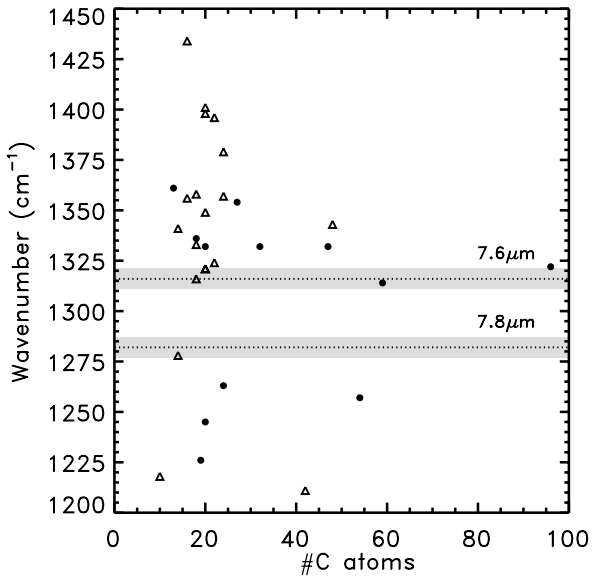

Figure 3.25 — A plot of the dominant feature position in the wavelength region of the 7.7 μm complex as a function of molecular size. The positions and typical FWHM of the interstellar 7.6 and 7.8 μm components of class $\mathcal{A}$ discussed in Sect. 3.3.2 are indicated by the horizontal shaded bands. The two components of the 7.7 μm complex in Class $\mathcal{B}$ peak at 7.6 and from 7.8 to 8.0 μm respectively. Open symbols correspond to experimentally measured positions. Solid symbols are frequencies computed using B3LYP quantum calculations (Hudgins et al. 2001; Bauschlicher 2002, Bauschlicher, Hudgins, and Allamandola 2002 (in prep.)). Theoretical positions typically have uncertainties of 5-10 wavenumbers, with a few bands showing shifts of 15 to 20 wavenumbers.

dominant 7.8 μm component.

As discussed above for the pure CC stretching features near 6.25 μm, we have theoretically considered how molecular symmetry and heterogeneity influence the peak position of the 7.7 μm complex in order to understand what molecular properties might be responsible for the interstellar position. Breaking the high symmetry of PAH molecules, either by removing rings or by substituting a nitrogen atom at several different positions within the carbon network again produces IR activity in modes which were weak or completely forbidden (Bauschlicher, Hudgins, and Allamandola 2002, in prep.). In this case however, while a few examples are found in which intense bands fall in this gap, these results seem random and no clear structural relationship has yet emerged. Thus, this sort of molecular modification does not account for the interstellar 7.8 μm component.

Furthermore, as with the 6.2 μm feature, dehydrogenation and the charge of the PAH molecules do not play a major role in determining the peak position (see Sect. 3.6.1).

In summary, the 7.6 μm (class A$'$) interstellar band is consistent with a mixture of large and small, pure and hetero-atomic PAHs. These PAHs also contribute emission at 7.8 μm

as illustrated in Fig. 3.22. However, the PAHs so far considered reveal a dearth of strong spectral features longwards of 7.7 μm and thus have difficulty reproducing the class B′ 7.7 μm band. There are only a few PAHs in the database which have their strongest band at 7.8 μm and the data is insufficient to make any generalisations concerning the properties which cause strong IR activity at this position. As above, there are several other PAH related species that are likely to be important in the emission zones and which should be considered.

3.7 Astronomical implications

From the wealth of IR spectra, it is clear that the UIR bands at 3.3, 6.2, 7.7, 8.6 and 11.2 μm represent a single class of spectral features that come and go together. The ISO observations presented here in Sect. 3.3.1, 3.3.2 and 3.3.3, show that the peak positions and profiles of the 6.2, 7.7 and 8.6 μm features vary significantly from source to source. Moreover, as discussed in § 3.4, these variations in the different bands are correlated with each other and with the type of object considered (i.e. HII region, YSO, Post-AGB star and so on). These variations stand in marked contrast to the behaviour of 3.3 and 11.2 μm bands. While the latter modes show some variation in profile, their peak position is relatively invariant with both bands wandering by only 0.2% (Tokunaga et al. 1991; Hony et al. 2001, Chapter 4, Peeters et al. 2002, in prep.). Furthermore, while the 3.3 and 11.2 μm band intensities are correlated with each other (Hony et al. 2001), their strengths do not correlate well with that of the 6.2 and 7.7 μm features.

3.7.1 The observed trends

It is shown that class $\mathcal{A}$ and $\mathcal{B}$ have distinctly different profiles, peak position and relative intensities of the features in the 6–9 μm region. We attribute these differences between the two classes to variation in the PAH families present around the sources; i.e. different molecular mixtures are found around the sources of the two classes whose combined IR spectral fingerprints change the overall PAH spectrum in the 6–9 μm region significantly.

Class $\mathcal{B}$ corresponds to regions where $G_0 > 10^4$. For such high G_0, very small grains (VSG) emit in the 6-9 μm region (Cesarsky et al. 2000). Since the range in G_0 present in class $\mathcal{B}$ is also present in class $\mathcal{A}$, these VSG are not responsible for the observed differences. Furthermore, these differences in the observed emission features and hence in the PAH families is not directly related with G_0.

Hony et al. (2001) derived the molecular structure of the PAHs based upon the 10-15 μm spectra and concluded that the PNe contain large, compact PAHs with long straight edges while HII regions contain smaller or more irregular PAHs. Clearly, the HII regions and non-isolated Herbig Ae Be stars all belong to class $\mathcal{A}$ and have a weak $I_{11.2}/I_{12.7}$ ratio. But, for the PNe considered in Hony et al. (2001), no link is found between the $I_{11.2}/I_{12.7}$ intensity ratio and the profile classes. This supports the above mentioned observations that the CH modes seems to behave independently of the CC modes.

3.7.2 The feature assignments and carriers

In general, the peak position of the PAH vibrations may be affected by charge (anion, cation, and neutral states), size, symmetry and molecular structure and heterogeneity. It is therefore important to understand the precise transitions involved in producing these interstellar fea-

tures if we are to fully interpret what these transitions tell us about the nature of the carriers, their history and the local physical environment.

The 6.2 μm feature

The observations presented here (Figs. 3.6 through 3.11) show that the peak position of the interstellar PAH CC stretching band varies between 6.2 and 6.3 μm. The interstellar feature seems more red-shaded (i.e. asymmetric with a red wing) when it peaks at 6.2 μm (class A emitters, Table 2) then when it peaks near 6.25 μm (class B emitters, Table 2). For Class A emitters, the observed half-widths (0.11 μm, 28 cm^{-1}) are close to the expected intrinsic line width of an emitting PAH molecule or cluster (roughly 30 cm^{-1}), for class B emitters the observed widths (0.15 μm, 38 cm^{-1}) are slightly larger and Class C emitters have the smallest widths (0.099 μm, 25 cm^{-1}).

The variation in the observed peak positions and profiles are interwoven and may reflect the effects of a class of PAHs, each with its individual peak position, or the effects of anharmonicity inherent to the emission process in higher vibrationally excited PAHs, or both.

Emission by a PAH family As discussed in Sect. 3.6.1 and illustrated in Fig. 3.23, pure PAHs (i.e. those containing only carbon and hydrogen) composed of >20-30 C atoms can reproduce the position of the interstellar 6.3 μm component but cannot account for the 6.2 μm component. Based on the currently-available experimental and theoretical data, the most probable carriers of the 6.2 μm component are hetero-atom (e.g. N, O, Si) substituted PAHs, PAH clusters and/or PAH complexes with a metal atom such as iron (i.e. metallocenes). Interactions in such species may alter a PAH molecule in two ways : they may lower the molecule's symmetry and they may alter the electron distribution within the molecule. Both of these effects may shift the dominant CC stretching modes toward shorter wavelengths.

In summary, the observed profiles of the 6.2 μm band complex can be a "blend" of emission bands by different carriers with slightly shifted peak position for the main CC mode. Pure PAHs represent the 6.3 μm component and substituted PAHs or PAH-like species emits the 6.2 μm component. The profile of the 6.2 μm band complex reflects then the relative abundance of the different species in the PAH population and so different sources contain different amounts of each type of species. Typically, the PAH population in Post-AGB objects, PNe and isolated Herbig AeBe stars is skewed toward pure-C PAHs, while HII regions, RNe, non-isolated Herbig AeBe stars and galaxies have a dominant contribution from substituted complexed PAHs. However, the PAH family in some PNe also contains an important substituted/complexed PAH population. NGC 7027 is a case in point. This interpretation raises interesting questions on the origin and evolution of circumstellar and interstellar PAHs which will be addressed in Sect. 3.7.3. In principle, the family could consist of two (distinct) species only. However, we consider that unlikely.

Anharmonicity It is also possible to interpret the observed (red shaded) profiles in terms of emission from a single PAH (or a collection of PAHs with very similar peak position) which is (are) highly vibrationally excited. If a molecule is sufficiently highly vibrationally excited, emission from levels above the first excited state become important. Due to the anharmonic nature of the potential well, these band spacings become smaller and smaller the higher up the vibrational ladder one samples and emission between these levels falls slightly and progressively to the red producing a long wavelength wing reminiscent of the observed

wing (Barker et al. 1987). In addition, anharmonic coupling of the emitting mode with other modes also shifts the peak position of the emitting band to lower energies. Integrating over the energy cascade as the emitting species cools down will then in a natural way give rise to a red shaded profile (Barker et al. 1987; Pech et al. 2001; Verstraete et al. 2001).

Pech et al. (2001) and Verstraete et al. (2001) have modelled the IR emission spectrum of PAHs based upon extensive laboratory studies of the shift in peak position as a function of temperature of the emitter which is a direct measure of the anharmonicity (Joblin et al. 1995). They obtained excellent fits to the red shaded appearance of the observed profiles of the 3.3, 6.2 and 11.2 μm bands. However, for the 6.2 μm band no good fit to the peak position is obtained for sources with class $\mathcal{A}$ spectra, because the laboratory and theoretical studies have been limited to pure-C PAHs. Nevertheless, the principle remains the same and small, highly vibrationally excited, N-substituted PAHs are also expected to have red shaded emission profiles.

Within this interpretation, the class A profiles which are highly asymmetric are due to a relatively limited number of small highly excited N-substituted complexed PAHs. The class C profiles, which peak at 6.3 μm and are fairly symmetric (cf. Fig. 3.9), are carried by much less highly excited pure-C PAHs. The "low" excitation of these pure-C PAHs may reflect either the cool nature of the illuminating source in these two Post-AGB objects (CRL 2688 and IRAS 13416) or it may reflect an on-average larger size of the emitting species, or both. Class B profiles show a less pronounced blue rise and a less pronounced red wing. We note that class B sources typically have a higher $I_{11.2}/I_{12.7}$ intensity ratio than class A sources (Hony et al. 2001). A high $I_{11.2}/I_{12.7}$ intensity ratio indicates the dominance of rather large ($\sim$ 150 C-atoms) PAHs (Hony et al. 2001) and anharmonicity effects are expected to be smaller for such large PAHs (Pech et al. 2001). The YSO, BD +40 4124, which belongs to class A shows a symmetric profile, possibly indicating that the photochemical survival of the fittest (i.e. most robust) members of the PAH family has been of great importance in this source (Van Kerckhoven 2002).

The 6.2 μm band of many of these sources have very similar profiles, irrespective of the harshness of the illuminating radiation field - as measured by its strength or effective temperature. As exemplified by the model study of Verstraete et al. (2001), this indicates that the typical size of the emitting PAH is larger in regions which are illuminated by hotter stars. This coupling between size and the "colour" of the illuminating radiation field may be a natural consequence of emission from a family of PAH species; that is, the smallest size of PAHs which can survive in a radiation field will depend on the average photon energy in the illuminating FUV field. To phrase it differently, both the minimum size and the profile of the 6.2 μm band may be a measure of the average excitation of the emitting PAH (Verstraete et al. 2001). The more symmetric profiles of class $\mathcal{C}$ may then reflect that the PAHs in these cool Post-AGB objects have not yet been exposed to harsh radiation fields and their composition still reflects the condition during their formation at high temperatures. As a corollary, this implies that there are no small PAHs ($\leq$ 25 C atoms) with peak positions longwards of 6.3 μm. The coolness of the radiation field and symmetric profiles imply then that the PAHs in these sources are only moderately excited.

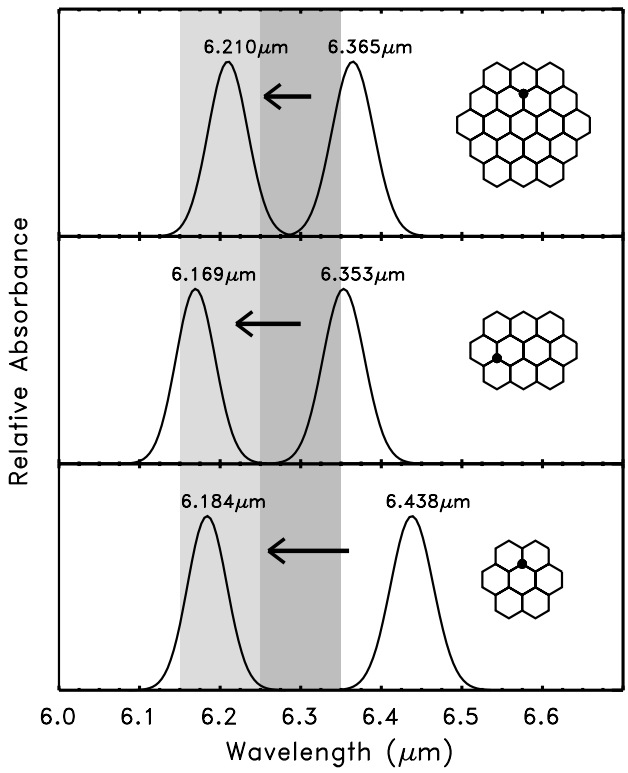

Figure 3.24 — The effect of PAH nitrogenation on the positions of the strongest band in the CC stretching region for the three PAHs coronene, ovalene, and circumcoronene. The right profile indicates the position for the unsubstituted PAH, the left for the nitrogenated species. The position of nitrogen substitution is indicated by the filled circle in the structures. The vertical grey shaded bands indicate the position and width of the interstellar class A and B bands discussed in Sect. 3.3.1.

tribution. To investigate this influence on PAH spectroscopy, Bauschlicher, Hudgins, and Allamandola (2002, in prep.) have studied the effects of introducing different hetero-atoms into different positions within the carbon network of several PAHs. This affects, in particular, the position of the 6.2 μm band. A few examples are presented in Fig. 3.24. Here the positions of the strongest band in this region are shown for the cations of the pure PAHs coronene, ovalene, and circumcoronene and their counterparts which have one of the carbon atoms replaced by a nitrogen. In all cases nitrogen substitution shifts the strongest CC stretching vibration to the 6.2 μm interstellar band position. Further within a given PAH, the shift depends somewhat on the "depth" of the substitution in the carbon skeleton. For example, when nitrogen is substituted for a carbon atom on the outermost ring of the circumcoronene cation, the strongest band in the CC stretching region falls at 6.16 μm; when this substitution is made on the next innermost ring (shown in Fig. 3.24), it falls at 6.21 μm; and when on

form of larger grains. The dust (and gas) in these two Post-AGB objects is very close to the central star and hence dust particles might attain high enough temperature to emit strongly around 8 μm. The large width of the 8.22 μm band lends some credence to a grain-like carrier for this band. Various carbonaceous materials show an emission near 8 μm, including HAC, QCC, coal, and partially hydrogenated C_{60} (Mortera & Low 1983; Sakata et al. 1984; Colangeli et al. 1995; Guillois et al. 1996; Scott et al. 1997; Schnaiter et al. 1999; Stoldt et al. 2001). However, the profiles in these solid state materials peak close to 8 μm and are much broader then the 8.22 μm component. These materials do provide reasonable fits to the 8 μm feature as observed toward IRAS 22272+5435 (Buss et al. 1993; Guillois et al. 1996; Kwok et al. 2001) but cannot be the carriers of the 8.22 μm feature.

3.7.3 Formation/Evolution

It was recognised some time ago that there are two main classes of contributors to the 7.7 μm band, one peaking near 7.6 μm which is associated with HII regions, and one peaking near 7.8 μm, associated with planetary nebulae (Bregman 1989; Cohen et al. 1989). In this paper, we reported three main classes. These classes are indeed related with the type of object (see Sect. 3.4). In general, HII regions, RNe, non-isolated Herbig AeBe stars and the extragalactic sources form one class ($\mathcal{A}$) with dominant bands at $\sim$ 6.22 μm, $\sim$ 7.6 μm and $\sim$ 8.6 μm. The local radiation field G_0 in the latter sources ranges from 3E2 to 7E6. Isolated Herbig AeBe stars, PNe, HD44179, HR4049 - with a local radiation field G_0 between 6E4 and 2E7 - form a second class ($\mathcal{B}$) with dominant bands in the range of 6.24-6.28 μm, longwards of 7.7 μm and longwards of 8.62 μm. Two peculiar Post-AGB stars form a third class ($\mathcal{C}$) with a 6.3 μm and a 8.22 μm feature; with a local radiation field G_0 of 5E3 in one of these two stars. Two Post-AGB stars and one PN belong as well to class $\mathcal{A}$. As discussed in the previous section, class $\mathcal{A}$ is probably built up by nitrogen substituted or complexed PAHs while class $\mathcal{B}$ seems to be dominated by pure PAHs in their dust collection. The PAH spectrum in the 6 to 9 μm region apparently reflects local physical conditions and the accumulated effect of processing from the formation sites in the AGB or post-AGB phases to the ISM.

The two main PAH classes identified through the peak position of their CC modes - classes $\mathcal{A}$ and $\mathcal{B}$ - imply two distinct histories. Because these two PAH classes are connected to classes of astronomical objects, these histories are likely locally determined. Hence, we interpret class $\mathcal{B}$ as the PAHs formed in the stellar ejecta presumably through chemical processes similar to terrestrial soot formation. Extensive laboratory studies and theoretical calculations have shown that in that case highly condensed, "pure" carbon PAHs are the favoured molecular intermediaries in the dust condensation route (Frenklach 1990; Frenklach & Feigelson 1989; Cherchneff et al. 1992). The PAHs in class $\mathcal{A}$, on the other hand, likely represent a modification of those in class $\mathcal{B}$ in the harsh environment of the interstellar medium (Allamandola et al. 1999b). Interstellar PAHs could be substantially chemically processed in the warm gas of strong shock waves. Alternatively, energetic processing through UV and/or cosmic rays may lead to some modification of the PAH structure (Strazulla et al. 1995; Bernstein et al. 1999; Ricca et al. 2002a,b).

Hony et al. (2001) concluded from their study of the CH out-of-plane bending modes that evolution is an integral aspect of the life of interstellar PAHs. Specifically, the spectra of PNe point towards the presence of large ($\sim$ 150 C-atoms) compact PAH with regular molecular edge structures. In contrast, HII regions are dominated by highly irregular molecular edge structures. In their view, these molecular differences are driven by energetic processing in the

harsh condition of the ISM of PAHs initially formed in stellar outflows. Our study of the CC modes complements this view. The spectral variation in the CC modes in these very different environments similar attest to the chemical evolution of the family of PAHs.

3.8 Summary

The most striking aspect of the features in the 6–9 μm region is their variability. All features shift in peak position from source to source, show different profiles and each seems to be composed of several subfeatures. Moreover, the variations in the 6.2 and 7.7 μm bands seem to be correlated with each other. In addition, these variations depend on the type of source considered and apparently reflect local physical conditions or the accumulated effect of processing from the formation sites in the AGB or post-AGB phases to the ISM. In particular, the sources with a profile $\mathcal{A}$ 6.2 μm feature have a "7.7" feature peaking at 7.6 μm, while for those with a component $\mathcal{B}$ 6.2 μm feature, the "7.7" feature peaks longwards of 7.7 μm. The class $\mathcal{C}$ objects, with a 6.2 μm feature peaking at 6.3 μm do not show a "7.7" feature but instead show a broad emission band at 8.2 μm. These variations stand in marked contrast to the behaviour of 3.3 and 11.2 μm bands whose profiles and peak positions are quite invariable (Hony et al. 2001, Chapter 4, Peeters et al. 2002, in prep.).

We have summarised laboratory data and quantum chemical calculations for the 6–9 μm region. We attribute the observed 6.2 μm profile and peak position to the combined effect of a PAH family and anharmonicity with pure PAHs representing the 6.3 μm component and substituted/complexed PAHs the 6.2 μm component. The 7.6 μm component is well reproduced by both pure and substituted/complexed PAHs but the 7.8 μm component remains an enigma. In addition, the exact identification of the 8.22 μm feature remains unknown.

The observed spectral variations in the CC modes are coupled to the astronomical characteristics of the sources (object type). We find this strong support for the presence of a family of PAHs whose composition and/or emission characteristics are sensitive to the local physical conditions. An analysis of the CH out-of-plane bending modes in a similar sample has drawn essentially the same conclusion. Apparently, the interstellar PAH family is readily processed in space environments.

The past decade has witnessed great experimental and theoretical progress in understanding the spectroscopic properties of PAHs under interstellar conditions. However, the new observational data presented here poses significant new questions concerning the nature of the band carriers, questions whose answers will yield insight into the nature of the emitters and history of the emission zones.

Acknowledgements

We would like to thank the referee Dr. L. Verstraete whose comments have helped to improve the paper. The laboratory work was supported by NASA's Laboratory Astrophysics Program (grant number 344-02-04-02). IA^3 is a joint development of the SWS consortium. Contributing institutes are SRON, MPE, KUL and the ESA Astrophysics Division. This work was supported by the Dutch ISO Data Analysis Center (DIDAC). The DIDAC is sponsored by SRON, ECAB, ASTRON and the universities of Amsterdam, Groningen, Leiden and Leuven. This research has made use of the SIMBAD database, operated at CDS, Strasbourg, France and the NASA/IPAC Extragalactic Database (NED), operated by JPL, CalTech and NASA.

harsh condition of the ISM of PAHs initially formed in stellar outflows. Our study of the CC modes complements this view. The spectral variation in the CC modes in these very different environments similar attest to the chemical evolution of the family of PAHs.

3.8 Summary

The most striking aspect of the features in the 6–9 μm region is their variability. All features shift in peak position from source to source, show different profiles and each seems to be composed of several subfeatures. Moreover, the variations in the 6.2 and 7.7 μm bands seem to be correlated with each other. In addition, these variations depend on the type of source considered and apparently reflect local physical conditions or the accumulated effect of processing from the formation sites in the AGB or post-AGB phases to the ISM. In particular, the sources with a profile $\mathcal{A}$ 6.2 μm feature have a "7.7" feature peaking at 7.6 μm, while for those with a component $\mathcal{B}$ 6.2 μm feature, the "7.7" feature peaks longwards of 7.7 μm. The class $\mathcal{C}$ objects, with a 6.2 μm feature peaking at 6.3 μm do not show a "7.7" feature but instead show a broad emission band at 8.2 μm. These variations stand in marked contrast to the behaviour of 3.3 and 11.2 μm bands whose profiles and peak positions are quite invariable (Hony et al. 2001, Chapter 4, Peeters et al. 2002, in prep.).

We have summarised laboratory data and quantum chemical calculations for the 6–9 μm region. We attribute the observed 6.2 μm profile and peak position to the combined effect of a PAH family and anharmonicity with pure PAHs representing the 6.3 μm component and substituted/complexed PAHs the 6.2 μm component. The 7.6 μm component is well reproduced by both pure and substituted/complexed PAHs but the 7.8 μm component remains an enigma. In addition, the exact identification of the 8.22 μm feature remains unknown.

The observed spectral variations in the CC modes are coupled to the astronomical characteristics of the sources (object type). We find this strong support for the presence of a family of PAHs whose composition and/or emission characteristics are sensitive to the local physical conditions. An analysis of the CH out-of-plane bending modes in a similar sample has drawn essentially the same conclusion. Apparently, the interstellar PAH family is readily processed in space environments.

The past decade has witnessed great experimental and theoretical progress in understanding the spectroscopic properties of PAHs under interstellar conditions. However, the new observational data presented here poses significant new questions concerning the nature of the band carriers, questions whose answers will yield insight into the nature of the emitters and history of the emission zones.

Acknowledgements

We would like to thank the referee Dr. L. Verstraete whose comments have helped to improve the paper. The laboratory work was supported by NASA's Laboratory Astrophysics Program (grant number 344-02-04-02). IA^3 is a joint development of the SWS consortium. Contributing institutes are SRON, MPE, KUL and the ESA Astrophysics Division. This work was supported by the Dutch ISO Data Analysis Center (DIDAC). The DIDAC is sponsored by SRON, ECAB, ASTRON and the universities of Amsterdam, Groningen, Leiden and Leuven. This research has made use of the SIMBAD database, operated at CDS, Strasbourg, France and the NASA/IPAC Extragalactic Database (NED), operated by JPL, CalTech and NASA.

4

The profiles of the 3 to 12 μm PAH features

To appear as :

B. van Diedenhoven, E. Peeters, C. Van Kerckhoven, S. Hony,
D.M. Hudgins, L.J. Allamandola, A.G.G.M. Tielens

Submitted to Astronomy & Astrophysics

Abstract We present spectra of the 3.3 μm and 11.2 μm features of a large number of stellar sources, planetary nebulae, reflection nebulae, H II regions and extragalactic sources, obtained with the SWS spectrograph on board ISO. Clear variations are present in the profiles of these features. Most of the sources show a symmetric 3.3 μm feature peaking at $\sim$3.290 μm, while only very few show an asymmetric 3.3 μm feature peaking at a slightly longer wavelength ($\lesssim$ 0.007 μm). The profiles of the 11.2 μm feature are distinctly asymmetric with a steep blue rise and a red tail. The majority of the sources has a 11.2 μm feature peaking between 11.20 and 11.24 μm, with a very steep blue rise and a low tail-to-top ratio. A few sources show 11.2 μm features with a peak position of $\sim$11.25 μm, a less steep blue rise and a high tail-to-top ratio. The sources are classified independently based on the 3.3 and 11.2 μm feature profiles and peak positions. Correlations between these classes and those based on the 6–9 μm features (Chapter 3) are found. In particular, sources with the most common profiles in the 6–9 μm region also show the most common 3.3 and 11.2 μm feature profiles. However, the uncommon profiles do not correlate with each other. Also, these classifications depend on the type of object. In general, H II regions, non-isolated Herbig AeBe stars, YSO's and galaxies in our sample all show common profiles for all 3-12 μm features. Some of the planetary nebulae and Post-AGB stars show uncommon feature profiles. The observed pronounced contrast in the spectral variations for the CH modes versus the CC modes is striking : the peak

wavelengths of the features attributed to CC modes vary by $\sim$25–50 cm^{-1}, while for the CH modes the variations are $\sim$4–6.5 cm^{-1}. We summarise existing laboratory data and theoretical calculations of the modes emitting in the 3–12 μm region of PAH molecules. We attribute the variations in peak position of the 3.3 and 11.2 μm feature to the presence of a mixture of PAH molecules. The variations in FWHM of the 3.3 μm feature remains an enigma while those of the 11.2 μm can be explained by anharmonicity and molecular structure. The possible origin of the observed contrast in profile variations between the CH modes and the CC modes is highlighted.

4.1 Introduction

The infrared spectra of a wide variety of sources are dominated by strong emission features at 3.3, 6.2, 7.7, 8.6 and 11.2 μm (3040, 1615, 1310, 1160, 890 cm^{-1}), commonly called the unidentified infrared (UIR) emission features (cf., Gillett et al. 1973; Geballe et al. 1985; Cohen et al. 1986). These features have been detected and studied in a large number of stellar sources – planetary nebulae, reflection nebulae, H II regions and extragalactic sources – indicating that the emitters of these features are surprisingly widespread and extremely stable, and therefore form a very important component of the interstellar medium (Allamandola et al. 1989b).

The UIR features are generally attributed to PAHs or PAH related molecules (Allamandola et al. 1989b), although the exact molecular identification remains uncertain. Compelling evidence suggests that the features are due to a complex mixture of ionised and neutral, possibly substituted/complexed PAHs of many different sizes (Schutte et al. 1993; Bakes & Tielens 1994; Boulanger et al. 1998b; Bakes et al. 2001; Hony et al. 2001; Verstraete et al. 2001; Pech et al. 2001, Chapter 3). Therefore the overall appearance of the features including the profiles, relative strengths and peak positions, are determined by a large number of PAH related parameters, parameters which are determined by local conditions and the PAH history.

High-resolution spectroscopy, as obtained with the *Infrared Space Observatory* (ISO, Kessler et al. 1996), has revealed the richness of these widespread variations in the relative strength and profiles of the features from source to source and within sources (Verstraete et al. 1996; Tielens et al. 1999; Maillard et al. 1999; Joblin et al. 2000; Hony et al. 2001, Chapter 3). Peeters et al. (Chapter 3) have shown that there are even variations in the position and profiles of the major peaks and have classified the sources in their sample according to the peak positions of the 6.2, 7.7 and 8.6 μm features independently (Fig. 3.17 and 4.4, panels b and c). Interestingly, the classifications of the different features were found to correlate and three main classes with significant different feature profiles were identified. Most sources in their sample are in class $\mathcal{A}$ (A_{6-9} hereafter). Sources with features peaking at significantly longer wavelengths were referred to as class $\mathcal{B}$ (B_{6-9} hereafter). The two sources in their sample showing a 6.3 μm feature exhibit neither a 7.7 μm complex nor a 8.6 μm feature. Instead, both sources show a broad emission feature at 8.22 μm. These sources are referred to as class $\mathcal{C}$ (C_{6-9} hereafter). Furthermore, the observed 6–9 μm PAH spectrum was found to depend on the type of object and linked to local physical conditions.

To extend our insight of the PAH family and its dependency on the local physical conditions, we study and classify the profiles of the 3.3 and 11.2 μm feature in the ISO-SWS spectra of a wide variety of sources. In Sect. 4.2 our sample and the observations are pre-

sented; the data reduction, the influence of extinction and the decomposition of the spectra are discussed. In Sect. 4.3, the 3.3 and 11.2 μm features are first classified according to their profile and the relations between the classifications of all features in the 3–12 μm range are investigated, as well as their correlation with object type. Subsequently, variations in features associated with CH and CC modes are compared. In Sect. 4.4, the spectral characteristics of PAHs in the 3–12 μm range as measured in the laboratory and calculated by quantum chemical theories are summarised. The implications of the spectroscopic and observational conclusions made in this paper are discussed in Sect. 4.5. Finally, in Sect. 4.6 our main results are summarised.

4.2 The data

4.2.1 The sample

For this study, we take the sample of Peeters et al. (Chapter 3) and reduce it to contain spectra with sufficient signal-to-noise (S/N) in the 3.3 and/or 11.2 μm regions (Table 4.1). This reduced sample includes 49 sources from a wide variety of objects, ranging from Reflection Nebulae (RNe), (compact) H II regions, Young Stellar Objects (YSO), Post-AGB stars, Planetary Nebulae (PNe) to galaxies.

4.2.2 Observations and reduction

All spectra in the sample were obtained with the Short Wavelength Spectrometer (SWS, de Graauw et al. 1996) on board ISO, using the AOT01 scanning modes at various speeds or the AOT06 mode, with a resolving power ($\lambda/\Delta\lambda$) of $\sim$500-1500.

The data were processed with the SWS Interactive Analysis package IA^3 (de Graauw et al. 1996) using calibration files and procedures equivalent with pipeline version 7.0 or later. Further data processing consisted of bad data removal and rebinning with a constant resolution, as described in Chapter 2.

In case of high fluxes, the spectra can suffer from memory effects. Here, this only applies to the 11.2 μm feature. At the time the data reduction was done, no memory correction tool was available and the average of the up and down scans is taken. The influences of memory effects is investigated as described in Chapter 3 and are found not to alter the 11.2 μm feature profile significantly.

The 11.2 μm band is situated at the end of the AOT band 2C (7–12.3 μm). Near the end of the AOT band, the noise level increases due to a lower responsivity of the instrument. This responsivity effect in combination with residual fringes (mostly noticeable at the end of this band in a few detectors) results in a large increase of the noise level, starting around 11.3 μm.

4.2.3 The continuum

To study the feature profiles in different sources, we subtract a local continuum. This continuum determination is somewhat arbitrary. A local spline continuum or a polynomial of order 2 is fitted to the spectra in a wide wavelength region around the features (Fig. 4.1). In the 3.3 μm region, the plateau from about 3.2 to 3.6 μm was subtracted after the subtraction of the continuum, using a Gaussian with peak position 3.42 μm and a FWHM of 0.242 μm. For the 11.2 μm feature, the plateau and the continuum are fitted together using a single spline. To

Table 4.1 — The classifications of the 3–12 μm PAH features.

Source	PAH features					Object type
	3.3[a]	6.2[a,b]	7.7[a,b]	8.6[a,b]	11.2[a]	
IRAS 10589-6034[†?]	A	A	A	A	A	compact H II region
IRAS 12063-6259[†]	A	A	A	A	A	compact H II region
IRAS 15384-5348[†]	A	A	A	A	A	compact H II region
IRAS 15502-5302[†]	A	A	A	y	y	compact H II region
IRAS 18116-1646[†?]	A	A	A	A	A	compact H II region
IRAS 18032-2032[†]	A	A	A	A	A	compact H II region
IRAS 18317-0757[†]	A	A	A	A	A	compact H II region
IRAS 18434-0242[△,†]	A	A	A	♮	A	compact H II region
IRAS 19442+2427[△,†]	A	A	A	A	A	compact H II region
IRAS 21190+5140	A	A	A	A	A	compact H II region
IRAS 22308+5812	A	A	A	A	A	compact H II region
IRAS 23030+5958	A	A	A	A	A	compact H II region
IRAS 23133+6050	A	A	A	A	A	compact H II region
W3A 02219+6125[△,†]	A	A	A	A	A	compact H II region
OrionBar D2	B1	A	A	A	A	H II region
OrionBar D5	A	A	A	A	A	H II region
OrionBar D8	A	A	A	A	A	H II region
OrionBar H2S1	A	A	A	A	A	H II region
OrionBar BRGA	A	A	A	A	A	H II region
Orion PK1[†,♭]	A	A	A	A	A	H II region
Orion PK2[†,♭]	A	A	A	A	A	H II region
G327.3-0.5[†]	A	A/B1	A	A	A	H II region
IRAS 02575+6017[†,♭]	A	A	A	A	A	H II region +YSO
GGD-27 ILL[†,♭]	A[V]	A	A	A	A	star forming region
S106 (IRS4)[†,♭?]	A	A	A	A	A	YSO
IRAS 03260+3111	A	A	A	A	A	Herbig AeBe star
BD+40 4124	A	A	A	A	A	Herbig AeBe star
CD-42 11721[†?]	A	A	A	A	A	Herbig AeBe star
CD-42 11721(off)[†?]	A	A	A	A	A	Herbig AeBe star
HD 97048[△]	A	A	AB	A	A	Herbig AeBe star
HD 179218	B?[V]	B1/2	B	B	y	isolated Herbig AeBe star
NGC 7023 I	A	A	A	A	A	RN
NGC 2023	A	A	A	A	A	RN
MWC 922[△]	B1	B1	A	♮	y	emission-line star
CRL 2688	A	C	C	C	y	Post-AGB star
HD 44179[△]	B2	B2	B	B	B	Post-AGB star
HR 4049[◇]	B	B2	B	B	B	Post-AGB star
IRAS 16279-4757	A	A	A	A	A	Post-AGB star
IRAS 13416-6243[◇]	B	C	C	C	y	Post-AGB star

Table 4.1 — Continued.

Source	PAH features					Object type
	3.3[a]	6.2[a,b]	7.7[a,b]	8.6[a,b]	11.2[a]	
IRAS 21282+5050	A	A	AB	A	A(B)	Post-AGB star
BD+30 3639[△]	A	B1	B	B	A(B)	PN
Hb5	A	A	◁	A	B	PN
HE 2-113	A	B2	B	B	B	PN
IRAS 07027-7943	A	B2/3	B	B	y	PN
IRAS 17047-5650[△]	A	B1	B	B	B	PN
NGC 7027[△]	A	A	B	B	A(B)	PN
circinus[†]	y	A	A	A	B	Seyfert 2 galaxy
M 82[†?,♭]	A	A	A	A	A(B)	Startburst galaxy
NGC 253[♭]	A	A	A	A	A(B)	Seyfert galaxy

[a]: Central wavelength is given in μm; [b]: Directly taken from Chapter 3. y: Feature is present but too weak and/or too noisy to classify; [♮]: Source with an unusual 8.6 μm feature (see Chapters 3 and 8); [△]: Sources suffering from memory effects at 11 μm; [†]: Silicate absorption (9.7 μm) present; [♭]: Water ice absorption around 3 μm; [◇]: Up- and down-scans disagree around 3.3 μm feature, but profile clearly of class B; [◁]: Strong [NeVI] present on top of the 7.6 μm feature hampers the classification; [V]: Classification by Van Kerckhoven (2002).

assess the sensitivity of the resulting profiles to the continuum or plateau choice, two extreme fits were defined and subtracted. In general, the influence of the continuum and/or plateau determination on the profile is very small and hence does not change the classification/profiles of the sources.

4.2.4 Extinction

The data are not corrected for extinction. The influence of extinction on the 3.3 and 11.2 μm feature profiles is investigated as described in Chapter 3. The extinction is found to be quite gray over the short wavelength region and thus has no significant influence on the profiles of the features.

Seven sources show water ice absorption around 3 μm (see Table 4.1). The 3.3 μm feature is situated in the red wing of the water band and, hence, its profile could be influenced (Gibb et al. 2000). Since we draw a local spline continuum around the 3.3 μm feature, we neglected the ice absorption and assume it has no influence on the profiles.

4.2.5 Scaling

After subtracting the continuum and/or plateau, the spectra were scaled to have the same integrated intensity in the investigated wavelength range. In the case of the 3.3 μm feature, the lower and upper limits for integration are chosen to be 3.26 and 3.32 μm, respectively. Obviously, the H recombination line, Pfδ, at 3.296 μm is excluded in the integration. For the 11.2 μm feature, the lower limit (11.1 μm) is chosen so as to exclude the 11.0 μm feature,

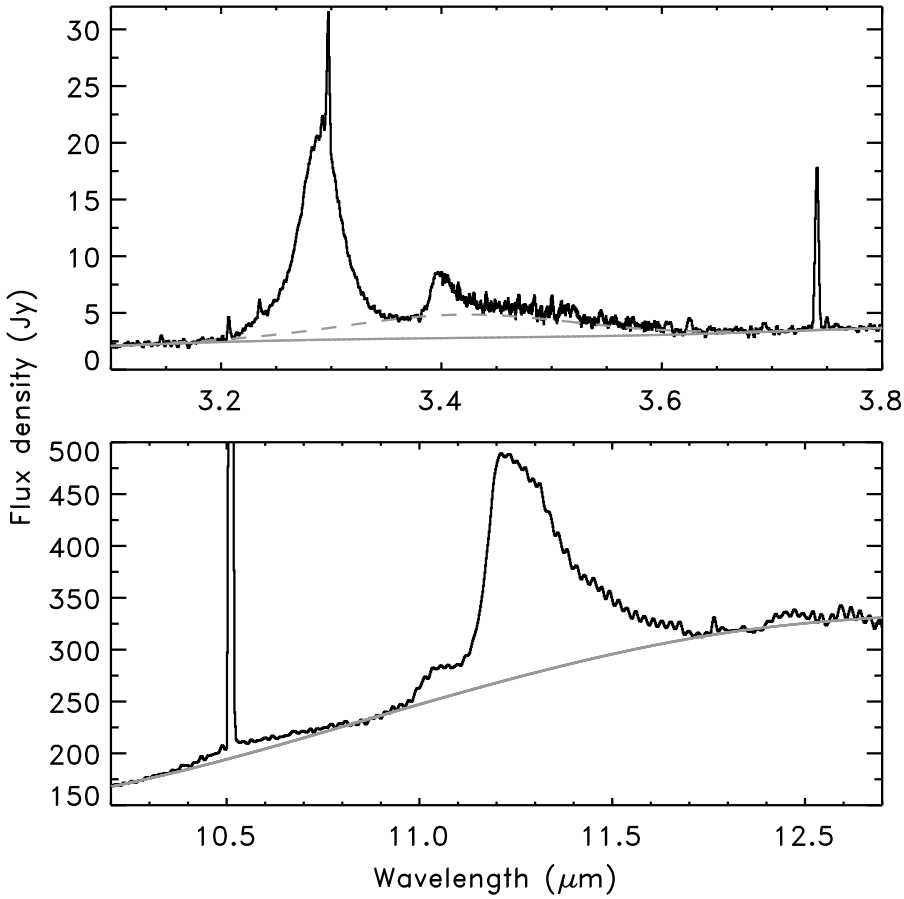

Figure 4.1 — Illustrative examples of the continuum underneath the 3.3 and 11.2 μm features exemplified by NGC 7027. The full line represents the local continuum and the dashed line in the top panel represents the continuum the plateau. See text for details (Sect. 4.2.3).

while the upper limit is determined by the most extreme end of the feature (11.6 μm).

4.3 The feature profiles

4.3.1 The 3.3 μm feature

Nearly all sources in our sample show a pronounced 3.3 μm feature. Only for Circinus the S/N in this region was insufficient for the classification. The extreme similarity of most observed 3.3 μm feature profiles is very striking (Fig. 4.2, top panel). Only six sources in our sample show deviations in their 3.3 μm features (see Table 4.1 and Fig. 4.2, middle and bottom panel).

Based on the profile of the 3.3 μm feature, the sources can be classified into three classes, designated as $A_{3.3}$, $B1_{3.3}$ and $B2_{3.3}$ (Tables 4.1 and 4.2). Class $A_{3.3}$, containing most

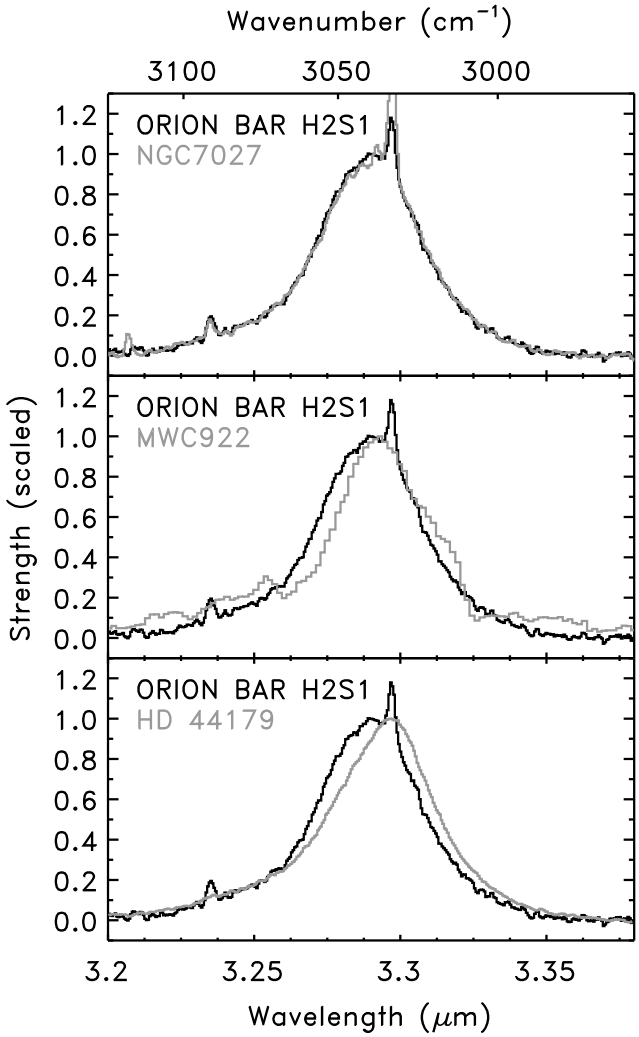

Figure 4.2 — Some examples of the 3.3 μm feature. The spectra are scaled so that the peak intensity equals 1. Note that a H recombination line (Pfδ at 3.296 μm) is present in the spectrum of the Orion Bar and NGC 7027. The top-panel illustrates the similarity of the class $A_{3.3}$ features observed in most sources. The middle- and bottom-panel show the difference between class $A_{3.3}$ and $B1_{3.3}$ (MWC 922) and $B2_{3.3}$ (HD 44179), respectively.

sources, has a symmetric profile with a peak position of $\sim$3.290 μm and a FWHM of 0.040 μm (Fig. 4.2, top panel). Class $B1_{3.3}$ and $B2_{3.3}$ have asymmetric profiles with peak positions of $\sim$3.293 and $\sim$3.297 μm respectively, both with a FWHM of 0.037 μm. The profile of class $B2_{3.3}$, represented by HD 44179, is shifted with respect to class $A_{3.3}$, and has a less steep blue wing (Fig. 4.2, bottom panel). The profile of class $B1_{3.3}$, represented by MWC 922, is intermediate; its red wing is similar to the $A_{3.3}$ profile, but the blue wing is clearly shifted

Table 4.2 — Overview of the defined classifications of the 3.3 and 11.2 μm PAH features. See text for details.

Class	peak wavelength		FWHM	profile
	μm	cm^{-1}	μm	
$A_{3.3}$	∼3.290	∼3039	∼0.040	symmetric
$B1_{3.3}$	∼3.293	∼3037	∼0.037	asymmetric
$B2_{3.3}$	∼3.297	∼3033	∼0.037	asymmetric
$A_{11.2}$	∼11.20-11.24	∼889.6-892.9	$\sim$ 0.17	asymmetric
$A(B)_{11.2}$	∼11.20-11.24	∼889.6-892.9	$\sim$ 0.21	asymmetric
$B_{11.2}$	$\sim$ 11.25	∼888.9	$\sim$ 0.20	asymmetric

and the peak position is slightly to the red compared to the $A_{3.3}$ profile (Fig. 4.2, middle panel). The up- and down-scans of HR 4049 and IRAS 13416-6243 disagree around the peak. Nevertheless, these sources can be clearly classified as $B_{3.3}$. The 3.3 μm feature of Elias 1 is similar to that of HD 44179 (class $B_{3.3}$, Van Kerckhoven 2002). Also HD 179218 is probably of class $B_{3.3}$, i.e. its 3.3 μm feature agrees much better with the class $B_{3.3}$ profile than with class $A_{3.3}$ (Van Kerckhoven 2002).

Tokunaga et al. (1991) also recognised two types of 3.3 μm features. The profile, peak position and width of their type 1 agree well with class $A_{3.3}$, defined here. Their type 2, based on spectra of HD 44179, Elias 1 and WL 16, has a similar peak wavelength compared to our classes $B_{3.3}$, but is much narrower, with a FWHM of ∼0.020 μm. These conclusions were based on spectra taken with a $2.7''$ aperture. Kerr et al. (1999) showed, in a detailed spatial study of HD 44179, that the 3.3 μm profile width clearly varies with distance from the central source, and at one positions, even has a FWHM of ∼0.041 μm. The 3.3 μm profile of HD 44179 in our sample is a combined spectrum of all these profiles, due to the large beam of the SWS spectrograph ($14''$x$20''$), thereby explaining its large FWHM compared to the profile found by Tokunaga et al. (1991).

4.3.2 The 11.2 μm feature

All sources in the sample of Peeters et al. (Chapter 3) exhibit emission at 11.2 μm. However, in several sources, this emission is too weak and/or too noisy to be able to study the 11.2 μm profile in detail. In addition, HD 100546 exhibits crystalline silicates (Malfait et al. 1998) and hence the 11.2 μm emission band is a combination of PAH emission and crystalline silicate emission. Therefore, these sources are excluded from our profile study. As a consequence, the 11.2 μm band profile is not studied for the class C_{6-9} sources. In addition, only 5 sources of class B_{6-9} are included in this sample (Table 4.1).

All 43 sources in this reduced sample show a pronounced 11.2 μm feature, sometimes preceded by a weak feature at about 11.0 μm. The emission profiles of the 11.2 μm feature

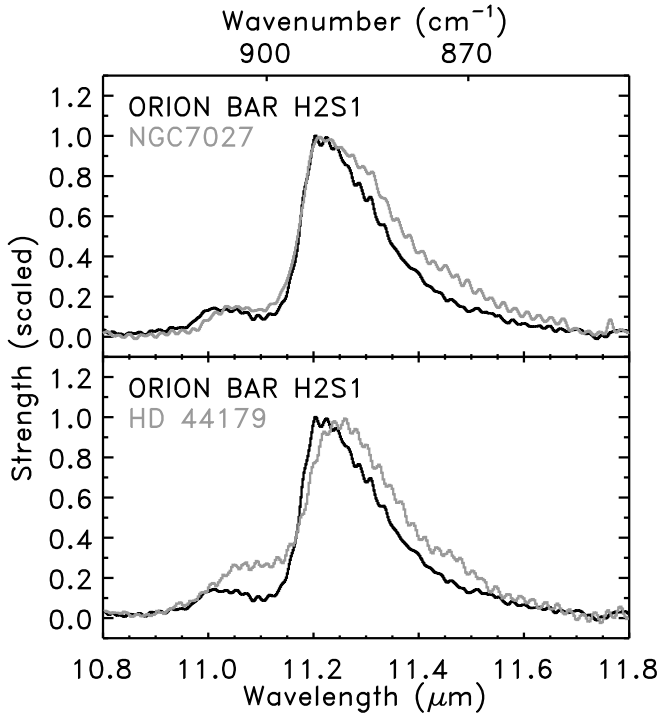

Figure 4.3 — Some examples of the 11.2 μm feature. The spectra are scaled so that the peak intensity equals 1. The top-panel shows the class $A_{11.2}$ feature, represented by the Orion Bar and the class $A(B)_{11.2}$ feature, represented by NGC 7027. The difference between class $A_{11.2}$ and $B_{11.2}$ (HD 44179) is illustrated in the bottom panel.

are distinctly asymmetric with a steep blue rise and a red tail. Although the profile of the 11.2 μm feature is similar for all the sources (Fig. 4.3, top panel), when examined in detail small differences become apparent (Fig. 4.3, bottom panel). A definite range in peak positions and in the strength of the red tail relative to the peak strength (denoted as tail-to-top ratio) is present in our sample. Perusing the derived profiles, we recognise 2 main classes, which we will designate by $A_{11.2}$ and $B_{11.2}$ (Table 4.2, Fig. 4.3). First, the majority of the 11.2 μm bands peak between 11.20 and 11.24 μm, show a very steep blue rise, and have low tail-to-top ratio (Fig. 4.3, top panel). This group will be referred to as class $A_{11.2}$. Within this class, the peak position and the top of the profiles vary slightly. Class $B_{11.2}$ represent sources with a peak position of $\sim$11.25 μm, a less steep blue rise (compared to class $A_{11.2}$) and a high tail-to-top ratio (Fig. 4.3, bottom panel). A few sources (class $A(B)_{11.2}$) clearly belong to class $A_{11.2}$ in term of peak position and steepness of the blue wing, but have a tail-to-top ratio similar to class $B_{11.2}$ (Fig. 4.3, top panel).

4.3.3 Feature profile correlations

Comparing the 3.3, 11.2 and 6–9 μm classifications in Table 4.1, we recognise a correlation between them. In general, an A classification in 6–9 μm region also implies an $A_{3.3}$ and

$A_{11.2}$. However, this does not seem true for the B and C classifications; $B_{3.3}$ and $B_{11.2}$ do not necessarily correlate with each other or with B_{6-9} or C_{6-9}.

To illustrate the observed variations in the class B profiles, a few examples can be given. HD 44179 and HR 4049 have class B profiles, considering all features. BD+30 3639, however, has 6–9 μm features of class B and 3.3 and 11.2 μm features of class A. Other sources, as IRAS 17047-5650 and He 2-113, have 3.3 μm features of class $A_{3.3}$, but class B for the longer wavelength features. Of the two sources of class C_{6-9}, one (IRAS 13416-6243) has a 3.3 μm feature of class class $A_{3.3}$ and the other (CRL 2688) of class $B_{3.3}$. In contrast, within the 6–9 μm range, spectral class $B_{7.7}$ also (almost) invariably implies $B_{6.2}$ and vice versa. The 11.2 μm classes follow in this respect much more the 6–9 μm than the 3.3 μm behaviour.

Perusing the spectra, it is striking that the variations in the 6–9 μm region are much more pronounced than those of the 3.3 or 11.2 μm features (cf., Fig 4.4; Table 4.2). Specifically the peak position in wavenumber space varies by about 26, 51 and 11 cm^{-1} for the 6.2, 7.7 and 8.6 μm features, respectively, and only by about 6.5 and 4.0 cm^{-1} for the features at 3.3 and 11.2 μm, respectively.

From an astronomical point of view, correlations between the classes and the different object types are found. Almost all H II regions, non-isolated Herbig AeBe stars and YSO's in our sample are in the class A, considering all features. An interesting exception is the Orion Bar position D2, showing a $B1_{3.3}$ feature and class A 6–12 μm features. The galaxies in our sample are in the class A, considering all features, except for the 11.2 μm feature, which is of class $A(B)_{11.2}$ or $B_{11.2}$. Most PNe have 6–9 μm features of class B_{6-9}, a 3.3 μm feature of class $A_{3.3}$ and a 11.2 μm feature of class $B_{11.2}$ or $A(B)_{11.2}$. The PN Hb5 is of class A_{6-9} and has a 3.3 μm feature of class $A_{3.3}$, and a 11.2 μm feature of class $B_{11.2}$. The Post-AGB stars in our sample are spread over the classes. IRAS 16279-4757 is in class A considering all features. IRAS 21282+5050 is of class A_{6-9} and has a 3.3 μm feature of class $A_{3.3}$, and a 11.2 μm feature of class $A(B)_{11.2}$. The two extreme metal poor binary system Post-AGB stars, HD 44179 and HR 4049, are in class B considering all features. The same is true for the isolated Herbig AeBe star HD 179218, although its 11.2 μm feature is too weak/noisy to be classified. Thus, in conclusion, the correlation between spectral class and object is much tighter in the 6–9 μm region than in the 3.3 and 11.2 μm regions.

We also checked for correlations between the different classes of the 3.3 and 11.2 μm features and the local radiation field G_0. For both features individually, the range in G_0 of the sample sources classified as class A straddles that of class B sources and $A(B)_{11.2}$ sources.

To summarise, considering the correlation between the spectral classes and object type, the 3–12 μm PAH spectrum apparently reflects local physical conditions or the accumulated effect of processing from the formation sites in the AGB or post-AGB phases to the ISM or the influence of disk chemistry (Peeters et al., Chapter 3). This correlation reflection is more apparent in the 6–9 μm region than in the 3.3 and 11.2 μm regions. The variations in the local physical conditions are found to cause larger variations in profiles of the features in the 6–9 μm region than in those of the 3.3 and 11.2 μm features. Furthermore, the 3.3 μm feature is very invariant under highly variant physical conditions.

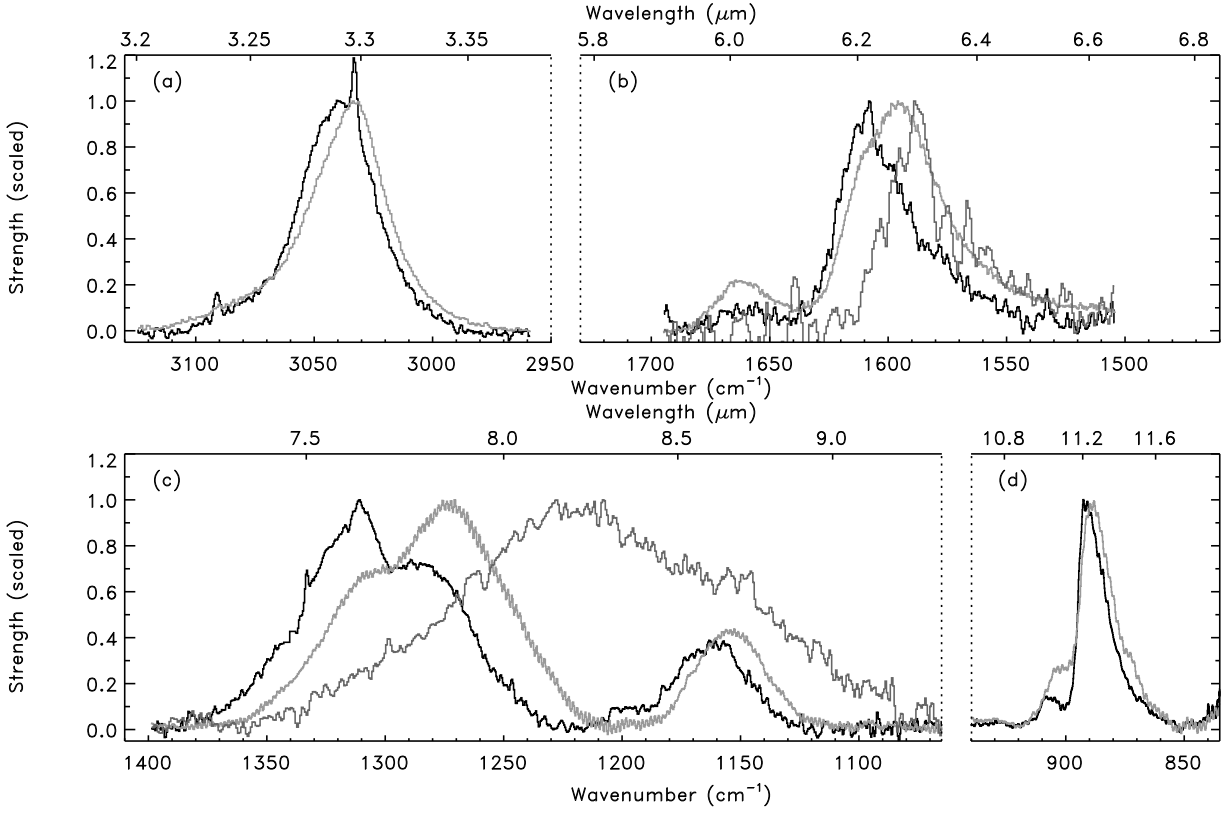

Figure 4.4 — An overview of the observed variations in the profiles of the 3–12 μm PAH features. The spectra in each panel are scaled independently so that the peak intensity equals 1. For all features, class A peaks at the shortest wavelengths (black line), and class B peaks at longer wavelength. In the 6–9 μm region, another class (C) is defined peaking at even longer wavelength and having a deviating spectral appearance (see Sect. 4.1 and Chapter 3 for details). Class A is represented by the IRAS 23133 in the 6–9 μm region and by the Orion Bar for the 3.3 and 11.2 μm features. HD 44179 represents class B and IRAS 13416 represents class C. Note that a H recombination line (Pfδ at 3.296 μm) is present in the spectrum of the Orion Bar.

4.4 The infrared emission features and PAHs

The 3.3 and 11.2 μm bands arise from the radiative relaxation of CH stretching and CH out-of-plane bending vibrations of highly excited polycyclic aromatic hydrocarbons. This is in contrast with the nature of the 6.2 and 7.7 PAH features which originate from vibrations mainly involving CC stretching motions. Thus, while one would expect strong global correlations amongst all of the bands that arise from the same family of molecules, when comparing the behaviour of bands involving CH modes with those involving CC modes, subtle important differences are expected. These differences reflect not only differences in local conditions, but also structural differences within the emitting family itself, and – in the case of the 3.3 μm band emission – distinct differences in the subset of the emitting PAH population.

4.4.1 The CH stretching mode and the 3.3 μm band

The interstellar 3.3 μm band has been assigned to the PAH C-H stretching mode since it correlates with the presence of the other PAH emission features and falls squarely in the wavelength range canonically attributed to aromatic C-H stretches (3100–3000 cm^{-1} (3.23–3.33 μm), Silverstein & Bassler, 1967; "near 3030 cm^{-1} (3.3 μm)", Bellamy, 1958). As with all fundamental vibrational frequencies, the precise position depends on many factors including molecular size, charge state, structure, molecular heterogeneity, and so on. The vast majority of the data available to address each of these has been measured in *absorption*. In the astrophysical case, where PAH emission spectra are measured in emission and not absorption, the level of molecular excitation also effects peak position and profile. Each of these factors which influence fundamental band position will now be discussed.

Before focusing on the individual properties which influence the intrinsic positions and profiles of the absorption bands, it is important to place this all in the context of the emission process, keeping in mind that the interstellar spectrum arises from the combined emission of a complex *mixture* of PAHs. In emission, each *individual* line should have an approximately 30 cm^{-1} FWHM, consistent with the natural linewidth expected from each emitting molecule (Allamandola et al. 1989b). This natural linewidth arises from intra-molecular vibrational energy redistribution, not the blending of individual rotational lines in the emitting molecules which remain *rotationally* cool throughout the excitation/emission process (e.g. Brenner & Barker 1992; Williams & Leone 1995; Cook & Saykally 1998). Due to the high internal energy content of the emitting molecules, a 10 to 20 cm^{-1} redshift is intrinsic to this emission process (Flickinger et al. 1991; Brenner & Barker 1992; Colangeli et al. 1992; Williams & Leone 1995; Joblin et al. 1995; Cook et al. 1998).

PAH size is particularly important in the case of the interstellar 3.3 μm band since this feature originates from the smallest members of the emitting PAH population (Allamandola et al. 1989b; Schutte et al. 1993). PAHs containing between roughly 25 to 70 carbon atoms contribute most of the emission in this feature, with the dominant species between $N_C \sim 25$ to 50. This is in contrast to the situation for the longer wavelength emission features which arise from increasingly larger, and overlapping members of the interstellar PAH population. Mattioda et al. (2003, in preparation) have carried out a spectroscopic study of 10 different isolated PAHs with N_C between 36 and 50 in their neutral as well as positively and negatively charged states. The molecules in this study contain a variety of edge structures. The mean position of the all the C-H stretching bands in this sample can be grouped by charge. These are 3084 cm^{-1}, 3102 cm^{-1} and 3062 cm^{-1} (3.24 μm, 3.22 μm, and 3.27 μm) for the neu-

tral, cationic, and anionic forms respectively. Variations are also found within an individual charge state, variations which arise from the differences in size and molecular structures. For the neutrals, the mean position ranges between 3071 and 3095 cm^{-1} (3.256 and 3.231 μm), for the cations they fall between 3089 and 3113 cm^{-1} (3.237 and 3.212 μm), and for the anions they span from 3047 to 3088 cm^{-1} (3.282 and 3.238 μm). The breadth and small variance of the interstellar 3.3 μm emission band likely arises because the CH stretching position (in absorption) for the vast majority of PAHs of a single charge class range over 25 to 30 cm^{-1}. With the 10 to 20 cm^{-1} redshift inherent in emission, the observed range and position can be used to place constraints on the PAHs responsible for the 3.3 μm band.

PAH edge structure is also important. As this becomes more complex, the local environment of the different C-H bonds in the same molecule sample can vary sufficiently and influences the individual stretching frequencies. Thus, for a large molecule with long straight edges, there is little interaction between the stretching motions of CH groups on adjacent rings and the FWHM of the dominant peak in the region is 18 cm^{-1} (0.019 μm at 3.3 μm). On the other hand, if a similarly large molecule that has jagged edges with many "notches" and "bay regions", CH groups on opposing sides of these gaps interact perturbing their stretching motions. As a result, the FWHM of the CH stretching feature in such a species is substantially broadened and may be as wide as 70 cm^{-1} (0.074 μm) or more (Mattioda et al. 2003, in preparation).

Regarding hetero-atom substitution, Mattioda et al. (2003, in preparation) have investigated the spectra of 11 nitrogen-substituted PAHs, spanning the N_C range from 9 to 21 and found that nitrogen substitution does not influence the CH stretching band frequency.

Analysis of the interstellar 3.3 μm feature with this information provides important new insight into the nature of the smallest members of the interstellar PAH population. The strongest conclusion concerns charge state of the emitting species. Taking into account the 10 to 20 cm^{-1} redshift inherent in the emission process, and the frequency ranges for neutral, cationic and anionic PAHs listed above, cations can be ruled out as significant contributors to the 3.3 μm band. Based on position alone, neutral and negatively charged PAHs can only contribute. This is in contrast to the emission at longer wavelengths (6-10 μm) where intensity arguments have shown that emission at these wavelengths is dominated by positively charged PAHs.

4.4.2 The CH out-of-plane bending modes

Chemists have long recognised the diagnostic value of the aromatic CH out-of-plane bending features in the 11 to 15 μm spectral region for the classification of the aromatic ring edge structures present in a particular sample (Bellamy 1958). Specifically, the positions and intensities of the bands in this spectral region reflect the type and number of adjacent CH groups on the peripheral rings of the PAH structure (Bellamy 1958; Allamandola et al. 1985; Cohen et al. 1985; Léger et al. 1989; Roche et al. 1989; Witteborn et al. 1989; Allamandola et al. 1999b; Hudgins & Allamandola 1999a). Traditionally, aromatic rings carrying CH groups which have no neighbouring CH groups (termed "non-adjacent" or "solo" CH groups) show IR activity between 11.1 and 11.6 μm. Likewise, activity between 11.6 and 12.5 μm is indicative of two adjacent CH groups ("duet" CH's) on the periphery of the PAH. Three adjacent CH groups ("trio" CH's) are indicated by activity in the 12.4 to 13.3 μm region, and four adjacent CH groups ("quartet" CH's) by activity between 13 and 13.6 μm. Five adjacent CH groups ("quintuply-adjacent" or quintet CH's) are indicated by features falling

in the 13 to 13.7 μm range. The availability of a database of astrophysically-relevant PAH infrared spectra exploring a wide range of structures, sizes and ionisation states has now permitted us to deepen our understanding of this region of the spectrum (Hudgins & Allamandola 1999a; Hony et al. 2001). Our current understanding is illustrated below in Fig. 4.5 which schematically compares the average interstellar emission spectrum with the wavelength regions associated with different CH adjacency classes for neutral and ionised, isolated PAHs. Inspection of this Figure shows that, while the ranges for matrix-isolated neutral PAHs do not differ substantially from those reported in the literature, ionisation produces some notable changes in region boundaries. Regarding the ISO SWS observations of the dominant 11.2 μm interstellar band, and taking into account the roughly 0.1 μm red-shift in the peak wavelength of PAH bands in emission relative to their position in absorption, we can draw the following conclusions:

- The weak interstellar emission band sometimes observed on the short wavelength side of the dominant 11.2 μm band and peaking near 11.0 μm falls in the region attributable to the solo-CH modes of PAH cations.

- The peak of the 11.2 μm interstellar band falls squarely within the region for the solo-CH modes of *neutral* PAHs and at the extreme long wavelength end of the range for solo cationic modes.

- The variable red wing of the interstellar 11.2 μm band likely carries a contribution from the duet-CH modes of PAH cations, particularly those with condensed structures whose features tend to fall near the lower extreme of the characteristic region shown in Fig. 4.5 (Hudgins & Allamandola 1999a).

4.4.3 The CC stretching modes

The CC stretching modes occur in the 6–9 μm range. Within this range, the band at the longer wavelengths (6.5–9 μm) have a mixed CC stretch and CH in-plane-bending vibration character. All CC modes bands are very weak relative to the CH modes in neutrals, but become the dominant bands in ions (Szczepanski & Vala 1993b; Langhoff 1996; Hudgins & Allamandola 1999a; Kim et al. 2001). Hence, we will focus here on the CC modes in cations. The peak position of the pure CC stretch is influenced by molecular size, structure, and molecular heterogeneity (see e.g. Chapter 3). Extensive laboratory and theoretical quantum mechanical studies have shown that a peak as blue as 6.2 μm does not occur for pure-C PAH cations in the (interstellar) size range 20-100 C-atoms. Substitution of N in the ring induces strong IR activity of the CC modes at the highest frequencies within this range and bands around 6.2 μm do become intense. This is the result of the localisation of the charge on the N in the ring. While there is presently no corroborating experimental or theoretical evidence, a similar behaviour may occur for large PAHs with uneven and irregular edge structures, PAH clusters and/or PAH complexes with metals. For the longer wavelength modes, both pure-C PAH cations as well as N-substituted PAH cations can show prominent bands near the interstellar 7.6 μm position. The 7.8 μm band is more enigmatic, however, and no good match with laboratory species exists.

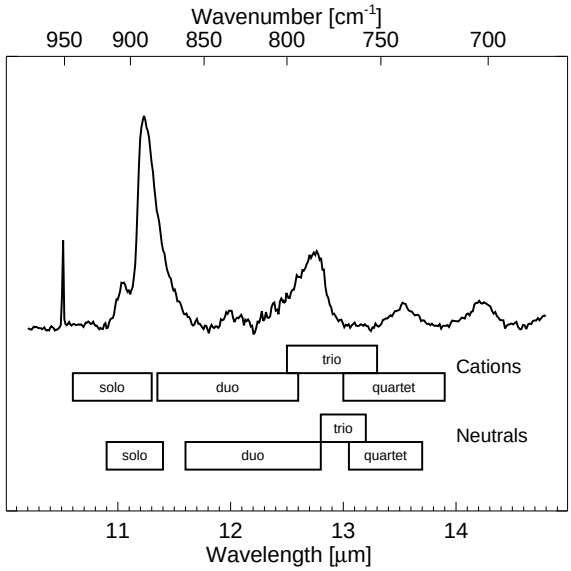

Figure 4.5 — A comparison of the average interstellar spectrum (top) with the ranges characteristic of the out-of-plane bending modes of neutral and cationic PAHs (bottom). Details of the average interstellar spectrum are given in Hony et al. (2001). The boxes indicate the wavelength regions associated with the out-of-plane bending vibrations of the various adjacency classes of the peripheral CH groups as determined from matrix isolation spectroscopy. Figure adapted from Hony et al. (2001).

4.5 Discussion

As discussed in Sect. 4.4, the detailed peak positions and profiles of emission bands due to PAHs are affected by the charge, the size, the emitting subset of the PAH family and the molecular structure of the family of PAHs present in the source. In addition, these spectral characteristics also depend somewhat on the excitation of the molecule (Barker et al. 1987; Joblin et al. 1995; Pech et al. 2001). Due to the many parameters involved, the interpretation of the variations in the profiles is a complex problem and further laboratory and theoretical studies are required to unambiguously identify the underlying causes for these variations. However, any explanation of the observed variations should explain the main observational conclusions of this paper: the observed variation in the 3.3 and 11.2 μm features and the observed large contrast in the spectral variations for the CH modes versus the CC modes.

4.5.1 The variations in the CH emission features

Anharmonicity

The profiles of the 6.2 and 11.2 μm bands are fairly asymmetric with a steep blue rise and a pronounced red wing (cf., Fig. 4.4, Witteborn et al. 1989; Roche et al. 1996, Chapter 3). This behaviour is very characteristic for anharmonic broadening in highly vibrationally excited molecules (Barker et al. 1987; Verstraete et al. 2001; Pech et al. 2001). Due to cross-coupling between different modes, the peak position of an IR band will shift towards lower frequencies. Integration over the energy cascade, leads then in a natural way to a red shaded profile.

The red wing can be further enhanced due to emission from vibrationally excited levels (eg., vibrational hot bands, $v = 2 \rightarrow 1$) which are generally shifted towards the red due to the anharmonicity of the vibrational potential of the mode. These anharmonicities can be quite different for different modes. Anharmonicity parameters for a few small PAHs have been estimated from laboratory studies on the temperature dependence of the peak wavelength and width of the absorption bands (Joblin et al. 1995) and from the difference between low temperature absorption measurements and infrared multi-photon dissociation studies of trapped PAH ions (Oomens et al. 2002, in preparation).

Models are very successful in explaining the general characteristics of the observed profiles of the interstellar 6.2 and 11.2 μm bands: the steeper blue rise and the pronounced red tail (Pech et al. 2001). However, these models cannot explain the large shift observed in the 6.2 μm band between classes A, B, and C. That still has to reflect a chemical/structural modification of the emitting PAHs, for example due to the incorporation of N (Peeters et al., Chapter 3). In their study of the 11.2 μm band, Pech et al. (2001) focused on the observations of the PN, IRAS 21282+5050, a class $A(B)_{11.2}$ profile. Perusing their calculated profiles, we notice that an increase in excitation – either through a decreased size or an increase in internal energy – does increase the strength of the red wing but does not shift the peak position or change the blue rise. Thus, the profile of the mixed class, $A(B)_{11.2}$, (cf., Table 4.2) can be interpreted as a change in the excitation in the same population of PAHs. In contrast, the variation in profiles between classes $A_{11.2}$ and $B_{11.2}$ is not readily explained within the anharmonicity model; e.g., excitation variation leads to imperceptible redshifts and do not affect the blue rise. So, differences between classes $A_{11.2}$ and $B_{11.2}$ must reflect variations in the composition or molecular structure of the emitting PAH family. The profiles of the 3.3 μm feature show more deviations with the calculated profiles of Pech et al. (2001) and Verstraete et al. (2001), in particular in the peak position and the red wing. Perusing the calculated profiles of the 3.3 μm feature by Pech et al. (2001), we notice that an increase in excitation – either through a decreased size or an increase in internal energy – shifts the peak position towards the red and simultaneously increases the FHWM. Our class $B_{3.3}$ profiles peak at longer wavelengths but have smaller FWHM compared to class $A_{3.3}$ profiles. Thus, the variation in profiles between classes $A_{3.3}$ and $B_{3.3}$ can not be due to anharmonicity.

Molecular edge structure

The 3.3 μm feature If we assume that the FWHM of the 3.3 μm feature is mainly influenced by the molecular edge structure, the observed variation in FWHM (and hence in class) implies that the PAH family present in three sources in our sample (i.e. HD 44179, MWC 922, HR 4049) are dominated by more compact PAH molecules compared to the PAH family present in all other sources in our sample (Sect. 4.4.1 and Table 4.2). Based on the relative strengths of the CH out-of-plane bending modes, the molecular structure of the PAH molecules can be deduced (Hony et al. 2001). Let's consider the following sources : HD 44179 belonging to $B_{3.3}$ and $B_{11.2}$; NGC 7027, member of $A_{3.3}$ and $B_{11.2}$ and the IRAS 18317 representing classes $A_{3.3}$ and $A_{11.2}$. Hony et al. (2001) found that NGC 7027 is dominated by large, compact PAHs with straight edges and IRAS 18317 by smaller or irregular PAHs. Although these two sources represent the extremes in the observed intensity ratio in their sample and hence the extremes in molecular structure, they both belong to $A_{3.3}$. In addition, the relative strengths of the CH out-of-plane bending modes of HD 44179 are comparable to NGC 7027 and hence their molecular structure is similar (Hony et al. 2001).

However, their 3.3 μm features belong to different classes. Therefore, we can conclude that the molecular edge structure is not the main cause of the variation in the FWHM of the 3.3 μm feature.

The 11.2 μm feature The invariance of the CH out-of-plane bending modes may be an inherent property of interstellar PAHs. Within the subset of PAHs studied in the laboratory or quantum chemically, the peak position of the solo modes in neutral PAHs falls very closely to the observed interstellar peak position of 11.2 μm. Now, possibly, any molecular structure variations, which lead to shifts in the 6–9 μm CC bands, may be inherently accompanied by modification of the CH peripheral structure which turn CH solo's into duo's or trio's.

The 11.2 μm feature correlates well with the 3.3 μm band and hence may trace the emission by neutral PAHs. However, duet CH's of compact PAH cations may contribute to the red wing of the 11.2 μm band (Sect. 4.4.1 Hudgins & Allamandola 1999a; Hony et al. 2001). Hence, it is possible that the observed variation in the 11.2 μm band reflects variation in the contribution of these cationic duet modes. This would imply that B and A(B) objects have more compact PAH cations. Indeed, the analysis of the pattern of emission features in the CH out-of-plane bending modes region (i.e. 10–15 μm) strongly supports this conclusion.

PAH family and the survival of the fittest

The variation in peak position of the CH modes is likely due to the presence of a family of PAH molecules each emitting at a similar but slightly different frequency. The variation in the peak position of the 3.3 and 11.2 μm band, measured in the laboratory or quantum-chemically calculated, is much larger (0.02 μm; 20 cm^{-1} and 0.3 μm; 20 cm^{-1} respectively) than observed in space ($\sim$ 0.007 μm; 6 cm^{-1} and $\sim$ 0.05 μm; 4 cm^{-1} respectively). It is clear that only a small subset of the PAHs studied by these means is present in space. The physical/chemical characteristics of this subset are presently unclear but may well prove important in identifying the PAHs present in space and the processes that regulate their interstellar abundances.

The local radiation field

Tokunaga et al. (1991) noted that the central stars of the few sources known to show a 3.3 μm feature deviating from the class $A_{3.3}$ profile, all had relatively low effective temperatures ($\sim 10^4$ K), suggesting a correlation between stellar effective temperature and PAH feature profiles. However, some objects in our sample, IRAS 03260+3111 for example, have relatively low effective stellar temperatures (Hony et al. 2001), but show $A_{3.3}$ class profiles. Furthermore, within HD 44179 classifications of the 3.3 μm feature change from class $B_{3.3}$ to class $A_{3.3}$ (Kerr et al. 1999). Also in our sample, similar behaviour is seen in the Orion Bar, of which position D2 shows a $B1_{3.3}$ feature, while at the other positions the 3.3 μm features are of class $A_{3.3}$. For these reasons, the lower effective temperatures cannot be the main cause for variation in the 3.3 μm feature. Similar conclusions have been drawn for the longer wavelength features by Van Kerckhoven (2002) and Peeters et al. (Chapter 3).

Since variations are seen within objects (cf. HD 44179 and the Orion Bar), it may be that the local radiation field, G_0, influences the profiles of the feature. However, no link between G_0 and the different classes of the 3.3 and 11.2 μm features is found. Analogously, Peeters

et al. (Chapter 3) found no relation between G_0 and the 6–9 μm PAH emission features. Hence, we can conclude that the observed variation in the main PAH emission features are not directly related with G_0.

To summarise, the variation in peak position is likely due to the presence of a mixture of PAH molecules. Both anharmonicity and molecular structure can explain variation in the FWHM of the 11.2 μm feature but can not explain the difference in peak position. In contrast, the variation in the FWHM of the 3.3 μm feature remains an enigma.

4.5.2 The CH modes versus the CC modes

Perusing the spectra, it is striking that the variations in the 6–9 μm region are much more pronounced than those of the 3.3 or 11.2 μm features (cf., Fig 4.4; Table 4.2). Specifically the peak position in wavenumber space varies by about 26, 51 and 11 cm^{-1} for the 6.2, 7.7 and 8.6 μm features, respectively, and only by about 6.5 and 4.0 cm^{-1} for the features at 3.3 and 11.2 μm, respectively. The 6.2 and 7.7 μm features have an exclusive or large CC stretching character, while the 3.3 and 11.2 μm features are assigned to CH modes. The 8.6 μm feature is due to a combination of CC and CH modes (Allamandola et al. 1989b). This implies that variations in the features assigned to CC modes are significantly larger than those assigned to CH modes.

Charge state

Experimentally and quantum chemically, it is well established that the 6–9 μm CC modes are dominated by cations while the 3.3 μm CH stretching mode is due to neutrals (Szczepanski & Vala 1993b; Langhoff 1996; Hudgins & Allamandola 1999a; Kim et al. 2001, Mattioda et al. 2003, in preparation). There is some observational support that this dichotomy between the CC and CH stretching modes, also extends to the 11.2 μm CH out-of-plane bending mode. Specifically, the strength of the astronomical 11.2 μm mode correlates well with the 3.3 μm CH stretching band and not with the 6.2 μm CC stretching band. This may be taken to imply that the interstellar 11.2 μm band also predominantly originates in neutral carriers (Hony et al. 2001). This is corroborated to some extent by models of the infrared emission of PAHs in the ISM which show that the out-of-plane bending modes have a large neutral component (Bakes et al. 2001). Within this framework, the difference in spectral variations between CH and CC modes may then merely reflect that they probe different parts of the interstellar PAH population. For example, the chemical modification process might be mainly operative on cations and not on neutrals. In that respect, because ionisation and neutralisation of interstellar PAHs occurs on a very rapid timescale, this would imply a similar fast chemical exchange. It is unlikely that this is connected to the incorporation of N in the PAH rings. However, PAH clusters or PAH-metal complexes may be formed and broken on a similar timescale (Van Kerckhoven 2002).

Size

The invariance of the 3.3 μm feature with respect to the CC modes and even to the CH out-of-plane bending modes is likely also related to distinct subsets of emitting PAH molecules. Indeed, the 3.3 μm feature originates from the smallest members of the emitting PAH population while the PAH features in the 6–12 μm region originates from somewhat larger PAHs

in the population. Similar as with PAH charge, the chemical modification process is mainly operative on larger PAH molecules. This would indicate that photo-chemistry is not the driving force behind the observed spectral variation since smaller PAHs will be much more susceptible to unimolecular dissociation following photon absorption.

CH out-of-plane bending modes

As mentioned already, any molecular structure variations, which lead to shifts in the 6–9 μm CC bands, may be inherently accompanied by modification of the CH peripheral structure which turn CH solo's into duo's or trio's.

Substituted/complexed PAHs

Substitution of nitrogen in the ring induces strong IR activity of the CC modes at the highest frequencies within this range and bands around 6.2 μm do become intense. However, it does not influence the peak position of the CH modes while the peak positions of the 7.7 μm complex are influenced but not in a systematic way. Therefore, nitrogen substitution might cause variations in the 6.2 μm feature but does not influence the other features. Complexes of PAHs with each other or with metal atoms might also cause the spectral variation in the 6–9 μm range. However, the influence of complexity on the CH modes still has to be investigated in the laboratory.

To summarise, several parameters can cause the difference in the amount of variation between the CH and CC modes, i.e. the charge state, the size, the CH out-of-plane bending modes and substituted/complexed PAHs. Further laboratory studies are required to determine which of these parameters(s) controls the spectral characteristics of PAHs in space.

4.6 Conclusions

We have studied the profiles of the 3.3 and 11.2 μm PAH features of a wide variety of sources and found that clear variations are present. Both features shift in peak position and show different profiles from source to source. Comparing the 3.3, 6–9 and 11.2 μm classifications, we recognise a correlation between them. In general, and A classification in 6–9 μm region also implies an $A_{3.3}$ and $A_{11.2}$. However, this seems not true for the B and C classifications; $B_{3.3}$ and $B_{11.2}$ do not necessarily correlate with each other or with B_{6-9} or C_{6-9}. In addition, these variations depend on the type of object considered and apparently reflect local physical conditions or the accumulated effect of processing from the formation sites in the AGB or post-AGB phases to the ISM. However, the most striking aspect of the features in the 3–12 μm regions is the pronounced contrast in the profile variations between the CH modes and the CC modes. Specifically, the peak position in wavenumber space varies by about 26, 51 and 11 cm^{-1} for the 6.2, 7.7 and 8.6 μm features, respectively, and only by about 6.5 and 4.0 cm^{-1} for the features at 3.3 and 11.2 μm, respectively.

We summarise existing laboratory data and theoretical calculations of the modes emitting in the 3–12 μm region of PAH molecules. We attribute the variations in peak position of the 3.3 and 11.2 μm feature to the presence of a mixture of PAH molecules. The variations in FWHM of the 3.3 μm feature remains an enigma while those of the 11.2 μm can be explained by anharmonicity and molecular structure. The possible origin of the observed contrast in profile variations between the CH modes and the CC modes is highlighted.

5

The Infrared Emission Features in the spectrum of WR 48a

Appeared as :

J.E. Chiar, E. Peeters, A.G.G.M. Tielens
Astrophysical Journal Letters, 2002, 579

Abstract We present the first detection of unidentified infrared (UIR) emission features at ~ 6.4 and 7.9 μm in the spectrum of the dusty WC8 Wolf-Rayet star WR 48a. Based on the H-deficient nature of WC-stars, we attribute the emission features to large carbonaceous molecules or amorphous carbon dust grains in the circumstellar environment of WR 48a. The 6.4 μm feature resembles the emission feature seen toward H-deficient PNe, while the 7.9 μm profile resembles that of some planetary nebulae with H-deficient WC10 central stars. These similarities point towards a similar origin of the dust in these H-deficient environments, and highlights the apparent sensitivity of the UIR bands to physical conditions. In the case of WR 48a and the [WC10]-PNe, shock processing may play a major role in dust formation.

5.1 Introduction

Infrared (IR) spectroscopy is a powerful tool for the study of the evolutionary link between interstellar and circumstellar polycyclic aromatic hydrocarbons (PAHs) and carbon dust. Dust and PAH composition is likely to reflect variations in chemical and physical conditions and history in different astrophysical environments. An inventory of PAH emission regions and their spectral characteristics has been carried out by Hony et al. (2001) and in Chapters 3 and 4. These authors find a correlation between the profiles of the PAH IR emission features and the astrophysical environment.

Despite their harsh environment - fast stellar winds and high stellar effective temperatures - some WC-type Wolf-Rayet stars are known to produce copious amounts of carbon dust in their winds. Wolf-Rayet stars represent one of the final stages of stellar evolution for massive stars. In general, they are thought to follow an evolutionary sequence divided into three phases WN - WC - WO, corresponding to the prevalence of different emission lines in their spectra (see van der Hucht 2001, for a review). Late-type WC stars are now known to be surrounded by heated circumstellar dust (Williams et al. 1987), although the process by which this dust forms and survives in the harsh WC-star environment is not well-understood (Cherchneff et al. 2000). The dust-producing WC stars have been divided into subtypes depending on the regularity of their dust formation. Of the five WC stars with the densest dust shells studied by van der Hucht et al. (1996), three (WR 104, WR 112, WR 118) are classified as persistent dust makers, one (WR 98a) is classified as having variable dust formation, and one (WR 48a) exhibits episodic dust formation (Williams 1999). In general, dust formation appears to be the effect of colliding winds in WC+OB binary systems (e.g., Williams 1997; van der Hucht 2001, and references therein).

The ISO/SWS spectra of a sample of WC stars have recently been analysed by Chiar & Tielens (2001). They identified an absorption feature at 6.2 μm with large (1 μm), circumstellar, amorphous carbon dust grains. In spite of the difficulty of condensing large grains in the harsh WC-star environment, subsequent studies (of WR 112 and WR 118) also suggest the presence of large grains in the dust shells of these stars (Marchenko et al. 2002; Yudin et al. 2001). Here, we present the IR spectrum of WR 48a which shows emission features at ~ 6.4 and 7.9 μm similar to the well-known UIR bands seen throughout the cosmos.

5.2 Observations and data reduction

We present the 2.5–30 μm spectrum of WR 48a obtained with the Short-Wavelength Spectrometer (SWS) on the Infrared Space Observatory (ISO). Astronomical Observing Template (AOT) 01 speed 2 (TDT 07902703, $R \sim 270 - 700$) data are presented in the range 2.5–30 μm, excepting wavelengths 5.48–7.62, 7.98–8.88 μm where AOT 06 (TDT 60701201, $R \sim 900 - 2400$) data were available. All data presented here were reduced using the Interactive Analysis (IA^3) tool at the University of Groningen with pipeline version (OLP) 10.1 which uses the latest responsivity corrections. Standard data reduction techniques were used to correct for memory effects, subtract dark current, and calibrate for the responsivity of the detectors. The spectra from the individual detectors are flat-fielded (normalised), points lying $\sim 3\sigma$ above the norm are clipped, then the result is rebinned to a constant resolution appropriate for each band. This is done for each of the 12 bands. A final spectrum (Fig. 5.1) is created by shifting adjoining bands using a multiplicative factor within the known flux uncertainties for each band.

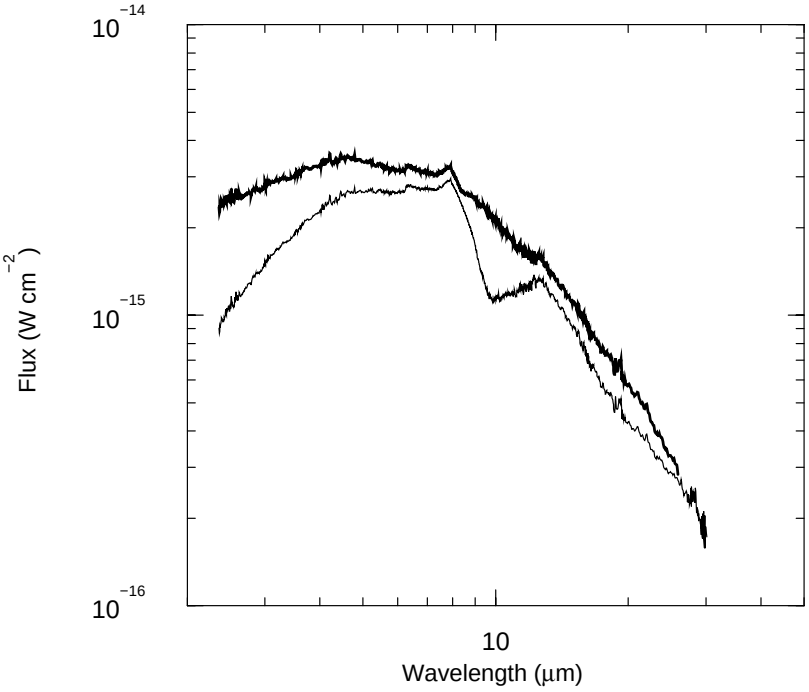

Figure 5.1 — ISO-SWS spectrum of WR 48a from 2.3–40 μm. Interstellar silicate absorption is present at 9.7 and 18 μm (thin line). The spectrum of WR 48a corrected for silicate absorption by applying an interstellar extinction curve (heavy line).

5.3 Analysis

The infrared spectrum of WR 48a shows clear emission features at ~ 6.4 and 7.9 μm, and silicate absorption features at 9.7 and 18 μm. The latter two features are likely due to interstellar absorption (Roche & Aitken 1984; van der Hucht et al. 1985). In order to analyse the profiles of the emission features, the continuum had to be defined, most notably by correcting for silicate absorption. Chiar & Tielens (in preparation) analyse the 9.7 and 18 μm interstellar silicate absorption features toward several heavily extincted WR stars. They use the silicate spectrum of WR 98a along with the general interstellar extinction curve deduced by Martin & Whittet (1990) to construct a new interstellar extinction curve from 1–25 μm. This extinction curve is applied to the WR 48a spectrum to "correct" for silicate absorption in its spectrum, leaving behind emission features at ~ 6.4 and 7.9 μm (Fig. 5.1). We then fit and subtract a fourth order polynomial between 5.5–9 μm (Fig. 5.2, top), to produce the emission spectrum shown in Fig. 5.2 (middle).

5.4 The UIR bands of WR 48a

The IR spectrum of WR 48a exhibits a weak, highly asymmetric emission band at ~ 6.4 μm, and a symmetric emission band at 7.9 μm (Fig. 5.2). These positions are close to the

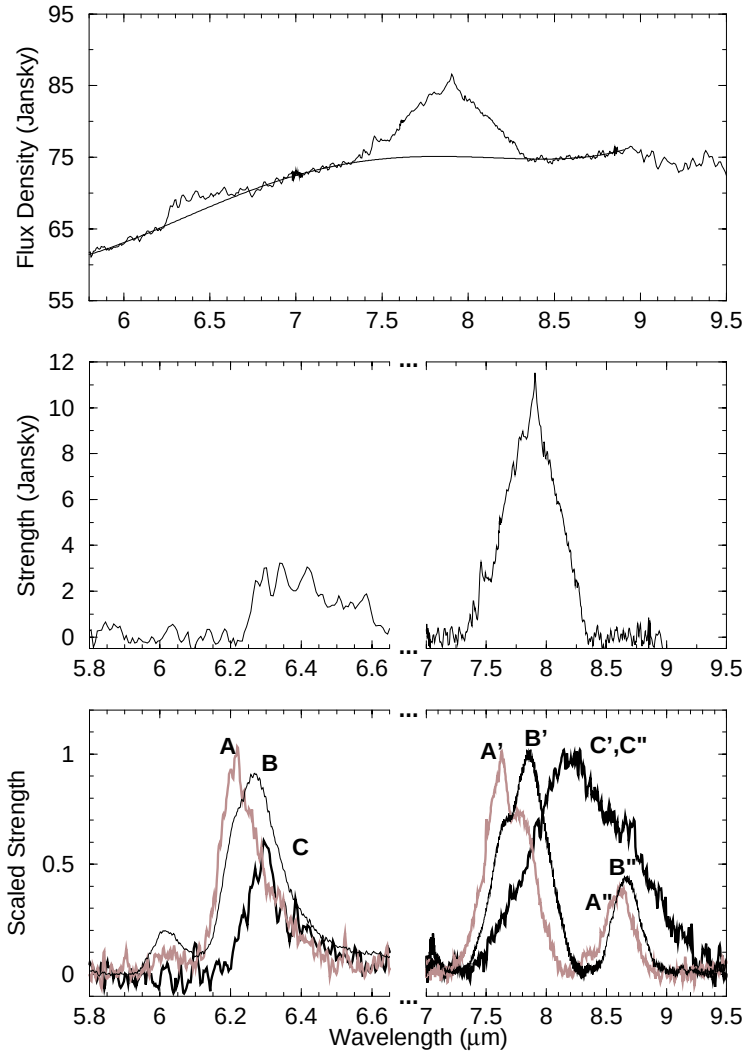

Figure 5.2 — [top] WR 48a extinction corrected flux density spectrum from 5.5–9.5 μm shown with fourth degree polynomial continuum fit. [middle] WR 48a continuum subtracted spectrum. UIR emission features at $\sim$ 6.4 and 7.9 μm are evident. [bottom] Overview of possible classes of UIR emission bands as classified in Chapter 3. The spectra are normalised such that the peak intensity in the 8 μm region equals one. Classes A, A$'$, A$''$ are represented by the compact HII region IRAS 23133+6050; B, B$'$, B$''$ are represented by the post-AGB star HD 44179; C, C$'$, C$''$ are represented by the post-AGB star IRAS 13416+6243.

characteristic wavelengths of UIR bands at 6.2 and 7.7 μm.

A systematic analysis of a large sample of sources representing a variety of astrophysical environments reveals the presence of large variations in profile and peak position of these two

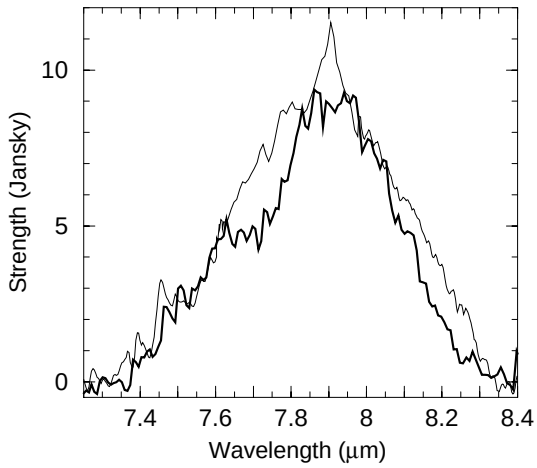

Figure 5.3 — UIR profile at 7.9 μm for WR 48a [thin line] compared to the scaled profile of Henize 2-113 [thick line], a planetary nebula with a WC10 central star.

UIR bands (Chapt. 3). These authors defined three classes for the observed 6.2 μm feature based on its peak position, i.e. sources with a 6.2 μm UIR band peaking at $\sim$ 6.22 μm, at 6.24–6.28 μm, and at $\sim$ 6.3 μm, belong to respectively class A, B and C. Similarly, three classes were defined for the 7.7 μm complex. Sources with a dominant 7.6, 7.8, and 8.2 μm component form class A$'$, B$'$, and C$'$, respectively. Sources with an 8.6 μm feature that peaks between 8.58–8.62 μm and beyond 8.62 μm, form classes A$''$ and B$''$, respectively. Sources with no 8.6 μm component form class C$''$. Astrophysically speaking, the 6–9 μm spectrum is also found to be sensitive to the type of object (Chapter 3), i.e. the local physical conditions where the carriers reside. HII regions, reflection nebulae, Herbig AeBe stars with associated HII regions, and extragalactic sources have class A, A$'$, and A$''$, 6.22, 7.6 and 8.6 μm features, respectively. Isolated Herbig AeBe stars, some post-AGBs, and most PNe belong to a second class of objects exhibiting features at 6.24–6.28, 7.8 and $>$ 8.62 μm (classes B, B$'$, and B$''$, respectively). Finally, two post AGB stars, that exhibit features at $\sim$ 6.3, 8.22, but none near 8.6 μm, form class C, C$'$, C$''$, respectively. An overview of the variations in the 6.2 and 7.7 μm UIR bands are shown in the bottom panel of Figure 5.2; the middle panel of this Figure compares the derived profiles for WR 48a.

The observed emission bands in WR 48a coincide with the wavelength range where UIR emission bands are observed. Following the classification of Chapter 3, the observed 6.4 μm feature belongs to class C. Nevertheless, the derived profile is unique; i.e. it is broader and more asymmetric compared to the class C profile (see Fig. 5.2). The 6.4 μm feature resembles that seen by Harrington et al. (1998) toward the hydrogen deficient PNe Abell 78 and IRAS 15154-5258. In contrast, the observed 7.9 μm complex belongs to class B$'$ and is similar to that of Hen 2-113, IRAS 07027-7934 and HD 100546 (see Fig. 5.3 and Fig. 15 in Chapter 3. Hen 2-113 and IRAS 07027-7934 are planetary nebulae with WC10 central stars

([WC]-PNe) while HD 100546 is an isolated Herbig AeBe star. These sources show a class B "6.2" μm feature distinct from that of WR 48a. Thus, WR 48a belongs to two classes, B$'$ and C, derived from the "7.7" and "6.2" μm, features respectively. Such mixed classes are present within the original sample as well (Chapter 3).

5.5 The Nature of the UIR Carrier in WR 48a

In Sect. 5.4, it is shown that the observed 6.4 and 7.9 μm emission features in WR 48a are similar to the so-called 6.2 and 7.7 μm UIR bands observed around some evolved stars and an isolated Herbig AeBe star. Nevertheless, WR 48a does not exhibit the 3.3, 8.6 and 11.2 μm UIR bands. These bands are attributed to the CH stretching and bending modes of PAHs and hence their non-appearance reflects the low H-content of the ejecta of WC stars (($< 10^{-2}$ by number relative to helium; Nugis & Niedzielski 1995; Torres 1988). As a consequence, PAHs cannot be present there and the condensation of soot in hydrogen poor environments must occur by pathways that bypass acetylene (C_2H_2)-rich molecular intermediaries. Carbon soot (i.e., amorphous carbon) formation in these environments is expected to be initiated through the formation of carbon chains (C_2, C_3, C_4, etc.) followed by the formation of aromatic ring structures (Cherchneff et al. 2000). The coalescence of large monocyclic rings may then form fullerene molecules (Rubin et al. 1991; von Helden et al. 1993; Kroto 1994). Amorphous carbon structures and grains can then form from carbon clusters of the fullerene family (Zhang et al. 1986).

The strongest bands for linear carbon chains with 3–20 C-atoms fall in the 4.4–5.0 μm range (Allamandola et al. 1999a) and, hence, these species cannot be responsible for the observed features in WR 48a. The vibrational characteristics of (non-aromatic) carbon ring molecules are unknown. Fullerenes have been studied in the laboratory. Specifically, the IR spectrum of C_{60} exhibits emission bands at 7.5, 8.6, 17.5 and 19.0 μm (Frum et al. 1991; Nemes et al. 1994). Two emission bands of C_{60}^+ have been measured; they peak at 7.1 and 7.5 μm (Fulara et al. 1993). All of these peak positions clearly deviate from the positions of the observed emission bands in WR 48a. Coal and amorphous carbon show emission in the 6–9 μm region (Borghesi et al. 1987; Colangeli et al. 1995; Guillois et al. 1996). However, the presently available amorphous carbon and coal data either do not show emission features in the 7.4–11 μm region (Borghesi et al. 1987) or the profiles do not match the astronomical data (Colangeli et al. 1995; Guillois et al. 1996). More experimental data are needed on carbon rings and fullerene molecules as well as hydrogen-poor carbonaceous dust to settle this question.

It has proven to be very difficult to distinguish purely spectroscopically between molecular and grain carriers for the UIR bands. Essentially, the mid-IR spectrum reflects the bonding between nearest neighbour atoms and is little sensitive to the characteristics of the emitting species at large. From that point of view, it is unclear whether the carrier of the 6.4 and 7.9 μm feature in WR 48a is molecular or dust-like in nature. In general, the assignment of PAHs as the molecular carrier for the UIR bands is based mainly on two arguments (Tielens et al. 1999). First, the UIR bands are observed in reflection nebulae and the diffuse ISM where classical grains are too cool to emit at 3.3 μm (Sellgren 1984). Second, the observed high feature-to-continuum ratio is characteristic of a molecular carrier. For WR 48a, on the other hand, there is no unambiguous evidence for a molecular carrier. The dust continuum in the IR spectrum of WR 48a peaks at $\sim$ 5–6 μm, i.e. in the same wavelength region as

the emission bands, disqualifying the first argument. A dust-like carrier is insinuated by the low observed feature-to-continuum ratio in WR 48a (~ 0.1). Thus, although molecules may contribute to the emission features, in this source, the emission may also be carried by dust grains.

5.6 Conclusions

We have detected emission features at ~ 6.4 and 7.9 μm in the spectrum of the late-type WC star WR 48a. The central wavelengths of these features fall within the range of the well-known UIR emission features. Since late-type WC Wolf-Rayet stars lack hydrogen in their stellar winds, polycyclic aromatic hydrocarbon molecules cannot be responsible for the emission features. Instead, we attribute the emission to large "pure" carbon molecules or amorphous carbon dust.

The 6.4 μm emission feature in the WR 48a spectrum closely resembles that observed toward the H-deficient PNe Abell 78 and IRAS 15154-5258. For these objects, the 6.4 μm feature is attributed to small transiently heated H-free carbonaceous grains (Harrington et al. 1998) due to the non-detection of the corresponding C-H modes (at 8.6 and 11.2 μm) of aromatic compounds. Only one of the H-deficient PNe (IRAS 15154-5258) shows a hint of a broad emission feature near 8 μm. On the other hand, Hen 2-113 and IRAS 07027-7934, planetary nebulae with hydrogen deficient WC10 central stars, show an emission feature at 7.9 μm that resembles the one seen in WR 48a (Fig. 5.3). However, the "6.2" μm feature toward these [WC10]-PNe falls shortward of that toward WR 48a, at 6.27 μm. In addition, the Herbig AeBe star, HD 100546, also shows a feature at 7.9 μm like the one seen in the WR 48a spectrum, but like the [WC10]-PNe, the "6.2" μm feature also falls shortward of that toward WR 48a, at 6.25 μm.

Physical conditions certainly have an effect on the profiles of the UIR bands. The C-rich H-deficient conditions in the objects discussed above (with the exception of HD 100546) have the effect of shifting the "6.2" and "7.7" μm features toward longer wavelengths. An additional requirement may be associated with shock induced dust condensation or modification of the PAHs. However, these are not the only conditions which promote such spectral shifts. In particular, HD 100546 has a similarly shifted "7.7" μm peak position and profile as WR 48a. Nevertheless, the similarity of the "7.7" μm UIR band in WR 48a, a Population I WR star, and in the two Population II [WC10]-PNe is intriguing. This might indicate that the dust formation in these environments is alike. For WR 48a, dust is formed in the interaction region of the winds of the O-star and the WR star (e.g., Usov 1991). In the [WC10]-PNe systems, interaction between the fast wind from the WC nucleus with the cooler slowly moving ejecta of the AGB phase produces the necessary shock conditions. However, unlike WR 48a, Hen 2-113 and IRAS 07027-7934 show emission due to C-H stretching and bending modes at 3.3 and 11.2 μm (Cohen et al. 1989; Hony et al. 2001), indicative of a region of hydrogen-rich PAHs and dust. Perhaps, the strong shocks caused by the [WC10] wind modify the H-containing nebular PAHs and dust formed during an earlier evolutionary phase.

Five WC stars with dense dust shells were studied by van der Hucht et al. (1996): WR 48a, WR 98a, WR 104, WR 112, WR 118. The spectrum of WR 48a is the only one that shows evidence for emission features at the known UIR wavelengths, although Chiar & Tielens (2001) attribute an absorption feature at 6.2 μm in these objects to circumstellar amorphous carbon dust. Large grains (~ 1 μm) were inferred based on the 6.2 μm profile's integrated

absorption, the intrinsic strength of amorphous carbon and the small circumstellar visual extinction. Perhaps WR 48a provides a snapshot of the general dust condensation process in WC stars, frozen out due to the transient nature of the dust formation process in this object; a stage which is obfuscated in other dusty WC stars due to rapid dust growth. In this sense, a search for molecular intermediaries in the dust formation process (e.g. C_n chains) in this source may prove to be fruitful.

6

Deuterated PAHs in space

To appear as :

E. Peeters, L.J. Allamandola, C.W. Bauschlicher Jr., D.M. Hudgins,
S.A. Sandford and A.G.G.M. Tielens

Submitted to Nature

Abstract The cosmic deuterium to hydrogen (D/H) ratio is of key importance from a cosmological and stellar evolution perspective since deuterium originates from big-bang nucleosynthesis and is destroyed by stellar thermonuclear reactions (Pagel 1997). Further, from the interstellar perspective, the galactic distribution of deuterium and the D/H ratio among various molecular species also traces interstellar chemical evolution. Over the past few decades, radio observations have enabled the study of a handful of small, deuterated interstellar species (Roueff et al. 2000; Turner 2001). However, the number of deuterated species detected and environments probed are limited, raising issues of selection effects that hamper generalization and applications to other environments. Infrared spectroscopy of the interstellar medium offers a distinct advantage in this regard as the extent of deuteration of entire chemical families, rather than one species, can be probed (Allamandola 1993; Teixeira et al. 1999). These observations require space borne telescopes because the molecular vibrations involving D which produce the strongest IR bands fall in spectral regions which are obscured by terrestrial CO_2 absorption (Allamandola 1993). Here we report the tentative detection of the CD stretching vibration from deuterated interstellar polycyclic aromatic hydrocarbons in the Orion nebula. Since the PAH emission features are widespread and probe many different types of cosmic environments, follow up observations of deuterated PAHs will provide fundamental, far reaching new insight and perspective into galactic and extragalactic processes (Cox & Kessler 1999).

Most interstellar sources with associated dust and gas - including H II regions, reflection nebulae, planetary nebulae, late-type stars, the general diffuse interstellar medium (ISM), galactic nuclei, and active star forming regions - show strong emission features at 3.3, 6.2, 7.7, 8.6 and 11.2 μm (Cox & Kessler 1999). These bands are generally attributed to vibrational fluorescence from UV pumped, large polycyclic aromatic hydrocarbon molecules (PAHs, Allamandola et al., 1989b). As a class, these species are the most abundant polyatomic molecules in space having an abundance by number of $\sim 10^{-7}$ relative to H and containing 5 to 10 % of the elemental carbon (Allamandola et al. 1989b).

Deuterium atoms substituted on the periphery of PAHs participate in the same characteristic types of vibrational motions as hydrogen atoms. These include CD stretching motions as well as in-plane and out-of-plane bending motions. However, due to the larger mass of the deuterium atom, all of these vibrations are shifted to lower frequencies. For the CD stretching modes, the frequency is lowered by a factor of ≈ 1.3 (Allamandola 1993; Hudgins et al. 1994; Bauschlicher et al. 1997). In addition, the vibrational motions of deuterium atoms cannot couple effectively with those of adjacent, lighter hydrogen atoms. At the low levels of deuteration expected in the interstellar PAH population, the overwhelming majority of peripheral deuterium atoms will be "non-adjacent" or "solo" – that is, they will be "isolated", having no neighboring deuterium atoms with whose motion they can strongly interact (for a discussion of CH group adjacency in PAHs, see c.f. Hudgins & Allamandola 1999a).

The various classes of CD vibrational features in deuterated PAHs (PADs) are not all equally attractive as targets for an astronomical search for interstellar PADs. It is therefore reasonable to search for the feature, or features, that offer the greatest prospect for success – those whose intensity is expected to be detectable and whose spectral position minimizes ambiguity in attribution. Both criteria point to the CD stretching vibrations of isolated D atoms on PAHs as being the most promising features for which to search. As with hydrogen, deuterium atoms associated with interstellar polycyclic networks will be bonded to either aromatic carbons (those that share in the delocalized pi bonding of the molecule) or aliphatic carbons (those which carry only sigma or single bonds) (Bernstein et al. 1996). In the purely aromatic case, a deuterium atom merely replaces a hydrogen atom at the periphery of the aromatic network without altering that network. The stretching band of the resulting aromatic CD bond falls at 4.4 ± 0.06 μm (Hudgins, Bauschlicher & Sandford, in preparation). With all the PAD aromatic CD stretching features falling in this relatively narrow range, the composite emission of interstellar PADs is expected to give rise to a single band near this position analogous to the more familiar 3.3 μm CH stretching band of interstellar PAHs. Deuterium atoms can also *add* to the periphery of a PAH changing the character of the carbon atom at the addition site from aromatic to aliphatic or replace an H atom already present on an aliphatic sidegroup. The stretching band of the aliphatic CD bond on the periphery of the hexagonal C-skeleton (a D_n-PAH) falls at 4.67 ± 0.06 μm (Hudgins, Bauschlicher & Sandford, in preparation). Both the aromatic and aliphatic CD stretching bands fall in a spectral region (4 – 5 μm) that is free of other PAH emission features, thereby eliminating ambiguity in their assignment. Thus any observation of emission bands at these positions in the interstellar spectrum is consistent with the PAH model and provides strong evidence for PADs.

The prospects for identifying interstellar PAD features in other parts of the spectrum are not as good. For the aromatic case, the CD in-plane modes, which fall between 9.5 and 12 μm, are distributed over a relatively wide range and are weak. The CD out-of-plane bending

modes, although they are generally more intense, are also problematic. Unlike the solo-H modes, which tend to fall within the relatively narrow range from 10.9 to 11.4 μm (for a discussion of CH group adjacency in PAHs, see c.f. Hudgins & Allamandola 1999a), the CD out-of-plane features are spread out over a much wider range (14.2 to 16.5 μm) due to the greater structural heterogeneity experienced by solo-D atoms (Hudgins, Bauschlicher & Sandford, in preparation). Solo-D's are all effectively non-adjacent by virtue of the low isotopic abundance of deuterium, not by virtue of the peripheral structure of the PAH as is the case for solo-H's. Consequently, on average, solo-D atoms sample a wider range of molecular environments than do solo-H's. As a result, CD out-of-plane bending in interstellar PADs would be expected to produce a broad, low contrast plateau between 14 and 17 μm that would be much more difficult to detect with certainty (Hudgins, Bauschlicher & Sandford, in preparation). Moreover, this wavelength range is also the domain of aromatic CC skeletal vibrations, introducing ambiguity of assignment (Moutou et al. 1996; Van Kerckhoven et al. 2000). A similar situation holds for the aliphatic CD bending (deformation) case. Here the bands would be expected to fall near 7 to 8 μm (Allamandola 1993, Hudgins, Bauschlicher & Sandford, in preparation), a region overwhelmed by intense PAH emission.

Figure 6.1 compares the ISO-SWS spectrum (Kessler et al. 1996; de Graauw et al. 1996) of the Orion Bar, position 4, between 3.0 and 5.5 μm[1] (top trace) to the absorption spectrum of a partially deuterated PAH mixture (solid line-lower trace) and the calculated aliphatic CD stretching absorption of D_n-PAHs (dotted line-lower trace). The 3.0 to 5.5 μm emission from Orion (upper trace) is dominated by the well-known 3.3 μm aromatic CH stretch band. Also evident in the spectrum are weaker bands between 3.3 and 3.6 μm (Allamandola et al. 1989b, Hudgins, Bauschlicher & Sandford, in preparation) and a feature centered near 5.2 μm (Allamandola et al. 1989a). The spectrum shows that new features may be present centered 4.4 and 4.67 μm. The two hydrogen recombination lines at 4.05 μm (Brα) and at 4.652 μm (Pfβ) have been removed. To assess the reality of the 4.6 μm feature which is blended with the Pfβ emission line, its integrated strength and uncertainty was determined by removal of the Pfβ line based upon the Brα line intensity. This analysis clearly showed emission in addition to that at the Pfβ position. The fluxes of the two candidate features together with the flux of the bands near 3.3 and 5.25 μm are given in Table 6.1. The errors listed in Table 6.1 have been determined by comparing the independently reduced up and down scans. These errors are dominated by uncertainty in the dark current subtraction, resulting in some wavelength dependent error as well. Taking this into account, we conclude that the 4.4 and 4.6 μm features are present at the 1.9 and 4.3 sigma levels, respectively.

The solid line portion of the lower trace in Figure 6.1 presents the spectrum produced by combining the laboratory absorption spectra of a variety of individual PADs, PAHs, and H_n-PAHs. Here the aromatic CH stretches produce the 3.3 μm band, aliphatic CH stretches and the overtones and combinations of CC modes produce the weak features between 3.35 and 3.6

[1]The Orion Bar position D5 (05 35 19.8 -05 25 10 (2000)) was observed in the astronomical observations template 01 full scan mode speed 2 (Target dedicated time number 83101507), by scanning the grating over its full mobility range and back, yielding two independent scans (the up and down scan). Deviations between the up and down scans vary between 0 and 2 Jy. The 3 μm region has a spectral resolving power of $\lambda/\Delta\lambda = 500$, and the 4 to 5.5 μm region a spectral resolving power of $\lambda/\Delta\lambda = 250$. An independent AOT 06 observation had insufficient S/N to be considered. The data were processed with IA^3, the SWS Interactive Analysis package (de Graauw et al. 1996) using calibration files and procedures equivalent with the pipeline version 10.1 (IA^3 test, April 2002). Further data processing consisted of flat-fielding, bad pixel removal and rebinning with a constant resolution. Details on the data reduction procedure can be found in Chapter 2.

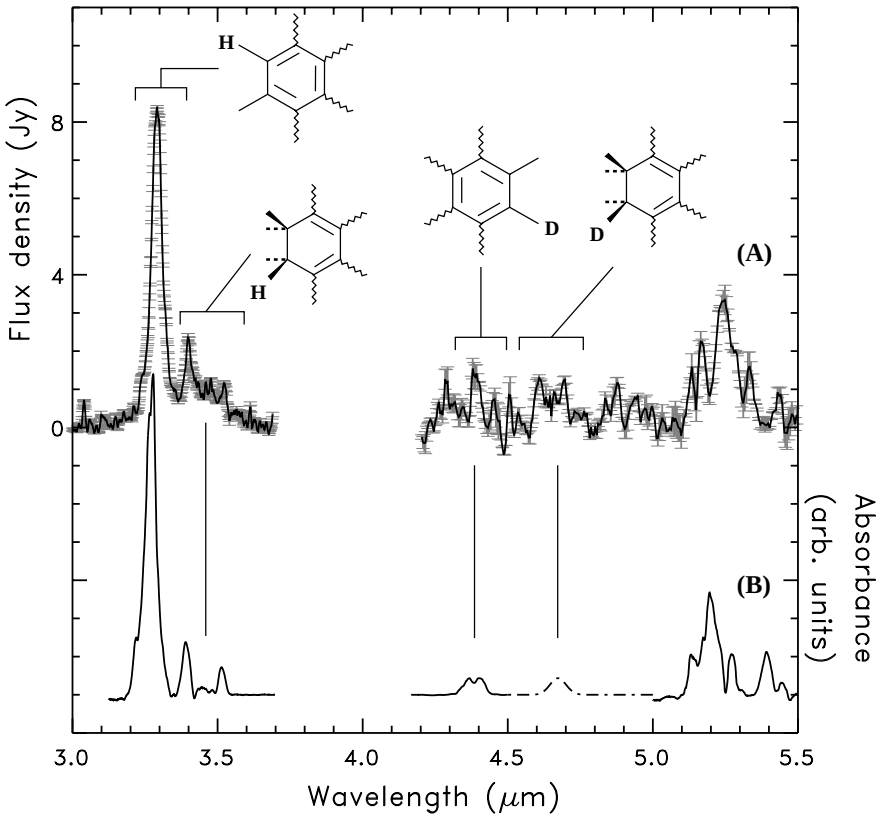

Figure 6.1 — Comparison of the 3.0 to 5.5 μm continuum-subtracted ISO spectrum of the Orion Bar (trace a) to the absorption spectrum of a partially deuterated PAH mixture (solid line, trace b) and the computed absorption spectrum of a D_n-PAH (dashed line, trace b). Two hydrogen recombination lines (Pfβ and Pfδ) have been removed based on the strength of Brα line and the case B recombination theory. The solid line portions of trace b is the absorption spectrum produced by coadding the spectra of individual perdeuterated PADs and fully hydrogenated PAHs in D/H = 1/20 ratio. The PAH mixture contains: naphthalene, phenanthrene, pyrene, chrysene, 7,8-dihydrobenzo[a]pyrene, d_8-naphthalene, d_{10}-phenanthrene, d_{10}-pyrene, and d_{12}-chrysene. The dashed line of the trace b is the computed spectrum of D_n-PAHs : dihydropyrene, dihydrocoronene and dihydrocircumcoronene. In this composite spectrum, the aromatic and aliphatic CH stretches produce the bands in the 3 μm region, the CD stretches in PADs and D_n-PAHs produce the bands at 4.4 and 4.67 μm, and the feature centered near 5.2 μm is due to overtones of the longer wavelength CH bending vibrations.

μm and the complex structure centered near 5.2 μm is due to overtones and combinations of the longer wavelength CH bending vibrations. The band centered near 4.4 μm in the spectrum arises from the aromatic CD stretches of the PADs within the molecular mixture. The dashed line portion of the lower trace presents the computed position of the aliphatic

Table 6.1 — Feature fluxes and uncertainties.

Wavelength (μm)	Flux (W/μm)	σ
3.3	1.1 10^{-13}	45
3.4	1.4 10^{-14}	12
3.5	4.0 10^{-15}	6.5
4.4	7.2 10^{-15}	1.9
4.6	1.5 10^{-14}	4.4
5.25	4.6 10^{-14}	9.4

CD stretch in D_n-PAHs with two aliphatic D-atoms (the frequencies are computed using the B3LYP hybrid density functional approach in conjunction with the 4-31G basis set).

On the basis of the band position correspondence between the interstellar and the laboratory model spectra seen in Figure 6.1, we attribute the possible new interstellar feature near 4.4 μm to the aromatic CD stretch from deuterated interstellar PAHs and the second broader feature centered near 4.67 μm to the aliphatic CD stretch. The sum of the intensities of the possible 4.4 and 4.67 μm features provides a measure of the amount of deuterium in the PAH population. The D/H ratio of the emitting PAH population can be estimated by taking the ratio of this sum to the analogous sum of the 3.3 μm and weaker satellite bands which provide a measure of the hydrogen in the PAH population. Assuming that the integrated absorbance values of the corresponding CH/CD modes are the same, we estimate that the D/H ratio within the family of interstellar PAHs at position 4 in the Orion ionization ridge is 0.17 $\pm$ 0.07. Within the framework of our proposed identifications, the aliphatic groups have a much higher deuterium fraction than the aromatic groups, as implied by the high 4.6/3.4 intensity ratio compared to the 4.4/3.3 ratio. If born out, this difference in fractionation may provide important clues to the processes fractionating interstellar PAHs.

Deuterium fractionation occurs due to the different zero-point energies of CH and CD bonds, resulting in slightly more stable CD bonds (Tielens 1997b; Millar et al. 2000). For PAHs, there are at least four distinctly different astrochemical processes that should drive D-enrichment (Sandford et al. 2001). First, PAH deuterium enrichments can result from low temperature ($T < 50$ K), ion-molecule reactions occurring in the gas phase (Tielens 1997b; Millar et al. 2000). Second, PAHs can become deuterium enriched in ice mantles in dense interstellar clouds. Gas-grain chemistry (Charnley et al. 2001) should produce large D enrichments in grain mantles where reduction is occurring due to the high atomic D fractionation of the accreting gas (Tielens 1992; Charnley et al. 1997). Third, additional D-enrichment can occur to PAHs within these ices when they are processed by UV and cosmic ray radiation (Sandford et al. 2000). In this case both aromatic and aliphatic CD bonds are produced (Hudgins, Bauschlicher & Sandford, in preparation). Lastly, D-enrichment by unimolecular photodissociation can also occur to PAHs in the gas phase (Allamandola et al. 1989b). In contrast to the previous processes, this does not require low temperatures and is expected to

be most significant for PAHs in the size range from about $C_{10}H_8$ (naphthalene) to $C_{42}H_{18}$ (hexabenzocoronene), the portion of the interstellar PAH population expected to dominate the emission in this region of the spectrum. With time, interstellar PAHs should become enriched in deuterium by any or all of the above processes. Since PAHs are considerably more stable and more abundant in the ISM than many of the smaller species that show D enrichments (PAH/$H_2 \sim 10^{-6}$ compared to HCN/$H_2 \sim 10^{-8}$), and PAHs carry more H atoms per molecule than simpler molecules, PAHs are likely to represent the largest reservoir of D-enriched interstellar materials.

While interstellar PAHs are expected to be enriched in deuterium, the extent of the enrichment depends on the local environment and history, making the PAH D/H ratio a particularly useful new interstellar probe. In particular, PAHs freshly ejected by stars would be expected to contain little deuterium since most of the parent star's original deuterium will have been destroyed during nucleosynthesis. In contrast, PAHs in dense clouds have experienced a long period of interstellar evolution and will have had ample opportunity to become enriched in deuterium by ion-molecule and unimolecular photodissociation reactions occurring in the gas phase and by radiation-driven exchange reactions in ice mantles. Some of the highest D/H ratios in gas phase PAHs might be expected in the transition zones, such as the Orion Ionization Ridge studied here, where H II regions are exposing fresh dense cloud material to the strong stellar radiation field. Indeed, H_n-PAHs have been identified in the Orion Bar(Sloan et al. 1997), so it is reasonable to find evidence for their deuterated counterparts. These environments drive rapid gas phase enrichments and this is where D-enriched PAHs frozen in ice grains will be released into the gas phase. Here, the PAH D/H ratio may serve as a probe of the past interstellar heritage and age. If born out, the difference in fractionation between aromatic and aliphatic hydrogen suggested by the Orion data may reflect that they drive largely from different reservoirs. For example, enriched D_n-PAHs and methylated PAHs may result from exchange reactions and photochemistry in ice mantles (in the dense-cloud phase). In contrast, the fractionation of the aromatic H may be controlled by ion-molecule, and unimolecular photodissociation reactions in the gas. The understanding gained by further observations of the PAH D/H ratio in the Galaxy can be used as a template to interpret the PAH and PAD emission spectra obtained from other galaxies.

Closer to home, deuterium enrichments have been identified in both bulk meteoritic materials (Yang & Epstein 1983; Epstein et al. 1987) and within specific classes of meteoritic molecular species including aromatic hydrocarbons (Kerridge et al. 1987). While the specific processes leading to these species are still unclear, the D-enrichment is generally taken as evidence that meteoritic organics contain relics of presolar, interstellar materials (Zinner 1997). The measurements reported here are an attempt to establish the first family of deuterium enriched compounds which are common to interstellar space and the Solar System. This holds the promise to become a powerful means to link interstellar chemistry directly to the organics in primitive Solar System materials, matter which may have played a key role in the origin of life on earth.

Acknowledgements

This work was supported by NASA's Long Term Space Astrophysics and Laboratory Astrophysics programs.

7

The PAH emission spectra of Large Magellanic Cloud H II regions

Based on :

R. Vermeij, E. Peeters, A.G.G.M. Tielens, J.M. van der Hulst
Astronomy & Astrophysics, 2002, 382, 1042

Abstract

A set of ISOPHOT spectra from a sample of H II regions in the Large Magellanic Cloud (LMC) is presented. In all the spectra, emission bands arising from Polycyclic Aromatic Hydrocarbons (PAHs) are clearly present. These features are observed to vary considerably in relative strength to each other from source to source and even within 30 Doradus. The LMC spectra have been compared with ISO-SWS spectra from Galactic H II regions and with the ISOCAM observation towards a quiescent molecular cloud in the SMC (Reach et al. 2000). A correlation is found between the $I_{7.7}/I_{11.2}$ versus $I_{6.2}/I_{11.2}$ and the $I_{8.6}/I_{11.2}$ versus $I_{6.2}/I_{11.2}$ ratios. A segregation between the sources in the different types of environment (Milky Way – LMC – SMC) is present. Furthermore, within the LMC observations, a clear distinction between 30 Doradus and non-30 Doradus pointings is found. We discuss the variations in the relative strength of the PAH features in view of the different physical environments and highlight the relation with the PAH/dust ratio and the extinction curve. We conclude that 1) the same conditions responsible for the observed trends in the relative PAH-feature strengths also affect the carrier of the 2175 Å bump leading to the differences in strength of the latter, and 2) the molecular structure is the major cause of the observed variations in the relative strength of the PAH features. In the SMC and 30 Doradus compact PAH species dominate, while PAHs with an open, uneven structure are the dominant ones in Galactic H II regions and the non-30 Dor LMC sources.

7.1 Introduction

Ground-based, airborne, and space-based observations have shown that the mid-infrared spectra of many objects with associated dust and gas are dominated by the well-known emission features at 3.3, 6.2, 7.7, 8.6 and 11.2 μm commonly called the unidentified infrared (UIR) bands (cf. Gillett et al. 1973; Geballe et al. 1985; Cohen et al. 1986; Roche et al. 1989). These bands are now generally attributed to vibrational relaxation of UV-pumped Polycyclic Aromatic Hydrocarbons (PAHs) containing $\simeq$ 50 carbon atoms (Léger & Puget 1984; Allamandola et al. 1985, 1989b; Puget & Léger 1989; Tielens et al. 2000). The band at 3.3 μm is due to CH stretching vibrations, the 6.2 μm band corresponds largely to pure CC stretching motions, whereas the 7.7 μm feature arises from combinations of CC stretching and CH in-plane bending motions. The 8.6 and 11.2 μm features arise from CH in-plane and out-of-plane bending motions respectively. Underlying the 6.2 μm, 7.7 μm and 8.6 μm bands as well as underlying the 11.2 μm band, is a quasi-continuum or pedestal originating from larger PAHs and clusters of small PAHs.

Since the emission arises not from a single species but from a complex mixture of PAHs (Léger & Puget 1984; Allamandola et al. 1985), the interstellar PAH spectra reflect a combination of individual molecular features, and hence the overall PAH spectrum appears very similar from source to source. The exact PAH family (molecular structure and size) present in a source fine-tunes the PAH spectrum in terms of relative strengths and peak positions of the individual PAH features (Schutte et al. 1993; Verstraete et al. 1996; Allamandola et al. 1999b; Moutou et al. 1999c; Hony et al. 2001; Peeters et al. 2002a). Laboratory studies and quantum-chemical calculations have shown that ionisation of the PAH molecules has a remarkable effect on the spectrum. While the peak positions of the UIR bands are modestly affected by ionisation, the influence on the intensity is striking - particularly in the 5 to 10 μm region (Allamandola et al. 1999b; Bakes et al. 2001). As a result, the emitted spectrum will depend on the local physical conditions. In addition, dehydrogenation may also influence the PAH spectrum, in particular in the strength of the different CH modes (Pauzat et al. 1997).

With the launch of the Infrared Space Observatory (ISO), a huge amount of infrared spectral data became available, showing the omnipresent nature of these PAH features. By now, the features have been detected in a wide range of objects and environments, from post-AGB stars and planetary nebulae, to H II regions, reflection nebulae, the diffuse interstellar medium and extragalactic sources. As demonstrated by the galaxy survey by Helou (1999), the mid-IR spectrum of the ISM in galaxies is dominated by the UIR bands. A spectroscopic survey of the nuclei of nearby ($z < 0.3$) starburst galaxies has also revealed the presence of bright UIR bands (Boselli et al. 1997; Lutz et al. 1998).

Studies have also been performed for the Magellanic Clouds. ISOCAM studies of the large SMC H II region N 66 (Contursi et al. 2000) and of the SMC molecular cloud B1#1 (Reach et al. 2000) show the presence of PAHs even in such a metal-deficient environment. A similar study of the H II region complex N4 in the LMC also hints at the presence of PAHs (Contursi et al. 1998). An ISO-SWS AOT1 spectrum of 30 Doradus taken at our position #3 also shows the clear presence of PAHs (Sturm et al. 2000).

The study of PAHs in the Magellanic Clouds is of interest because of the different physical environment encountered there. The best known of these differences is the low-metalicity of the Magellanic Clouds relative to the Galaxy. Furthermore, the prodigious starformation activity inundates the Magellanic Clouds with diffuse UV radiation (e.g. Cole et al. 1999).

Table 7.1 — The ISOPHOT and ISO-SWS pointings and dates of the observations. The coordinates are J2000.0. The designations for the Magellanic Cloud sources, except for 30 Doradus, are those of Henize (1956). The Galactic sources (except the Orionbar) are designated by their IRAS number.

LMC				Milky Way				
Object	RA	Dec.	Date	Object	RA	Dec.	Date	AOT
N4A	4 52 08.4	-66 55 23.4	29-Apr-96	Orionbar#1	05 35 21.4	-05 25 40.1	11-Oct-97	01
N83B	4 54 25.8	-69 10 56.7	31-Oct-97	Orionbar#2	05 35 19.8	-05 25 10.0	24-Feb-98	01
N11A	4 57 16.3	-66 23 22.9	16-Aug-96	Orionbar#3	05 35 18.2	-05 24 39.9	11-Oct-97	01
N159-5	5 40 04.2	-69 44 42.9	24-Sep-97	12331−6134	12 36 01.9	-61 51 03.9	10-Sep-96	01
30 Dor#1	5 38 33.5	-69 06 27.1	05-Dec-97	15384−5348	15 42 17.1	-53 58 31.5	10-Sep-96	01
30 Dor#2	5 38 35.4	-69 05 41.2	13-Apr-96	18317−0757	18 34 24.9	-07 54 47.9	08-Mar-97	01
30 Dor#3	5 38 46.0	-69 05 07.9	20-Jul-97	18434−0242	18 48 04.1	-02 39 20.0	12-Apr-97	06
30 Dor#4	5 38 54.2	-69 05 15.3	05-Aug-97	21190+5140	21 20 44.9	+51 53 27.0	30-Nov-97	06
				22308+5812	22 32 45.9	+58 28 21.0	12-May-96	01
				23030+5958	23 05 10.6	+50 14 41.0	06-Dec-97	06
				23133+6050	23 15 31.4	+51 07 08.0	06-Jun-97	06

NOTE. - Units of right ascension are hours, minutes, and seconds, and units of declination are degrees, arcminutes, and arcseconds.

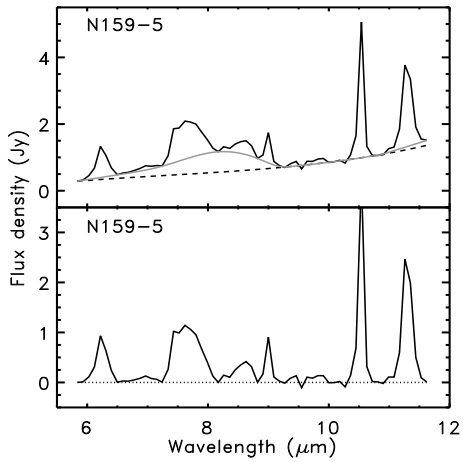

Figure 7.1 — The ISOPHOT spectrum of N159-5. The upper panel shows the spectrum and the components of the fitted continuum. The lower panel shows the continuum subtracted spectrum.

In this paper, a set of mid-IR spectra from a sample of H II regions in the Large Magellanic Cloud is presented, and all of these show the strong presence of PAH features. These spectra give us the opportunity to investigate the influence of the completely different environment in the LMC on the PAH spectra and their carriers. We therefore make a comparison between our sample H II regions in the LMC and those of our own Milky Way and the SMC. In section 7.2 the data are presented, with special emphasis on the way the PAH-feature strengths have been determined. Section 7.3 describes the general trends in the observed PAH-feature strengths. In section 7.4, the connection with extinction is highlighted and the possible underlying causes for the observed trends are examined. Finally, section 7.5 summarises our results.

7.2 The Data

7.2.1 Observations

The sample includes a set of Large Magellanic Cloud H II regions. The spectra were obtained with the ISOPHOT/PHT-S instrument on board ISO in staring mode using the PHT-40 template (Lemke et al. 1996). The observation log is given in Table 7.1. The PHT-S instrument covers the spectral ranges from 2.5 - 4.8 μm (the PHT-SS part) and from 5.8 - 11.6 μm (the PHT-SL part). Both spectral ranges have their own linear detector block consisting of 64 pixels each with a spectral resolution of 85 in the SS part and 95 in the SL part. The ISOPHOT spectra were reduced with PIA V8.4 using standard routines. Special attention is paid to the de-glitching of the signal from every separate pixel. This is done to make sure that no spurious feature would contaminate the spectra. In addition to these ISOPHOT data, the ISO-SWS AOT 01 spectrum of 30 Dor#3 (Sturm et al. 2000) was taken from the ISO archive and reduced in a similar way as the spectra of the Galactic H II regions. Representing the Small Magellanic Cloud in this work is the ISOCAM observation from Reach et al. (2000) of the molecular cloud B1#1. The sample of H II regions in the Milky Way was taken from the Galactic 'Ultra Compact H II region' ISO program (Peeters et al. 2002b) complemented with spectra of the Orionbar also taken from the ISO archive (Orion bar#3 : Cesarsky et al. (2000)). The spectra have been obtained with the Short Wavelength Spectrometer (SWS) in

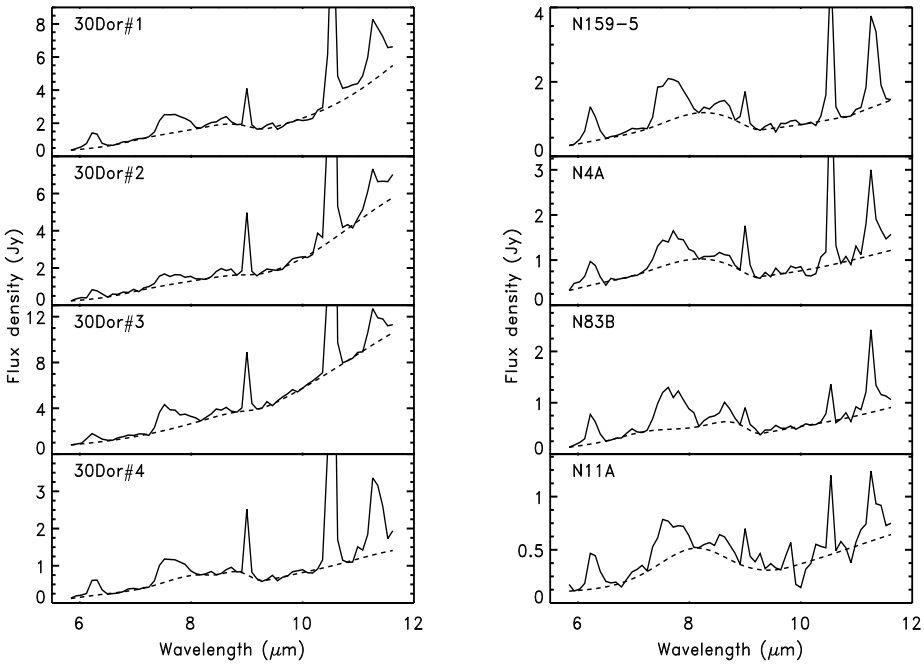

Figure 7.2 — The ISOPHOT spectra of the sample objects in the Large Magellanic Cloud.

the AOT 01/AOT 06 scanning mode (see Table 7.1). A detailed account of the reduction of the AOT 01 spectra can be found in Peeters et al. (2002b). The AOT 06 spectra were reduced in a similar way as the AOT 01 data.

7.2.2 The spectra

The ISOPHOT spectra of the LMC sources are shown in Figure 7.2. Only the part of the spectra ranging from 5.9 to 11.6 μm is shown here. The spectra of the LMC H II regions resemble the spectra of Galactic H II regions very much. All the major PAH features, i.e. the 6.2, 7.7, 8.6 and 11.2 μm bands, are clearly present. Only in some cases (e.g. N4A), a trace of the 3.3 μm feature was seen. This is not surprising since this feature is known to contribute typically only 6% to the total luminosity carried by the PAH features (Cohen et al. 1989) and can therefore easily be hidden in the noise in the ISOPHOT spectra. Even the weak PAH features at 6.0 and 11.0 μm (Hony et al. 2001; Peeters et al. 2002a) can be discerned in some of the spectra (e.g. N4A, 30Dor#4). In addition to the PAH emission bands, the [Ar II] 6.9 μm, [Ar III] 8.9 μm and [S IV] 10.5 μm fine-structure lines are observed, the former being rather weak. The Pfα line at 7.5 μm might be present in the spectra, but at the resolution of PHT-S it is not possible to disentangle the Pfα line from the 7.7 μm PAH feature. This line and the PAH feature are easily separated at the resolution of SWS. In the SWS spectrum of 30 Dor#3, this Pfα line is clearly present. The silicate absorption feature at 9.7 μm was not detected in

Table 7.2 — The ISOPHOT fluxes of the different PAH features in units of 10^{-18} W cm^{-2}. The errors given in this table are only the measurement errors. Also included are the fluxes from SMC B1#1 and the SWS-AOT1 spectrum of 30 Doradus#3.

Object	3.3 μm	6.2 μm	7.7 μm	8.6 μm	11.2 μm
N4A	d	0.92 ± 0.05	1.67 ± 0.02	0.29 ± 0.01	0.68 ± 0.03
N83B	n	0.85 ± 0.01	2.05 ± 0.02	0.46 ± 0.04	0.56 ± 0.02
N11A	n	0.60 ± 0.01	0.92 ± 0.02	0.26 ± 0.01	0.29 ± 0.01
N159-5	n	1.45 ± 0.02	2.83 ± 0.02	0.54 ± 0.05	1.14 ± 0.01
30 Dor#1	d	1.59 ± 0.03	2.87 ± 0.02	0.51 ± 0.01	1.48 ± 0.01
30 Dor#2	n	0.79 ± 0.05	1.50 ± 0.03	0.48 ± 0.01	0.92 ± 0.02
30 Dor#3°	d	1.27 ± 0.02	4.50 ± 0.04	0.81 ± 0.01	1.51 ± 0.02
30 Dor#3*	0.23	1.16	3.66	0.74	1.23
30 Dor#4	n	0.65 ± 0.02	1.38 ± 0.02	0.11 ± 0.05	1.07 ± 0.04
SMC B1#1†	-	0.37	0.76	0.11	1.26

$^{\circ}$: flux derived from the ISOPHOT data. * : flux derived from the ISO-SWS AOT 01 spectrum (Sturm et al. 2000). † : flux derived from the ISOCAM spectrum (Reach et al. 2000), see Section 7.2.3. n : not detected. d : detected.

any of the spectra of the Magellanic sources.

Already at first glance, variations in the relative PAH-feature strengths from one object to another are obvious. These variations are not only present when comparing different H II regions, but also for the different pointings within the giant H II region 30 Doradus. At first sight, the shape of the features also seems to vary. This is the most pronounced for the 7.7 μm feature, but here the possible presence of the Pfα line at 7.5 μm should be taken into account. While tantalizing, we conclude that these profile variations may not be significant due to the low resolution of the PHT-S instrument. Note, however, that the Galactic H II regions show little profile variations for the 6.2, 7.7 and 8.6 μm features (see Peeters et al. 2002a). Small variations are present in the 11.2 μm PAH feature (see Peeters et al. 2002, in prep.) but these cannot be seen at the PHT-S resolution. Furthermore, the PAH profiles in extragalactic sources are similar to those in the Galactic H II regions (Peeters et al. 2002a).

7.2.3 Continuum fitting and flux determination

For both the ISOPHOT and the ISO-SWS spectra the continuum subtraction was done with the same two-step procedure by fitting a spline through selected points in the spectra.

In the first step of the continuum subtraction, an underlying dust continuum was defined. For the ISOPHOT spectra, the spline points for this continuum were located at ~ 5.8 μm, in the 9 - 10 μm region, and at the blue base of the [S IV] 10.5 μm line. The wavelength coverage of ISOPHOT (ending at 11.6 μm) hampers the determination of the continuum redwards of the [S IV] 10.5 μm line. Without continuum points beyond 11.6 μm, it is difficult to ascertain

the presence of a broad plateau underlying the 11.2 μm feature and, if present, to distinguish it from the underlying dust continuum. Therefore, no points were added in this region to constrain the fit to the underlying continuum. However, as can be seen in, for example, Figure 7.1, some residual flux is present underneath the 11.2 μm feature. In the spectra where such a residual flux was present, it was removed by defining a simple straight-line continuum superimposed on the underlying continuum.

For H II regions, the 5 - 9 μm spectral range is also characterized by a broad plateau underlying the features in this range (Peeters et al. 2002a). In the second step, a continuum was fit to this plateau and subtracted. Anchor points for the fit to this plateau were located at $\sim$5.8 μm, between the 6.2 μm and the 7.7 μm features, at the blendpoint of the 7.7 μm and 8.6 μm features, and at the base of the [Ar III] 8.9 μm line. As an example, the resulting composite continuum and the continuum-subtracted spectrum of N159-5 are shown in Figure 7.1.

For fitting the underlying continuum in the SWS spectra, points in roughly the same wavelength ranges were taken. A spline was fitted through points in the range from 5 - 6 μm, between the 6.2 μm and the 7.7 μm features (near 7 μm), between the 7.7 μm and 8.6 μm features (near 8.2 μm), in the 9 - 11 μm range and through points near 11.7 μm.

In this way, a local continuum around the 6.2 μm and the 11.2 μm features is determined. The presence of a silicate absorption feature at 9.7 μm (in some Galactic H II regions) has been ignored in determining the fit but will strongly influence the 8.6 μm feature. Therefore, when examing the 8.6 μm feature, the Galactic H II regions with obvious silicate absorption (IRAS 15384, IRAS 18317, IRAS 18434) are disregarded.

The fluxes of the PAH features have been derived from the continuum subtracted spectra by simple pixel integration. The fluxes of the 6.2 μm, 7.7 μm, 8.6 μm and 11.2 μm features were derived by integration over the wavelength intervals of 6.1 - 6.6 μm, 7.1 - 8.2 μm, 8.3 - 8.9 μm and 11.1 - 11.6 μm, respectively. To make sure that the fluxes for the SMC B1#1 cloud can be compared, these have been rederived in the same way rather than taking the fluxes from Reach et al. (2000). The fluxes will be sensitive to the continuum determination and the decomposition of the 6 to 9 μm region in terms of the PAH features and the PAH plateau. However, this will influence all spectra in the same way. In particular, this will not introduce spurious differences between the Galactic and the LMC sources.

The fluxes for the LMC and SMC sources are given in Table 7.2. For 30 Doradus#3, both the flux derived from the ISOPHOT data as well as the SWS data is given in Table 7.2. The only uncertainty quoted in the Table is the one arising from noise in the spectra. The relative flux calibration uncertainty of the ISOPHOT spectra is estimated to be around 10% (Acosta-Pulido & Ábrahám 2002). The 7.7 μm flux could be contaminated by the Pfα line, but a comparison between the 7.7 μm fluxes and the Pfα fluxes for the same objects from Vermeij et al. (2002b) showed this contamination to be not higher than $\sim$10%. For the Galactic H II regions, the intensity of the Pfα line is less then 8% of the intensity of the 7.7 μm PAH band.

7.3 Correlations

Given the differences in the physical environments of the Milky Way and the Magellanic Clouds, it is of interest to investigate the differences - if any - in the PAH spectra between Galactic and Magellanic Cloud H II regions. Here we want to study variations in the relative strength of the PAH bands to each other, not the differences in absolute intensities due to

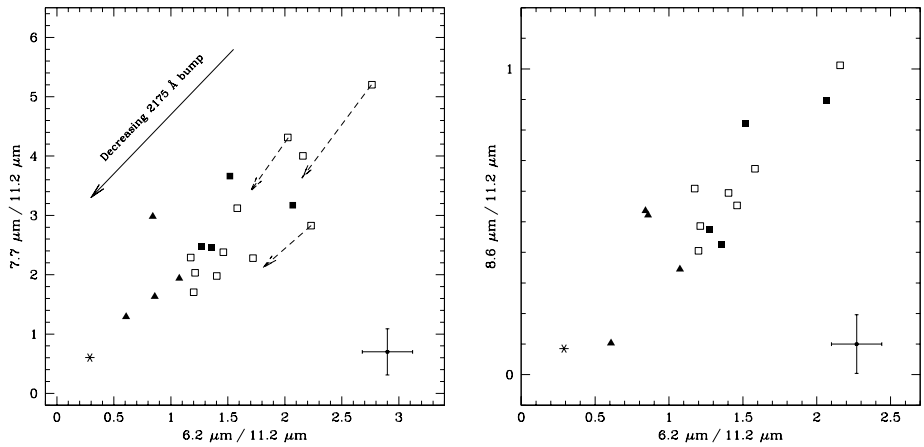

Figure 7.3 — The correlations between the different relative PAH-feature strengths. The feature fluxes have been normalised relative to the 11.2 μm flux so as to eliminate the differences in the distance to the source. The Galactic sources are shown as open squares, the non-30 Dor sources as solid squares and the 30 Dor pointings as solid triangles. The asterisk represent the SMC B1#1 molecular cloud. Shown in the lower right corner is a typical error bar. The dashed arrows show the shift in position of the observed ratios when an extinction correction is applied (see text). The solid arrow shows the direction in which the contrast of the 2175 Å bump to the general extinction decreases.

intrinsic luminosity and distance of the sources. We therefore use 3-feature intensity ratio plots. The relation between the different PAH-feature strengths is shown in Figure 7.3.

Three of our Galactic sources suffer from extinction (IRAS 15384, IRAS 18317, IRAS 18434; Martín-Hernández et al. 2001). For these sources, both the observed and intrinsic ratios are shown in the left panel of Figure 7.3 (the dashed arrows). The extinction A_K is derived from hydrogen recombination lines. These sources are not shown in the right panel of Figure 7.3 since silicate absorption influences the relative strength of the 8.6 μm feature. For the LMC sources, the pointing with the highest extinction (30 Dor#4) has an A_V of 1.7 (Vermeij et al. 2002b). Therefore, extinction only has a minor influence on the observed strengths of the PAH features in the LMC.

Both panels clearly show linear correlations between the different PAH-feature strengths. Most striking is a segregation between the sources of different type of environment, i.e. from the Milky Way to the LMC and to the SMC. Interesting, however, is the fact that for 30 Doradus the measured PAH-feature ratios lie further down the sequence than those of the other LMC pointings, showing a clear distinction between the pointings in 30 Doradus and the non-30 Doradus sources. This distinction is clearly visible for the $I_{6.2}/I_{11.2}$ ratio, but is much less pronounced for the $I_{7.7}/I_{11.2}$ and the $I_{8.6}/I_{11.2}$ ratios (Fig. 7.3). Three of the pointings in 30 Doradus show a $I_{7.7}/I_{11.2}$ and $I_{8.6}/I_{11.2}$ ratio similar to those of the Galactic and non-30 Dor sources. Note that the non-30 Dor LMC H II regions behave more like the Galactic H II regions in our sample.

We also investigated the relative contribution of every PAH feature to the total emitted PAH flux in all the features. These are shown in Figure 7.4. The SMC point is in all the plots

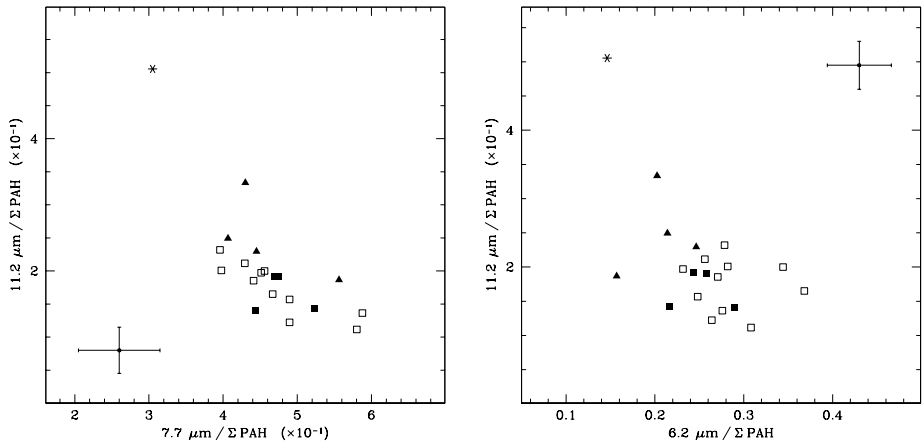

Figure 7.4 — The relative contribution of the 6.2, 7.7 and 11.2 μm PAH features to the total energy output within all the PAH bands. For an explanation of the symbols see Figure 7.3. Shown in both panels is a typical errorbar.

clearly separated from the other objects. The Galactic and Magellanic Cloud sources show a similar range in the fraction of the PAH emission emitted in the 7.7 μm and the 8.6 μm band. In contrast, there is a clear difference between the Galactic sources and the 30 Dor and SMC sources when considering the 6.2 and 11.2 μm bands (Figure 7.4, right panel). The 6.2 μm feature is relatively stronger in the Galactic sources whereas its 11.2 μm band is relatively weaker. This latter difference, however, is only slight. Here too, the 30 Dor pointings and the SMC source are situated in different regions in the plot compared to the Galactic sources and the non-30 Dor sources. A similar separation is not noticed for the $I_{7.7}/\Sigma$ PAH versus $I_{11.2}/\Sigma$ PAH ratio (Figure 7.4, left panel).

7.4 Discussion

7.4.1 Extinction : the 2175 Å bump

Much work has been done on determining the extinction characteristics of many lines-of-sight towards the LMC and also the SMC (e.g. Borgman et al. 1975; Nandy et al. 1981; Koornneef & Code 1981; Prevot et al. 1984). A common result found in this work for the LMC is that the extinction in the UV is significantly higher and rises more sharply than for Galactic lines-of-sight and that the 2175 Å bump is about 50% weaker. This change in the characteristics of the extinction curve is even more pronounced for the SMC. It has also been pointed out that there seems to be an anti-correlation between the 2175 Å bump strength and the slope of the FUV rise.

For a long time, it was assumed that the extinction curve derived for the LMC was applicable for the galaxy as a whole. However, this early work was based solely on stars near 30 Doradus. Later work by Fitzpatrick (1985, 1986) and Clayton & Martin (1985) showed the extinction curve outside the 30 Dor region to be much less different from the Galactic ones than previously thought, with the 2175 Å feature significantly stronger than in 30 Dor.

The carrier of the 2175 Å bump has not yet been positively identified, but one of the possible candidates could be PAHs (Joblin et al. 1992).

Our pointings are nicely distributed over the LMC and can be divided into a 30 Dor group and a non-30 Dor group. Some of the stars used by Fitzpatrick (1986) in the derivation of his non-30 Dor curves are located near our sample objects N11A, N4A and N83B (e.g. Sk 19-66, Sk 2-67, Sk 19-69). It is therefore interesting to compare our PAH spectra with the properties of the extinction curves.

A comparison between the absolute PAH-feature fluxes for our 30 Dor pointings and for our other LMC objects does not show many differences (see Table 7.2). The relative intensity ratios though show a clear sequence, going from the Galaxy and the non-30 Dor pointings to 30 Dor and the SMC object B1#1 (see Figure 7.3). A similar sequence can be found for the 2175 Å bump strength, which decreases in strength going from the Milky Way to the non-30 Dor and the 30 Dor pointings and is even completely absent in the SMC (e.g. Rodrigues et al. 1997). The latter suggests a possible connection between the strength of the 2175 Å bump on one hand and the PAHs and their structure on the other hand. The direction in which the contrast of the 2175 Å feature decreases relative to the general extinction is shown in Figure 7.3.

The confirmation or refutation of PAHs as carrier of the 2175 Å bump is difficult though. Extinction curves are commonly derived from lines-of-sight towards hot stars, and it is not easy to asses the impact of the environment on the molecules. Moreover, the possibility exists that the same physical conditions responsible for our observed trends in the relative PAH-feature strengths also affect the carrier of the 2175 Å bump leading to the differences in strength of the latter. To really settle the problem of the possible PAH nature of the bump carrier, observations of PAHs and extinction curves in the same line-of-sight are needed. In the next section, we will discuss several processes affecting the strength of the different PAH features.

7.4.2 Variations in the observed PAH spectrum

Many different factors play a role in shaping the PAH spectra and their relative PAH-feature strengths. Among these are the balance between ionized and neutral PAHs, the degree of hydrogenation of the PAHs, and the size and molecular structure of the PAHs present in the source (e.g. Schutte et al. 1993; Allamandola et al. 1999b; Hudgins & Allamandola 1999a; Bakes et al. 2001). The problem one faces when analyzing a PAH spectrum is the fact that all these possible factors are interconnected, which makes it hard to single out one of those as the decisive one in shaping the spectrum. In this section, the possible contribution of the different factors to the observed trends is investigated. The connection with the PAH/dust ratio is also highlighted.

Ionization balance

The PAH charge is known to influence the PAH spectrum remarkably. Upon ionisation, the intrinsic strength of the features in the 5-10 μm region increases while the intrinsic strength of those in the 10-15 μm region decreases (Langhoff 1996; Allamandola et al. 1999b; Hudgins & Allamandola 1999a; Peeters et al. 2002a). The PAH charge is governed by the photoionization rate and electron recombination rate, and is therefore a function of the local physical conditions (Bakes & Tielens 1994; Bakes et al. 2001), in particular the electron density and

the strength of the FUV field illuminating the PDR (generally measured in units of the interstellar radiation field in the solar neighbourhood).

To investigate the possible role of the ionization balance in the observed trends, these two quantities have been determined for our sample sources. The Lyman continuum flux and the rms electron density of the H II regions were derived from radio measurements. For the LMC objects N4A, N11A, N83B and N159-5, this was based on new 6 cm radio data obtained with the Australia Compact Array radio telescope (Martín-Hernández et al. 2002, in prep.). For the Galactic sources, the radio data were taken from the literature when available (for an overview, see Martín-Hernández et al. 2002a). The Lyman continuum flux was converted to solar luminosities using the models from Vacca et al. (1996). By using the radio sizes, the local radiation field is obtained expressed in units of 1.6×10^{-6} W cm^{-2}. A distance of 55 kpc was adopted for the LMC, the distances of the Galactic sources are taken from Peeters et al. (2002b).

For 30 Doradus the estimate for the local radiation field is based on stellar population studies. Assumed is that all the radiation is emitted by R136, the stellar cluster at the core of 30 Doradus. The stellar content of R136 is taken from the stellar population list of Massey & Hunter (1998). From this stellar list a total luminosity is derived by using the same stellar atmosphere models as for the other sample objects. The flux at the pointing position is then determined from the projected distance from the center of R136 to the ISOPHOT pointings. For the derivation of the rms electron density at our positions, a 6 cm radio map of 30 Doradus is used that was kindly provided to us by Lazendic et al. (in prep.) prior to publication. As a check on the results for the radiation field as determined from the stellar population study, the Lyman continuum has also been derived from these radio data. The two different results are in very good agreement.

The balance between neutral and ionized PAHs is governed by the ratio of the local radiation field and the electron density, G/$< n_{\rm e} >$. The Galactic H II regions are found to have a systematically lower G/$< n_{\rm e} >$ than the Magellanic sources. However, no correlation is found between this parameter and any of the possible relative PAH-feature strengths. As an example, the relative PAH-feature strength $I_{6.2}/I_{11.2}$ as a function of G and G/$< n_{\rm e} >$ is shown in Figure 7.5. We therefore conclude that the differences between the relative PAH-feature strengths cannot be attributed to the ionization balance of the PAHs. It is interesting to see that, although for the four 30 Dor positions G/$< n_{\rm e} >$ shows a reasonable variation, the $I_{6.2}/I_{11.2}$ ratio for these pointings is roughly the same.

To provide us with a further check on the local radiation field and also to get an additional constraint on the derived electron density, PDR diagnostic fine-structure line ratios have been determined from the SWS and LWS data of all our LMC objects (except N11A for which no LWS data is available - Vermeij et al. (2002b)) and all the IRAS sources (Peeters et al. 2002b). This is necessary because the PAH spectrum is formed in the PDR, whereas the physical parameters derived from the radio data are more indicative of the body of ionized gas making up the H II region.

The combination of the [C II] 158 μm/[O I] 63 μm line ratio with the ([C II] 158 + [O I] 63 + [Si II] 35)/FIR ratio defines a unique set of density and radiation field G (e.g. Wolfire et al. 1990). It turns out that the Galactic and Magellanic sources have similar diagnostic ratios. Our sources lie between the $\log\, G = 3$ and $\log\, G = 4$ tracks in the diagnostic diagrams from Wolfire et al. (1990), which is in reasonable agreement with our values of the local radiation field from the radio data. The LMC and Galactic H II regions show a similar efficiency of

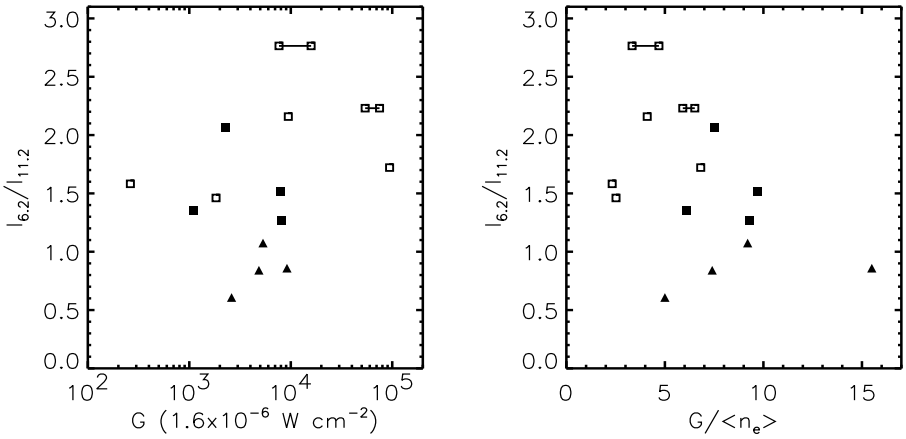

Figure 7.5 — The $I_{6.2}/I_{11.2}$ ratio versus the local radiation field G and the parameter G/$< n_e >$. The full lines join G and G/$< n_e >$ as derived using both the near and far solar distance. Plotting symbols are the same as in Fig. 7.3.

photoelectric heating as measured by the ([C II] 158 + [O I] 63 + [Si II] 35)/FIR ratio. The photoelectric effect is governed by the ionization state of the PAHs (Bakes & Tielens 1994), so these findings lend further support to our conclusion that the ionization balance of the PAHs is not responsible for the observed differences in the PAH-feature strenghts.

Dehydrogenation

Theoretical studies of dehydrogenation of interstellar PAHs have shown that for PAHs larger than $\sim$25 carbon atoms hydrogenation through reactions with abundant atomic hydrogen is more important than *de*hydrogenation through FUV photo-dissociation (Tielens et al. 1987; Allamandola et al. 1989b; Jochims et al. 1994, 1999; Allain et al. 1996). With a typical PAH size of 50 C-atoms (Tielens et al. 2000), dehydrogenation should therefore be minimal and no effect on the PAH spectrum should be seen.

Observationally, the degree of dehydrogenation can be probed best by the features in the 10 - 15 μm region. The peak position and strength of the PAH features present in this range depend on the structure of the molecule, in particular on the number of neighbouring H-atoms per ring (e.g. Bellamy 1958; Hudgins & Allamandola 1999a; Hony et al. 2001). Aromatic rings carrying CH groups which have no neighbouring CH groups are termed 'solo' CH groups, two adjacent CH groups 'duet' CH groups, and so on. Other ways to assess the degree of dehydrogenation include a non-linear behaviour between the 3.3 and 11.2 μm PAH features upon dehydrogenation (Hony et al. 2001) and the change in the ratio of the CC and CH modes.

In their observational study, Hony et al. (2001) conclude that dehydrogenation is unimportant for the objects in their sample, which includes the Galactic sources contained in ours. The LMC source with the smallest $I_{6.2}/I_{11.2}$ ratio for which there is also a reliable 3.3 μm flux (30 Dor#3), has a $I_{3.3}/I_{11.2}$ ratio that is consistent with those found in Hony et al. (2001) implying that the PAHs in this source are not dehydrogenated. This can unfortunately not be

confirmed by its 10 - 15 μm region since the PAH features there are very weak and no significant 12.7 μm feature has been detected (Sturm et al. 2000, see Section 7.4.2). Nevertheless, our conclusion is that the effect of dehydrogenation cannot fully account for the observed differences in the PAH-feature strengths.

Molecular size

With decreasing size of the molecules, the ratio of CC to CH bonds also decreases. This CC/CH ratio is most clearly reflected in the $I_{6.2}/I_{3.3}$ ratio, since the 3.3 μm band is produced by *all* the CH bonds. The 3.3 μm feature though is hardly detected in our ISOPHOT spectra, so we have to rely on the $I_{6.2}/I_{11.2}$ ratio.

Since the 11.2 μm band is only produced by the solo CH groups, the $I_{6.2}/I_{11.2}$ ratio is influenced by both the molecular structure as well as the size. If we assume that there is only a size effect and restrict ourselves to PAHs with more than 50 carbon atoms, the lower $I_{6.2}/I_{11.2}$ ratio observed in 30 Doradus and the SMC would at first suggest that the PAHs are smaller than in the Galaxy and non-30 Dor LMC sources (Schutte et al. 1993). However, the position with the lowest $I_{6.2}/\Sigma$ PAH and $I_{6.2}/I_{11.2}$ ratio (30 Dor#3) has a $I_{6.2}/I_{3.3}$ ratio that is consistent with the range observed for the Galactic H II regions. This would suggest that differences in molecular size are not responsible for the observed PAH-feature strengths.

Molecular structure

As was already mentioned in section 7.4.2, the strength of the PAH features in the 10 - 15 μm region depends on the number of neigbouring CH groups. The strength of the 11.2 μm feature, and hence the $I_{6.2}/I_{11.2}$ ratio, is therefore influenced by the molecular structure. If the observed trend in this ratio were only due to the molecular structure, this would imply that the PAH emission in the SMC source and 30 Doradus is dominated by 'smooth-edged' species (the so-called 'compact' species in Hony et al. (2001) which have long straight edges and few corners, cf. their Fig. 9) while open, 'rough-edged' structures (the so-called open, uneven species in Hony et al. (2001) with many corners, cf. their Fig. 9) are the dominant ones in the Galactic and non-30 Doradus H II regions. To have a strong handle on this, the features in the 10-15 μm spectral region are indispensible.

We carefully re-examined the spectrum of 30 Dor#3. A hint of the 12.7 μm feature is found, but it is clearly no $3\,\sigma$ detection. In order to get a feeling for the $I_{12.7}/I_{11.2}$ ratio, we took the spectra from Hony et al. (2001) with the lowest and highest $I_{12.7}/I_{11.2}$ ratio and scaled them in such a way that their 11.2 μm feature is as strong as in the 30 Dor#3 spectrum (see Figure 7.6). It is obvious from Fig. 7.6 that for the Galactic source with the highest $I_{12.7}/I_{11.2}$ ratio (IRAS 18317), the scaled 12.7 μm feature cannot be hidden in the noise of the spectrum of 30 Dor#3. The same is not true, however, for the Galactic source with the lowest $I_{12.7}/I_{11.2}$ ratio (NGC 7027). The source with a similar $I_{12.7}/I_{11.2}$ ratio as 30 Dor#3, is the reflection nebula NGC 7023, which is intermediate in the range of $I_{12.7}/I_{11.2}$ ratios studied by Hony et al. (2001). We can therefore conclude that the PAHs in 30 Dor#3 are certainly more compact when compared to those in the Galactic H II region IRAS 18317 and are probably similar to those in the reflection nebula NGC 7023.

The SMC B1#1 molecular cloud strongly exhibits a 12.7 μm feature (Reach et al. 2000). The observed $I_{12.7}/I_{11.2}$ and $I_{6.2}/I_{11.2}$ ratios for this source also point towards species that are more compact compared to those in the Galactic H II regions (Hony et al. 2001).

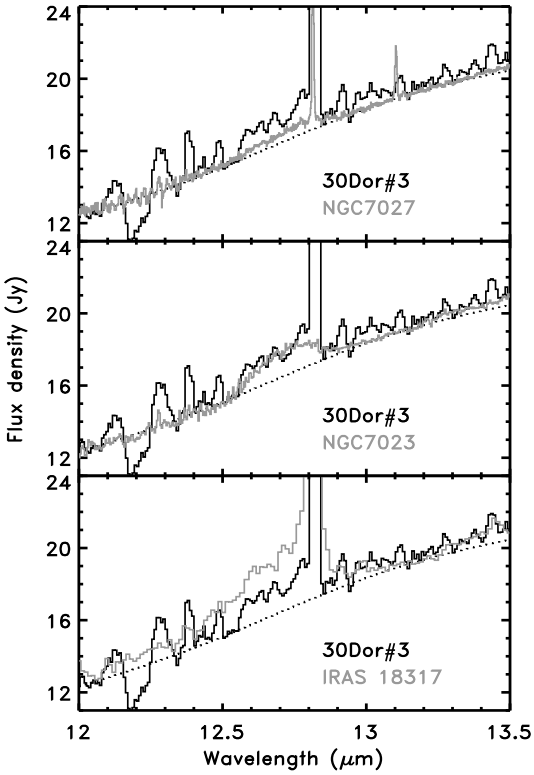

Figure 7.6 — A comparison between the 12.7 μm feature of 30 Dor#3 and the scaled 12.7 μm feature of NGC 7027 (top), NGC 7023 (middle) and IRAS 18317 (bottom). The scaling is such that the 11.2 μm feature is equally strong in all spectra. The 30 Dor#3 spectrum is shown in solid black and the scaled spectra in grey. The dotted line represents the continuum.

To summarise, the few observations present to date point towards the dominance of compact PAH species in the SMC and 30 Doradus while open, uneven structures are the dominant ones in Galactic H II regions and the non-30 Dor LMC sources.

PAH/dust abundance

An indicator of the PAH/dust abundance is the ratio between the total emission in the PAHs and the far-infrared (FIR) emission. We derived the FIR emission from LWS spectra of the objects (Vermeij et al. 2002b; Peeters et al. 2002b). The Σ PAH / FIR ratios are very similar for the Galactic and LMC sources except that the four pointings towards 30 Doradus show lower values. However, the LWS aperture is much larger compared to the ISOPHOT and ISO-SWS apertures. This ratio will therefore be influenced by the aperture differences for sources more extended then the mid-IR beam or for sources which are not isolated. It is quite certain that the mid-IR and FIR beams receive radiation from different regions in 30 Doradus. After correcting for the aperture difference (assuming a uniform, infinitely extended source), the Σ PAH / FIR ratios for the 30 Doradus observations are similar to the ratio of the other sources. Note, however, that some of the other sources are not isolated or are more extended then the mid-IR beam (but certainly smaller then the FIR beam) and could therefore suffer from the same problem.

If we assume that all the UV radiation absorbed by the dust is re-emitted in the IR, the

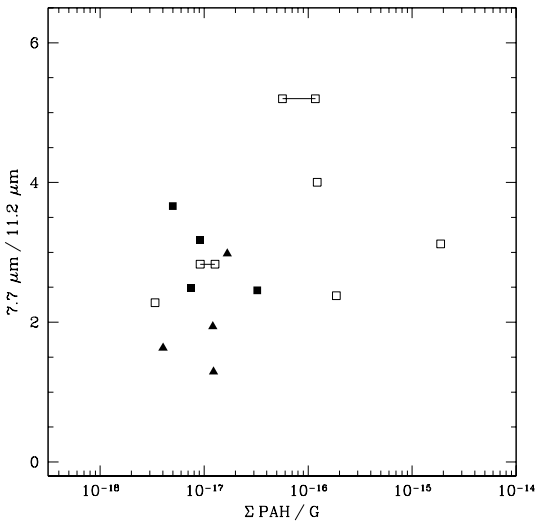

Figure 7.7 — The correlation between the $I_{7.7}/I_{11.2}$ ratio and the Σ PAH / G ratio. The full lines join the Σ PAH / G as derived using both the near and far solar distance.

Σ PAH/G ratio is an additional indicator for the PAH/dust abundance. As can be seen in Figure 7.7, the PAH/G ratio in the LMC lies at the lower end of the range covered by our sample H II regions. Both the 30 Doradus and non-30 Doradus observations have a similar Σ PAH/G ratio. The PAH / dust abundance thus appears to be very similar for the LMC sources. However, the difference in the Σ PAH/G ratio between the Magellanic Cloud and Galactic sources seems significant.

It is currently believed that PAHs form either as byproducts or intermediaries in soot formation (Frenklach & Feigelson 1989; Cherchneff et al. 1992) or as shattering products of grains (Jones et al. 1996). Apparently, the differences in metalicity and general conditions in the ISM or in soot-forming regions have some influence on the PAH/dust ratio.

7.5 Summary

In this paper a set of ISOPHOT spectra from H II regions in the Large Magellanic Cloud is presented. In all the spectra, emission bands arising from Polycyclic Aromatic Hydrocarbons (PAHs) are clearly present. These features are observed to vary considerably in relative strength to each other from source to source and even within 30Dor. The LMC spectra have been compared with ISO-SWS spectra from Galactic H II regions and with the ISOCAM observation towards a quiescent molecular cloud in the SMC (Reach et al. 2000).

A correlation is found between the $I_{7.7}/I_{11.2}$ versus $I_{6.2}/I_{11.2}$ and the $I_{8.6}/I_{11.2}$ versus $I_{6.2}/I_{11.2}$ ratios. A segregation between the sources of different type of environment, i.e. from the Milky Way to the LMC and to the SMC, is present. Furthermore, within the LMC observations, a clear distinction between 30 Doradus and non-30 Doradus pointings is found. So, the relative strength of the IR emission features correlate with the local environment.

A similar sequence can be found for the 2175 Å bump strength, which decreases in

strength from the Milky Way to the non-30 Dor pointings, to the 30 Dor pointings and is even completely absent in the SMC (e.g. Rodrigues et al. 1997). Since the lines-of-sight for the extinction derivation and for the ISOPHOT observations are very similar, this suggests that probably the same conditions responsible for the observed trends in the relative PAH-feature strengths also affect the carrier of the 2175 Å bump leading to the differences in strength of the latter.

We have discussed the different factors that influence the spectra and might explain the observed variations. Most important of these factors is the ionisation balance of the PAHs which shows no difference between the Magellanic and Galactic sources. The PAH / G ratio, which is an indicator of the PAH / dust abundance, appears to be very similar for the LMC sources, but the difference in the Σ PAH/G ratio between the Magellanic Cloud and Galactic sources seems significant. The differences in metalicity and general conditions in the ISM or in soot-forming regions have apparently some influence on the PAH / dust ratio.

The few observations present to date point towards the molecular structure as the major cause of the observed variations. Compact PAH species dominate in the SMC and in 30 Doradus, while PAH species with an open, uneven structure are the dominant ones in Galactic H II regions and the non-30 Dor LMC sources. This may reflect the effects of the local physical conditions on the composition and characteristics of the PAH family.

Acknowledgements

PIA is a joint development by the ESA Astrophysics Division and the ISO-PHT consortium.

8

A mid-IR spatial study of the compact H II regions IRAS 18434-0242 and IRAS 21190+5140

To appear as :

E. Peeters, A.G.G.M. Tielens, J. Cami, A.C.A. Boogert, T.L. Hayward

Submitted to Astronomy & Astrophysics

Abstract We present mid-infrared images and long-slit 8–13 μm spectra of the compact H II regions IRAS 18434-0242 and IRAS 21190+5140. We detect a new broad emission feature at $\sim$8.9 μm in IRAS 18434. Previous studies have shown that the 7.7 μm PAH emission feature can shift to 8.22 μm in some sources. Possibly, this new discovered 8.9 μm band is an extreme example of such a shift and its carrier is closely related to the carriers of the UIR bands. We find that in IRAS 18434, the dust continuum emission in the mid-infrared is dominated by thermal emission of dust co-located with the ionised gas and that the carrier of the 8.9 μm feature also resides inside the H II region while the PAH emission originates from the PDR. The 10 μm spectrum of IRAS 21190 reveals the presence of three different "dust" components: PAHs, silicates, and dust continuum-carriers. We calculated spectra composed of dust continuum emission and silicate emission assuming an MRN size distribution and a size dependent temperature law. We found a temperature gradient within the source for both the dust and the silicates. Furthermore, the temperature of the dust and

the silicates correlates well with each other. This correlation vanishes to the north-east of the source. We find that in this source, the dust and silicates are also co-located with the ionised gas in the arc, but to the north-east of the source, they originate in the PDR. In the arc, they are heated predominantly by trapped Lyman α photons while to the north-east they are not.

8.1 Introduction

The origin and evolution of dust in regions of massive star formation is one key question in interstellar dust research. The distribution of dust in and around the ionised gas may well contain important clues to address this question. In particular, it has long been speculated that during the star formation process, dust infall is stopped by radiation pressure from the luminous nacient protostar. Indeed, the wall of dust formed this way may stop or even reverse the infall motion of the gas as well (Larson & Starrfield 1971; Kahn 1974; Yorke 1986; Wolfire & Cassinelli 1987). This process has potentially important implications. It may control the maximum mass of stars formed (Larson & Starrfield 1971; Kahn 1974; Yorke 1986; Wolfire & Cassinelli 1987). It may also lead to deviating abundance patterns in massive stars (e.g. Mathis 1970). And, of course, it could lead to dust-free gas regions surrounding massive stars (Larson & Starrfield 1971; Kahn 1974; Yorke 1986; Wolfire & Cassinelli 1987). Furthermore, dust can also be destroyed in the ionised gas by physical or chemical sputtering (Barlow & Silk 1977; Draine & Salpeter 1979a,b).

Infrared spectroscopy can provide direct information on the composition of interstellar dust. The overall mid-infrared spectra of H II regions are dominated by strong emission features at 3.3, 6.2, 7.7, 8.6 and 11.2 μm which are generally attributed to emission by Polycyclic Aromatic Hydrocarbon (PAH) molecules (Gillett et al. 1973; Geballe et al. 1985; Cohen et al. 1986; Léger & Puget 1984; Allamandola et al. 1985, 1989b; Puget & Léger 1989; Roelfsema et al. 1996; Peeters et al. 1999; Hony et al. 2001, Chapters 2, 3 and 4). Spectroscopy of a large sample of sources whose spectra are dominated by the Unidentified InfraRed (UIR) bands have now firmly established that the detailed characteristics of these bands vary from source to source and even within sources (Bregman 1989; Bregman et al. 1989; Geballe et al. 1989; Joblin et al. 1996b; Roelfsema et al. 1996; Verstraete et al. 1996; Maillard et al. 1999; Joblin et al. 2000; Hony et al. 2001; Verstraete et al. 2001, Chapters 2, 3 and 4). These variations are likely due to chemical modifications of the interstellar PAH family reflecting local physical conditions. Potentially, studies of these variations may reveal much about the chemical characteristics of the emitting PAH family.

In Orion, this PAH emission originates from the Orion Bar, the Photo-Dissociaton Region (PDR) surrounding the ionised gas. The neutral atomic/molecular gas in the PDR is heated, photo-ionised and photo-dissociated by FUV photons ($h\nu < 13.6eV$). In some objects, the silicates have been detected in emission from regions closer to the ionising star; notably the Trapezium region in the Orion H II region (Stein & Gillett 1969; Ney et al. 1973; Forrest et al. 1975). This dichotomy – PAH emission solely from the PDR and silicate emission either absent or from the ionised gas – in the mid-infrared spectra in Orion is not well understood. Partly, it may reflect that silicate grains in the PDR in Orion are too cold ($\sim$ 75 K) to emit in the mid-infrared. PAH molecules, on the other hand, are heated to high temperatures ($\sim$1000 K) through the absorption of a single FUV photon and have to dump their energy at mid-infrared wavelengths. This interpretation of this dichotomy has two implications. First,

there are few very small ($\lesssim$30 Å) silicates which could be transiently heated by a single photon to temperatures of some 300 K (i.e., emit in the 10 μm feature). The precise limits on the abundances of such small silicates are still somewhat controversial (Desert et al. 1986, 1990; Draine & Li 2001), but it is clear that, from an energetic point of view, such small silicates have to be unimportant. Second, PAH molecules have to be rapidly ($\lesssim 10^5 year$) destroyed in the ionised gas in Orion. Such PAH molecules might be destroyed by the much more energetic (upto 54 eV) photons available inside the H II region. PAHs could also be destroyed through chemical reactions initiated by energetic photons ($E_K \sim 1eV$). Spatially resolved studies of the relative strength of the PAH features in the PDR already point towards the importance of photo-chemical modifications of the PAHs, even at the lower photon energies and kinetic energies available in the FUV (Geballe et al. 1989; Joblin et al. 1996a). It is clear that further observational studies on the spatial distribution of the various emission components is very important to address these questions.

Here, we have selected two sources - IRAS 18434-0242 (G29.96-0.02, hereafter IRAS 18434) and IRAS 21190+5140 (M1-78, hereafter IRAS 21190) – for a detailed spatially resolved spectroscopic study of the IR characteristics of the PAHs and dust in the 10 μm ground-based window. The ISO-SWS spectrum of IRAS 18434 shows – beside the well-known UIR bands – a strong emission band around 8.6 μm. This emission feature is much stronger and much broader then the 8.6 μm PAH emission features observed in a variety of astronomical sources (Chapter 3). Therefore, this band is a unique spectral characteristic of this source and a further study is warranted to investigate its characteristics and, in particular, its relationship to the UIR bands. The source IRAS 21190 shows a "classic" UIR band spectrum (Roelfsema et al. 1996; Peeters et al. 1999; Hony et al. 2001, Chapters 3 and 4) superimposed on silicate emission and a rising dust continuum. Hence, this seems a good object to study spatially the distribution of the PAH emission features in relation to the dust continuum and the silicate emission feature.

In Sect. 8.2, we review the characteristics of both sources. Sect. 8.3 describes the observations and the data reduction. Subsequently, the data are presented and analysed in Sect. 8.4. In Sect. 8.5, the nature of the newly detected emission feature in IRAS 18434 is highlighted; the silicate emission feature and the dust continuum in IRAS 21190 is reproduced by a simple model and subsequently, the implications of the spatial distribution of the different dust components in both sources are described. Finally, Sect. 8.6 summarises our main results.

8.2 Source characteristics

IRAS 18434-0242 is one of the best studied compact HII region and classified as cometary (Wood & Churchwell 1989). This compact H II region appears as a sharp edge-brightened arc-like structure with a low surface-brightness tail of emission trailing off opposite the bright arc (Wood & Churchwell 1989, 1991; Afflerbach et al. 1994; Cesaroni et al. 1994; Fey et al. 1995; Kim & Koo 2001).

In order to explain the cometary morphology and velocity structure of this source, two competing models has been proposed : the bow shock model (Wood & Churchwell 1989, 1991; Mac Low et al. 1991; van Buren & Mac Low 1992; Afflerbach et al. 1994) and the champagne flow model (Fey et al. 1995; Lumsden & Hoare 1996; Pratap et al. 1999; Lumsden & Hoare 1999). In the bow shock model, the cometary morphology is considered to be formed by the bow shock of the wind of a massive star moving supersonically through the

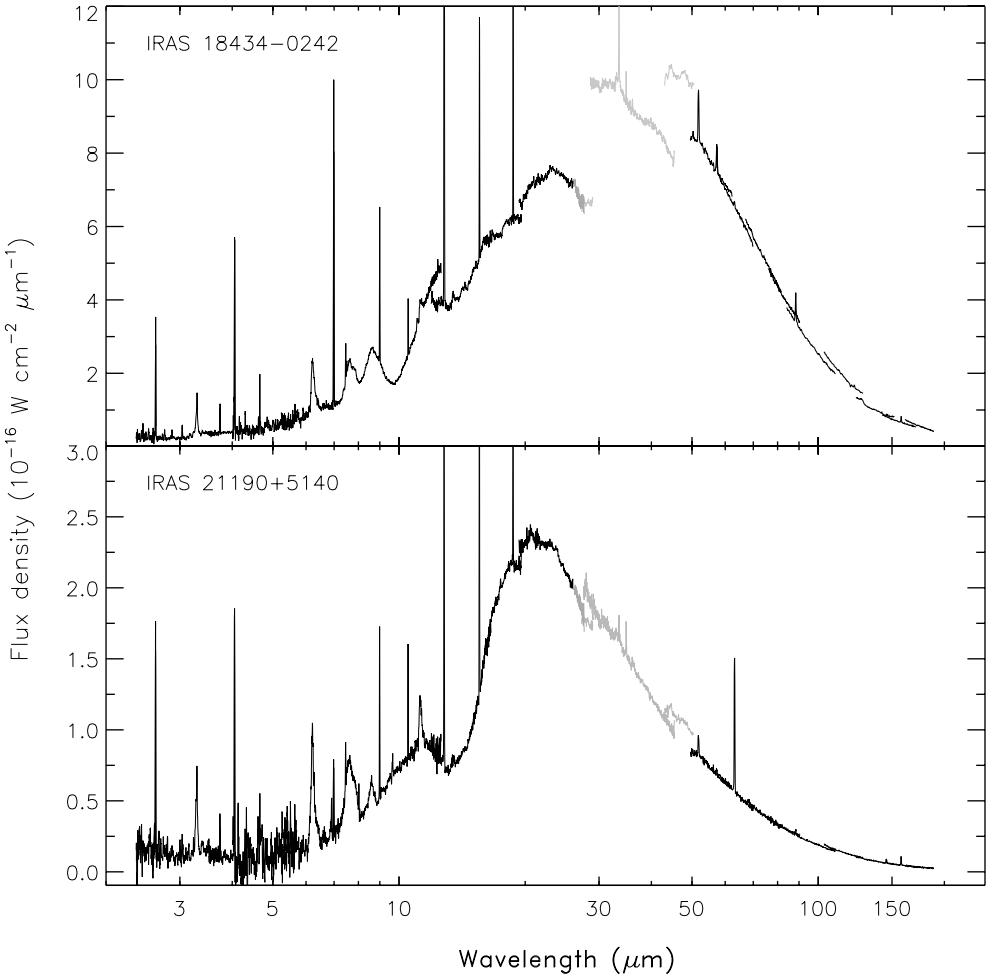

Figure 8.1 — The combined SWS-LWS spectra of IRAS 18434 and IRAS 21190 (Peeters et al., Chapter 2). The parts of the spectra corresponding to the poorly calibrated SWS Band 3E and 4, the leak in band 3D and LWS SW1 detector are shown in gray tones (for details see Chapter 2).

surrounding molecular cloud (Hughes & Viner 1976; Weaver et al. 1977; van Buren et al. 1990). In the champagne model, this morphology is due to the expansion of the H II region into a molecular medium with a steep density gradient (Yorke 1986).

Using near-infrared imaging, Fey et al. (1995), Lumsden & Hoare (1996), Watson et al. (1997) and Pratap et al. (1999) found that IRAS 18434 is embedded in a young stellar cluster and identified the bright star in the center of the nebula as the exciting star of IRAS 18434. Watson & Hanson (1997) obtained the first K-band spectrum of the ionising star which indicates a spectral type between O5 and O8 assuming it is a main sequence star. Recent

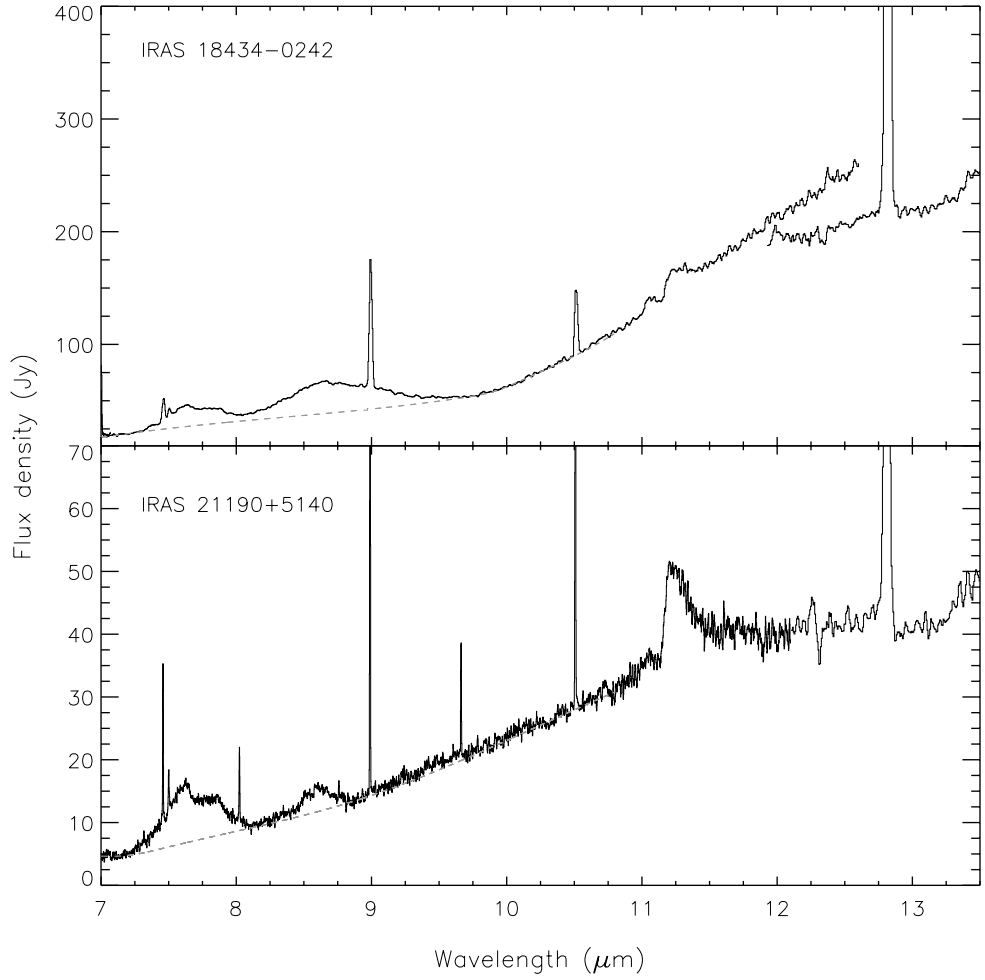

Figure 8.2 — The ISO-SWS spectra of IRAS 18434 and IRAS 21190 in the mid-infrared wavelength range accessible from earth (Peeters et al. 1999, Peeters et al., Chapter 2). The top panel shows the spectrum of IRAS 18434. Note the strong, broad emission band around 8.6 μm. The bottom panel shows the high-resolution spectrum of IRAS 21190 except longwards of 12 μm where the medium-resolution spectrum of this source is shown. The adopted continuum is shown by the dashed lines in both panels.

high resolution K-band spectroscopy of this ionising star narrows the spectral type to O6-O5 (Kaper et al. 2002a,b). An overview of the spectral type derived by different methods is given by Martín-Hernández et al. (2003).

The IRAS 18434 H II region is embedded in a molecular cloud that has been extensively studied at low spatial resolution (Churchwell et al. 1990, 1992). Subsequent high resolution

data indicate the presence of a hot core (HC) located $\sim 2''$ west of the arc (Cesaroni et al. 1994, 1998; Hatchell et al. 1998; Pratap et al. 1999; Maxia et al. 2001). This HC has been recently observed at mid-infrared wavelengths (De Buizer et al. 2002). Detection of H_2O, H_2CO and CH_3OH masers (Pratap et al. 1994; Hofner & Churchwell 1996; Walsh et al. 1998; Minier et al. 2000; Minier & Booth 2002) which are strongly associated with recent star formation towards the core and the $\sim 2''$ separation between the hot core and the compact H II region indicate that the hot core is not heated by the ionising star of IRAS 18434 but rather harbours a massive proto-star which has not yet ionised a compact H II region. This is supported by recent millimeter studies indicating the presence of an embedded outflow in the hot core perpendicular to the direction of the H II region (A. Gibb, private communication).

Watson et al. (1997) derived a map of the apparent extinction based upon the 2 cm radio continuum map (Fey et al. 1995) and their 2.17 μm Brγ map. They found that the apparent extinction at Brγ varies from 1.8 to 2.6 mag being higher in the arc and toward the end of the extension in the southeast. They give a mean value A_K = 2.14 $\pm$ 0.25 and A_K = 2.2 $\pm$ 0.25 for the ionising star. Pratap et al. (1999) estimated A_K = 2.2 $\pm$ 0.1 towards the ionising star based on the stars H-K colour. Based on hydrogen recombination lines observed with ISO-SWS, Martín-Hernández et al. (2002a) reported an average extinction of A_K=1.6. Martín-Hernández et al. (2002a) attribute their lower extinction to the fact that the contribution of the extended envelope around the compact H II region (Kim & Koo 2001) to the SWS aperture may cause ISO-SWS to observe a lower hydrogen column density than the ones observed by the high $\sim 1''$ resolution observations of Watson et al. (1997) and Pratap et al. (1999). In addition, Pratap et al. (1999) concluded that the extinction up to an $A_K \sim 1.3$ is dominated by foreground extinction which appears to arise primarily from the diffuse ISM.

Prior to ISO, IRAS 18434 was first observed at mid-infrared wavelengths by Soifer & Pipher (1975). Subsequent observations were mainly focused on the fine-structure lines (Herter et al. 1981; Lacy et al. 1982; Simpson et al. 1995; Afflerbach et al. 1997; Watarai et al. 1998) in order to derive the elemental abundances and/or the spectral type of the ionising star. The appearance of IRAS 18434 at mid-infrared wavelengths is very similar to the radio maps (Ball et al. 1996) and low-resolution mid-infrared spectra revealed the presence of a strong dust continuum, silicate in absorption and PAH emission (Soifer & Pipher 1975; Faison et al. 1998; Jourdain de Muizon et al. 1990; Zavagno et al. 1992). The ISO spectrum of this source is shown in Figs. 8.1 and 8.2. It is dominated by a strong continuum due to the thermal emission of dust with peak at about ~ 40 μm implying a temperature of some 70 K. The presence of silicate absorption indicates that IRAS 18434 is surrounded by cold dust. In addition, it shows bright mid-infrared PAH emission features. Hence, IRAS 18434 exhibits an infrared spectrum typical for compact H II regions (Chapter 2). The only peculiarity is the broad emission band around ~ 8.6 μm which is clearly different from the "classical" 8.6 μm PAH emission feature (Chapter 3).

The Galactocentric distance to IRAS 18434 is 4.6 kpc. Arguments based on extinction and the spectral type of the ionising star proposed by Pratap et al. (1999) favour the near heliocentric distance. Hence, we adopt the near distance of 5.7 kpc (Chap. 2). At this distance, $1'' = 0.028$ pc.

IRAS 21190+5140 has first been classified as a planetary nebula but is now generally classified as a compact H II region. To establish its object type, this source has been extensively studied at radio and sub-millimeter wavelengths (Zuckermann et al. 1977; Scott & Harris

1978; Purton et al. 1982; Isaacman 1984b; Puche et al. 1988; Zijlstra et al. 1990; Gussie & Taylor 1995). This compact H II region appears as a shell expanding into a molecular cloud situated to the south (Zijlstra et al. 1990).

Scott & Harris (1978) reported the presence of an optical nebula on the POSS-I[1] R band with a significant central concentration possibly indicative of an exciting star (positioned at 21h20m44.66s±0.05s, 51d53m25.7s±0.4s; J2000). Furthermore, at the position of IRAS 21190, emission is also seen in the POSS-II[1] B, R and I bands and in the 2MASS[2] J, H, and K_s bands. The fact that an optical nebula is observed towards IRAS 21190 is consistent with the derived extinction, based on the hydrogen recombination lines, of A_K = 0 (Martín-Hernández et al. 2002a).

Several near-infrared spectra of IRAS 21190 have been obtained showing emission of atomic hydrogen and helium, [Fe II] and molecular hydrogen (Isaacman 1984a; Hora et al. 1999; Lumsden et al. 2001a,b). The source has been imaged in the K-band (Latter et al. 1995), showing a similar morphology as the radio data. The only mid-infrared spectra of this source prior to the ISO observations, were taken by Cohen & Barlow (1974) and by IRAS-LRS (Jourdain de Muizon et al. 1990; Zavagno et al. 1992) and exhibit a steep rise longwards of 3.6 μm. The ISO spectrum of this source is unique (Figs. 8.1 and 8.2). Unlike most other sources, it shows clear silicate emission bands at about 10 and 20 μm. From the profile of the bands an emission temperature of some 140 K is implied. In addition, it shows bright mid-infrared PAH emission features typical for H II regions (Chapters 3 and 4) and does not suffer from extinction.

The spectral type of the ionising star can be determined in various indirect ways. First, the total bolometric luminosity obtained from the IRAS PSC fluxes is $\log L/L_\odot$ = 5.3 (Chapter 2). The flux seen by ISO in the four IRAS bands at 12, 25, 60 and 100 μm agrees well to within the uncertainty with the IRAS PSC fluxes (cf. Chapter 2) indicating that there are no contributions from other sources to the derived luminosity. Using the calibration of Vacca et al. (1996) for a main sequence star, this luminosity corresponds to a star with an effective temperature T_{eff} of 40 kK. This effective temperature, using the new calibration of Martins et al. (2002) based on non-LTE line blanketed atmosphere models including stellar winds, corresponds to a spectral type of O6. Second, the number of Lyman continuum photons derived from radio observations is $\log(N_{Lyc}) = 48.6$ s^{-1} (Martín-Hernández et al. 2002a). This value must be taken as a lower limit of the true stellar ionising flux since a significant fraction of the UV radiation might be absorbed by dust located within the ionised gas. Based on the Vacca et al. (1996) calibration, this corresponds to a star with an effective temperature T_{eff} of $\geq$ 36 kK and hence to a spectral type earlier than O7.5 (Martins et al. 2002). Third, based on the dependence of the fine-structure line ratios [S IV]/[S III] 10.5/18.7 μm and [Ne III]/[Ne II] 15.5/12.8 μm on the stellar effective temperature T_{eff} as given by photoionisation models, an indication of the spectral type can be obtained. Martín-Hernández et al.

[1]The Digitized Sky Survey was produced at the Space Telescope Science Institute under U.S. Government grant NAG W-2166. The images of these surveys are based on photographic data obtained using the Oschin Schmidt Telescope on Palomar Mountain and the UK Schmidt Telescope. The National Geographic Society - Palomar Observatory Sky Atlas (POSS-I) was made by the Caltec with grants from the National Geographic Society. The Second Palomar Observatory Sky Survey (POSS-II) was made by the Caltec with funds from the National Science Foundation, the NASA, the National Geographic Society, the Sloan Foundation, the Samuel Oschin Foundation, and the Eastman Kodak Corporation.

[2]The Two Micron All Sky Survey (2MASS) is a joint project of the University of Massachusetts and IPAC/CALTECH, funded by NASA and the National Science Foundation.

(2002c) present predictions for the [S IV]/[S III] 10.5/18.7 μm and [Ne III]/[Ne II] 15.5/12.8 μm line ratios as a function of T_{eff} using the photoionisation code CLOUDY in combination with the WM-basic stellar atmosphere models by Pauldrach et al. (2001) (for a number of hydrogen ionising photons of $Q_H = 10^{48}$ photons s^{-1} and $n_H = 10^3\,cm^{-3}$). The observed SWS line ratios of [S IV]/[S III] 10.5/18.7 μm and [Ne III]/[Ne II] 15.5/12.8 μm (Chapter 2) fall in the range of 35–40 kK (Fig. 2 of Martín-Hernández et al. 2002c). Based on the Martins et al. (2002) calibration, this corresponds to a main sequence star with spectral type of O6–O8. Summarising, these three indirect methods to derive the spectral type of the ionising star agree very well and point towards a star with spectral type of O6–O8.

The assumed distance is 8.9 kpc (Chapter 2). At this distance, 1″ = 0.043 pc.

8.3 Observations and Data Reduction

We observed IRAS 21190+5140 and IRAS 18434-0242 on the night September 10-11, 2000 and the night July 5-6, 2001 respectively using the SpectroCam-10 (SC10) mid-IR imaging spectrograph (Hayward et al. 1993) on the 5m Hale telescope at Palomar Observatory. SC10 uses a 128×128 Si:As BIBIB (Back Illuminated Blocked Impurity Band) array and can function as both a camera and a long-slit spectrograph. Its pixels subtend 0.″256 on the sky. All observations were made using a standard chop and nod sequence in beam-switching mode in order to correct for background emission from the telescope and the sky. The chopper throw is 30″ in the N-S direction for all observations. Images were made through the filters ($\sim$1 μm bandpass) centered at 10.3 and 11.7 μm of IRAS 21190 and through the filters centered at 8.8, 10.3 and 11.7 μm of IRAS 18434. In addition, low-resolution spectra are taken through 1″×16.″4 and/or 2″×16.″4 slits which provided a spectral resolution of R=$\lambda/\Delta\lambda \sim$ 100 and 60 respectively. The spectra were taken in three overlapping segments : 8.0–10.5, 9.2–12.2 and 10.4–13.4 μm. These observations are diffraction limited since we use the MINC tip-tilt system. During the second night the seeing was worse leading to a FWHM of 0.7–1.2" for a standard star. The log of the observations of both sources can be found in Table 8.1. The absolute positions of the mid-infrared sources are unknown. No attempt was made to achieve accurate astrometry at the telescope due to time constraints.

The images and spectra are processed using a library of custom routines written for the IDL environment by Hayward. The data processing includes removing bad pixels and/or frames, co-adding individual frames of an integration, dividing by flat-field images and combining the three spectral segments into a single two-dimensional (1 spectral and 1 spatial dimension) 8-13.2 μm spectral image of the sources along the different slits.

The images are flux-calibrated against γ Aql for IRAS 18434 and γ Aql and β Peg for IRAS 21190 observed at similar air-mass. The mutual registration of the images was based on the assumption that the overall morphology is the same at every wavelength. In this way, the peak intensities observed in each filter coincide for IRAS 21190 while for IRAS 18434, the position of the peak intensities at the three wavelengths are offset by 0.″256.

The spectra are wavelength calibrated using the 9.49 and 11.73 μm telluric absorption features as reference points. Some observations (slit 4 for IRAS 18434 and slits 4 and 6 for IRAS 21190) have no or low flux and hence show no or low S/N telluric absorption features. In this case, the wavelength calibration is done using the fine-structure emission lines of [S IV] at 10.5 (if present) and of [Ne II] at 12.8 μm and the PAH emission feature at 11.2 μm.

Table 8.1 — Journal of observations.

Source	Spectroscopy Slit[a]	width	t_{int} [b] (s)	Imaging Filter	t_{int} [b] (s)
IRAS 21190	1	1″	3802	10.3	163
	2	2″	950	11.7	366
	3	2″	950		
	4	2″	1267		
	5	2″	950		
	6	2″	950		
IRAS 18434	1	1″	2546	8.8	79
	2	1″	3819	10.3	118
	3	1″	3819	11.7	432
	4	1″	3819		

[a] : Slit positions indicated in Fig. 8.8.
[b] : Total integration time. The on-source integration time is ∼40% of t_{int} due to chopping and nodding.

The spectra of IRAS 18434 are flux-calibrated against γ Aql observed through the same slit and at similar air-mass as the target in combination with the absolute αLyr model from Cohen et al. (1992). The spectra of IRAS 21190 are flux-calibrated against β Peg observed through the same slit and at similar air-mass as the target in combination with archival SC10 ratio spectra of this star versus αLyr and the absolute αLyr model from Cohen et al. (1992).

While observing the standard star through the 2″ slit, we de-focused in order to obtain a similar spectral resolution as that of the observations of the extended source IRAS 21190 in this slit. In this way, the telluric absorption features in the source's spectra are properly removed. As a consequence, part of the total flux of the standard star falls outside the slit and hence the absolute flux calibration is not accurate. By comparing observations of the standard star in the 2″ slit, both focused and de-focused, an estimate of the loss is obtained and this is used for optimising the absolute flux calibration. Analogously, an estimate of the flux loss in the 1″ slit is obtained and is used for optimising the absolute flux calibration of the spectra of IRAS 21190 observed through the 1″ slit. For IRAS 18434, no correction is applied to the absolute flux calibration for this effect since all observations are done with a 1″ slit. Hence the same factor applies for all spectra and cancels out when taking relative fluxes. No cross calibration is done for the different slits.

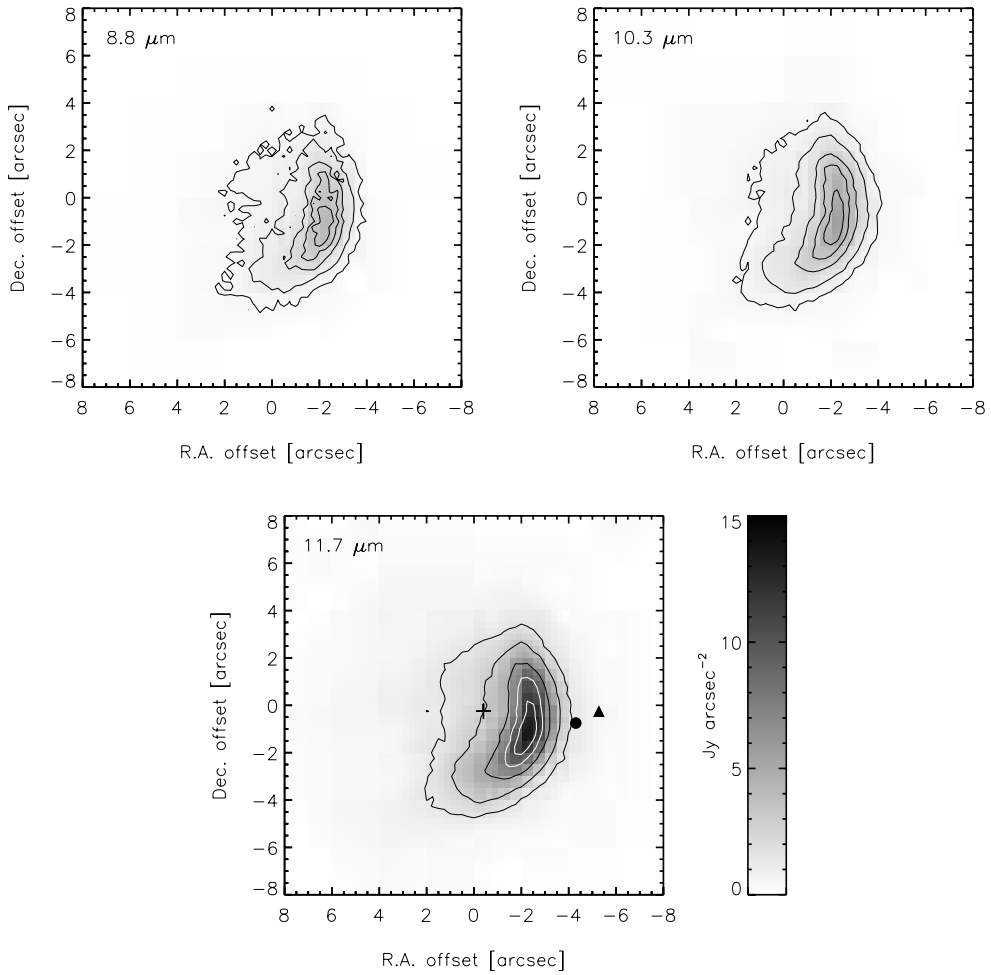

Figure 8.3 — Shown are the 8.8, 10.3 and 11.7 μm image of IRAS 18434 ($\sim$1 μm bandpass). The gray scale is the same for all plots and indicated by the colorbar. The contour levels are 0.1, 0.2, 0.4, 0.6 and 0.8 times the peak intensity for each image. This corresponds to 6, 12, 24, 37 and 49 times the image rms σ = 77 mJy arscec^{-2} for the 8.8 μm image; to 7, 14, 28, 42 and 56 times the image rms σ = 85 mJy arscec^{-2} for the 10.3 μm image and to 11, 22, 44, 66 and 88 times the image rms σ = 136 mJy arscec^{-2} for the 11.7 μm image. The position of the ionising star is shown by $+$, the NH_3 emission (Cesaroni et al. 1998) by the $\bullet$ and the the methanol maser (Minier et al. 2000) by a filled $\triangle$.

8.4 The Data

8.4.1 Infrared images

IRAS 18434

The three broad band images centered at 8.8, 10.3 and 11.7 μm are shown in Fig. 8.3. The three images are registered to the same coordinate system so that a given location represents

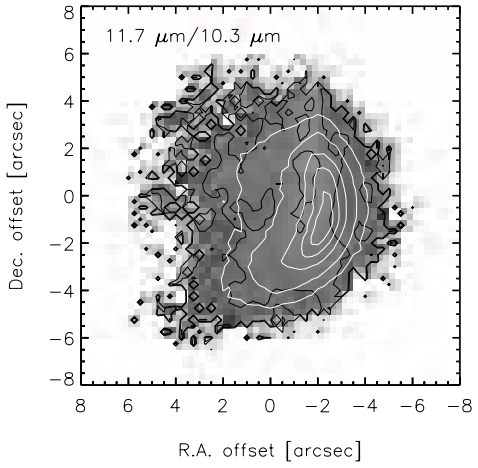

Figure 8.4 — Shown is the ratio of the 11.7 μm to the 10.3 μm images of IRAS 18434 by the gray-scale image and the black contours for those regions where both the 10.3 and 11.7 μm emission exceeds 2σ. The contour levels are 0.38, 0.45 and 0.6 times the maximum value of the ratio. The white contours are those of the 11.7 μm image in 8.3.

the same physical point in the source in all three maps. In each image, the contours present the surface brightness at the same level relative to the peak surface brightness while the gray scale in the three images is over the same range of absolute intensities.

Like at other wavelengths (e.g. Wood & Churchwell 1989; Watson et al. 1997; De Buizer et al. 2002; Martín-Hernández et al. 2003), this source has a cometary appearance in the mid-infrared (Ball et al. 1996, see Fig. 8.3). Comparing the images at different mid-infrared wavelengths with each other, we note the similarity in the cometary morphology. The filamentary-like structures observed at 2 cm Fey et al. (1995) and in the Brγ map (Watson et al. 1997) are not seen in our images. De Buizer et al. (2002) observed the hot core in their high resolution images of this source in the N-band filter (λ_0=10.46 μm, $\Delta\lambda$=5.1 μm) with a flux density of 113$\pm$17mJy. We see no evidence for this HC in our images, probably due to the lower spatial resolution and lower sensitivity of our data. Furthermore, our filters are much narrower than the N band filter of De Buizer et al. (2002).

A comparison of the different maps also illustrate well the increase in flux towards longer wavelengths. This increase towards longer wavelengths is due to the combination of a rising dust continuum with increasing wavelength and the presence of the silicate absorption feature partially included in both the 8.8 and 10.3 μm filters (see Fig. 8.2). The ratio of the 11.7 μm to the 10.3 μm images is shown in Fig. 8.4. Since the variation of the extinction over the source is relatively small (Watson et al. 1997), this ratio corresponds to the colorindex. The ratio changes very little over the source i.e. the ratio over most of the source is in the range of 0.38–0.45 of the peak ratio. The extreme values are only seen at the edges and are likely not significant. This is consistent with the results of (Ball et al. 1996). These authors found that the dust temperature is nearly uniform based upon their 8.5 and 12.0 μm images.

Because of the unknown absolute position of the mid-infrared source, comparison with

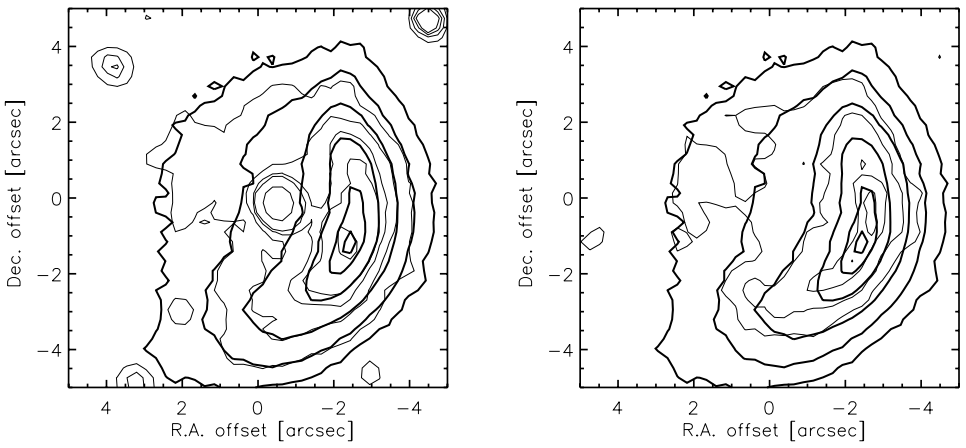

Figure 8.5 — Comparison of the 11.7 μm map of IRAS 18434 with the 6 cm radio map of Wood & Churchwell (1989) (right panel) and the H_2 map of Martín-Hernández et al. (2003) (left panel). Registration of the mid-infrared map is by alignment of the arcs at near-infrared and mid-infrared. The thick black contours represent the 11.7 μm map and the thin black contours show the 6 cm radio map and the H_2 map in respectively the right and left panel.

maps at other wavelengths is not straightforward. However, given the similarity of the morphology of the arc at near -and mid-infrared and radio wavelengths, we would expect both arcs to closely coincide. Comparison of the H_2 map of Martín-Hernández et al. (2003) with the 6 cm observations of Wood & Churchwell (1989) - both with known absolute positions - reveals that the overall morphology of the source is very similar, though the peak intensity in both maps is slightly displaced and the arcs are slightly tilted. Registration of the mid-infrared data to the H_2 map of Martín-Hernández et al. (2003) by alignment of the peak intensities reveals a very good match (see Fig. 8.5, right panel). The arc and the peak intensity coincide at both wavelengths. In the H_2 map, the ionising star is present. The right panel of Fig. 8.5 compares the radio data and the mid-infrared data (registered to the H_2 map). The offset in peak intensities at IR and radio wavelengths may result from variation in density which tend to enhance radio emission more. We note that the radio peak is located at the position where the bow shock interacts with the hot core and the density is likely highest.

IRAS 21190

The two broad band images centered at 10.3 and 11.7 μm are shown in Fig. 8.6. The two images are registered to the same coordinate system so that a given location represents the same physical point in the source in both maps. In each image, the contours present the surface brightness at the same level relative to the peak surface brightness while the gray scale in both images is over the same range of absolute intensities.

Both maps show an overall oval structure encompassing a prominent arc of which the tail at both sides converge towards a blob of emission at the northeast. The arc seems to be slightly thicker in the 10.3 μm image compared to the 11.7 μm image. At a distance of 8.9

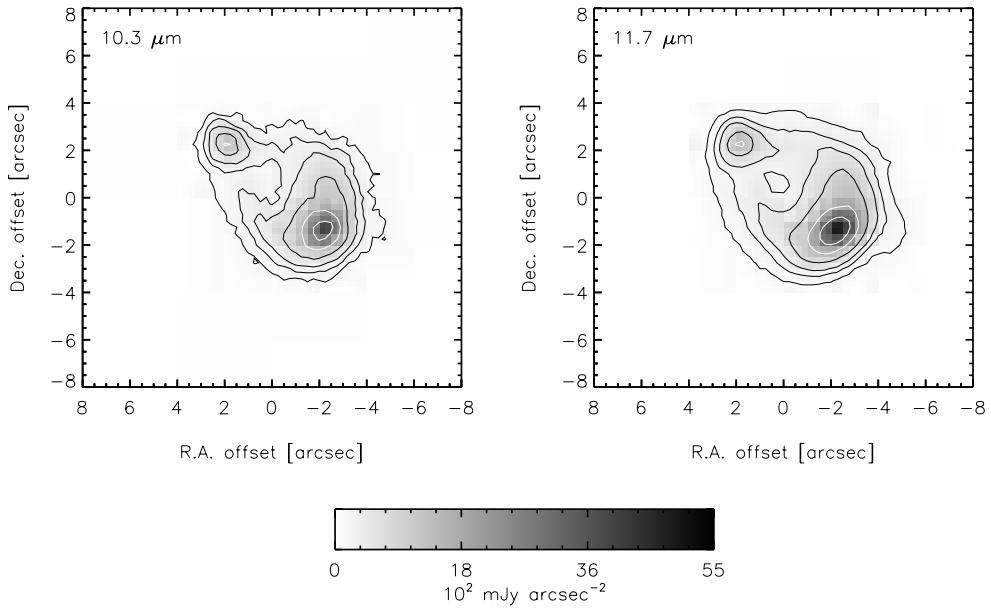

Figure 8.6 — Shown are the 10.3 μm image (top panel) and 11.7 μm image (bottom panel) of IRAS 21190 (both with $\sim$1 μm bandpass). The gray scale is the same for the two plots and indicated by the colorbar. The contour levels are 0.03, 0.06, 0.1, 0.2, 0.4 and 0.7 times the peak intensity for each image. This corresponds to respectively 7, 14, 24, 48, 95 and 167 times the image rms σ = 19 mJy arscec^{-2} for the 10.3 μm image and to respectively 15, 30, 50, 99, 198 and 346 times the image rms σ = 9 mJy arscec^{-2} for the 11.7 μm image.

kpc, the size of 9 $''\times$ 8 $''$ corresponds to 0.39 pc $\times$ 0.34 pc. A comparison of the different maps also illustrates well the slight increase in flux towards longer wavelengths. This increase towards longer wavelengths is due to PAH emission and/or the rising dust continuum dominating the decrease of the silicate emission (see Fig. 8.2). For this source, no direct physical interpretation can be attached to the ratio of the 11.7 μm to the 10.3 μm images since different emission components (silicate and PAH emission and dust continuum) are present.

Because of the unknown absolute position of the SC10 images, comparison with maps at other wavelengths is not straightforward. For comparison with the K-band image of Latter et al. (1995) – with a spatial resolution of 0.12$''$ / pixel – we therefore align the peaks of the arc of the K-band and mid-infrared (11.7 μm) emission in order to stress any spatial difference. Likely, the most natural way to overlay these images is to align the center of the oval structure. The overlay of the both infrared maps is shown in Fig. 8.7. Clearly, the separation between the blob in the northeast and the peak emission in the arc is different, being largest at the mid-infrared. The separation between the two peaks is 4.9$''$ in the K-band and 5.4$''$ in the mid-infrared. Despite this difference in scale size, the general morphology is very similar. As in the mid-infrared, the K-band image shows a prominent arc of which the tail converge towards the blob of emission at the northeast. The 4.9 and 1.42 GHz radio maps (Zijlstra et al. 1990; Puche et al. 1988) also show similar structure as the infrared data.

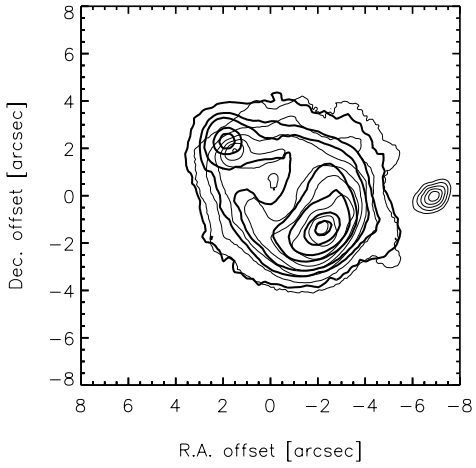

Figure 8.7 — Comparison of the 11.7 μm map of IRAS 21190 with the K-band image of Latter et al. (1995). Registration of the mid-infrared map is by alignment of the peak intensities at mid-infrared and near-infrared for the emission in the arc in order to stress the spatial variation. The thick black contours represent the 11.7 μm map and the thin black contours show the K-band image. Contour levels of the 11.7 μm map are as in Fig. 8.6. It is clear that the source's spatial distribution differs between both wavelengths.

The POSS-II B image clearly shows two emission peaks of which one is centered on the arc and the second emission peak is centered to the west of the arc - at the same location as the point-source in the K-band (see Fig. 8.7). The POSS-II R and I bands show a similar spatial structure that encompasses the two peaks seen in the POSS-II B band and 2MASS observed one main peak with a extension towards the West.

8.4.2 The Spectra

The position of the different slits typically to $\pm 0.5''$ accuracy are shown on top of the 11.7 μm image of IRAS 18434 and IRAS 21190 in Fig. 8.8. The 6 slits of IRAS 21190 completely cover the emission of the source at mid-infrared wavelengths but for IRAS 18434 complete coverage was not achieved. For further study, we have divided each slit into 7 zones for IRAS 18434 and 5 zones for IRAS 21190. We extracted spectra from each of these zones from the calibrated 2-D spectral image, which represent the flux densities within a zone.

IRAS 18434

Fig. 8.9 presents a few typical spectra of IRAS 18434 illustrating the spectral variety. These mid-infrared spectra clearly show a broad emission band at $\sim$8.6 μm, silicate absorption at 9.7 μm and fine-structure line emission of [Ne II] at 12.8 μm on top of a dust continuum (see also Sect. 8.2). Fine-structure line emission of [Ar III] at 8.98 μm as well as the 11.2 μm PAH emission band are weakly present in some spectra. In contrast, there is no evidence for the "classical" 8.6 μm PAH band and no significant emission is seen from the fine-structure line of [S IV] at 10.5 μm in all but three individual spectra.

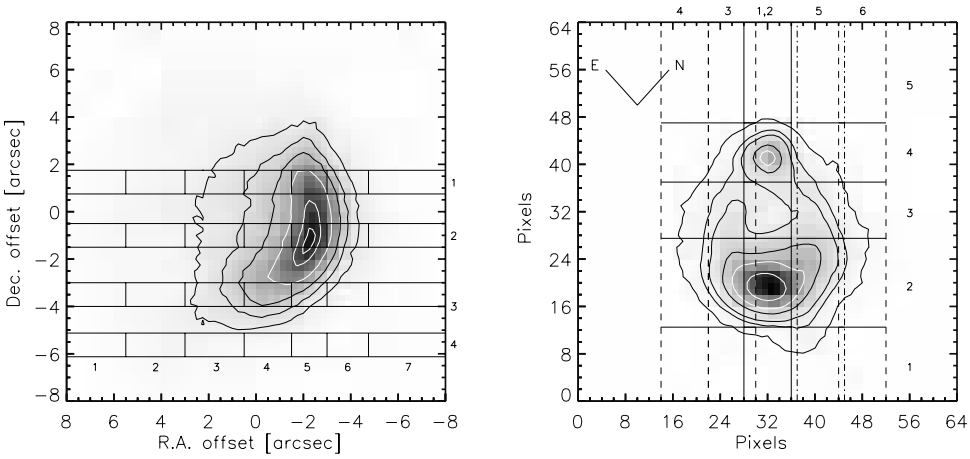

Figure 8.8 — The positions of the spectrograph slit and the zones used to extract the spectra for IRAS 18434 (left) and IRAS 21190 (right) on top of its 11.7 μm image. Contour levels are as in Figs. 8.3 and 8.6. *(Left)* The slit number is shown at the right axis and the zone numbering is shown in the plot window at the bottom. *(Right)* The slit number is shown above the top axis and the zone numbering is shown at the right in the plot window. Slit 2 is represented by full lines, slit 1 is at similar position but has a width of $1''$, slits 3, 4 and 6 are represented by stripes and slit 5 by dot-stripes.

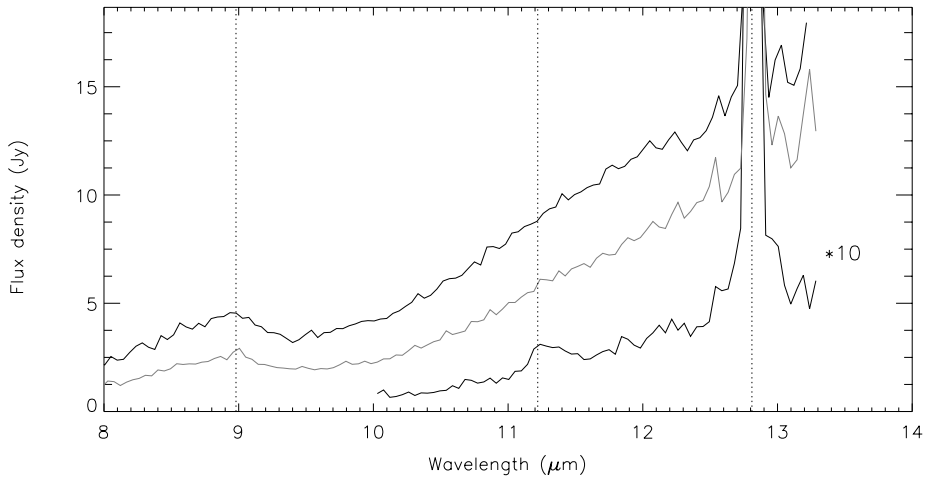

Figure 8.9 — Typical spectra of IRAS 18434 normalised to an area of $1'' \times 1''$ and corresponding to slit 2, zone 3 (top spectrum), slit 3, zone 4 (middle spectrum) and to slit 4, zone 7 (bottom spectrum). The present emission features are the [Ar III] fine-structure line at 8.98 μm, the silicate absorption feature at 9.7 μm, the PAH feature at 11.2 μm and the [Ne II] fine-structure line at 12.8 μm. Remark also the broad emission feature from 8 to 9.5 μm which is also seen in the ISO data (Fig. 8.2).

Table 8.2 — The average apparent extinction in each zone (see text for details).

Slit	A_K						
	Zone 1	Zone 2	Zone 3	Zone 4	Zone 5	Zone 6	Zone 7
1	2.1	2.1	2.2	2.3	2.4	2.0	1.6*
2	2.1	2.1	2.2	2.4	2.5	2.1	1.6*
3	2.2	2.1	2.3	2.3	2.1	1.8	1.6*
4	2.1	2.0	2.0	1.6*	1.6*	1.6*	1.6*

$*$: Martín-Hernández et al. (2002a), others derived from Fig. 4 of Watson et al. (1997).

Since the profile of the emission band at 8.6 μm may be strongly influenced by silicate absorption, we correct the spectra for extinction. The extinction at mid-IR wavelengths is derived by using the results tabulated in Mathis (1990); namely, $A_{9.7}/A_K$ = 0.544 for the 9.7 μm silicate feature in combination with the astronomical silicate profile of Draine (1985). The extinction due to the silicate absorption at 9.7 μm depends on the line-of-sight (Draine 1989) and both the shape and strength of this feature seem to vary. The silicate profile of Draine (1985) has been based on the observed Trapezium silicate profile which is generally associated with H II regions and molecular clouds. The local extinction in IRAS 18434 is due to the molecular cloud surrounding the H II region; however, part of the apparent extinction towards IRAS 18434 is associated with foreground extinction through the diffuse ISM (Pratap et al. 1999) for which the silicate profile is generally represented by the profiles of μ Cepheï. In Table 8.2, we quote for each zone from which we extracted spectra, the average apparent extinction derived from the extinction map of Watson et al. (1997) derived by comparing the 2 cm radio continuum map of Fey et al. (1995) and their 2.17 μm Brγ map. For regions not covered by this map, we adopted the average extinction determined by Martín-Hernández et al. (2002a) from the HI recombination lines in the (large) ISO-SWS aperture. Subsequently, we applied the "standard" extinction law to the derived spectra of each zone in each slit. Similar, we corrected the ISO-SWS data for extinction with an A_K of 1.6. Fig. 8.10 and 8.11 show respectively the observed and subsequently extinction corrected ISO-SWS spectrum and SC10 spectrum of zone 4 in slit 2 corresponding to an A_K of 2.4 mag. We emphasise that there is no spurious 9.7 μm emission/absorption feature present in the resulting spectrum due to an over/under correction for extinction. Furthermore, the broad emission feature at 8.6 μm still remains and is thus not an arte-fact due to the combination of dust continuum, silicate absorption and our limited spectral coverage.

Figs. 8.12 and 8.13 show the spatial variation across each slit of the different emission features and of the strength of the dust continuum. The spectra are corrected for extinction as described above. The spectra observed in slit 4 have no or low flux below 10 μm and hence we consider only the long wavelength part (> 10 μm) of these spectra. The line fluxes are measured by subtracting a polynomial of order 2 fixed just outside the wavelength range covered by the emission line followed by fitting a Gaussian. A line is defined as being

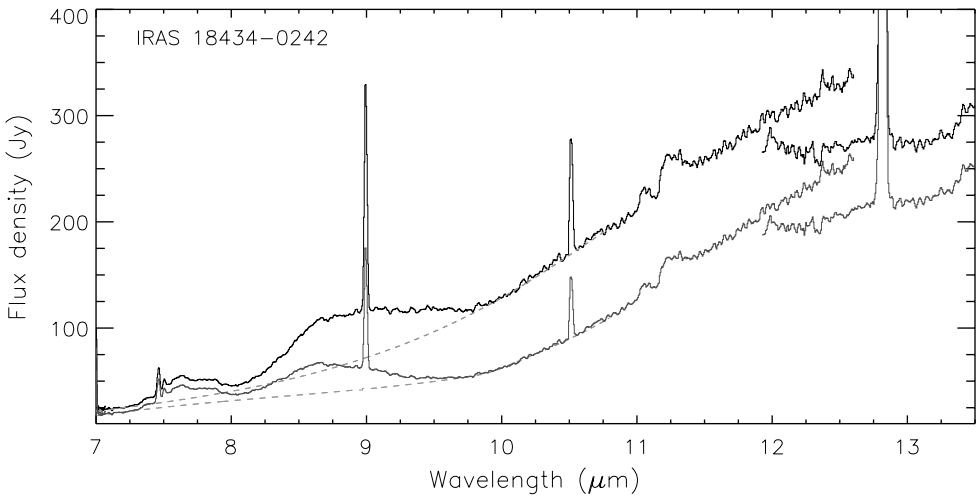

Figure 8.10 — The oberved and extinction corrected ISO-SWS spectra of IRAS 18434. Note the strong, broad emission band around 8.6 μm. The adopted continua is shown by the dashed lines.

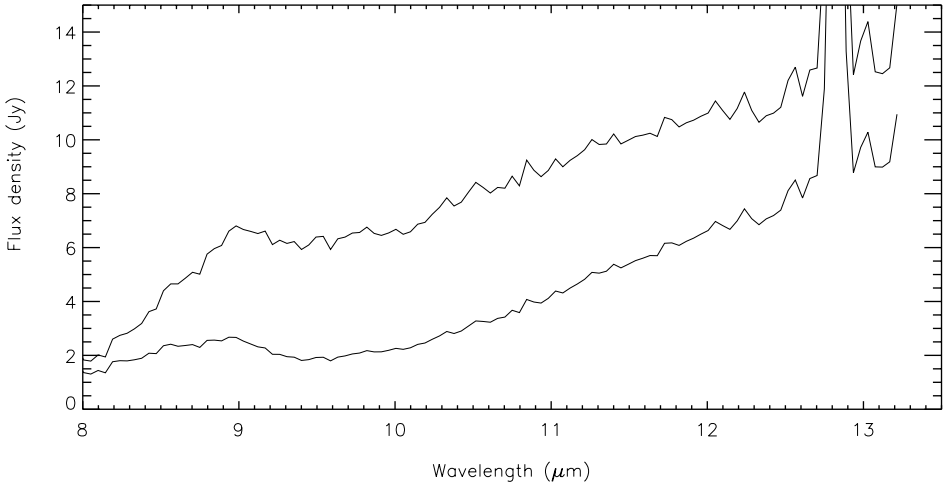

Figure 8.11 — Typical spectrum of IRAS 18434 normalised to an area of $1'' \times 1''$ and corresponding to slit 2, zone 4 (bottom spectrum). Silicate absorption is present at 9.7 μm. The top spectrum is this spectrum corrected for silicate absorption by applying the "standard" extinction law described in the text.

detected when its peak intensity is at least three times the rms noise of the local continuum and when the line has a FWHM similar to the spectral resolution element. Due to the low

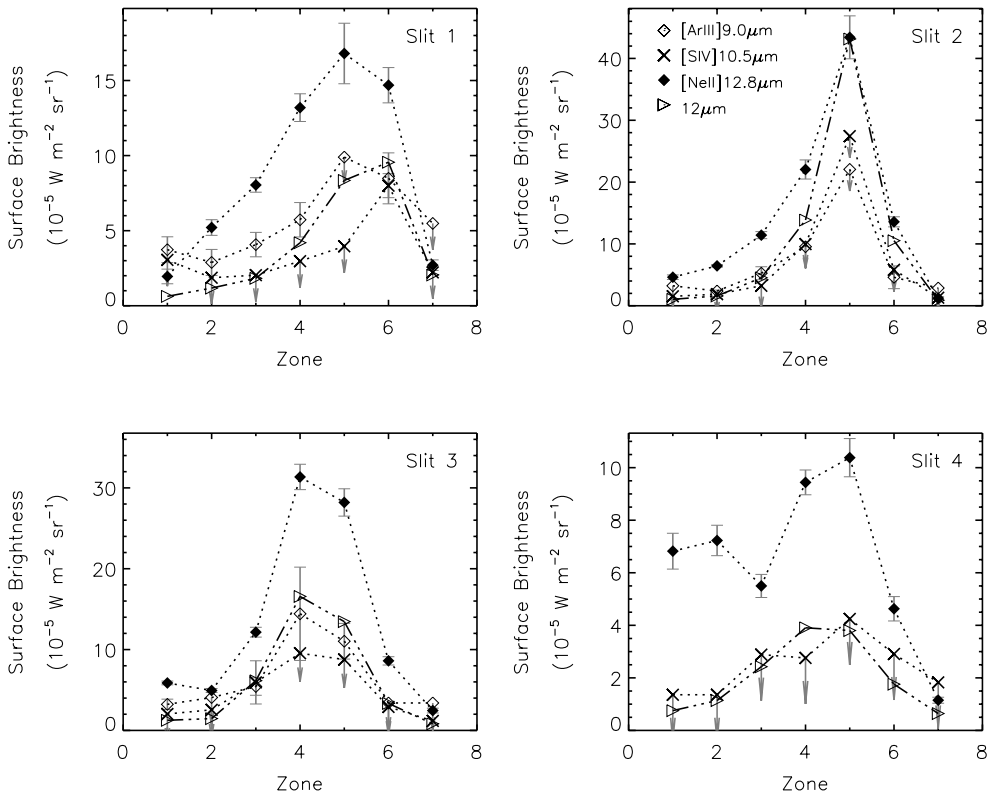

Figure 8.12 — The spatial distribution of the emission features across each slit of IRAS 18434. The fluxes are corrected for extinction. The fine-structure lines of [Ar III] 8.98 μm, [S IV] 10.51 μm and [Ne II] 12.81 μm are shown by open $\diamond$, $\times$ and filled $\diamond$ symbols respectively and each of them are connected by a dotted line. The strength of the dust continuum at 12 μm given in units of 10^{-16} Wm^{-2} μm^{-1}sr^{-1} is shown by filled $\triangleright$ symbols and connected by a $-\cdots$ line. Furthermore, the [Ne II] fluxes are divided by 10 and the strength of the dust continuum by 70. Note that for slit 4, only the long wavelength region (> 10 μm) of the spectra are useful.

spectral resolution and the often low intensity of the [Ar III] emission line, the derivation of its flux is hampered by the presence of the 8.6 μm emission feature.

For the slits 1, 2 and 3 - positioned on the source - the [Ne II] and [Ar III] fine-structure lines clearly peak on the arc and decrease gradually with the distance from the arc, showing a similar spatial distribution. Except possibly for zone 1 in slit 1, the [Ar III]/[Ne II] ratio is very constant and equals 0.05$\pm$0.01. This is in contrast to the observed ISO-SWS ratio, i.e. after correction of the ISO-SWS spectrum for extinction with an A_K of 1.6 (Martín-Hernández et al. 2002a), a [Ar III]/[Ne II] ratio of 0.16$\pm$0.02 is found (see Chap. 2). We do not think that this difference can be attributed to extinction. First, the extinction has been determined independently by Watson et al. (1997), Pratap et al. (1999) and Martín-Hernández

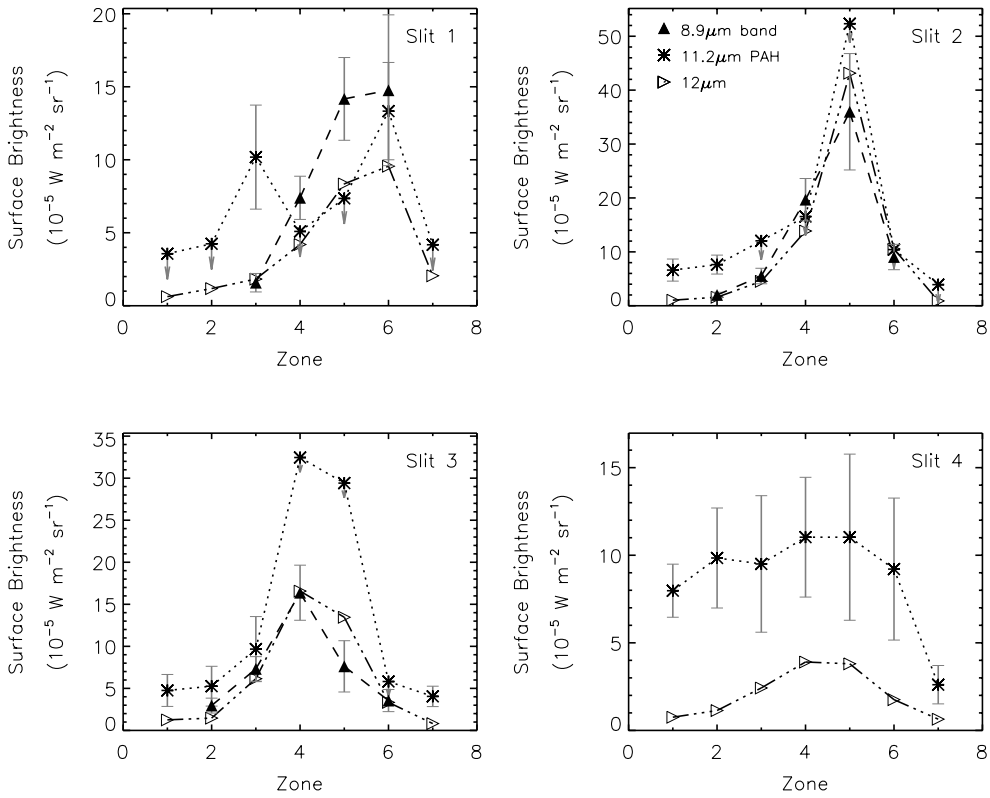

Figure 8.13 — The spatial distribution of the emission features across each slit of IRAS 18434. The fluxes are corrected for extinction. The 8.6 μm emission feature is shown by filled $\triangle$ symbols and connected by a dashed line, the 11.2 μm PAH emission feature by $\star$ symbols and connected by a dotted line. The strength of the dust continuum at 12 μm given in units of 10^{-16} Wm^{-2} μm^{-1}sr^{-1} is shown by filled $\triangle$ symbols and connected by a $-\cdots$ line. Furthermore, the flux of the 8.6 μm emission feature by 20 and the strength of the dust continuum by 70. Note that for slit 4, only the long wavelength region (> 10 μm) of the spectra are useful.

et al. (2002a) and is in good agreement. Second, the extinction correction factor is small. Possibly, this difference is due to extended low surface brightness [Ar III] emission which is included in the large SWS aperture but is below the detection limit of the SC10 study. [S IV] emission is detected for only 3 positions and its relation to the other lines is difficult to ascertain. However, its distribution in slit 1, with a strong detection in zone 6 and relative low upper limits in the other zones, seems to suggest otherwise. While the dust emission and the ionised gas tracers show great similarities in their overall structure, the dust emission is more sharply peaked in the arc then the [Ne II] line (Fig 8.12 and 8.14) . The 11.2 μm PAH emission feature is detected in 50% of the obtained spectra. In slit 4, all zones exhibit 11.2 μm emission while for slits 2 and 3, emission is only detected in the most eastern/western

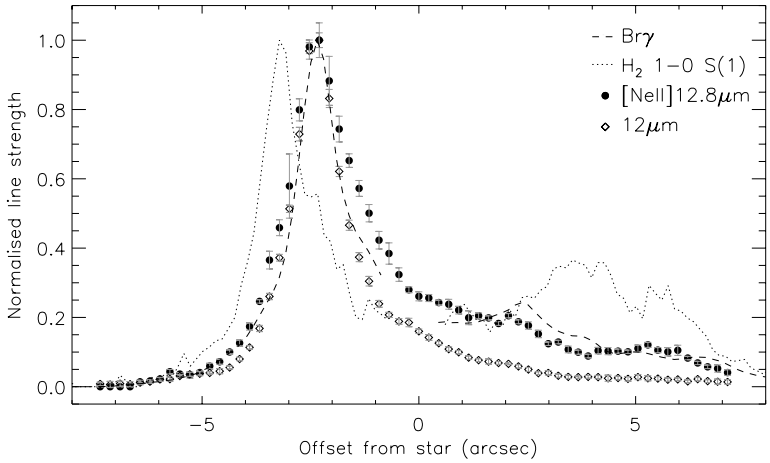

Figure 8.14 — Spatial variation of the [Ne II] 12.8 μm fine-structure line and the strength of the 12 μm continuum across slit 2 projected on the symmetry axis of the object (63.8 degrees with respect to the north-south axis). The normalised [Ne II] and 12 μm continuum intensity are compared to the Brγ and H_2 1-0 S(1) of Martín-Hernández et al. (2003). The origin corresponds to the position of the ionising star. Note that both the [Ne II] and the dust emission peak at the same location as the Brγ emission and that the dust emission is confined by the [Ne II] emission. Note that the [Ne II] 12.8 μm fine-structure line and the strength of the 12 μm continuum are *not* corrected for extinction.

zones. Slit 1 behaves particular showing 11.2 μm emission in zones 3 and 6. Hence, the latter is the only detection of PAH emission located at the arc. The emission in slit 1 also suggests that the 11.2 μm PAH emission distribution differs considerably from that of the strength of the dust continuum at 12 μm as well as the fine-structure lines. Finally, the 8.6 μm emission feature is present in all but the outer zones in the three slits located on the source and has a spatial distribution different from that of the strength of the dust continuum, the [Ne II] fine-structure line and the 11.2 μm PAH emission.

Martín-Hernández et al. (2003) obtained high resolution, long-slit K-band spectra of this source and studied the spatial variation of the strongest H I, He I and H_2 lines across the symmetry axis (in the H_2 image) of the source (116.2 degrees with respect to the north-south axis). They found that the He I and Brγ distributions trace each other very well but that the H_2 distribution is distinct (see Fig. 3 of Martín-Hernández et al. (2003) and Fig. 8.14). It peaks 0.93″ ahead of the Brγ maximum and exhibits a different structure in the tail of IRAS 18434. Due to the strong emission of the [Ne II] 12.8 μm fine-structure line and the 12 μm dust continuum, we are able to measure their strength for each spatial pixel (0.256″) in slit 2 (located on the center of the source with the ionising star on the edge of the slit) and subsequently projected our spatial position on the symmetry axis of the source to obtain the projected distance from the ionising star. Fig. 8.14 shows the obtained spatial variations. Clearly, both the [Ne II] and the dust emission peak at the same location as the Brγ emission. In addition, the dust emission is completely confined by the [Ne II] emission

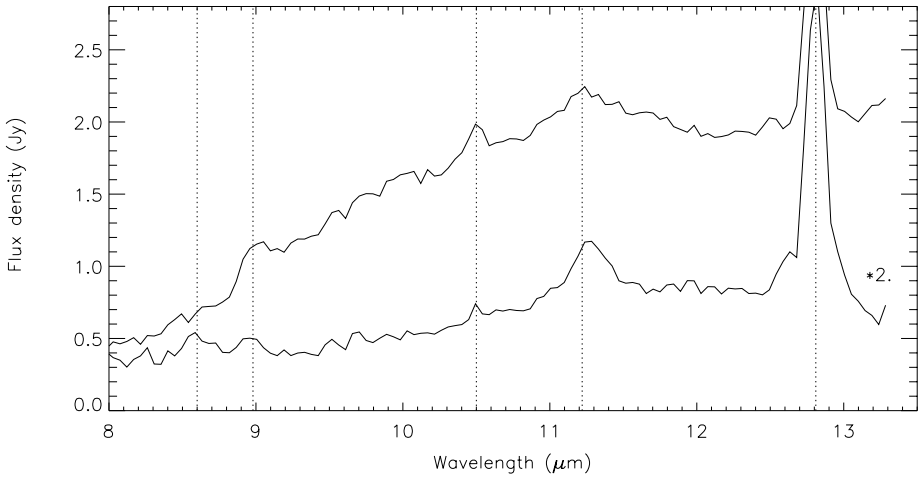

Figure 8.15 — Typical spectra of IRAS 21190 normalised to an area of $1'' \times 1''$ and corresponding to slit 2, zone 2 (top spectrum) and to slit 3, zone 3 (bottom spectrum). Emission features are the PAH feature at 8.6 and 11.2 μm, the [Ar III] fine-structure line at 8.99 μm, the [S IV] fine-structure line at 10.5 μm and the [Ne II] fine-structure line at 12.8 μm. In addition, silicate in emission is present in the top spectrum.

and is, relative to the arc intensity, weaker in the tail then the [Ne II] emission. Furthermore, the [Ne II] emission shows a second emission peak at similar location ($\sim 2.3''$) as does the Brγ emission though a similar third bump in the [Ne II] emission ($\sim 5.3''$ is not present in the Brγ emission. This second bump seems to be also present in the dust emission, though much weaker. The secondary peak in the H_2 emission at $3.8''$ is not present in either the [Ne II] line and the dust continuum.

Summarising, the fine-structure line emission of [Ar III] at 8.98 μm and [Ne II] at 12.81 μm show similar spatial distribution while that the different tracers of the "dust" – the continuum, the 11.2 μm emission feature and the 8.6 μm emission feature – all show different spatial distributions in IRAS 18434.

IRAS 21190

Fig. 8.15 shows some typical spectra of IRAS 21190. These mid-infrared spectra show clearly continuum emission of dust, fine-structure line emission of [Ar III] at 8.98 μm, of [S IV] at 10.5 μm and of [Ne II] at 12.8 μm and PAH emission at 11.2 μm and weakly at 8.6 μm. Furthermore, silicate in emission is present in several spectra.

The spectra observed in slit 4 and 6 have no flux shortwards of 10 μm and hence we consider only the long wavelength part (> 10 μm) of these spectra. In addition, in each zone, the spectra observed in these two slits are identical to within the error in shape and absolute flux. Therefore, we averaged both slits to produce higher signal-to-noise spectra. The spectra observed in slit 3 and slit 5 are very similar in zones 3, 4 and 5 but differ significantly in zones 1 and 2. Therefore, we treat these two slits separately.

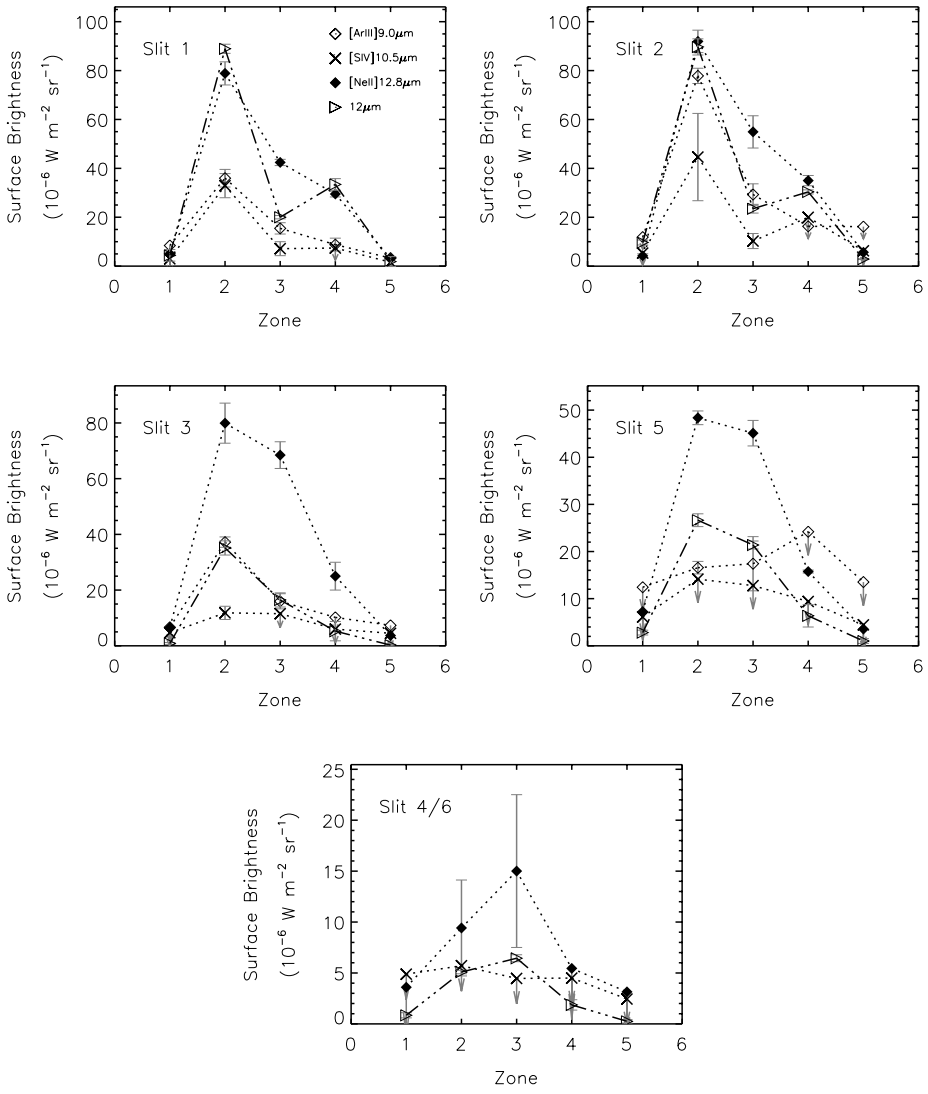

Figure 8.16 — The spatial distribution of the emission features across each slit of IRAS 21190. The fine-structure lines of [Ar III] 8.98 μm, [S IV] 10.51 μm and [Ne II] 12.81 μm are shown by open $\diamond$, $\times$ and filled $\diamond$ symbols respectively and each of them are connected by a dotted line. The [Ne II] fluxes are divided by 2. The flux at 12 μm given in units of 10^{-15} Wm^{-2} μm^{-1}sr^{-1} is shown by filled $\triangleright$ symbols and connected by a $- \cdots$ line. Note that both the silicate emission feature and the dust continuum contribute to the flux at 12 μm.

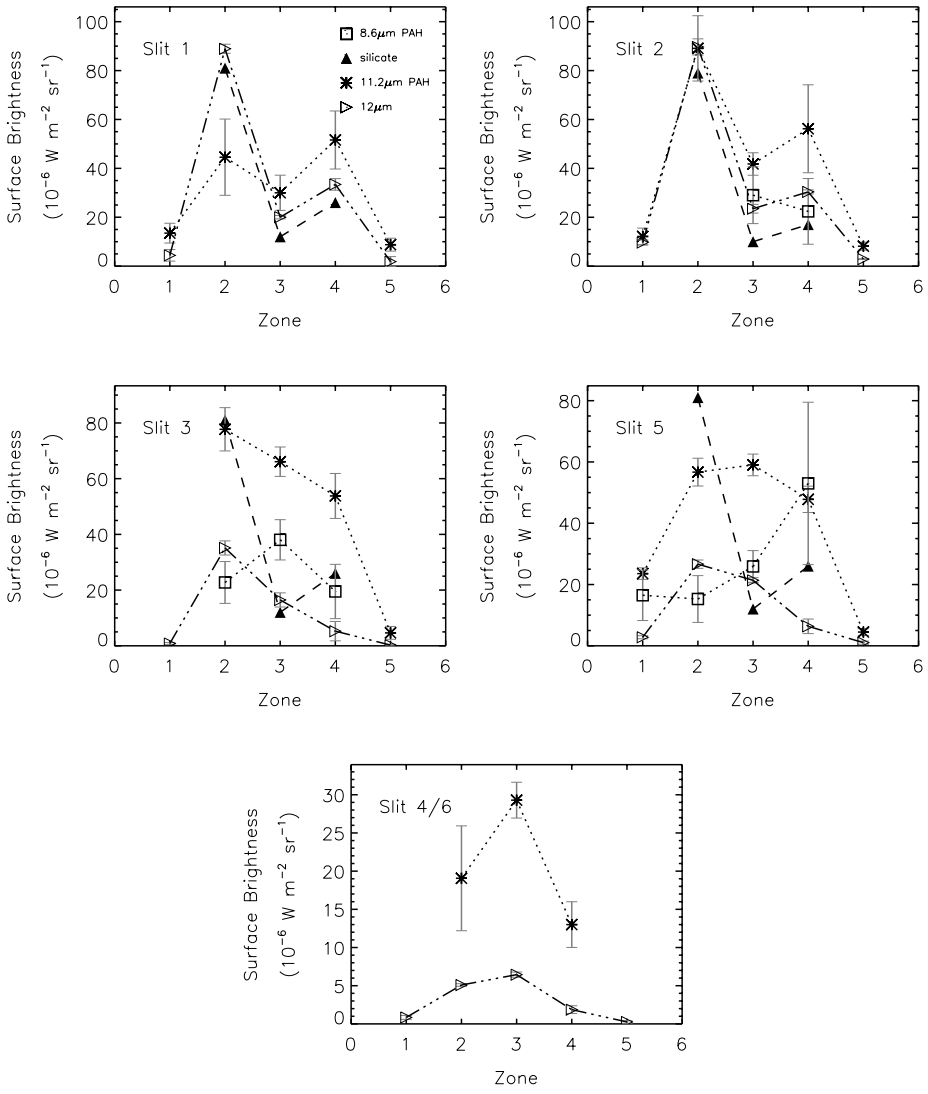

Figure 8.17 — The spatial distribution of the emission features across each slit of IRAS 21190. The 8.6 and 11.2 μm PAH emission features are shown by $\Box$ and $\star$ symbols respectively and connected by a dotted line. The flux at 12 μm given in units of 10^{-15} Wm$^{-2}\,\mu$m^{-1}sr^{-1} is shown by filled $\triangleright$ symbols and connected by a $-\cdots$ line. Note that both the silicate emission feature and the dust continuum contribute to the flux at 12 μm. The strength of the silicate emission is represented by the scaling factor K (see Sect. 8.5.2) and shown by filled $\triangleright$ symbols and connected by a dashed line.

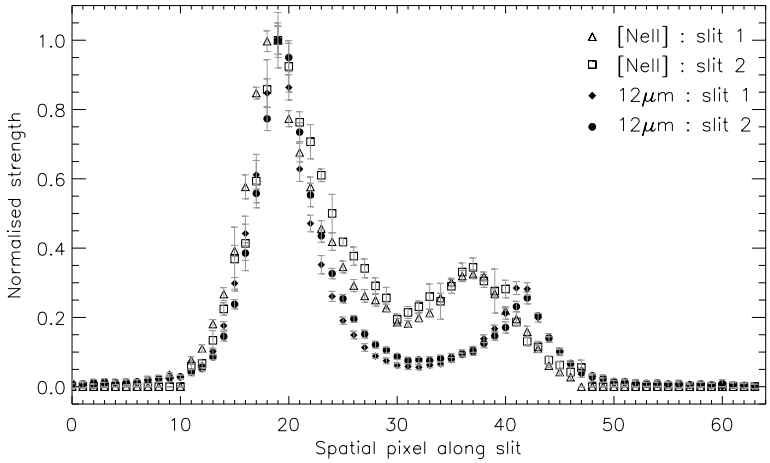

Figure 8.18 — Spatial variation of the [Ne II] 12.8 μm fine-structure line and the flux at 12 μm along slit 1 and slit 2. Note that both the silicate emission feature and the dust continuum contribute to the flux at 12 μm. The peak at pixel 19 corresponds to the arc structure in the various images (Fig. 8.6). The secondary [Ne II] peak at pixel 37 corresponds to the blob of emission in the K-band image (Fig. 8.7).

Figs. 8.16 and 8.17 shows the spatial distribution of the three fine-structure lines and the PAH emission features. The line fluxes were measured in the same way as for IRAS 18434. For comparison purposes, the [Ne II] fluxes are divided by 2 and the strength of the dust continuum is multiplied by 10. Due to atmospheric absorption, the low S/N and the low flux level shortwards of 9 μm, it is sometimes hard to tell whether the apparent emission around 8.6 μm is real PAH emission or whether it is an arte-fact. A flux for the 8.6 μm PAH feature is only plotted in Fig. 8.17 when there is a clear excess emission on top of the continuum at this wavelength.

The detailed distribution of the different ions differs somewhat. In slits 1 and 2 positioned on the center of the source, the three fine-structure lines peak in the arc (i.e. zone 2) and decreases gradually with the distance from the arc. In [Ne II], the emission associated with the arc shows a broader peak in slit 3 and 5 then in slits 1 and 2. In contrast, the peak in the [Ar III] line is as narrow in slit 3 as in slits 1 and 2. In addition, the relative intensity of the [Ne II] 12.81 μm over the [Ar III] 8.98 μm fine-structure lines varies throughout the source. Note that these variations are over the defined zones. A finer spatial resolution gives a more detailed view on the variations (see Fig. 8.18). The 11.2 μm PAH emission has a different distribution compared to that of the three fine-structure lines. In slits 1 and 2, the 11.2 μm emission also peaks in the arc – as the fine-structure lines – but shows extra emission in the blob (i.e. zone 4). Similar, in slits 3 and 5, the 11.2 μm emission associated with the arc shows a broader peak – as the [Ne II] emission – but also shows extra emission in zone 4, i.e. the regions next to the blob. Finally, in slit 4/6, the 11.2 μm PAH intensity is slightly stronger then the [Ne II] fine-structure line emission and shows a similar distribution. Assuming that

the excess emission around 8.6 μm is due to PAH emission, the 8.6 and 11.2 μm PAH intensity have a different spatial distribution. The silicate emission peaks in the arc and - as for the 11.2 μm PAH feature - has extra emission in the blob (i.e. zone 4). Therefore, it has qualitatively a similar spatial distribution as the 11.2 μm PAH emission, albeit with much larger variations. Fig. 8.18 shows the variation of the [Ne II] emission line and the observed flux at 12 μm, composed of both silicate emission and dust continuum emission. As for IRAS 18434, in the arc, the dust emission is located inside the [NeII] emission. Remark however that the second peak (i.e. the blob) is clearly located at different spatial position for the dust and the ionised gas. Furhtermore, the blob is narrower and hence the region between the arc and the blob is more extended in the dust emission (Fig. 8.6).

Comparing slit 1 and 2, both centered on the source but with a different width, reveals that the intensity ratio of the [Ar III]/[Ne II] fine-structure lines is enhanced by a factor of $\sim$2 in the 2$''$ slit mainly due to the weakness of the [Ar III] emission in slit 1. Probably, the 1$''$ slit is slightly off the peak emission of the [Ar III] emission line. In addition, the 11.2 μm PAH emission increase more in the arc with respect to the other zones in the 2$''$ slit then in the 1$''$ slit. Similar to [Ar III], the 1$''$ slit seems slightly off the peak of the 11.2 μm PAH emission.

Summarising, the fine-structure lines show somewhat different spatial distributions, all indicating that the H II region is located at the arc and that the blob in the north-east is on the outskirts of the H II region, consistent with early radio observations (Scott & Harris 1978; Puche et al. 1988; Zijlstra et al. 1990). The 11.2 μm PAH feature and the strength of the silicate emission feature show similar distributions but distinct from that of the fine-structure lines. In particular, the PAHs and the dust show extra emission at the blob in the north-east suggesting the presence of a large column of dust. In addition, the data also seems to indicate that the 11.2 and 8.6 μm PAH features have different spatial distribution.

8.5 Discussion

8.5.1 IRAS 18434

The 8.9 μm feature

In order to derive the profile of this new emission feature at 8.6 μm, we subtracted a local spline continuum from the extinction corrected ISO-SWS spectrum. Continuum points are taken at wavelengths shortwards of 7.3 μm and longwards of 10 μm (see Fig 8.2 a). Fig. 8.19 a shows the derived normalised profile. For comparison, the emission profile of this 8.6 μm feature is also derived from the spectrum before extinction correction in the same way. Clearly, while extinction has a large influence on the derived profile and the relative strength of this 8.6 μm emission feature and the 7.7 μm PAH complex, the reality of this new feature is not in doubt. Due to the low spectral resolution of the ground-based SC10 data, it is not possible to determine whether the profile changes with spatial position.

From the wealth of IR spectra of H II regions, it is clear that in these regions the UIR bands at 3.3, 6.2, 7.7, 8.6 and 11.2 μm represent a single class of spectral features that come and go together. Since the ISO-SWS spectrum of IRAS 18434 clearly shows PAH emission features at 3.3, 6.2, 7.7 and 11.2 μm (see Chapters 2, 3 and 4), the 8.6 μm PAH emission feature might be hidden in our derived profile of the 8.9 μm band. Therefore, we scaled the continuum subtracted ISO-SWS spectrum of IRAS 21190 (the continuum is shown in Fig. 8.2) so that the peak strength of the 7.7 μm complex is equal in both sources (Fig. 8.19 b). Since all H II regions have the same profile for the 6.2, 7.7 and 8.6 μm PAH emission

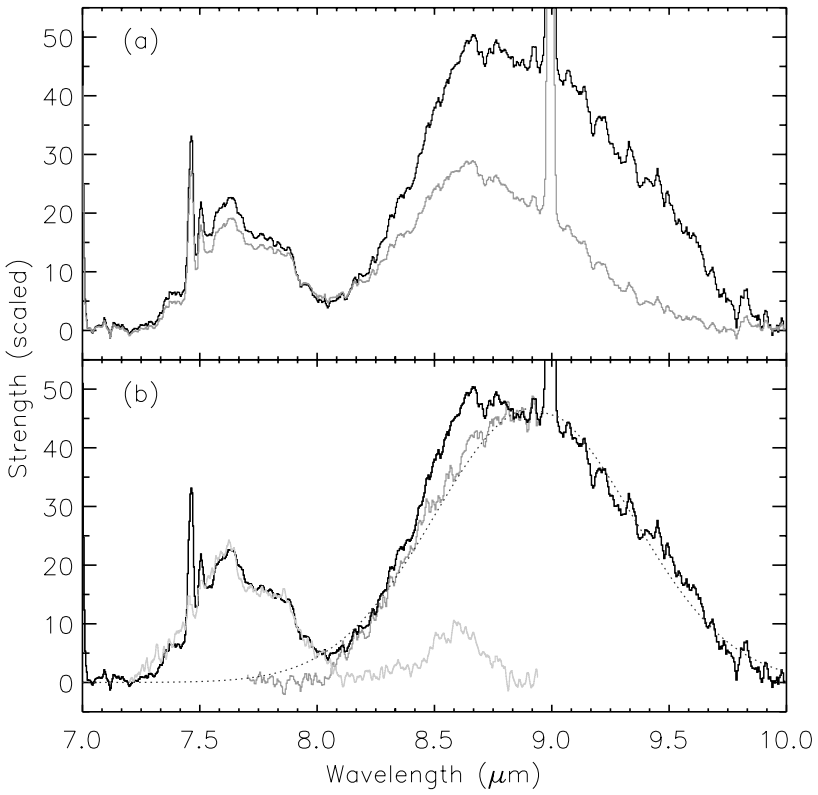

Figure 8.19 — By subtracting the continuum shown in Fig. 8.2, the profile of the broad emission feature at 8.6 μm is obtained and shown in panel a. The black profile shows the derived profile after correcting for extinction. The grey profile is the derived profile when no extinction correction is applied. Panel b shows the derived profile after extinction correction (black line), the light grey curve represents the PAH emission bands in the SWS spectrum of IRAS 21190, which can be used as a PAH template for H II regions (Chapter 3), scaled to the strength of the 7.7 μm profile of IRAS 18434. By subtracting this PAH template from the continuum subtracted spectrum of IRAS 18434, the dark grey curve is obtained; the dotted line is a Gaussian fitted to this resulting profile.

features (see Chapter 3), this continuum subtracted spectrum of IRAS 21190 - which suffers no extinction (Martín-Hernández et al. 2002a) - can serve as a PAH template for H II regions and is used here to correct the profile of the 8.6 μm feature for a contribution from the 8.6 μm PAH band. Subsequently, we subtracted this PAH template to derive the intrinsic profile of the new emission feature. Clearly this shifts the peak position of this new feature to 8.9 μm, hence we further denote it as the 8.9 μm feature. This 8.9 μm profile is well fitted by a single Gaussian with a peak position of 8.92$\pm$0.01 μm and a FWHM of 0.99$\pm$0.01 μm (Fig. 8.19 b).

The presence of this feature in a source otherwise characterised by PAH emission features may be taken to suggest a similar carrier. The spectral characteristics of the emission features

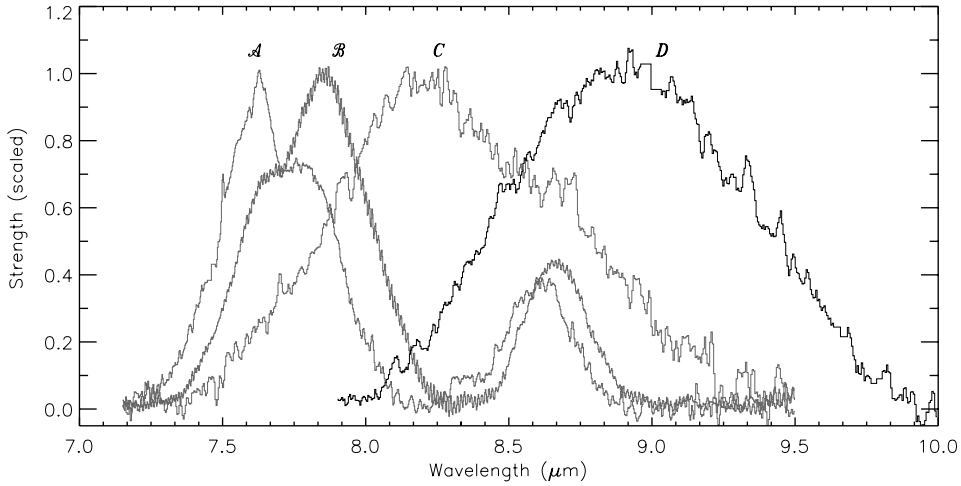

Figure 8.20 — Overview of possible classes of PAH emission bands as classified in Chapter 3. The spectra are normalised such that the peak intensity in the 8 μm region equals one. Clearly, the new emission band at 8.9 μm does not fall in any of the classes ($\mathcal{A}$, $\mathcal{B}$ or $\mathcal{C}$).

in the 6–9 μm region are know to be highly variable (Chapter 3). Comparison of the profile of the 8.9 μm feature with those of other sources reveals that this feature is clearly distinct and unique (Fig. 8.20). Indeed, the peak position is redshifted by > 0.7 μm compared to any PAH-related emission profile found so far. Furthermore, only the profile of class $\mathcal{C}$ has a comparable FWHM (see Chapter 3). On the basis of this comparison, it is suggestive that the higher redshift of the profile seems connected to a broader and more "amorphous" feature. Accepting for the moment a PAH-related carrier, the shift and broadening of profile $\mathcal{C}$ of the "7.7 μm" feature as well as that of the new 8.9 μm feature may reflect an increased modification of the carrier. Possibly, this is due to an increased clustering into larger and larger units. Given that the 8.9 μm feature in IRAS 18434 has a different spatial distribution from the 11.2 μm PAH feature, whatever process is modifying the PAHs has to be active within this source. Since the 11.2 μm feature is concentrated in the outskirts while the 8.9 μm feature is more closely connected to the arc, density variations may be at the bottom of the spectral variation. We do want to emphasise that it is by no means given that the carrier of the 8.9 μm feature is PAH-related. Arguments in favour of a PAH-related carrier are the presence of the 8.9 μm feature in a "PAH" source which does not show any other discernible dust feature (except silicate in absorption) and the spectral sequence illustrated in Fig. 8.20. Arguments against a connection of the 8.9 μm feature with PAHs are that while the PAH features are widespread, this is the only source, with such a remarkable shift, in a large sample (cf. Chapter 3) and possibly the different spatial distribution of the 11.2 μm PAH feature and the 8.9 μm feature in IRAS 18434.

In this respect, the large FWHM of the feature lends some credence to a grain-like carrier. Various carbonaceous materials show an emission near 8 μm, including HAC, QCC, coal, and partially hydrogenated C_{60} (Mortera & Low 1983; Sakata et al. 1984; Colangeli et al.

1995; Guillois et al. 1996; Scott et al. 1997; Schnaiter et al. 1999; Stoldt et al. 2001). However, the profiles in these solid state materials peak close to 8 μm and are much broader then the 8.9 μm feature. Therefore, these materials cannot be the carriers of this 8.9 μm feature. Various O-rich materials also show emission in this wavelength region (Speck 1998; Molster et al. 2002). The most likely candidate is silica (SiO_2) which shows emission features at 9.2, 20 and 13 μm - in order of relative strength - (Speck 1998; Speck et al. 2000; Fabian et al. 2000). However, the 9.2 μm silica profile is clearly asymmetric and peaks at slightly longer wavelengths compared to the 8.9 μm feature and no emission at 20 μm is seen in the ISO-SWS data. Furthermore, while silica may be present in some O-rich late type stars, it is then only a weak shoulder on top of the strong broad 9.7 μm silicate feature (Speck 1998; Molster et al. 2002). So, this identification does not seem very likely.

In conclusion, the carrier of the newly discovered 8.9 μm feature is likely related to PAHs, although the precise relationship awaits further laboratory and astronomical studies.

The spatial distribution of the dust and molecular species

The spatial distribution of the continuum, the 11.2 PAH emission and the 8.9 μm band are very different (Sect. 8.4.2). These differences may reflect differences in the spatial distribution of the temperature of their carriers or differences in the spatial distribution of the density. Here, we first discuss the continuum emission and then the PAH and the 8.9 μm carrier.

The spatial distribution of the dust in this source closely resembles that of the ionised gas (Fig. 8.14). Furthermore, the derived colour index hardly varies over the source (Fig. 8.4, Ball et al., 1996) indicating that the dust temperature is nearly uniform. Likely, the observed continuum emission is due to thermal emission of dust grains. If so, this constant dust temperature implies that the dust is located at a constant distance from the ionising star. This does not constrain the location of the dust, i.e. the dust can be located either (in a shell) inside the H II regions or in the PDR. However, comparison of the spatial distribution of the Brγ, H_2, [Ne II] and dust continuum emission might pin down the exact location of the dust further. Indeed, since the observed H_2 emission likely arises from the PDR (Martín-Hernández et al. 2003), the separation between the H_2 and the tracers of the ionised gas (the H_2 emission peaks at 0.93$''$ ahead of the tracers of the ionised gas – Fig. 8.14) measures directly the FUV penetration size scale (Tielens & Hollenbach 1985). These authors found that in the PDR, the vibrationally excited molecular hydrogen $H_2^\star$ peaks around $\Delta A_{\rm V} \sim 2$ with respect to the ionisation front. Adopting a hydrogen column density, $N_{\rm H}$, per magnitude of visual extinction, $N_{\rm H}/A_{\rm V}$ = 1.9 10^{21} cm^{-2} and a distance of 5.7 kpc, the observed scale size of the region (0.93$''$) implies a neutral gas density of 4.7 10^4 cm^{-3} for a homogenous region viewed edge-on. This inferred density agrees well with independent estimates of the density of this region. The ionised gas has an estimated density of 1.0 10^4 cm^{-3} (Martín-Hernández et al. 2002a) and an estimated electron temperature of 5000-7500 K (Martín-Hernández et al. 2003). If we assume pressure equilibrium across the ionisation front, this estimate requires a neutral gas density of 1.0-1.5 10^5 cm^{-3} for a neutral gas temperature of 1000 K. In the standard PDR model (Tielens & Hollenbach 1985), the temperature of the dust originating in the PDR, peaks within the ionisation front. With the observed scale size of the H_2 emission, and assuming that there is a ΔA_V of $\simeq 0.5$ mag between the ionisation front and the dust emission peak in the PDR, a separation of 0.23$''$ between the peaks of the emission from dust located in the PDR and the tracers of the H II region (Brγ and [Ne II]) is obtained. However, our study has a spatial resolution of 0.256$''$/pixel and a seeing of 0.6$''$; hence a separation

of $0.23''$ is not resolved. Therefore, the fact that the dust emission shows a similar spatial distribution as the [Ne II] emission does not necessarily imply that the dust is co-located with the ionised gas instead of in the PDR surrounding the H II region. To resolve this separation, high spatial resolution observations by diffraction-unlimited or space-born instruments are needed. We do note that if the dust were located in the ionised gas, the observed constant temperature excludes that Lyman α photons provide the dominant heating source, in view of the large density variation observed (Afflerbach et al. 1994; Wood & Churchwell 1991).

In the well studied nearby H II region Orion, all the PAH emission features predominantly originate from the PDR rather than from the ionised gas (Tielens et al. 1993; Geballe et al. 1989; Sellgren et al. 1990). Our data for IRAS 18434 are consistent with this conclusion. While the dust continuum emission peaks in the arc, the 11.2 μm PAH emission is mainly detected off the arc. Although most upper limits do not add information on the PAH distribution, we can conclude that the PAH emission does not increase in the same way as the strength of the continuum emission; since otherwise we would be able to detect the PAHs in the arc. This is supported by the 11.2 μm emission and the strength of the dust continuum emission in slit 1. The 11.2 μm PAH emission clearly has a different spatial distribution than the dust continuum emission. In principle, these different spatial distributions might reflect differences in the temperature distribution of the carriers with position in the nebula; e.g. dust is in radiatively equilibrium with the radiation field at a temperature which will drop with distance from the star. The emission on the Wien side of the Planck function (as is the case here), is then heavily weighted towards the highest temperatures. In contrast, PAHs are transiently heated to the same temperature independent of position (i.e. strength of the radiation field). However, this is likely only to be a minor effect and most of the differences in spatial distribution between the IR emission features and the continuum likely reflects a difference in spatial distribution with the PAHs located in the PDR surrounding the H II region and the dust (i.e. the dust dominating the emission at mid-infrared wavelengths) within the ionised gas. We emphasize that there is also dust present in the PDR but this dust is outshone by the warmer dust within the H II region. The bulk of the (far-IR) dust emission likely originates from outside the H II region. Observations at longer wavelengths may be able to settle this issue. The 8.9 μm band follows more the emission from the dust than the emission from the PAHs. Hence, if the carrier of the 8.9 μm feature is related to the PAHs – as we surmised above –, then this carrier should be much less susceptible to destruction within the ionised gas. This is consistent with a larger size for the 8.9 μm carrier.

We conclude that the strength of the different tracers of the "dust" - continuum, 11.2 μm emission feature and the 8.9 μm emission feature - all show different spatial distributions in IRAS 18434. While these differences may reflect differences in excitation (radiative equilibrium versus transient temperatures) and spatial distribution, chemical variations or modifications of the PAHs either driven by the radiation field or by interaction with the ionised gas are likely to be important.

8.5.2 IRAS 21190

Silicate in emission

IRAS 21190 clearly shows silicate in emission (see Fig. 8.15). The FHWM of the profiles are quite large indicating the presence of a size and/or temperature distribution in the silicate grains. Whether a shift in peak position and hence a temperature gradient within the source

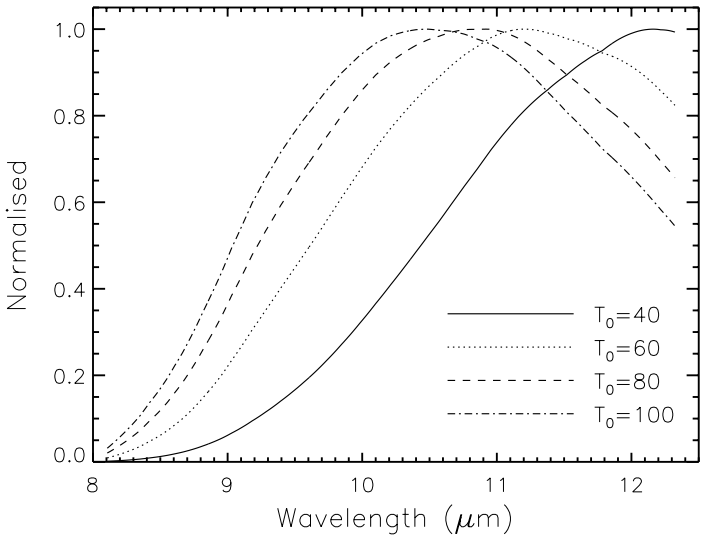

Figure 8.21 — The calculated silicate emission features for different T_0 (corresponding to the temperature of a 1 μm grain, see eq. 8.11) assuming an MRN size distribution and a size dependent temperature law. See text for details.

is present, is not clear at first sight due to the uncertainty in the continuum determination. Indeed, silicate has two prominent *blended* emission bands at 9.7 and 18 μm. Therefore, at the long wavelength end in our observations ($\sim$ 13 μm), the observed flux is a combination of dust continuum emission and silicate emission. In contrast, at the short wavelength end in our observations ($\sim$ 8 μm), the observed flux is entirely continuum emission (see Fig 8.2 b). Hence, it is not straightforward to determine the dust continuum. Clearly, a variation in the continuum influences the observed peak position of the silicate profile. Therefore, we modelled the observed spectra by calculating theoretical spectra consisting of a silicate emission feature and a dust continuum.

In this model, we represent the dust continuum emission by a straight line, $ux + v$, with a slope u and a offset v (when plotted in μm versus Jy). Subsequentely, the silicate profile is calculated assuming an MRN size distribution (Mathis et al. 1977) and a size dependent temperature law (see Appendix 8.A for a complete description).

For the wavelength dependence of the emission efficiency, P_ν, we use the normalised intrinsic profile of the Trapezium (Vriend 1999; Forrest et al. 1975; Draine & Lee 1984). This intrinsic profile of the Trapezium is derived by dividing the observed silicate profile towards this source by a blackbody at a temperature of 250 K. Therefore, it is implicitely assumed that all silicate grains in this source have the same size and the same temperature. This intrinsic profile of the Trapezium covers a wavelength range of 8.1–12.3 μm. Therefore, we limited the spectral coverage of our model spectra to the same wavelength range. The strength of the observed silicate emission band determines the scaling factor K needed so that the calculated profiles have similar strength. It is not necessary to include K as a free parameter in the

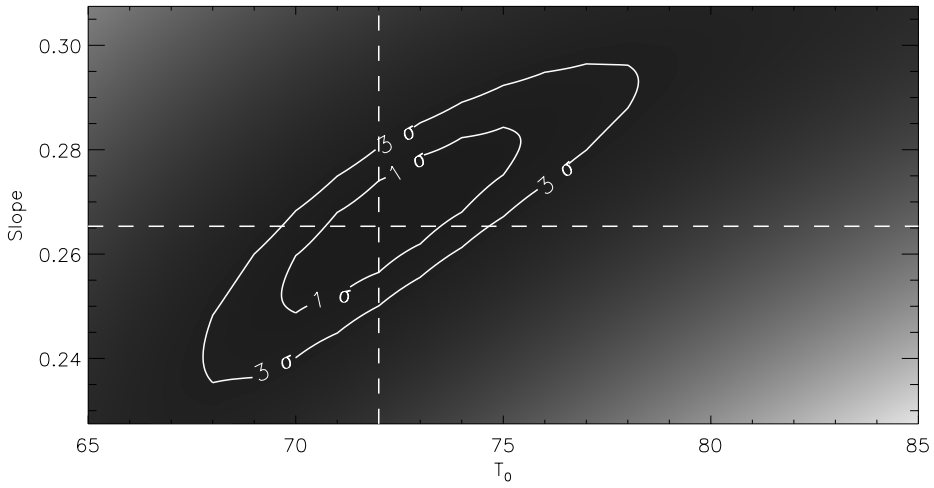

Figure 8.22 — The χ^2_ν contours for the parameters T_0, the temperature, and u, the continuum slope obtained for slit 1, zone 2.

model (see below).

As a consequence, the model has 3 free parameters : T_0 (corresponding to the temperature of a 1 μm grain, see eq. 8.11), the continuum slope u and the continuum offset v. Changing either of the parameters can considerably change the output of the calculated spectrum. Obviously, the calculated silicate profile is dependent on the slope of the continuum and vice versa. In contrast, the continuum offset has little effect on the derived silicate profile. The calculated silicate profiles for different T_0 are shown in Fig. 8.21. The parameter T_0 clearly influences the derived profile, i.e. higher temperatures shift the profile – and hence the peak position – towards the blue.

In order to derive the model parameters that provide the best fit to the observations, a quantitative comparison between the model spectrum and the observed spectrum needs to be made. This is done by calculating

$$\chi^2_\nu = \frac{\chi^2}{\nu} = \frac{1}{N_\mathrm{p} - m} \sum_i \frac{(y_0 - KF_\nu)^2}{\sigma^2} \tag{8.1}$$

where y_0 is the continuum subtracted flux values for the observations, F_ν the calculated silicate profile, K the scaling factor, σ are the uncertainties on the data points (assuming that the uncertainties on the model spectrum are negligible), the sum runs over all data points N_p in the spectrum and $\nu = N_\mathrm{p} - m$ is the number of degrees of freedom with m the number of free parameters. For a good fit, χ^2_ν should be low, of order unity.

The applied scaling factor K corresponds to that value for which χ^2 is minimal, $d\chi^2/dK = 0$ and thus :

$$K = \frac{\sum y_0 F_\nu/\sigma^2}{\sum F_\nu^2/\sigma^2}$$

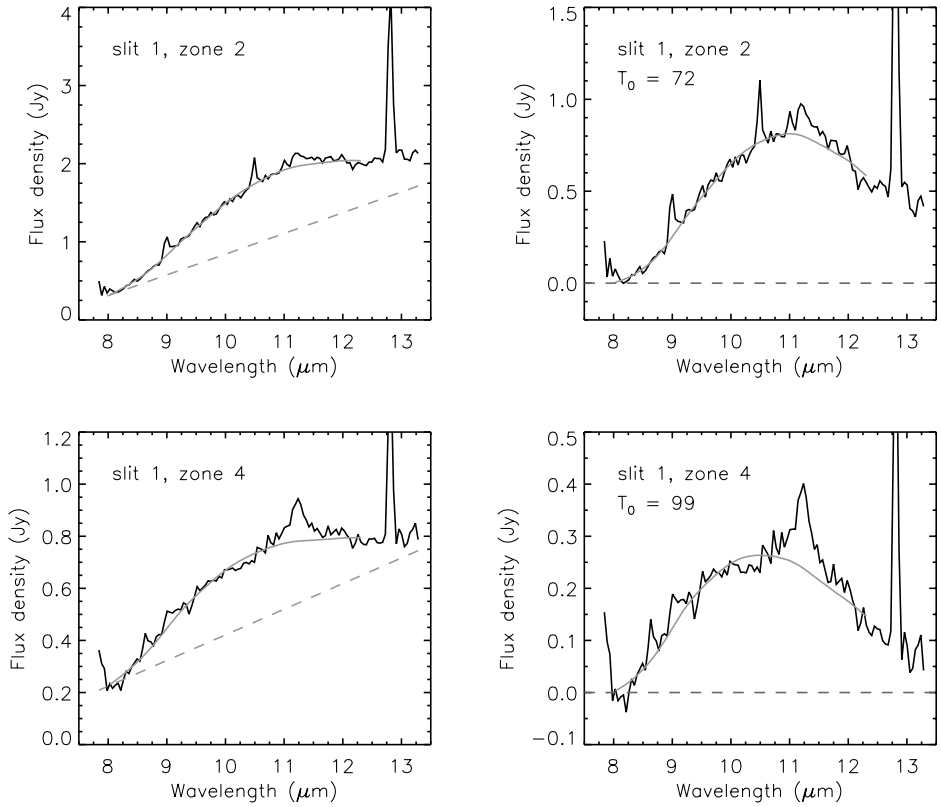

Figure 8.23 — The left panels show the observed spectra in slit 1, zone 2 and 4 respectively normalised to an area of $1'' \times 1''$. Also shown in the left panels is the continuum (dashed line in grey tones) and the calculated spectrum as determined in the simple model (solid line in grey tones). The right panels shows the continuum subtracted spectra overplotted with the calculated silicate profile (grey tones).

Therefore, once the continuum is determined, we can calculate the scaling factor K.

By minimising χ^2_ν, we obtain the best fit. Fig. 8.22 shows the χ^2_ν contours for the parameters T_0 and u. The error estimates are obtained by evaluating by which (T_0, u, v) values $\chi^2 < (\chi^2_{\rm min} + 3)$.

Figs. 8.23 and 8.24 show some of the observed spectra with the best fit derived with this model; the obtained parameters are given in Table 8.3. The spectra are fitted very well with our simple model and clear variations are present in the peak position and strength of the silicate emission feature (and hence the parameter T_0 and the scale factor K respectively) and the strength of the continuum slope (i.e. parameter u).

To test the dependence on the assumed silicate emission efficiency, we applied the same model to the data using the derived intrinsic profile of μ Ceph (Russell et al. 1975; Vriend

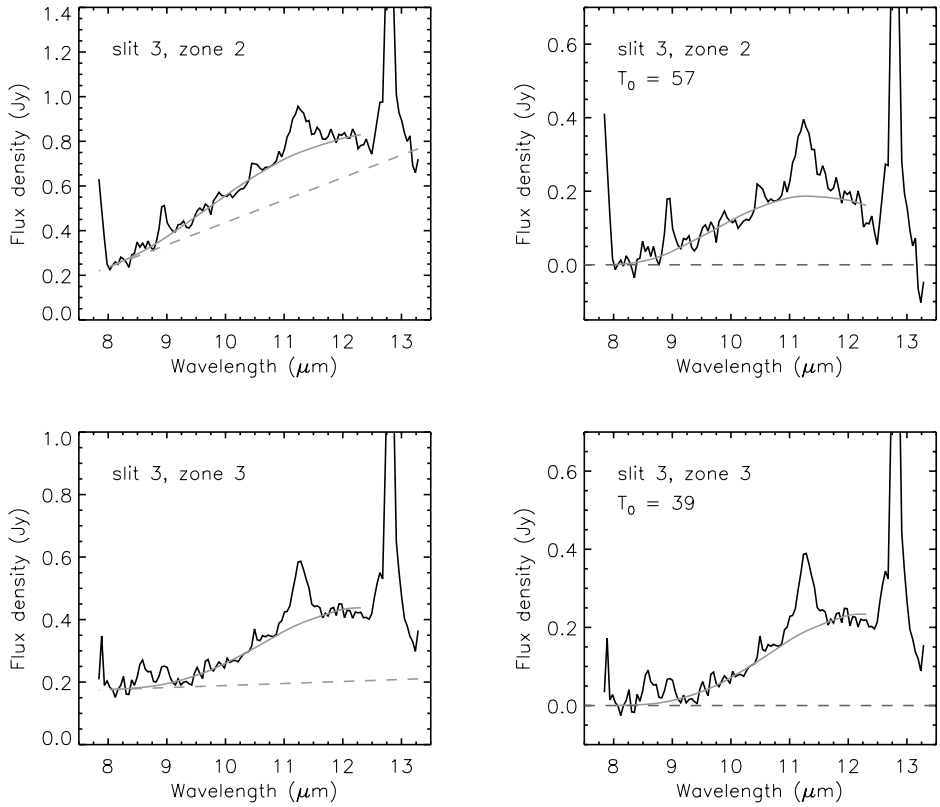

Figure 8.24 — Same as for Fig. 8.23 but now for slit 3, zone 2 and 3.

1999) and laboratory measurements of the optical constants of amorphous silicate (Jaeger et al. 1994). Comparison of the derived parameters using these three different intrinsic silicate emission profiles shows that the results are very robust.

The parameter T_0 is given in Table 8.3. Within each slit, a temperature gradient is present. In slit 1, the highest T_0 and hence highest temperature of the silicate component in the model is found in the blob, the smallest in the region between the arc and the blob. In contrast, in slit 3 and 5, located on the edges of the source, the temperature is highest in the arc. For slit 2, located on the centre as is slit 1, the temperature distribution is not well determined. The derived values of T_0 ranges from 39 to 128, indicating a temperature range of 84–139 for a 100 Å grain and of 57–129 for a 1000 Å grain (see eq. 8.11).

The silicate grains present in slit 2 have slightly higher temperatures than those present in slit 1. This somewhat curious result – both slits are located on the center of the source – may reflect that the ionising source is not located within the $1''$ slit and hence this difference may reflect the presence of a temperature gradient within the source.

The largest slope of the dust continuum is found in the arc. The slope of the continuum

Table 8.3 — The derived model parameters [a].

Slit	Zone	T_0	u	v	K	χ^2_ν
1	2	72^{78}_{68}	$0.27^{0.30}_{0.24}$	$-1.81^{-1.56}_{-2.07}$	$0.81^{0.91}_{0.71}$	0.36
1	3	59^{76}_{51}	$0.05^{0.07}_{0.03}$	$-0.31^{-0.14}_{-0.45}$	$0.12^{0.17}_{0.08}$	0.40
1	4	99^{121}_{85}	$0.10^{0.11}_{0.08}$	$-0.56^{-0.43}_{-0.69}$	$0.26^{0.29}_{0.25}$	0.58
2	2	86^{93}_{80}	$0.25^{0.27}_{0.22}$	$-1.56^{-1.36}_{-1.76}$	$0.79^{0.86}_{0.73}$	0.76
2	3	128^{216}_{87}	$0.08^{0.09}_{0.06}$	$-0.47^{-0.36}_{-0.58}$	$0.10^{0.11}_{0.09}$	0.86
2	4	96^{126}_{79}	$0.08^{0.09}_{0.06}$	$-0.37^{-0.24}_{-0.49}$	$0.17^{0.20}_{0.16}$	0.82
3	2	57^{66}_{53}	$0.10^{0.12}_{0.08}$	$-0.57^{-0.40}_{-0.73}$	$0.19^{0.26}_{0.12}$	0.98
3	3	39^{41}_{38}	$0.01^{0.03}_{0.00}$	$0.12^{0.18}_{-0.04}$	$0.23^{0.26}_{0.17}$	0.82
3	4	40^{43}_{37}	$0.00^{0.01}_{0.00}$	$0.06^{0.07}_{0.03}$	$0.09^{0.09}_{0.07}$	1.07
5	2	55^{65}_{50}	$0.07^{0.08}_{0.05}$	$-0.37^{-0.21}_{-0.52}$	$0.15^{0.21}_{0.10}$	0.35
5	3	49^{53}_{46}	$0.04^{0.06}_{0.02}$	$-0.20^{-0.01}_{-0.34}$	$0.17^{0.24}_{0.12}$	1.03

[a] See text for details on the model and the errors. The spectra are all normalised to an area of $1'' \times 1''$.

is an indication of the temperature of the dust responsible for the mid-infrared continuum emission. Hence, the continuum dust temperature is highest in the arc. As for the silicate grains, a clear temperature gradient is present in the continuum dust emitting at mid-infrared. In addition, Fig. 8.25 shows that the derived continuum dust temperatures correlate in general well with the silicate dust temperatures indicating that these two dust components are heated in a similar way, i.e. in equilibrium with the radiation field. There are three deviant regions i.e. the blob in both center slits and the region between the arc and the blob in the $2''$ center slit. Those three regions represent the highest obtained value of T_0 within the source.

The spatial distribution of the dust and molecular species

The data of the center slit shows that in the arc, the dust emission at 12 μm (composed of continuum and silicate emission with the continuum representing 70–80 % of the total emission) coincides with the emission from the ionised gas (as traced by [Ne II]). In contrast, in the blob to the north-east, the dust emission is displaced outwards from the emission of the ionised gas (Figs. 8.16, 8.17 and 8.18). The stratification of the emission observed in the north-east gives the impression of an edge-on PDR, where the [Ne II] emission traces the ionised gas and the dust emission originates in the neutral gas outside of the ionisation front. Within this interpretation, the dust must then have been removed from within the ionised gas volume either through radiation pressure or through destruction. Assuming that there is a ΔA_v of $\simeq 0.5$ mag between the ionisation front and the dust emission peak in the PDR and assuming standard dust properties, we infer a density of 6–7 10^3 cm^{-3} in the PDR from the observed separation. In contrast, in the arc, the dust emission coincides with that of the

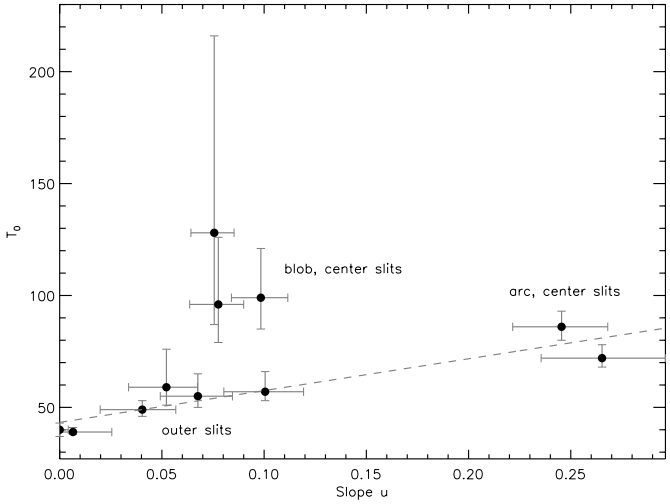

Figure 8.25 — The relation between the slope of the adopted continuum and the parameter T_0, indicative for the temperature of the grains and the silicates respectively.

ionised gas. Since we have spatially resolved the arc in both the dust and in the [Ne II] line, this cannot merely reflect a superposition of the ionised gas and the PDR in the beam due to a much smaller physical scale size (reflecting the much higher densities). Rather, it suggests that in the arc the carriers of the dust continuum and the silicates are spatially co-located with the ionised gas. Hence, either the dust/silicates have not yet been destroyed here (perhaps due to the limited time available since the dust entered the H II region through the shock) or radiation pressure plays a much more limited role at this distance from the ionising source.

We can compare these conclusions with the parameters derived with the model (see Table 8.3). The temperature distribution of both continuum and silicates suggests that the emission in the arc and in the outer slits follow a continuous, linear distribution while the emission in the blob is characterised by much higher silicate temperature then the continuum would indicate (Fig. 8.25). In line with spatial distribution of gas and dust of the center slit, we interpret this as follows : both the emission in the arc and outer slits traces the dust in the H II region while the blob emission is dominated by the PDR. The good correspondence between the dust emission, dust temperature distribution and the distribution of the ionised gas tracers suggest that the dust in the H II region is heated predominantly by trapped Lyman α photons and that this is at the basis of the linear correlation in silicate and continuum temperature (i.e. the dust is hottest in the center of the arc). Because the emission from the blob seems to be associated with a PDR, Lyman α heating cannot be important and hence these points do not partake in the general correlation of the temperature. It is unclear why the silicate temperature in the blob is among the highest temperatures while the continuum is so cool. Likely, the blob is more closely associated with the ionising star then the arc, but that does not explain the low temperature of the continuum carriers. Either the silicates and continuum carriers are not spatially coexistent (i.e., the dust continuum is dominated by background emission not associated with the blob) or the silicate (but not the continuum carriers)

size distribution differ between the PDR and the H II region. Specifically, if the silicate sizes in the PDR are much smaller then in the H II regions, they would be hotter. However, the physical processes responsible for such a spatial separation between silicates and continuum carriers or silicate size variations between the PDR and the H II region are not understood.

8.6 Summary

In this paper, mid-infrared images and long-slit 8–13 μm spectra of the compact H II regions IRAS 18434-0242 and IRAS 21190+5140 are presented indicating that clear variations are present in the spatial distribution of the different infrared emission components.

We detected a new broad dust emission feature at $\sim$8.9 μm in IRAS 18434. Previous studies have shown that the 7.7 μm UIR emission feature can shift to 8.22 μm in some sources. Possibly, this new discovered 8.9 μm band is just an extreme example of such a shift and its carrier is closely related to the carriers of the UIR bands. We found that in IRAS 18434, the dust continuum emission in the mid-infrared is dominated by thermal emission of dust co-located with the ionised gas and that the carrier of the 8.9 μm feature also resides inside the H II region while the PAH emission originates from the PDR.

The 10 μm spectrum of IRAS 21190 reveals the presence of three different "dust" components: PAHs, silicates in emission and dust continuum-carriers. The spatial distribution of the ionised gas and the dust emitted at 12 μm (i.e. silicate emission and dust continuum emission) reveals that in the arc, the dust resides within the H II region. In contrast, the location of the extra emission in the north-east of the source is clearly different for both the ionised gas and the dust, indicating that here the dust continuum emission in the mid-infrared is dominated by dust originating in the PDR. We calculated spectra composed of dust continuum emission and silicate emission assuming an MRN size distribution and a size dependent temperature law. We found a temperature gradient within the source for both the dust continuum emission and the silicate feature and this temperature of the dust and the silicate grains correlates well with each other. This correlation vanishes for the extra emission in the north-east of the source. We found that both the silicates and the dust in the arc are co-located with the ionised gas in the H II region and are heated predominantly by trapped Lyman α photons. Why the silicate temperature at the location of this extra emission, is among the highest temperatures while the continuum is cool, is not well understood.

It is clear that similarities and variations in the spatial distribution of the different IR emission components emphasise the importance of differences in location, excitation mechanism and of chemical modifications of the carriers.

Acknowledgements

We thank the staff of Palomar Observatory for assistance with the observations. We are grateful to A. Bik, E. Churchwell and A. Watson for providing the H_2 map, the radio map and the apparent extinction map of IRAS 18434 respectively, to L. Martín-Hernández and A. Bik for providing the data of the spatial variation of Brγ and H_2 across IRAS 18434 and to B. Latter for providing the K-band image of IRAS 21190. EP thanks N.L. Martín-Hernández and H. Spoon for useful discussions.

8.A The silicate profile

The flux density $F_\nu(a)$ emitted by a single spherical dust particle with radius ("size") a at temperature $T_{\rm d}(a)$ is given by

$$F_\nu(a) = 4\pi a^2 Q_{em}(\nu, a) B_\nu(T_{\rm d}(a)) \tag{8.2}$$

in which $Q_{em}(\nu, a)$ is the particle's frequency-dependent emission efficiency. In the optically thin limit, the emergent flux of a collection of grains at different sizes is then given by

$$F_\nu = \int_{a_{\rm min}}^{a_{\rm max}} F_\nu(a) n(a)\, da \tag{8.3}$$

$$= \int_{a_{\rm min}}^{a_{\rm max}} 4\pi a^2 Q_{em}(\nu, a) B_\nu(T_{\rm d}(a)) n(a)\, da \tag{8.4}$$

where $a_{\rm min}$ and $a_{\rm max}$ denote the minimum and maximum grains sizes respectively, and $n(a)$ the number of particles of size a in the collection of grains. The fact that we observe the silicate feature in emission implies that the optically thin limit is valid.

Mathis, Rumpl & Nordsieck (1977, MRN hereafter) studied the grain size distribution for the interstellar medium and concluded that the grain size distribution can be well represented by a power-law. We will adopt this grain size distribution, in the form presented by Draine & Lee (1984) :

$$n(a) = n_{\rm H} A_{\rm sil} a^{-3.5} \tag{8.5}$$

where $A_{\rm sil}$ is the abundance of silicates relative to hydrogen, and $n_{\rm H}$ is the number density of atomic hydrogen. The cutoffs to this distribution are found by MRN to be $a_{\rm min}$ = 0.005 μm and $a_{\rm max}$ = 0.25 μm.

At the IR wavelengths studied here, $2\pi a/\lambda < 0.5$ so that at each frequency $Q_{em}(\nu, a) \propto a$ (Draine & Lee 1984); in this case we can separate the wavelength- and size-dependent parts of the emission efficiency:

$$Q_{em}(\nu, a) = f P_\nu a \tag{8.6}$$

where f is a constant and P_ν contains the frequency dependence of the efficiency which is independent of grain size.

Assuming the grains are in thermal equilibrium with their environment, we can derive the grain temperature $T_{\rm d}(a)$:

$$\int_0^\infty \frac{L_\nu}{4\pi r^2} \pi a^2 Q_{abs}(a, \nu) d\nu = \int_0^\infty 4\pi a^2 Q_{abs}(a, \nu) B_\nu(T_d) d\nu \tag{8.7}$$

with $Q_{abs}(a, \nu) = Q_{em}(a, \nu)$.

The Planck averaged absorption efficiency is defined as

$$\overline{Q_{abs}} = \frac{\int_0^\infty Q_{abs}(a, \nu) B_\nu(T) d\nu}{\int_0^\infty B_\nu(T) d\nu} \tag{8.8}$$

Note that, since we are integrating over frequency, the dependence of Q_{abs} on frequency and grain radius becomes a dependence on temperature and grain radius for $\overline{Q_{abs}}$.

Now, multiply the top and bottom of the lefthand side of 8.7 by $\int_0^\infty B_\nu(T_{eff})d\nu = \sigma T_{eff}^4/\pi$ and the top and bottom of the righthand side of 8.7 by $\int_0^\infty B_\nu(T_d)d\nu = \sigma T_d^4/\pi$. We then have

$$\frac{L_{bol}\pi a^2\overline{Q_{abs}}(T_{eff},a)}{4\pi r^2} = 4\pi a^2\overline{Q_{abs}}(T_d,a)\frac{\sigma T_d^4}{\pi} \tag{8.9}$$

with $L_{bol} = 4\pi R_\star^2\sigma T_{eff}^4$.

The Planck averaged absorption efficiency of silicate grains at an effective temperature corresponding to an O6–O8 star can be assumed to be 1. Furthermore, Draine & Lee (1984) showed that $\overline{Q_{abs}}(T,a)/a \propto T^2$ for $\log(T) \leq 2$ so that Eq. 8.9 becomes

$$T_{\rm d}(a) = Ca^{-1/6} \tag{8.10}$$

in which C is a constant. With T_0 the temperature of an $a_0 = 1$ μm grain, we can write Eq. 8.10 as

$$T_{\rm d}(a) = T_0\left(\frac{a}{a_0}\right)^{-1/6} \tag{8.11}$$

Putting Eqs. 8.5, 8.6 and 8.11 into Eq. 8.4, we obtain :

$$F_\nu = \int_{a_{\rm min}}^{a_{\rm max}} 4\pi a^2 f P_\nu a \frac{2h\nu^3}{c^2}\frac{1}{\exp\left(\frac{h\nu}{kT_0}\left(\frac{a}{a_0}\right)^{1/6}\right)-1} n_{\rm H}A_{\rm sil}a^{-3.5}\,da \tag{8.12}$$

$$= \frac{8\pi hf}{c^2}n_{\rm H}A_{\rm sil}P_\nu\nu^3\int_{a_{\rm min}}^{a_{\rm max}}\frac{a^{1/2}}{\exp\left(\frac{h\nu}{kT_0}\left(\frac{a}{a_0}\right)^{1/6}\right)-1}\,d\ln a \tag{8.13}$$

9

Conclusions and future work

The key questions addressed in this thesis is to determine the characteristics of the IR emission features and their implications for the composition and evolution of their carriers.

9.1 What did we learn?

PAHs : an interstellar family

The detailed analysis of the UIR bands in astronomical spectra of a wide variety of objects allows us to extend our knowledge on which molecules or dust grains are responsible for specific UIR bands or their satellites.

The "traditional" UIR bands

Until quite recently, most of the interstellar emission bands were considered to be more-or-less invariant in position and profile. A study of the profiles and peak position of the main UIR bands (3.3, 6.2, 7.7, 8.6 and 11.2 μm) in a large sample of sources including reflection nebulae, H II regions, YSOs, evolved stars and galaxies, reveals however the opposite : the main IR emission features show pronounced variations in peak position and profile (see Chapters 3 and 4). Noticeable is the strong contrast in the spectral variations of the CC modes compared to those for the CH modes. In addition, the observed variations of the different UIR bands are directly linked with each other and depend on the type of object.

Analogously, laboratory measurements and theoretical calculations of several PAH molecules exhibit variability. The variation in the peak position of the 3.3 and 11.2 μm band, measured in the laboratory or quantum-chemically calculated, is much larger than observed in space. It is clear that only a small *subset* of the PAHs studied by these means is present in space. On the other hand, the variation in peak position of the CH modes is likely due to the presence of a *family* of PAH molecules each emitting at a slightly different frequency.

We attribute the observed 6.2 μm profile and peak position to the combined effect of a PAH family and anharmonicity with *pure* PAHs representing the 6.3 μm component and *substituted/complexed* PAHs representing the 6.2 μm component. Also *larger PAH related species* like PAH clusters or PAH platelets can be responsible for the latter component.

The 7.6 μm component is well reproduced by both pure and substituted/complexed PAHs but the 7.8 μm component remains an enigma. In addition, the exact identification of the 8.22 μm feature remains unknown.

The infrared spectrum of a particular H II region (see Chapter 8) shows – beside the traditional UIR bands – a new broad emission feature at 8.9 μm. This band is very similar to the 8.22 μm band seen towards two evolved objects : the band has a similar broad profile but is clearly redshifted. Probably, this band is due to *larger PAH related species* like PAH clusters or PAH platelets.

In Chapter 7, we study the infrared spectra of H II regions in the LMC and SMC. In these neighbouring galaxies, the metallicity (and hence the carbon abundance) is considerably lower then in our Milky Way. Comparison with H II regions in our Milky Way shows that the relative strengths of the UIR bands vary considerably and a segregation between the sources in the different types of environment (Milky Way – LMC : others – LMC : 30 Dor – SMC) is present. This effect is caused by the molecular structure of the PAHs : in star forming regions in the SMC and the LMC, the PAH molecules are *compact* and have *smooth edges* while in star forming regions in the Milky Way, the PAH molecules are *less compact* and *irregular*.

"Poor" PAHs

In chapter 5, we present the first detection of UIR emission features at ~ 6.4 and 7.9 μm in the spectrum of the dusty WC8 Wolf-Rayet star WR 48a. As expected in a hydrogen poor environment, emission due to the CH vibrational modes is not present, neither are PAH molecules. However, the apparent bands at 6.3 and 7.9 μm resemble the traditional UIR bands and hence are likely caused by *large carbonaceous molecules* or *amorphous carbon dust grains* in the circumstellar environment of WR 48a.

"Heavy" guys

In Chapter 6, we search for heavy PAHs. In these molecules, one or more hydrogen atoms is replaced by a deuterium atom without disturbing the PAH structure, the so-called *PADs*. Due to the higher mass of D, the CD vibrational modes occur at different frequencies then the CH ones. At these frequencies, we indeed find very weak emission in the Orion Bar.

Summarising, the interstellar PAHs form a family of compounds whose detailed composition reflects the local physical conditions.

Formation and evolution of PAHs

As mentioned above, the variations in peak position and profile of the main UIR bands (3.3, 6.2, 7.7, 8.6, 11.2 μm) are directly linked with the type of object (see Chapters 3 and 4). In particular, ISM-like sources all exhibit very similar UIR bands but quite distinct from those around evolved stars. These variations between different types of objects give us information on how PAHs form and evolve.

Around evolved stars, where the PAHs are formed, we find pure large PAHs (Chapter 3). How they are formed and which specific individual PAHs are formed is however not clear. In addition, we conclude that they (or similar molecules) can also be formed in H-poor environments (Chapter 5). Furthermore, the presence of high energetic radiation (as in the LMC and SMC) forms no objection for the formation of these molecules (Chapter 7). Since PAHs are

the building blocks in soot formation, these arguments are in a limited way also valid for the formation of stardust.

In the ISM – where PAHs are processed by high energetic irradiation, highly energetic particles and strong shocks – we mainly find heterogene PAHs (i.e. where the carbon atom is replaced by a hetero atom, likely nitrogen) or PAH clusters/platelets (Chapter 3). However, depending on the metallicity of the region, the PAHs are processed in different ways (Chapter 7). For example, in star forming regions in the LMC, the PAH molecules are compact and have smooth edges while in star forming regions in the Milky Way, the PAH molecules are less compact and irregular.

Deuterium fractionation of PAHs occurs due to the different zero-point energies of CH and CD bonds, resulting in slightly more stable CD bonds and so, with time, interstellar PAHs should become enriched in deuterium. When comparing the strength of the CD vibrational modes with that of the CH vibrational modes we then can estimate the deuterium enrichment of the PAHs (Chapter 6). This immediately offers the possibility to study the history of the environments where these PADs are detected : when those environments are young, we expect relatively low abundance of PADs while in old environments, the PADs will be more abundant.

In massive star forming regions, the local physical conditions strongly influence the distribution of PAHs and dust grains. In particular, the dust grains and PAHs undergo different processes inducing the presence of dust grains co-located with the ionised gas in the densest region of the H II regions while the PAH emission originates from the neutral regions in the surrounding PDR.

9.2 Future work

While in the past, progress in this area was limited by the astronomical observations, ISO-SWS has relocated the astronomical boundary and the key questions are now laboratory-oriented. There have been many comparisons between PAH spectra and the interstellar spectra over the years. Due to the large effort put in theoretical and laboratory studies of PAHs, the fit has now become striking. Nevertheless, in view of the quality of the new ISO spectra, important differences become apparent which have the potential of shedding further light on the interstellar PAH population.

Laboratory and theoretical side

The UIR bands are likely due to free gas-phase PAHs. To date, most laboratory studies of PAHs are done in matrices and only one study measures isolated, individual PAH molecules in the gas-phase. A good understanding of the influence of the matrix-isolation technique on the PAH emission bands is essential to interpret astronomical data with the present quality. Also, the ISO studies suggest that the interstellar PAH family contains very large molecules likely present in different charge states. Laboratory measurements and/or theoretical calculations of these molecules will certainly aid in the interpretation of the astronomical spectra.

In particular, the interstellar position of the 6.2 μm band coincides with the position of the 6.2 μm band in nitrogen substituted PAHs. However substituted/complexed PAHs, metallocenes or PAH clusters likely cause a similar effect on the peak position compared to

pure PAHs, i.e. a blueshift of the peak position towards 6.2 μm. Hence, to make a firm identification, further theoretical and experimental work is needed on these molecules.

The ISO spectra also revealed the weak points in the identification of the UIR bands with PAH molecules. For example, the PAHs measured in the lab or theoretically calculated can not account for the 7.8 μm emission and exhibit only weak emission at 8.6 μm. Other features as the 8.2 and 8.9 μm bands, are likely related to PAH molecules but are probably not caused by them. Here, theoretical and experimental work on PAH related species likely reveals the global structure of their carrier.

Astronomical side

To solve the mystery on the specific individual members of the PAH family, one can, in combination with laboratory and theoretical work, look for the electronic transitions (at UV and visual wavelengths) and the ro-vibrational structure (at submm and mm wavelengths) of PAHs. Several instruments are or become available to look for the electronic transitions e.g. William Hershel Telescope on La Palma, UVES on the VLT, COS (to be placed on the Hubble Telescope). The HIFI instrument on HERSCHEL and ALMA are ideally suited for the search for ro-vibrational structure associated with low-lying transitions and hence may a have a significant and unique role in the identification of the PAHs. These ro-vibrational transitions can also reveal information on the rotational temperature of PAHs which have a strong impact on current PAH models (Rouan et al. 1992). These studies can then be coupled with the UIR bands to probe the interrelationship of the spectral characteristics of PAHs.

The suggestion of substituted PAHs or metallocenes as carrier of the 6.2 μm band can be assessed by studying low metallicity galaxies in this wavelength region. The 6.2 and 7.7 μm features are expected to change with metallicity when due to N-substituted PAHs or PAHs complexed with metals since both the elemental N/C and Fe/C ratio varies with metallicity. The spectra of PAHs in low metallicity systems is also of interest for studies of the IR characteristics of galaxies in the early universe. While ISO-SWS has been able to probe the IR emission spectra of regions in the Milky Way, SIRTF, SOFIA and NGST, with their superb sensitivity, will allow us to extend these studies to nearby galaxies including such low metallicity systems.

Two properties influence the observed PAH spectra : the composition of the PAH family associated with the source and its ionisation fraction. With high spatial and spectral resolution IR spectroscopic data we can study the spatial variations of the PAH spectrum within a source and link the observed variations to both the physical conditions present in the source and the laboratory study on IR characteristics of PAHs. In this way, we may be able to disentangle the influence of these two properties, PAH family and charge state. Furthermore, we can link the PAH characteristics with those of the dust grains. This study can then also be extended to study the PAH spectra within galaxies. A plethora of 10-meter class telescopes are now becoming available. These observatories are or will be equipped with near -and mid-infrared imaging and spectroscopy instruments (e.g. VISIR, VLTI and MIDI on the VLT, Michelle and T-ReCS on Gemini) which will allow to probe variations in the spectroscopic spectrum of the PAHs on the smallest scales in order to determine, in detail, the interplay of physical conditions and PAH characteristics.

Nederlandse samenvatting

De hele wereld om ons heen lijkt opgebouwd uit een indrukwekkende hoeveelheid verschillende materialen. De chocolade die we eten lijkt in niets op de satijnen jurk die we dragen, het papier waarop we een proefschrift schrijven, de Red Bull die we daarbij drinken of de lucht die we inademen. Elk van die materialen heeft zijn eigen karakteristieke kenmerken die er voor zorgen dat we ze in het dagelijkse leven kunnen herkennen op basis van hun smaak, kleur, geur, textuur, ...

Die materialen zijn doorgaans echter zelf opgebouwd uit verschillende basisingrediënten. En net zoals een kok in de keuken een beperkt aantal basisingrediënten kan combineren tot zeer gevarieerde gerechten, zo brouwt de natuur (vaak een handje geholpen door de mens) zelf haar indrukwekkend scala aan verschillende materialen uit een relatief beperkt aantal basisstoffen. Zo kan je bijvoorbeeld caffeïne combineren met bepaalde stoffen tot Red Bull, maar als je dezelfde caffeïne met andere stoffen combineert, krijg je chocolade.

Elk van die basisstoffen heeft unieke eigenschappen, en bestaat eigenlijk uit een enorme verzameling van identieke, microscopisch kleine deeltjes die *moleculen* worden genoemd. Aangezien elk van die moleculen de eigenschappen van die basisstof in zich draagt, is één enkele molecule genoeg om die stof te identificeren en – tot op zekere hoogte – te bestuderen.

Vele moleculen die we op aarde kennen blijken zich ook in de ruimte te bevinden. Niet alleen eenvoudige moleculen als water zijn tot in de uithoeken van het heelal te vinden, maar ook complexe bouwstenen voor leven – aminozuren bijvoorbeeld – zijn al gedetecteerd in stenen van buitenaardse origine. Voor vele van deze moleculen is het vooralsnog een raadsel hoe ze in de ruimte gevormd kunnen worden, en of ze er schaars dan wel overvloedig aanwezig zijn.

In dit proefschrift bestuderen we een zeer belangrijke klasse van relatief complexe moleculen in de ruimte, het beste bekend onder de clan-naam PAHs. Zoals we zullen zien, kunnen sterrenkundige waarnemingen ons erg veel vertellen over de manier waarop die moleculen gevormd en/of vernietigd worden, en de omstandigheden waarin dat gebeurt. Maar het werkt ook andersom : door deze moleculen te bestuderen, kunnen we bijvoorbeeld ook veel bijleren over de omgeving waarin ze zich bevinden. Om goed te begrijpen hoe dit allemaal in zijn werk gaat, moeten we eerst wat meer vertellen over die PAHs, en over de sterrenkundige processen die we bestuderen.

We gaan daarom eerst op zoek naar PAH moleculen in de ruimte. Wat zijn ze, wat drijft ze, waar kunnen we ze vinden, waar komen ze vandaan en waarom zouden we er naar op

zoek gaan ?

9.3 PAHs : wat zijn ze ?

PAHs (in het Nederlands vaak PAKs genoemd – zie later) zijn op aarde bekend als teerachtige stoffen, die van nature uit voorkomen in bijvoorbeeld steenkool en ruwe olie. Ze worden echter ook gevormd bij de verbranding van allerhande koolstofrijke brandstoffen, en zijn zo onder andere ook aanwezig in uitlaatgassen van auto's, tabaksrook, kaarsroet en (bij de mindere keukengoden) aangebrande hamburgers. Vele van die PAHs zijn kankerverwekkend, en moeilijk te vernietigen. De grote hoeveelheden PAHs die door de industrie worden uitgespuwd, komen uiteindelijk in de bodem en het grondwater terecht, en kunnen zo in de voedselketen worden opgenomen – PAHs halen dan ook wel eens het nieuws vanwege hun milieuvervuilende eigenschappen.

PAHs zijn ook overvloedig aanwezig in de ruimte, en zijn daar allicht niet het gevolg van milieuvervuiling. Vooraleer we goed kunnen beschrijven hoe ze daar dan wel komen, en vooral waarom die PAHs zo belangrijk zijn, moeten we eerst even wat dieper ingaan op hoe die PAHs eruitzien, en hoe we ze kunnen detecteren in de ruimte.

9.3.1 Atomen en moleculen

Hoewel moleculen de kleinste deeltjes zijn die de eigenschappen van een bepaalde stof in zich dragen, bestaan ze op hun beurt weer uit kleinere eenheden : atomen. De vele tienduizenden verschillende moleculen die we kennen, zijn samengesteld uit niet meer dan een honderdtal verschillende atomen. Verscheidene atomen kunnen zich op een specifieke manier aan elkaar vasthechten, en vormen zo een molecule. Een molecule kan dus in eerste instantie beschreven worden door de atomen waaruit het is opgebouwd. Watermoleculen bijvoorbeeld bestaan uit twee waterstofatomen en één zuurstofatoom en kunnen we dus schrijven als H_2O.

Meer complexe moleculen luisteren naar een doorgaans ingewikkeldere formule. Zo is alcohol te schrijven als C_2H_6O, en de chronologisch vaak daaraan gerelateerde molecule aspirine als $C_9H_8O_4$ en caffeïne is dan weer $C_8H_{10}N_4O_2$. Hoewel er een honderdtal verschillende atomen bestaan, zijn erg veel moleculen – zelfs complexe als aminozuren – samengesteld uit de vier elementen koolstof (C), zuurstof (O), stikstof (N) en waterstof (H). Deze vier elementen zijn dus de belangrijkste bouwstenen voor moleculen. Moleculen die gebaseerd zijn op koolstof (C) worden ook wel "organische stoffen" genoemd.

9.3.2 Bindingen

Vaak is het niet voldoende om te weten uit hoeveel atomen van elke soort een molecule bestaat. Atomen kunnen zich op verschillende manieren aan elkaar vasthechten, en net zoals bij legoblokken kan je met dezelfde hoeveelheid blokken van dezelfde soort verschillende constructies bedenken, die in dit geval tot verschillende moleculen leiden. Het is dus ook van belang te weten wat het "bouwplan" – de structuur – van een molecule is. Dat bouwplan geeft aan op welke manier de verschillende atomen met elkaar verbonden zijn, en is uniek voor elke molecule. In zo een bouwplan wordt door middel van een streepje weergegeven welke atomen zich aan elkaar hebben vastgehecht.

Atomen hebben niet oneindig veel mogelijkheden om zich aan elkaar vast te hechten. Waterstof (H) kan zich maar aan één ander atoom vasthechten, zuurstof (O) maximaal aan twee en koolstof (C) heeft vier vrije hechtingsmogelijkheden. Stabiele moleculen zijn zodanig

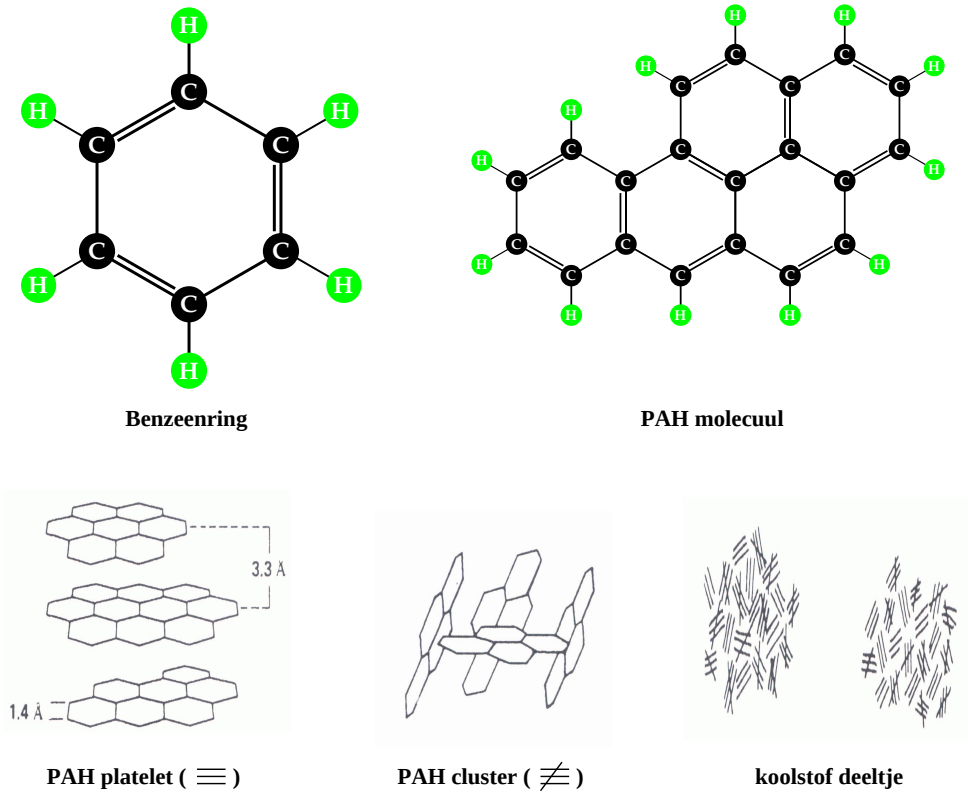

Figuur 1 — Koolstofatomen kunnen zich ordenen in een ring, een zogeheten benzeenring *(linksboven)*. Die ringen kunnen dan weer gebruikt worden als basisstructuur voor grotere moleculen, PAHs *(rechtsboven)*. De PAH moleculen kunnen dan op hun beurt op een specifieke manier geordend worden tot zogeheten PAH platelets of PAH clusters; stofdeeltjes die uit koolstof bestaan hebben een meer chaotische structuur.

gevormd dat elke hechtingsmogelijkheid benut is. Watermoleculen (H_2O) en koolstofdioxidemoleculen (CO_2) zien er dan bijvoorbeeld uit als :

$$H - O - H \qquad\qquad O = C = O$$

De twee bindingsmogelijkheden voor zuurstof (O) zijn in het eerste geval ingenomen door tweemaal een verbinding aan te gaan met waterstof (H); in het tweede geval zijn ze ingenomen door een “dubbele” – en dus sterkere – binding met koolstof (C). Zo hebben in beide gevallen ook waterstof (H) en koolstof (C) al hun bindingsmogelijkheden benut.

9.3.3 MAHs, PAHs en hun verwanten

Koolstofatomen kunnen zich ook in een ring ordenen, en samen met waterstofatomen een zeer stabiele molecule vormen die er uitziet als in Fig. 1. Zo’n ring wordt een benzeenring genoemd. Aan elk koolstofatoom zit precies één waterstofatoom. De koolstofatomen houden dan elk nog 3 vrije bindingsmogelijkheden over, en hechten zich aan elkaar vast door beurtel-

ings een enkelvoudige en een dubbele binding aan te gaan. Koolstofverbindingen van deze soort worden aromatische[1] verbindingen genoemd.

Die ring kan nu ook gebruikt worden als een basisstructuur voor grotere moleculen die uit een aantal van die ringen bestaan (Fig. 1), en daarom "polycyclische" moleculen worden genoemd. Als die moleculen enkel uit koolstof en waterstof bestaan, worden ze in het jargon *Polycyclic Aromatic Hydrocarbons* of kortweg PAHs genoemd (in het Nederlands wordt dat Polycyclische Aromatische Koolwaterstoffen of PAKs). Je zou dan ook één enkele benzeenring een "Monocyclic" Aromatic Hydrocarbon of MAH kunnen noemen. Door verschillende PAHs netjes op elkaar te stapelen, kunnen we PAH *platelets* vormen, en door een niet al te grote hoeveelheid PAHs op een geordende manier aan elkaar te plakken kunnen we PAH *clusters* vormen. Stofdeeltjes die uit koolstof bestaan, hebben een meer chaotische structuur.

9.4 Stralende PAHs

Op aarde kunnen we chemische stoffen onderzoeken door een staal te nemen en dat bijvoorbeeld onder een microscoop te bestuderen. Doorgaans worden er echter een hele resem andere technieken gebruikt om stoffen te bestuderen. In dit proefschrift hebben we de PAHs bestudeerd door middel van een techniek die spectroscopie heet – vooralsnog de enige manier om stoffen te bestuderen die zich op astronomische afstanden van de aarde bevinden.

9.4.1 Regenbogen van gas en sterren

Als we het licht van de zon door een prisma sturen, doen we net hetzelfde als de natuur doet tijdens een zonnige regenbui : we maken een regenboog. Zo kon Newton al aantonen dat de zon niet enkel het gele licht uitstraalt dat we zien op een zonnige dag, maar ook alle andere kleuren van de regenboog. En eigenlijk nog veel meer : uit het dagelijkse weerbericht weten we ook dat de zon gevaarlijke UV straling uitzendt, en veel mensen weten ook dat de warmte die we ontvangen van de zon eigenlijk infraroodstraling is. Die straling is eigenlijk niets anders dan licht van nog een andere kleur, waarvoor het menselijk oog niet gevoelig is. In plaats van "licht" hebben wetenschappers het dan doorgaans over "straling" en in plaats van kleur gebruiken ze "golflengte". Zo heeft UV straling een korte golflengte, blauw licht een iets langere golflengte, en rood licht en infraroodstraling nog langere golflengten. Die golflengte is ook een maat voor de energie van die straling : hoe korter de golflengte, hoe energetischer de straling is. UV straling is dus veel energetischer dan infraroodstraling.

Een spectroscoop is in feite niets anders dan een prisma – waarmee we het zonlicht kunnen omtoveren tot een regenboog – gecombineerd met een (tegenwoordig digitale) camera die van deze regenboog een foto maakt. Bij een regenboog is vaak te zien dat niet alle kleuren even helder zijn. Geel is doorgaans de helderste kleur, en violet is soms zelfs moeilijk te zien. Als we de helderheid van de verschillende kleuren in de regenboog zouden opmeten, zou dat er uitzien als Fig. 2a : een lage helderheid voor violet, het helderste bij geel, en weer minder intens naar het rode toe. Het op die manier weergeven van de helderheid voor verschillende golflengten heet een spectrum.

Als we nu een spectrum maken van een lichtbron zoals een gloeilamp, dan ziet dat eruit als iets in Fig. 2(a) : een continu helderheidsverloop dat bij een specifieke kleur het helderste is. Als we daarentegen het licht van een gas doorheen onze spectroscoop sturen, zien we iets

[1] De term "aromatisch" werd – lang voordat men wist wat atomen en moleculen waren – gebruikt om een aantal chemische stoffen te beschrijven die een erg bijzondere geur hebben.

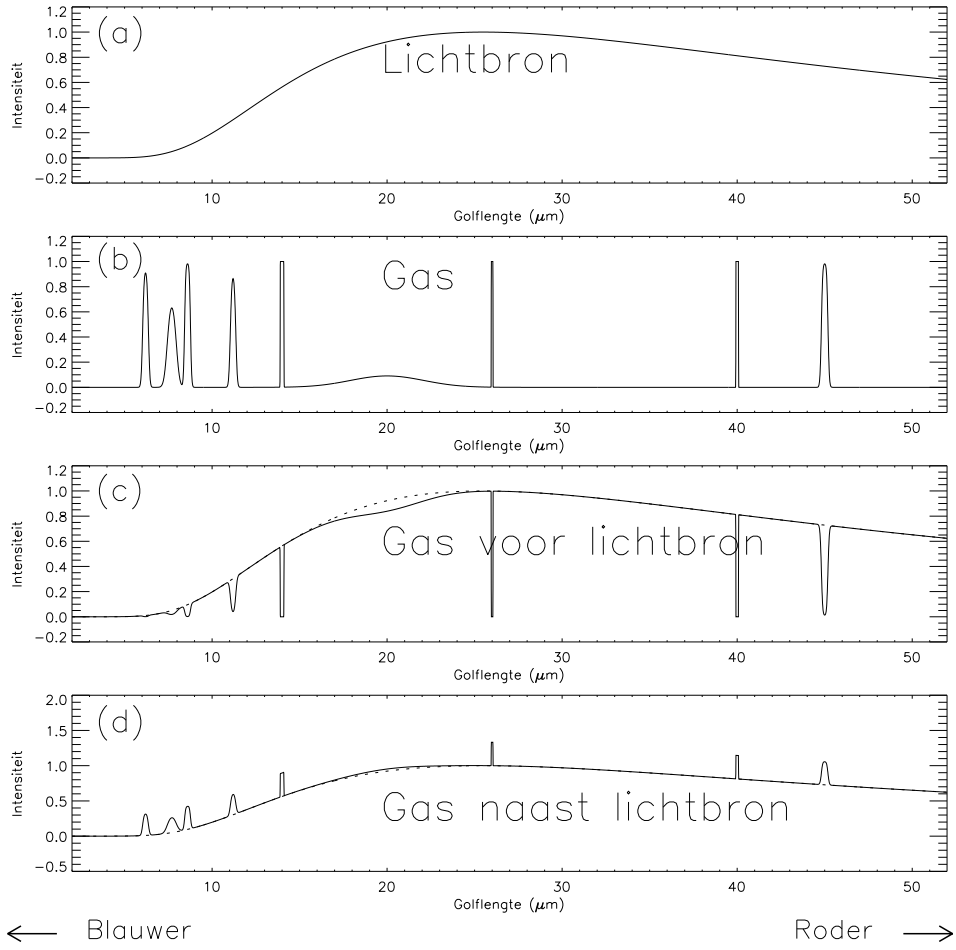

Figuur 2 — Verschillende objecten hebben een ander type spectrum : *(a)* een lichtbron zoals een gloeilamp straalt een *continu* spectrum uit; *(b)* een gas is herkenbaar aan een *lijnen*spectrum. *(c)* Het spectrum van een gas dat zich tussen de spectroscoop en de lichtbron bevindt vertoont *absorptie*lijnen. *(d)* Het spectrum van een gas dat zich naast een lichtbron bevindt is een continu spectrum met *emissie*lijnen.

als Fig. 2(b) : er is duidelijk geen continu verloop meer, maar eerder individuele pieken bij welbepaalde kleuren. Als we dan tenslotte een spectrum opmeten van een lichtbron, maar hetzelfde gas tussen die lichtbron en onze spectroscoop zetten, krijgen we iets als Fig. 2(b) : het continue verloop van de lichtbron wordt onderbroken door dalen op exact dezelfde positie als er pieken waren te zien in het spectrum van het gas alleen.

Als we nu een astronomisch spectrum bekijken, kunnen we dus in een oogopslag bepalen waar we naar kijken : als het eruit ziet als Fig. 2(a) kijken we enkel naar een lichtbron. Zien we enkel pieken, dan is de telescoop op een gas gericht. Als we iets zien als Fig. 2(c), dan

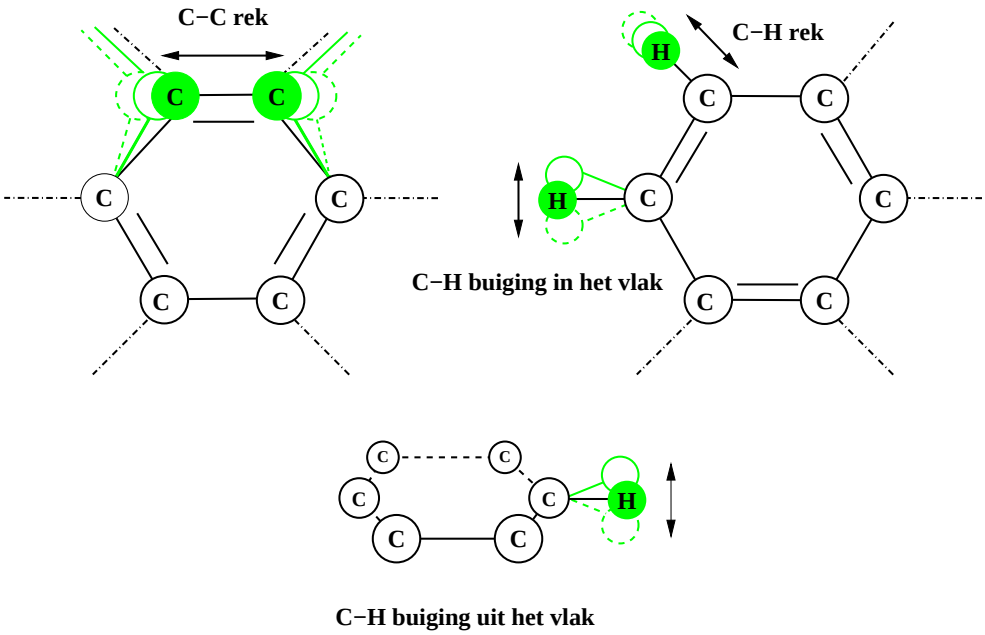

Figuur 3 — De verschillende manieren waarop de atomen van een PAH molecule onderling kunnen trillen.

weten we dat we naar een lichtbron kijken, maar dat er tussen ons en de lichtbron een gas zit. De meeste spectra beschreven in dit proefschrift zien er echter uit als Fig. 2(d) : we zien het karakteristieke continue verloop van een lichtbron, maar ook de pieken van een gas. Omdat we nu weten dat het gas zich niet voor de ster bevindt (want dan zou het er uit zien als Fig. 2(c)), moet dit gas zich naast de ster bevinden. Zo bestuderen we dus het gas in de directe omgeving van de ster in kwestie.

Elk gas heeft een eigen specifieke reeks pieken (of dalen). In aardse laboratoria kunnen we de spectra opmeten van bekende chemische stoffen, en zo bepalen waar precies die pieken liggen voor elk van deze stoffen. Als we nu een astronomisch spectrum naast de labspectra leggen, kunnen we in principe bepalen welke chemische stoffen rond welke sterren voorkomen.

9.4.2 Trillende PAHs

In bepaalde omstandigheden kunnen moleculen (en dus ook PAHs) licht – of straling – van een welbepaalde golflengte gedeeltelijk verduisteren, en in andere omstandigheden kunnen ze zelf ook licht (straling) uitzenden. Het mechanisme dat hierachter zit speelt zich onder andere af op het niveau van de bindingen tussen de verschillende atomen in een molecule.

Die bindingen kan je je best voorstellen als springveertjes. Twee atomen die aan elkaar vastzitten door middel van zo een veertje, kunnen wat heen en weer bewegen ten opzichte van elkaar. Het gekke is dat ze dit niet op eender welk ritme kunnen doen. Ze kunnen bijvoorbeeld wel twee keer per seconde over en weer gaan, of drie keer of meer keer, maar niet drie-en-een-halve keer. Bovendien kunnen ze niet zomaar overschakelen op een ander ritme. Als ze

op een hoger tempo willen trillen hebben ze energie nodig, en om op een lager tempo te trillen hebben ze energie te veel. In dat laatste geval wordt het energie-overschot uitgezonden als straling. Omdat het hierbij gaat om een nauwkeurig bepaald energie-overschot, en omdat de golflengte van straling een maat is voor de energie van die straling, zullen ze bij het overgaan naar een lager tempo dus straling uitzenden met een zeer specifieke golflengte. Dat verklaart waarom het spectrum van een gas enkel specifieke pieken bevat (zoals in Fig. 2b) : die pieken komen overeen met veranderingen in het trillingsritme.

Elk van die pieken wordt – in het geval van PAH moleculen – veroorzaakt door verschillende soorten trillingen, waarvan er een paar worden geïllustreerd in Fig. 3. Een waterstofatoom (H) in een PAH molecule kan bijvoorbeeld drie soorten trillingen uitvoeren, die elk een andere hoeveelheid energie vragen. Dit kan je je makkelijk voorstellen met een voorbeeld uit de keuken. Een lepel die je wat laat uitsteken over de rand van een tafel, kan je makkelijk ombuigen door het uiteinde naar beneden te duwen. Dat vraagt dus weinig energie. Het wordt al een stuk moeilijker (en vraagt dus meer energie) om die lepel in de andere richting – evenwijdig met het tafelblad – om te buigen. De lepel uitrekken is dan nog een pak moeilijker. Zo vraagt het ook relatief weinig energie om een waterstofatoom te laten trillen in een vlak loodrecht op de PAH molecule, iets meer om het te laten trillen in hetzelfde vlak als de PAH molecule en veel meer om de binding uit te rekken. De pieken die het gevolg zijn van de eerste soort trilling vind je dus bij lagere energieën – of dus langere golflengten – dan de andere. Dat is duidelijk te zien in Fig. 4.

9.5 De infrarode emissiebanden

In de loop van de jaren ’70 ontdekten astronomen dat de infrarood spectra van een hele resem astronomische objecten (stervormingsgebieden, jonge sterren, oude sterren, ...) een serie merkwaardige pieken vertonen rond 3.3, 6.2, 7.7, 8.6, 11.2 en 12.7 μm. Die pieken waren er óf allemaal, óf er was er geen enkele. Bovendien werden ze steeds gezien in emissie en nooit in absorptie. Omdat het lange tijd onduidelijk was welk materiaal verantwoordelijk is voor deze emissiebanden, staan ze nu bekend als de “Unidentified InfraRed (UIR) bands” – de “Niet-geïdentificeerde InfraRood banden”.

Na lang zoeken en gissen werd het stilaan duidelijk wat aan de oorsprong van deze banden ligt. De banden bleken namelijk een frappante gelijkenis te vertonen (zie Fig. 4) met iets wat op aarde goed bekend is : uitlaatgassen van auto’s ! De betreffende banden in het spectrum van die uitlaatgassen bleken afkomstig te zijn van PAH moleculen, en zo wordt thans algemeen aangenomen dat PAH moleculen verantwoordelijk zijn voor al deze infrarode banden.

Inmiddels weten we ook al dat de infrarode emissiebanden naar alle waarschijnlijkheid het gevolg zijn van C-C en C-H trillingen in die PAHs, en begrijpen we ook waarom we ze zo goed als altijd als emissiepieken zien. PAH moleculen kunnen namelijk gemakkelijk straling absorberen van hoge energie – meestal UV straling die in de ruimte overvloedig voorkomt. In een fractie van een seconde wordt deze energie verdeeld over alle atomen in de PAH moleculen en omgezet in trillingen van een hoog tempo. Om hun overtollige energie kwijt te spelen, gaan de PAHs langzamer trillen, en zenden ze dus de karakteristieke straling uit tengevolge van de C-H en C-C trillingen. Op deze manier, laten de PAH moleculen hun handtekening achter in de vorm van de infrarode emissie banden.

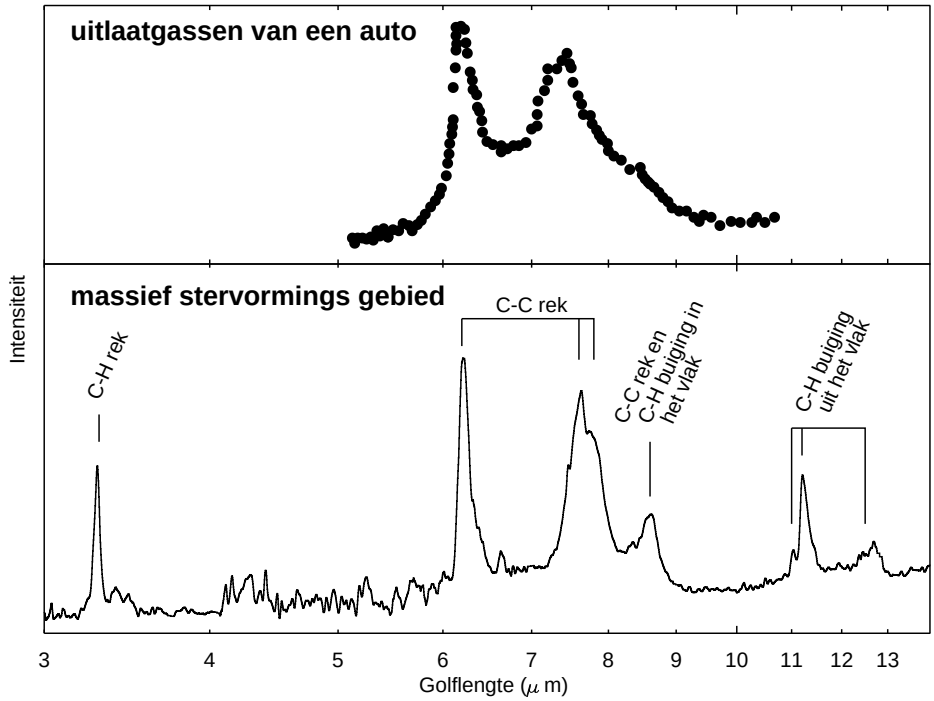

Figuur 4 — (onder) Een typisch infrarood spectrum van een massief stervormings gebied. De verschillende trillingen van PAH moleculen zijn aangegeven. (boven) Het infrarood spectrum van de roetdeeltjes in de uitlaatgassen van een auto.

9.6 De levenscyclus van ruimtestof

PAHs zijn vrij complexe moleculen, en zijn praktisch overal in het heelal te vinden. Hun hele levenscyclus is nauw verbonden met die van het ruimtestof.

Sterren bestaan aanvankelijk hoofdzakelijk uit waterstof en helium, de twee lichtste en eenvoudigste elementen die we kennen. Deze elementen worden gebruikt als brandstof om kernreacties te voeden in het sterinwendige. De straling die bij deze kernreacties vrijkomt zorgt ervoor dat de ster straalt, en de afvalproducten van deze reacties zijn zwaardere elementen als koolstof, stikstof en zuurstof. Lichte sterren brengen deze afvalproducten naar het steroppervlak in de laatste stadia van hun leven, waarna de buitenste sterlagen worden uitgestoten. Bij de meest massieve sterren worden er meer afvalproducten gevormd – zoals ijzer – en deze worden de ruimte ingeslingerd bij een gigantische explosie, een supernova.

Het afgestoten of geëxplodeerde materiaal is aanvankelijk nog heet, maar naarmate die lagen verder uitdeinen, daalt de temperatuur. Als de uitgestoten sterlagen voldoende zijn afgekoeld, worden er allerhande moleculen in gevormd; aanvankelijk kleine en eenvoudige moleculen, maar gaandeweg ook grotere en meer complexe moleculen. Tegelijkertijd wordt er ook ruimtestof gevormd, grotere korrels die lijken op roetdeeltjes en gedeeltelijk zijn opgebouwd uit deze moleculen. Deze uitdeinende en afkoelende sterlagen zijn zo de belangrijkste

geboorteplaatsen van moleculen en ruimtestof.

PAHs zijn een bijproduct van het stofvormingsproces van koolstofrijk ruimtestof, en worden dus ook gemaakt rond deze oude sterren. Een aantal van de PAHs wordt weliswaar geïncorporeerd tot ruimtestof, maar een deel van de hier gevormde PAHs ontsnapt als vrije moleculen. Rond deze oude sterren treffen we zo de grootste variëteit aan in stofcomponenten : zowel de moleculaire bouwstenen, als de stofdeeltjes in verschillende stadia van het stofvormingsproces.

De uitgestoten sterlagen – nu in de vorm van moleculen en ruimtestof – deinen verder uit, en komen zo in de ijle ruimte terecht, het zogeheten interstellair medium. Ook hier ondergaan moleculen en ruimtestof nog veranderingen. Stofdeeltjes of moleculen die met elkaar botsen blijven aan elkaar plakken, en groeien zo langzaamaan uit tot grotere stofdeeltjes. Ook de materialen die al in het interstellair medium aanwezig zijn – uitgestoten door andere sterren – kunnen worden opgenomen in de stofdeeltjes en de moleculen. Anderzijds is het interstellair medium geen stof-vriendelijke omgeving door de voortdurende aanwezigheid van hoog-energetische straling, hoog-energetische deeltjes en sterke schokgolven, die de moleculen en stofdeeltjes geheel of gedeeltelijk kunnen doen uiteenspatten. Enkel de stevigste en meest stabiele materialen kunnen hier overleven, en bijgevolg is de variëteit aan stofdeeltjes in het interstellair medium kleiner dan rond de oude sterren. PAH moleculen zijn doorgaans heel stabiel; en enkel de kleinste onder hen worden vernietigd door deze processen.

Al het ruimtestof en de moleculen die zich in het interstellair medium bevinden vormen stofwolken, die stilaan samenklonteren tot grote en dichte wolken. Het binnenste van die wolken is nu gedeeltelijk afgeschermd van de agressieve aanvallen uit het interstellair medium, maar het is er erg koud. Op de stofdeeltjes komt een laagje ijs te zitten, en de PAHs worden mee ingevroren. Onder invloed van UV straling reageren de PAHs nu met het ijslaagje waarin ze gevangen zitten, en vormen zo nieuwe moleculen – onder andere aminozuren. De kern van die dichte wolken trekt dan onder invloed van de zwaartekracht samen, en de temperatuur neemt toe. Na een tijdje wordt uit die kern een ster geboren, en de ijslagen op de stofdeeltjes smelten door de straling van deze pasgeboren ster. Zo worden de PAHs en de nieuw gevormde moleculen bevrijd.

Rond deze pasgeboren ster kan zich een planetenstelsel ontwikkelen uit de wolk die de ster omringt. Planeten én hun eventuele latere bewoners worden zo gevormd uit het ruimtestof en de moleculen die afkomstig zijn van een vorige generatie sterren, en zwaar gehavend na een lange en vermoeiende reis aan een nieuw leven beginnen.

Als de ster dan weer op haar beurt aan het einde van haar leven is gekomen, zal ook zij haar buitenste lagen afstoten, en begint de hele cyclus opnieuw.

9.7 In dit proefschrift

Omdat de aardse atmosfeer alle infraroodstraling tegenhoudt – op een paar kleine gebiedjes na – kunnen we de infrarode emissiebanden enkel bestuderen met behulp van satellieten. De waarnemingen die in dit proefschrift geanalyseerd zijn, zijn voor het overgrote deel uitgevoerd door de Europese infraroodsatelliet ISO (Infrared Space Observatory), en met name door de Short-Wavelength Spectrometer (SWS) die gebouwd is door SRON in Groningen. Dankzij SWS hebben we nu waarnemingen van hoge kwaliteit van het hele infraroodgebied, en dat maakt deze waarnemingen uniek. Het is dan ook de eerste keer dat de PAHs in de ruimte in hun volle glorie kunnen worden bestudeerd.

Alles bij elkaar hebben we in dit proefschrift een klein honderdtal SWS spectra geanalyseerd. Omdat het gaat om spectra van verschillende types sterren, kunnen we – zoals we zo meteen zullen zien – erg veel bijleren over PAHs, PAH verwanten en stofdeeltjes. Het onderzoek beschreven in dit proefschrift heeft dan ook heel wat nieuwe inzichten opgeleverd. Niet alleen weten we nu veel meer over het soort moleculen en stofdeeltjes dat in de ruimte voorkomt, we kunnen ook bepalen hoe en waar ze gevormd worden en hoe ze verder evolueren. Anderzijds kunnen we ook een en ander opsteken over de omgeving waar ze zich in bevinden.

9.7.1 PAHs : hun banden en trawanten

Het nauwgezet analyseren van infrarode emissiebanden in astronomische spectra van diverse aard heeft ons toegelaten om meer te weten te komen over welke moleculen of stofdeeltjes een aantal van die emissiebanden veroorzaken.

"Traditionele" emissiebanden

Tot dusver werd er van uit gegaan dat de infrarode emissiebanden van astronomische objecten er overal min of meer hetzelfde zouden uitzien. In hoofdstuk 3 en 4 (zie Fig. 5) tonen we aan dat dit zeer duidelijk niet het geval is : zowel de positie als de vorm van *alle* infrarode emissiebanden varieëren aanzienlijk wanneer we de spectra van verschillende objecten met elkaar vergelijken. Bovendien variëren de emissiebanden *tegelijkertijd* : als er bijvoorbeeld één band naar rechts is verschoven, zijn ze allemaal naar rechts verschoven.

Ook de laboratoriumspectra van een hele verzameling PAHs vertonen variaties. De variaties in de C-H banden op 3.3 en 11.2 micrometer (μm) zijn in de laboratoriumspectra echter veel groter dan degene die we zien in de astronomische spectra. Dat duidt erop dat slechts een deel van de PAHs die in het laboratorium zijn opgemeten ook daadwerkelijk in de ruimte voorkomt; anderzijds kunnen die banden niet veroorzaakt worden door slechts één enkele PAH, maar door een "familie" van PAHs.

Ook zien we in de laboratoriumspectra dat de positie van de piek in de C-C band voor de kleinste PAHs rond 6.6 μm ligt; die piek verschuift naar kortere golflengtes (dus naar links in Fig. 5) voor grotere PAHs maar nooit verder dan 6.3 μm. Dat komt net overeen met de spectra van een aantal sterren; dat betekent dus dat rond die sterren vooral grote PAHs voorkomen. Aangezien in de andere astronomische spectra deze piek bij nog kortere golflengtes ligt, kan die niet het gevolg zijn van "zuivere" PAHs. Wellicht is deze band het gevolg van "vuile" PAHs, die niet langer enkel uit koolstof en waterstof bestaan, maar waarbij een ander atoom (bijvoorbeeld stikstof) de positie van één of meerdere koolstofatomen heeft ingenomen. Ook zogenaamde PAH clusters zouden verantwoordelijk kunnen zijn voor deze band.

Het spectrum van een bijzonder stervormingsgebied (zie hoofdstuk 7) vertoont – naast de traditionele emissiebanden – nog een extra band rond 8.9 μm. Deze band lijkt op de 7.7 μm band zoals we die zien in een aantal oude sterren : de band heeft ruwweg dezelfde brede vorm maar is duidelijk verschoven naar rechts (langere golflengte). Allicht is deze band afkomstig van nog grotere (gemodificeerde) PAH verwanten als PAH clusters en PAH platelets.

In hoofdstuk 8 bestuderen we dan weer spectra van stervormingsgebieden in de Magelhaense Wolken. Dat zijn twee kleine sterrenstelsels, en de naaste buren van onze Melkweg. In de Grote Magelhaense Wolk (Large Magellanic Cloud of LMC) is er beduidend minder koolstof voorhanden dan in de Melkweg; de Kleine Magelhaense Wolk (Small Magellanic

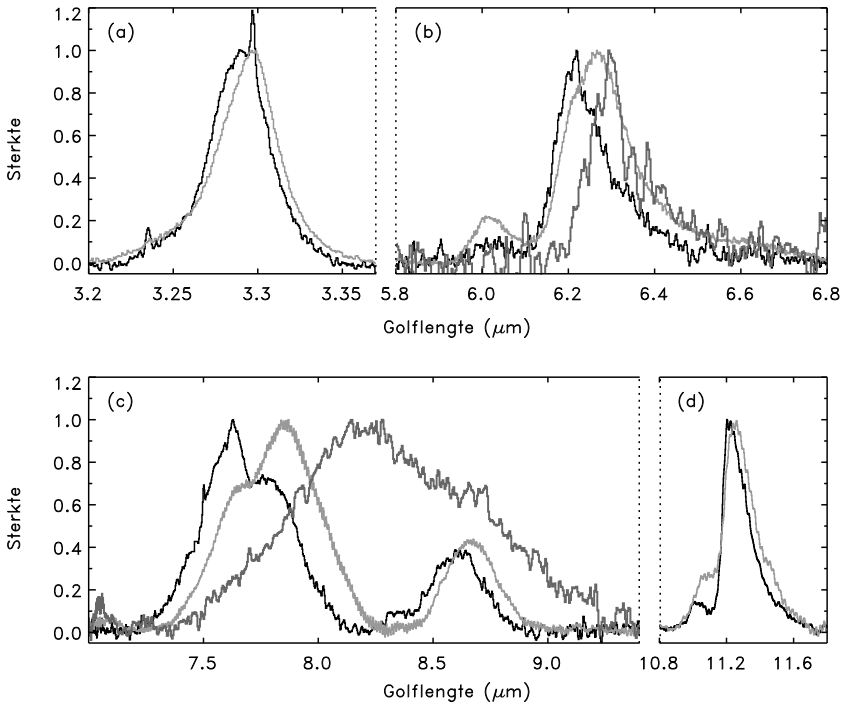

Figuur 5 — Deze figuur illustreert de verscheidenheid in de vorm en positie van de voornaamste PAH emissie banden. De zwarte lijn stelt de emissie banden van een stervormingsgebied voor, de grijze lijnen deze van twee oude sterren.

Cloud of SMC) is koolstof nog vele malen schaarser. Ook in de spectra van deze stervormingsgebieden zijn duidelijk de traditionele infrarode emissiebanden te zien. Een vergelijking tussen de verschillende spectra toont dat de grootte van de verschillende emissiebanden sterk afhankelijk is van de omgeving : in de SMC is de band op 6.2 μm bijvoorbeeld drie keer zwakker dan de 11.2 μm band, maar in de LMC is die maar weinig zwakker en in de Melkweg kan de 6.2 μm band dan weer tot twee keer sterker worden dan de 11.2 μm band. Dit effect wordt veroorzaakt door de structuur van de PAHs : in de SMC en LMC zijn de PAH moleculen compact en hebben gladde, gelijkmatige randen. In de Melkweg daarentegen zijn de randen van dezelfde moleculen onregelmatig en “rafelig” (zie Fig. 6).

Arme PAHs

In hoofdstuk 5 tonen we het spectrum van een zogenaamde Wolf-Rayet ster, een oude massieve ster waar nauwelijks waterstof te vinden is. Zoals te verwachten valt in een waterstofarme omgeving, zijn de C-H banden op 3.3, 8.6 en 11.2 μm niet te zien, en zitten er dus ten stelligste geen zuivere PAHs rond deze ster. Toch zijn in dit spectrum duidelijk infrarode emissiebanden te zien, en die zijn nooit eerder gezien in dit type sterren. De banden die we zien – rond 6.3 en 7.9 μm – lijken erg goed op de C-C banden rond 6.2 en 7.7

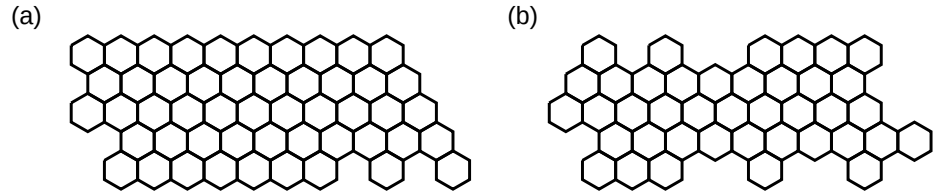

Figuur 6 — Links een "compact" PAH molecule met gladde, gelijkmatige randen zoals ze in ster vormings gebieden in de SMC en LMC voorkomen; rechts een "rafelig" PAH molecule dat karakteristiek is voor ster vormings gebieden in de Melkweg.

μm die we zien in "normale" spectra. Door de grote gelijkenis met die traditionele PAH banden, worden de emissiebanden in dit geval waarschijnlijk veroorzaakt door moleculen die nauw verwant zijn aan de PAHs. We kunnen deze moleculen echter nog niet identificeren, omdat geen enkele van de waterstofarme materialen die tot nog toe zijn onderzocht in het laboratorium banden vertonen op deze posities.

Zware jongens

In hoofdstuk 6 zijn we op zoek gegaan naar "zware" PAH trawanten. In deze moleculen is één of meerdere waterstofatomen vervangen door een deuteriumatoom (D), en daarom worden ze ook wel eens PADs genoemd. Deuteriumatomen zijn als het ware de zwaardere tweelingbroers van waterstofatomen. Ze lijken uiterlijk erg goed op waterstof en kunnen daarom makkelijk de plaats innemen van een waterstofatoom in een PAH molecule zonder dat de andere atomen er erg in hebben. De binding tussen een koolstofatoom en een deuteriumatoom is echter zo sterk, dat een verstoten waterstofatoom nooit meer z'n plek terug kan innemen. Zo worden in de loop der tijd langzaamaan meer en meer waterstofatomen vervangen door deuteriumatomen.

Deuterium is dubbel zo zwaar als een waterstofatoom, en bijgevolg vraagt het meer moeite en energie om zo'n deuteriumatoom in beweging te krijgen. Emissiebanden tengevolge van een C-D binding bevinden zich daarom op een andere golflengte dan de traditionele C-H banden. We kunnen uitrekenen op welke golflengte bijvoorbeeld de banden moeten zitten die het gevolg zijn van het rekken van een C-D binding. Op deze golflengtes hebben we inderdaad twee emissie banden ontdekt. Deze banden zijn erg zwak, omdat er veel minder deuteriumatomen in de ruimte zijn dan waterstofatomen. Door de sterkte van de gewone C-H banden te vergelijken met de sterkte van de C-D banden, kunnen we zo uitrekenen hoeveel waterstofatomen er vervangen zijn door deuteriumatomen.

Meteen hebben we de mogelijkheid om de geschiedenis te bestuderen van de gebieden die we onderzoeken : als die gebieden nog maar jong zijn, zullen er relatief weinig PADs voorkomen; als ze ouder zijn zullen er meer PADs zijn.

9.7.2 Vorming en evolutie van stof en PAHs

We kunnen nu ook de spectra op een rijtje zetten en zo een en ander leren over de vorming en evolutie van PAHs.

Alle spectra die de “traditionele” infrarode emissiebanden vertonen zijn erg makkelijk te klasseren omdat soortgelijke sterren zo goed als identieke spectra hebben : alle jonge sterren hebben erg op elkaar lijkende spectra, de spectra van alle oude sterren lijken als twee druppels water op elkaar enzovoort. Daarentegen zijn er erg grote verschillen te vinden tussen sterren van een ander type (zie bv. Figuur 5 : de zwarte profielen zijn deze van een stervormingsgebied en de grijze van een oude ster).

De variaties tussen de verschillende type van omgevingen geeft ons dan informatie over hoe de PAH moleculen evolueren en beinvloed worden door hun omgeving gedurende hun leven.

Rond oude sterren, waar de PAHs gevormd worden, vinden we “zuivere” PAHs, en dan met name grote PAHs. Hoe deze PAHs gevormd worden, en over welke PAHs het precies gaat, is echter niet duidelijk. Wel weten we dat de PAHs ook kunnen gevormd worden in gebieden waar maar weinig koolstof voorhanden is, en dat er ook PAH-achtige stoffen kunnen gevormd worden in gebieden waar maar weinig waterstof is. Ook de aanwezigheid van hoge doses hoog-energetische straling (zoals het geval is in de LMC en de SMC) zijn duidelijk geen bezwaar om PAHs te kunnen vormen. Gezien de vorming van PAHs en de vorming van ruimtestof innig met elkaar verweven zijn, gelden dezelfde argumtenten tot op zekere hoogte ook voor de vorming van dat ruimtestof.

In het interstellair medium – waar de PAHs gebombardeerd worden door hoog-energetische straling en kunnen botsen met andere deeltjes – vinden we dan vooral “vuile” PAHs, waarbij koolstof en/of waterstofatomen vervangen zijn door andere atomen. Al naargelang de energie van die straling, worden de PAHs op verschillende manieren bewerkt. In stervormingsgebieden in onze Melkweg hebben de PAHs een eerder rafelig uiterlijk vergeleken met deze in stervormingsgebieden in de LMC en SMC (zie Figuur 6).

Tegen de tijd dat de PAHs hun reis door het interstellair medium beëindigen en terecht komen in nieuwe stervormingsgebieden, zijn ze getekend door hun zware reis. Rond deze pasgeboren sterren wijkt de evolutie van stof kwalitatief af van die van de PAHs. Dit blijkt erg duidelijk uit hoofdstuk 7. Daar zien we bijvoorbeeld dat stofdeeltjes zich veel dichter bij de hete ster bevinden dan de PAH moleculen. Dat wijst erop dat PAH moleculen dicht bij de ster vernietigd worden door de intense straling van de ster terwijl de stofdeeltjes kunnen overleven.

Bibliography

Aannestad P.A., Kenyon S.J., 1979, *ApJ* 230, 771

Acosta-Pulido J., Ábrahám P., 2002, In: *ESA SP-481: The calibration legacy of the ISO mission*

Afflerbach A., Churchwell E., Acord J.M., et al., 1996, *ApJS* 106, 423

Afflerbach A., Churchwell E., Hofner P., Kurtz S., 1994, *ApJ* 437, 697

Afflerbach A., Churchwell E., Werner M.W., 1997, *ApJ* 478, 190

Allain T., Leach S., Sedlmayr E., 1996, *A&A* 305, 616

Allamandola L.J., 1993, In: *ASP Conf. Ser. 41: Astronomical Infrared Spectroscopy: Future Observational Directions*, 197

Allamandola L.J., Bregman J.D., Sandford S.A., et al., 1989a, *ApJ Lett.* 345, L59

Allamandola L.J., Hudgins D.M., Bauschlicher C.W., Langhoff S.R., 1999a, *A&A* 352, 659

Allamandola L.J., Hudgins D.M., Sandford S.A., 1999b, *ApJ Lett.* 511, L115

Allamandola L.J., Tielens A.G.G.M., Barker J.R., 1985, *ApJ Lett.* 290, L25

Allamandola L.J., Tielens A.G.G.M., Barker J.R., 1989b, *ApJS* 71, 733

Amari S., Hoppe P., Zinner E., Lewis R.S., 1992, *ApJ Lett.* 394, L43

Anders E., Zinner E., 1993, *Meteoritics* 28, 490

Araya E., Hofner P., Churchwell E., Kurtz S., 2002, *ApJS* 138, 63

Bakes E.L.O., Tielens A.G.G.M., 1994, *ApJ* 427, 822

Bakes E.L.O., Tielens A.G.G.M., 1998, *ApJ* 499, 258

Bakes E.L.O., Tielens A.G.G.M., Bauschlicher C.W., 2001, *ApJ* 556, 501

Ball R., Meixner M.M., Keto E., Arens J.F., Jernigan J.G., 1996, *AJ* 112, 1645

Barker J.R., Allamandola L.J., Tielens A.G.G.M., 1987, *ApJ Lett.* 315, L61

Barlow M.J., Silk J., 1977, *ApJ Lett.* 211, L83

Barsony M., 1989, *ApJ* 345, 268

Bauschlicher C.W., 2002, *ApJ* 564, 782

Bauschlicher C.W., Langhoff S.R., Sandford S.A., Hudgins D.M., 1997, *J. Phys. Chem.* 101, 2414

Becker R.H., White R.L., Helfand D.J., Zoonematkermani S., 1994, *ApJS* 91, 347

Beintema D.A., van den Ancker M.E., Molster F.J., et al., 1996, *A&A* 315, L369

Bellamy L., 1958, The infra-red spectra of complex molecules, 2nd ed. John Wiley & Sons, Inc., New York

Benedettini M., Nisini B., Giannini T., et al., 1998, *A&A* 339, 159

Bernstein M.P., Elsila J.E., Dworkin J.P., et al., 2002, *ApJ* 576, 1115

Bernstein M.P., Sandford S.A., Allamandola L.J., 1996, *ApJ Lett.* 472, L127

Bernstein M.P., Sandford S.A., Allamandola L.J., et al., 1999, *Science* 283, 1135

Blitz L., Fich M., Stark A.A., 1982, *ApJS* 49, 183

Boggess N.W., Mather J.C., Weiss R., et al., 1992, *ApJ* 397, 420

Boogert A.C.A., 1999, Ph.D. thesis, Groningen University

Borghesi A., Bussoletti E., Colangeli L., 1987, *ApJ* 314, 422

Borgman J., van Duinen R.J., Koornneef J., 1975, *A&A* 40, 461

Boselli A., Lequeux J., Contursi A., et al., 1997, *A&A* 324, L13

Boulanger F., 1999, In: *Solid Interstellar Matter : The ISO Revolution*, EDP Sciences, 20

Boulanger F., Abergel A., Bernard J.P., et al., 1996a, *A&A* 312, 256

Boulanger F., Abergel A., Bernard J.P., et al., 1998a, In: *ASP Conf. Ser. 132: Star Formation with the Infrared Space Observatory*, 15

Boulanger F., Abergel A., Cesarsky D., et al., 2000, *ESA-SP 455: ISO Beyond Point Sources: Studies of Extended Infrared Emission*, 91

Boulanger F., Boisssel P., Cesarsky D., Ryter C., 1998b, *A&A* 339, 194

Boulanger F., Reach W.T., Abergel A., et al., 1996b, *A&A* 315, L325

Brand J., Wouterloot J.G.A., 1994, *A&AS* 103, 503

Bregman J., 1989, In: *IAU Symp. 135: Interstellar Dust*, 109

Bregman J.D., Allamandola L.J., Witteborn F.C., Tielens A.G.G.M., Geballe T.R., 1989, *ApJ* 344, 791

Brenner J., Barker J.R., 1992, *ApJ Lett.* 388, L39

Bronfman L., Nyman L.., May J., 1996, *A&AS* 115, 81

Burton M.G., Ashley M.C.B., Marks R.D., et al., 2000, *ApJ* 542, 359

Buss R.H., Cohen M., Tielens A.G.G.M., et al., 1990, *ApJ Lett.* 365, L23

Buss R.H., Tielens A.G.G.M., Cohen M., et al., 1993, *ApJ* 415, 250

Carpenter J.M., Snell R.L., Schloerb F.P., 1990, *ApJ* 362, 147

Caswell J.L., Haynes R.F., 1987, *A&A* 171, 261

Cesaroni R., Churchwell E., Hofner P., Walmsley C.M., Kurtz S., 1994, *A&A* 288, 903

Cesaroni R., Hofner P., Walmsley C.M., Churchwell E., 1998, *A&A* 331, 709

Cesarsky C.J., Abergel A., Agnese P., et al., 1996, *A&A* 315, L32

Cesarsky D., Jones A.P., Lequeux J., Verstraete L., 2000, *A&A* 358, 708

Chan K., Onaka T., 2000, *ApJ* 533, L33

Charnley S.B., Rodgers S.D., Ehrenfreund P., 2001, *A&A* 378, 1024

Charnley S.B., Tielens A.G.G.M., Rodgers S.D., 1997, *ApJ Lett.* 482, L203

Cherchneff I., Barker J.R., 1989, *ApJ Lett.* 341, L21

Cherchneff I., Barker J.R., Tielens A.G.G.M., 1992, *ApJ* 401, 269

Cherchneff I., Le Teuff Y.H., Williams P.M., Tielens A.G.G.M., 2000, *A&A* 357, 572
Chiar J.E., Tielens A.G.G.M., 2001, *ApJ Lett.* 550, L207
Churchwell E., 1990, *A&AR* 2, 79
Churchwell E., Walmsley C.M., Cesaroni R., 1990, *A&AS* 83, 119
Churchwell E., Walmsley C.M., Wood D.O.S., 1992, *A&A* 253, 541
Cidale L., Zorec J., Tringaniello L., 2001, *A&A* 368, 160
Clavel J., Schulz B., Altieri B., et al., 2000, *A&A* 357, 839
Clayton G.C., Martin P.G., 1985, *ApJ* 288, 558
Clegg P.E., Ade P.A.R., Armand C., et al., 1996, *A&A* 315, L38
Cohen M., Allamandola L., Tielens A.G.G.M., et al., 1986, *ApJ* 302, 737
Cohen M., Barlow M.J., 1974, *ApJ* 193, 401
Cohen M., Barlow M.J., Sylvester R.J., et al., 1999, *ApJ Lett.* 513, L135
Cohen M., Tielens A.G.G.M., Allamandola L.J., 1985, *ApJ Lett.* 299, L93
Cohen M., Tielens A.G.G.M., Bregman J., et al., 1989, *ApJ* 341, 246
Cohen M., Walker R.G., Barlow M.J., Deacon J.R., 1992, *AJ* 104, 1650
Colangeli L., Mennella V., Bussoletti E., 1992, *ApJ* 385, 577
Colangeli L., Mennella V., Palumbo P., Rotundi A., Bussoletti E., 1995, *A&AS* 113, 561
Cole A.A., Nordsieck K.H., Gibson S.J., Harris W.M., 1999, *AJ* 118, 2280
Colgan S.W.J., Simpson J.P., Rubin R.H., et al., 1991, *ApJ* 366, 172
Contursi A., Lequeux J., Cesarsky D., et al., 2000, *A&A* 362, 310
Contursi A., Lequeux J., Hanus M., et al., 1998, *A&A* 336, 662
Cook D.J., Saykally R.J., 1998, *ApJ* 493, 793
Cook D.J., Schlemmer S., Balucani N., et al., 1998, *J. Phys. Chem. A* 102, 1465
Cox P., Kessler M. (eds.), 1999, The Universe as Seen by ISO, ESA-SP 427
Cox P., Roelfsema P., 1999, In: *Solid Interstellar matter: the ISO Revolution*, EDP Sciences, 151
Crampton D., Georgelin Y.M., Georgelin Y.P., 1978, *A&A* 66, 1
Crawford M.K., Tielens A.G.G.M., Allamandola L.J., 1985, *ApJ Lett.* 293, L45
Curl R.F., Smalley R.E., 1988, *Science* 262, 1017
Dalgarno A., Stancil P.C., Lepp S., 1997, *Ap&SS* 251, 375
Dartois E., Cox P., Roelfsema P.R., et al., 1998, *A&A* 338, L21
De Buizer J.M., Watson A.M., Radomski J.T., Piña R.K., Telesco C.M., 2002, *ApJ Lett.* 564, L101
de Graauw T., Haser L.N., Beintema D.A., et al., 1996, *A&A* 315, L49
De Pree C.G., Goss W.M., Palmer P., Rubin R.H., 1994, *ApJ* 428, 670
de Vries C.P., Brand J., Habing H.J., et al., 1984, *A&AS* 56, 333
Desert F.X., Boulanger F., Leger A., Puget J.L., Sellgren K., 1986, *A&A* 159, 328
Desert F.X., Boulanger F., Puget J.L., 1990, *A&A* 237, 215
di Francesco J., Evans N.J., Harvey P.M., Mundy L.G., Butner H.M., 1998, *ApJ* 509, 324
Dickel H.R., Dickel J.R., Wilson W.J., Werner M.W., 1980, *ApJ* 237, 711

Draine B.T., 1984, *ApJ Lett.* 277, L71
Draine B.T., 1985, *ApJS* 57, 587
Draine B.T., 1989, In: *Infrared Spectroscopy in Astronomy*, 93
Draine B.T., Anderson N., 1985, *ApJ* 292, 494
Draine B.T., Lee H.M., 1984, *ApJ* 285, 89
Draine B.T., Li A., 2001, *ApJ* 551, 807
Draine B.T., Salpeter E.E., 1979a, *ApJ* 231, 438
Draine B.T., Salpeter E.E., 1979b, *ApJ* 231, 77
Duley W.W., Williams D.A., 1981, *MNRAS* 196, 269
Dwek E., 1986, *ApJ* 302, 363
Ehrenfreund P., van Dishoeck E.F., Burgdorf M., et al., 1997, *Ap&SS* 255, 83
Epstein S., Krishnamurthy R.V., Cronin J.R., Pizzarello S., Yuen G.U., 1987, *Nature* 326, 477
Everett M.E., Depoy D.L., Pogge R.W., 1995, *AJ* 110, 1295
Fabian D., Jäger C., Henning T., Dorschner J., Mutschke H., 2000, *A&A* 364, 282
Faison M., Churchwell E., Hofner P., et al., 1998, *ApJ* 500, 280
Feldt M., Stecklum B., Henning T., et al., 1998, *A&A* 339, 759
Feldt M., Stecklum B., Henning T., Launhardt R., Hayward T.L., 1999, *A&A* 346, 243
Fey A.L., Gaume R.A., Claussen M.J., Vrba F.J., 1995, *ApJ* 453, 308
Fich M., 1986, *AJ* 92, 787
Fich M., 1993, *ApJS* 86, 475
Fich M., Blitz L., 1984, *ApJ* 279, 125
Fitzpatrick E.L., 1985, *ApJ* 299, 219
Fitzpatrick E.L., 1986, *AJ* 92, 1068
Flickinger G.C., Wdowiak T.J., 1990, *ApJ Lett.* 362, L71
Flickinger G.C., Wdowiak T.J., Gomez P.L., 1991, *ApJ Lett.* 380, L43
Forrest W.J., Gillett F.C., Stein W.A., 1975, *ApJ* 195, 423
Fouks B.I., Schubert J., 1995, *Proceedings of SPIE* 2475, 487
Frenklach M., 1990, In: *Carbon in the Galaxy: Studies from Earth and Space*, 259
Frenklach M., Feigelson E.D., 1989, *ApJ* 341, 372
Frum C.I., Engleman R., Hedderich H.G., et al., 1991, *Chem. Phys. Lett.* 176, 504
Fulara J., Jakobi M., Maier J.P., 1993, *Chem. Phys. Lett.* 211, 227
Garay G., Lizano S., 1999, *PASP* 111, 1049
Garay G., Lizano S., Gomez Y., 1994, *ApJ* 429, 268
Garay G., Rodriguez L.F., Moran J.M., Churchwell E., 1993, *ApJ* 418, 368
García-Lario P., Manchado A., Ulla A., Manteiga M., 1999, *ApJ* 513, 941
Geballe T.R., Lacy J.H., Persson S.E., McGregor P.J., Soifer B.T., 1985, *ApJ* 292, 500
Geballe T.R., Tielens A.G.G.M., Allamandola L.J., Moorhouse A., Brand P.W.J.L., 1989, *ApJ* 341, 278
Genzel R., Cesarsky C.J., 2000, *ARA&A* 38, 761

Genzel R., Lutz D., Sturm E., et al., 1998, *ApJ* 498, 579

Georgelin Y.M., Amram P., Georgelin Y.P., Le Coarer E., Marcelin M., 1994, *A&AS* 108, 513

Gesicki K., Zijlstra A.A., 2000, *A&A* 358, 1058

Gibb E.L., Whittet D.C.B., Schutte W.A., et al., 2000, *ApJ* 536, 347

Gillett F.C., Forrest W.J., Merrill K.M., 1973, *ApJ* 183, 87

Goto M., Kobayashi N., Terada H., Tokunaga, A. T., 2002, *ApJ* 572, 276

Gry C., Swinyard B., Harwood A., et al., 2000, *LWS handbook : http://www.iso.vilspa.esa.es/users/expl_lib/LWS_top.html*

Guillois O., Nenner I., Papoular R., Reynaud C., 1996, *ApJ* 464, 810

Gussie G.T., Taylor A.R., 1995, *MNRAS* 273, 801

Habing H.J., 1968, *Bull. Astr. Inst. Netherlands* 19, 421

Harrington J.P., Lame N.J., Borkowski K.J., Bregman J.D., Tsvetanov Z.I., 1998, *ApJ Lett.* 501, L123

Hatchell J., Thompson M.A., Millar T.J., MacDonald G.H., 1998, *A&AS* 133, 29

Hayward T.L., Miles J.E., Houck J.R., Gull G.E., Schoenwald J., 1993, In: *Proc. SPIE Vol. 1946, Infrared Detectors and Instrumentation*, 334–340

Helou G., 1999, In: *ESA SP-427: The Universe as Seen by ISO*, 797

Helou G., Lu N.Y., Werner M.W., Malhotra S., Silbermann N., 2000, *ApJ Lett.* 532, L21

Henize K.G., 1956, *ApJS* 2, 315

Henning T., Feldt M., Stecklum B., Klein R., 2001, *A&A* 370, 100

Herlin N., Bohn I., Reynaud C., et al., 1998, *A&A* 330, 1127

Herter T., Helfer H.L., Briotta D.A., et al., 1982, *ApJ* 262, 153

Herter T., Helfer H.L., Forrest W.J., et al., 1981, *ApJ* 250, 186

Ho P.T.P., Haschick A.D., Israel F.P., 1981, *ApJ* 243, 526

Hofner P., Churchwell E., 1996, *A&AS* 120, 283

Hofner P., Kurtz S., Churchwell E., Walmsley C.M., Cesaroni R., 1994, *ApJ Lett.* 429, L85

Hony S., Van Kerckhoven C., Peeters E., et al., 2001, *A&A* 370, 1030

Hora J.L., Latter W.B., Deutsch L.K., 1999, *ApJS* 124, 195

Hrivnak B.J., Volk K., Kwok S., 2000, *ApJ* 535, 275

Hudgins D.M., Allamandola L.J., 1999a, *ApJ Lett.* 516, L41

Hudgins D.M., Allamandola L.J., 1999b, *ApJ* 513, L69

Hudgins D.M., Bauschlicher C.W.J., Allamandola L.J., 2001, *Spectrochimica Acta Part A* 57, 907

Hudgins D.M., Sandford S.A., Allamandola L.J., 1994, *J. Phys. Chem.* 98, 4243

Hughes V.A., Viner M.R., 1976, *ApJ* 204, 55

Isaacman R., 1984a, *A&A* 130, 151

Isaacman R., 1984b, *MNRAS* 208, 399

Jaeger C., Mutschke H., Begemann B., Dorschner J., Henning T., 1994, *A&A* 292, 641

Joblin C., Abergel A., Bregman J., et al., 2000, *ESA-SP 456: ISO beyond the peaks: The 2nd ISO workshop on analytical spectroscopy.*, 49

Joblin C., Boissel P., Leger A., D'Hendecourt L., Defourneau D., 1995, *A&A* 299, 835

Joblin C., D'Hendecourt L., Leger A., Defourneau D., 1994, *A&A* 281, 923

Joblin C., Leger A., Martin P., 1992, *ApJ Lett.* 393, L79

Joblin C., Tielens A.G.G.M., Allamandola L.J., Geballe T.R., 1996a, *ApJ* 458, 610

Joblin C., Tielens A.G.G.M., Geballe T.R., Wooden D.H., 1996b, *ApJ Lett.* 460, L119

Jochims H.W., Baumgärtel H., Leach S., 1999, *ApJ* 512, 500

Jochims H.W., Ruhl E., Baumgartel H., Tobita S., Leach S., 1994, *ApJ* 420, 307

Jones A.P., Tielens A.G.G.M., Hollenbach D.J., 1996, *ApJ* 469, 740

Jourdain de Muizon M., Cox P., Lequeux J., 1990, *A&AS* 83, 337

Kahn F.D., 1974, *A&A* 37, 149

Kaper L., Bik A., Hanson M., Comeron F., 2002a, In: *Hot Star Workshop III: The Earliest Phases of Massive Star Birth*, ASP Conference series, 267, 95

Kaper L., Bik A., Hanson M., Comeron F., 2002b, In: *The Origins of Stars and Planets: The VLT View*, 291

Keane J.V., Tielens A.G.G.M., Boogert A.C.C., Schutte W.A., Whittet D.C.B., 2001, *A&A* 376, 254

Kerr T.H., Hurst M.E., Miles J.R., Sarre P.J., 1999, *MNRAS* 303, 446

Kerridge J.F., Chang S., Shipp R., 1987, *Geochim. Cosmochim. Acta* 51, 2527

Kessler M.F., Steinz J.A., Anderegg M.E., et al., 1996, *A&A* 315, L27

Kester D.J.M., 2001, *http://sws.ster.kuleuven.ac.be/*

Kim H.S., Wagner D.R., Saykally R.J., 2001, *Phys. Rev. Lett.* 86, 5691

Kim K., Koo B., 2001, *ApJ* 549, 979

Koornneef J., Code A.D., 1981, *ApJ* 247, 860

Kroto H., 1988, *Science* 242, 1139

Kroto H., 1994, *Nat* 369, 274

Kuchar T.A., Bania T.M., 1994, *ApJ* 436, 117

Kurtz S., Churchwell E., Wood D.O.S., 1994, *ApJS* 91, 659

Kurtz S.E., Watson A.M., Hofner P., Otte B., 1999, *ApJ* 514, 232

Kwok S., Volk K., Bernath P., 2001, *ApJ Lett.* 554, L87

Lacy J.H., Beck S.C., Geballe T.R., 1982, *ApJ* 255, 510

Langhoff S.R., 1996, *J. Phys. Chem.* 100, 2819

Larson R.B., Starrfield S., 1971, *A&A* 13, 190

Latter W.B., Dayal A., Bieging J.H., et al., 2000, *ApJ* 539, 783

Latter W.B., Kelly D.M., Hora J.L., Deutsch L.K., 1995, *ApJS* 100, 159

Lebrón M.E., Rodríguez L.F., Lizano S., 2001, *ApJ* 560, 806

Leech K., the SWS Instrument Dedicated Team and the SWS Instrument Support Team, 2001, *SWS handbook : http://www.iso.vilspa.esa.es/users/expl_lib/SWS_top.html*

Leger A., Dhendecourt L., 1985, *A&A* 146, 81

Léger A., D'Hendecourt L., Boissel P., Desert F.X., 1989, *A&A* 213, 351

Léger A., Puget J.L., 1984, *A&A* 137, L5

Lemke D., Klaas U., Abolins J., et al., 1996, *A&A* 315, L64

Lemke D., Mattila K., Lehtinen K., et al., 1998, *A&A* 331, 742

Lepp S., Dalgarno A., 1988, *ApJ* 324, 553

Lis D.C., 1991, *ApJ Lett.* 379, L53

Liszt H.S., 1992, *ApJS* 82, 495

Liszt H.S., Spiker R.W., 1995, *ApJS* 98, 259

Liu W., Dalgarno A., 1994, *ApJ* 428, 769

Low F.J., Young E., Beintema D.A., et al., 1984, *ApJ Lett.* 278, L19

Lucy L.B., Danziger I.J., Gouiffes C., Bouchet P., 1989, In: *IAU Colloq. 120: Structure and Dynamics of the Interstellar Medium*, 164

Lucy L.B., Danziger I.J., Gouiffes C., Bouchet P., 1991, In: *Supernovae*, Publisher: Springer-Verlag New York, 82

Lumsden S.L., Hoare M.G., 1996, *ApJ* 464, 272

Lumsden S.L., Hoare M.G., 1999, *MNRAS* 305, 701

Lumsden S.L., Puxley P.J., Hoare M.G., 2001a, *MNRAS* 320, 83

Lumsden S.L., Puxley P.J., Hoare M.G., 2001b, *MNRAS* 328, 419

Lutz D., Spoon H.W.W., Rigopoulou D., Moorwood A.F.M., Genzel R., 1998, *ApJ Lett.* 505, L103

Mac Low M., van Buren D., Wood D.O.S., Churchwell E., 1991, *ApJ* 369, 395

Maillard J.P., Joblin C., Mitchell G.F., Vauglin I., Cox P., 1999, In: *ESA SP-427: The Universe as Seen by ISO*, 707

Malfait K., 1999, Ph.D. thesis, Katholieke Universiteit Leuven

Malfait K., Waelkens C., Waters L.B.F.M., et al., 1998, *A&A* 332, L25

Marchenko S.V., Moffat A.F.J., Vacca W.D., Côté S., Doyon R., 2002, *ApJ Lett.* 565, L59

Martí J., Rodríguez L.F., Reipurth B., 1993, *ApJ* 416, 208

Martin P.G., Whittet D.C.B., 1990, *ApJ* 357, 113

Martín-Hernández N.L., 2002, Ph.D. thesis, Groningen University

Martín-Hernández N.L., Bik A., Kaper L., Tielens A.G.G.M., 2003, *A&A*, submitted

Martín-Hernández N.L., Peeters E., Morisset C., et al., 2002a, *A&A* 381, 606

Martín-Hernández N.L., Tielens A.G.G.M., van der Hulst J.M., 2002b, *A&A*, in press

Martín-Hernández N.L., Vermeij R., Tielens A.G.G.M., van der Hulst J.M., Peeters E., 2002c, *A&A* 389, 286

Martins F., Schaerer D., Hillier D.J., 2002, *A&A* 382, 999

Massey P., Hunter D.A., 1998, *ApJ* 493, 180

Mathis J.S., 1970, *ApJ* 159, 263

Mathis J.S., 1990, *ARA&A* 28, 37

Mathis J.S., Rumpl W., Nordsieck K.H., 1977, *ApJ* 217, 425

Mattila K., Lemke D., Haikala L.K., et al., 1996, *A&A* 315, L353

Maxia C., Testi L., Cesaroni R., Walmsley C.M., 2001, *A&A* 371, 287

McClure-Griffiths N.M., Green A.J., Dickey J.M., et al., 2001, *ApJ* 551, 394

Megeath S.T., Herter T., Gull G.E., Houck J.R., 1990, *ApJ* 356, 534

Mehringer D.M., 1994, *ApJS* 91, 713

Mehringer D.M., Goss W.M., Lis D.C., Palmer P., Menten K.M., 1998, *ApJ* 493, 274

Meikle W.P.S., Spyromilio J., Varani G.F., Allen D.A., 1989, *MNRAS* 238, 193

Meixner M., Ueta T., Dayal A., et al., 1999, *ApJS* 122, 221

Millar T.J., Roberts H., Markwick A.J., Charnley S.B., 2000, *Royal Society of London Philosophical Transactions Series A* 358, 2535

Minier V., Booth R.S., 2002, *A&A* 387, 179

Minier V., Booth R.S., Conway J.E., 2000, *A&A* 362, 1093

Miroshnichenko A.S., Mulliss C.L., Bjorkman K.S., et al., 1999, *MNRAS* 302, 612

Molster F.J., van den Ancker M.E., Tielens A.G.G.M., et al., 1996, *A&A* 315, L373

Molster F.J., Waters L.B.F.M., Tielens A.G.G.M., 2002, *A&A* 382, 222

Moorwood A.F.M., Lutz D., Oliva E., et al., 1996, *A&A* 315, L109

Morisset C., Baluteau J.P., Schaerer D., et al., 2002, *A&A* 386, 558

Mortera C., Low M.J.D., 1983, *Carbon* 21, 283

Moutou C., Leger A., D'Hendecourt L., 1996, *A&A* 310, 297

Moutou C., Sellgren K., Léger A., Verstraete L., Le Coupanec P., 1999a, In: *Solid Interstellar Matter : The ISO Revolution*, EDP Sciences, 90

Moutou C., Sellgren K., Verstraete L., Léger A., 1999b, *A&A* 347, 949

Moutou C., Verstraete L., Sellgren K., Léger A., 1999c, In: *ESA SP-427: The Universe as Seen by ISO*, 727

Muñoz Caro G.M., Ruiterkamp R., Schutte W.A., Greenberg J.M., Mennella V., 2001, *A&A* 367, 347

Nandy K., Morgan D.H., Willis A.J., Wilson R., Gondhalekar P.M., 1981, *MNRAS* 196, 955

Nemes L., Ran R.S., Bernath P.F., et al., 1994, *Chem. Phys. Lett.* 218, 295

Ney E.P., Strecker D.W., Gehrz R.D., 1973, *ApJ* 180, 809

Nugis T., Niedzielski A., 1995, *A&A* 300, 237

Pagel B., 1997, Nucleosynthesis and Chemical Evolution of Galaxies, Cambridge University Press, Cambridge

Papoular R., Conrad J., Giuliano M., Kister J., Mille G., 1989, *A&A* 217, 204

Pauldrach A.W.A., Hoffmann T.L., Lennon M., 2001, *A&A* 375, 161

Pauzat F., Talbi D., Ellinger Y., 1997, *A&A* 319, 318

Pech C., Joblin C., Boissel P., 2001, *A&A* 388, 639

Peeters E., Hony S., Van Kerckhoven C., et al., 2002a, *A&A* 390, 1089

Peeters E., Martín-Hernández N.L., Damour F., et al., 2002b, *A&A* 381, 571

Peeters E., Tielens A.G.G.M., Roelfsema P.R., Cox P., 1999, *ESA SP-427: The Universe as Seen by ISO* 427, 739

Plume R., Jaffe D.T., Evans N.J., 1992, *ApJS* 78, 505

Pratap P., Megeath S.T., Bergin E.A., 1999, *ApJ* 517, 799

Pratap P., Menten K.M., Snyder L.E., 1994, *ApJ Lett.* 430, L129

Prevot M.L., Lequeux J., Prevot L., Maurice E., Rocca-Volmerange B., 1984, *A&A* 132, 389
Puche D., Zijlstra A.A., Boettcher C., et al., 1988, *A&A* 206, 89
Puget J.L., Léger A., 1989, *ARA&A* 27, 161
Puget J.L., Leger A., Boulanger F., 1985, *A&A* 142, L19
Purton C.R., Feldman P.A., Marsh K.A., Allen D.A., Wright A.E., 1982, *MNRAS* 198, 321
Reach W.T., Boulanger F., 1998, *Lecture Notes in Physics* Berlin Springer Verlag, 506, 353
Reach W.T., Boulanger F., Contursi A., Lequeux J., 2000, *A&A* 361, 895
Reifenstein E.C., Wilson T.L., Burke B.F., Mezger P.G., Altenhoff W.J., 1970, *A&A* 4, 357
Reynoso E.M., Goss W.M., 2002, *ApJ* 575, 871
Ricca A., Bauschlicher C.W., Bakes E.L.O., 2002a, *Icarus*, in press
Ricca A., Bauschlicher C.W., Rosi M., 2002b, *Chem. Phys. Lett.*, in press
Rigopoulou D., Spoon H.W.W., Genzel R., et al., 1999 118, 2625
Roche P.F., Aitken D.K., 1984, *MNRAS* 208, 481
Roche P.F., Aitken D.K., Smith C.H., 1989, *MNRAS* 236, 485
Roche P.F., Lucas P.W., Hoare M.G., Aitken D.K., Smith C.H., 1996, *MNRAS* 280, 924
Rodrigues C.V., Magalhaes A.M., Coyne G.V., Piirola V., 1997, *ApJ* 485, 618
Roelfsema P.R., Cox P., Tielens A.G.G.M., et al., 1996, *A&A* 315, L289
Roelfsema P.R., Goss W.M., 1991, *A&AS* 87, 177
Roelfsema P.R., Goss W.M., Geballe T.R., 1988, *A&A* 207, 132
Roelfsema P.R., Goss W.M., Geballe T.R., 1989, *A&A* 222, 247
Rosenthal D., Bertoldi F., Drapatz S., Timmermann R., 1999, In: *ESA SP-427: The Universe as Seen by ISO*, 561
Rouan D., Leger A., Omont A., Giard M., 1992, *A&A* 253, 498
Roueff E., Tiné S., Coudert L.H., et al., 2000, *A&A* 354, L63
Rubin Y., Kahr M., Knobler C., Diederich F., Wilkins C., 1991, *J. Am. Chem. Soc.* 113, 495
Rudolph A.L., Brand J., de Geus E.J., Wouterloot J.G.A., 1996, *ApJ* 458, 653
Rudolph A.L., Simpson J.P., Haas M.R., Erickson E.F., Fich M., 1997, *ApJ* 489, 94
Russell R.W., Soifer B.T., Forrest W.J., 1975, *ApJ Lett.* 198, L41
Sakata A., Wada S., Tanabe T., Onaka T., 1984, *ApJ Lett.* 287, L51
Salama A., 2001, In: *ESA-SP 455: ISO Beyond Point Sources: Studies of Extended IR Emission*
Salama F., Bakes E.L.O., Allamandola L.J., Tielens A.G.G.M., 1996, *ApJ* 458, 621
Sandford S.A., Bernstein M.P., Allamandola L.J., Gillette J.S., Zare R.N., 2000, *ApJ* 538, 691
Sandford S.A., Bernstein M.P., Dworkin J.P., 2001, *Meteoritics and Planetary Science* 36, 1117
Schnaiter M., Henning T., Mutschke H., et al., 1999, *ApJ* 519, 687
Schutte W.A., Tielens A.G.G.M., Allamandola L.J., 1993, *ApJ* 415, 397
Scott A.D., Duley W.W., Jahani H.R., 1997, *ApJ Lett.* 490, L175
Scott P.F., Harris S., 1978, *MNRAS* 182, 657

Sellgren K., 1984, *ApJ* 277, 623

Sellgren K., Tokunaga A.T., Nakada Y., 1990, *ApJ* 349, 120

Serabyn E., 1999, *http://www.ngst.nasa.gov/doclist/bytitle.html/*

Shepherd D.S., Churchwell E., 1996, *ApJ* 457, 267

Shipman R., Lahuis F., 2000, *http://sws.ster.kuleuven.ac.be/*

Silverstein R.M., Bassler G.C., 1967, Spectrometric Identification of Organic Compounds. John Wiley & Sons, Inc., New York

Simpson J.P., Colgan S.W.J., Rubin R.H., Erickson E.F., Haas M.R., 1995, *ApJ* 444, 721

Simpson J.P., Rubin R.H., 1990, *ApJ* 354, 165

Sloan G.C., Bregman J.D., Geballe T.R., Allamandola L.J., Woodward C.E., 1997, *ApJ* 474, 735

Soifer B.T., Pipher J.L., 1975, *ApJ* 199, 663

Solomon P.M., Rivolo A.R., Barrett J., Yahil A., 1987, *ApJ* 319, 730

Speck A.K., 1998, *Ph.D. Thesis*

Speck A.K., Barlow M.J., Sylvester R.J., Hofmeister A.M., 2000, *A&AS* 146, 437

Spoon H., Keane J., Tielens A.G.G.M., Moorwood A.F.M., Lutz D., 2002, *A&A* 385, 1022

Stecklum B., Feldt M., Richichi A., Calamai G., Lagage P.O., 1997, *ApJ* 479, 339

Stein W.A., Gillett F.C., 1969, *ApJ Lett.* 155, L197

Stoldt C.R., Maboudian R., Carraro C., 2001, *ApJ Lett.* 548, L225

Strazulla G., Arena M., Baratta G.A., et al., 1995, *Adv. Space Res.* 16, 61

Sturm E., Lutz D., Tran D., et al., 2000, *A&A* 358, 481

Su K.Y.L., Hrivnak B.J., Kwok S., 2001, *AJ* 122, 1525

Swinyard B.M., Burgdorf M.J., Clegg P.E., et al., 1998, *Proceedings of SPIE* 3354, 888

Szczepanski J., Vala M., 1993a, *ApJ* 414, 646

Szczepanski J., Vala M., 1993b, *Nat* 363, 699

Szczerba R., Górny S.K., Stasińska G., Siódmiak N., Tylenda R., 2001, *Ap&SS* 275, 113

Takahashi H., Matsuhara H., Watarai H., Matsumoto T., 2000, *ApJ* 541, 779

Teixeira T.C., Devlin J.P., Buch V., Emerson J.P., 1999, *A&A* 347, L19

Tieftrunk A.R., Gaume R.A., Claussen M.J., Wilson T.L., Johnston K.J., 1997, *A&A* 318, 931

Tielens A.G.G.M., 1990, In: *Carbon in the Galaxy: Studies from Earth and Space*, 59

Tielens A.G.G.M., 1992, In: *IAU Symp. 150: Astrochemistry of Cosmic Phenomena*, 91

Tielens A.G.G.M., 1993, In: *Dust and Chemistry in Astronomy*, 103

Tielens A.G.G.M., 1997a, *Ap&SS* 251, 1

Tielens A.G.G.M., 1997b, In: *Astrophysical Implications of the Laboratory Study of Presolar Materials*, 523

Tielens A.G.G.M., Allamandola L.J., 1987, In: *ASSL Vol. 134: Interstellar Processes*, 397

Tielens A.G.G.M., Allamandola L.J., Barker J.R., Cohen M., 1987, In: *Polycyclic Aromatic Hydrocarbons and Astrophysics*, 273

Tielens A.G.G.M., Charnley S.B., 1997, *Origins Life Evolution Biosphere* 27, 23

Tielens A.G.G.M., Hollenbach D., 1985, *ApJ* 291, 722

Tielens A.G.G.M., Hony S., van Kerckhoven C., Peeters E., 1999, In: *ESA SP-427: The Universe as Seen by ISO*, 579

Tielens A.G.G.M., Meixner M.M., van der Werf P.P., et al., 1993, *Sci* 262, 86

Tielens A.G.G.M., van Kerckhoven C., Peeters E., Hony S., 2000, In: *IAUS 197: Astrochemistry: From Molecular Clouds to Planetary*, 349

Tokunaga A.T., Sellgren K., Smith R.G., et al., 1991, *ApJ* 380, 452

Torres A.V., 1988, *ApJ* 325, 759

Tran Q.D., Lutz D., Genzel R., et al., 2001, *ApJ* 552, 527

Turner B.E., 2001, *ApJS* 136, 579

Uchida K.I., Sellgren K., Werner M.W., Houdashelt M.L., 2000, *ApJ* 530, 817

Ueta T., Meixner M., Dayal A., et al., 2001, *ApJ* 548, 1020

Usov V.V., 1991, *MNRAS* 252, 49

Vacca W.D., Garmany C.D., Shull J.M., 1996, *ApJ* 460, 914

Valentijn E.A., Feuchtgruber H., Kester D.J.M., et al., 1996, *A&A* 315, L60

van Buren D., Mac Low M., 1992, *ApJ* 394, 534

van Buren D., Mac Low M., Wood D.O.S., Churchwell E., 1990, *ApJ* 353, 570

van den Ancker M., 1999, Ph.D. thesis, University of Amsterdam

van den Ancker M.E., Tielens A.G.G.M., Wesselius P.R., 2000a, *A&A* 358, 1035

van den Ancker M.E., Wesselius P.R., Tielens A.G.G.M., 2000b, *A&A* 355, 194

van der Hucht K.A., 2001, *New Astronomy Review* 45, 135

van der Hucht K.A., Jurriens T.A., Wesselius P.R., Olnon F.M., The P.S., 1985, In: *ASSL Vol. 120: Birth and Evolution of Massive Stars and Stellar Groups*, 167

van der Hucht K.A., Morris P.W., Williams P.M., et al., 1996, *A&A* 315, L193

van der Zwet G.P., Allamandola L.J., 1985, *A&A* 146, 76

Van Kerckhoven C., 2002. Ph.D. thesis, Katholieke Universiteit Leuven (Belgium)

Van Kerckhoven C., Hony S., Peeters E., et al., 2000, *A&A* 357, 1013

Van Kerckhoven C., Tielens A.G.G.M., Waelkens C., 1999, In: *ESA SP-427: The Universe as Seen by ISO*, 421

Vermeij R., Peeters E., Tielens A.G.G.M., van der Hulst J.M., 2002a, *A&A* 382, 1042

Vermeij R., van der Hulst J.M., Damour F., Baluteau J.P., 2002b, *A&A* 390, 649

Verstraete L., Leger A., D'Hendecourt L., Defourneau D., Dutuit O., 1990, *A&A* 237, 436

Verstraete L., Pech C., Moutou C., et al., 2001, *A&A* 372, 981

Verstraete L., Puget J.L., Falgarone E., et al., 1996, *A&A* 315, L337

von Helden G., Gotts M.T., Bowers N.G., 1993, *Nature* 363, 60

Vriend W.J., 1999, Master's thesis, University of Groningen

Waelkens C., Waters L.B.F.M., de Graauw M.S., et al., 1996, *A&A* 315, L245

Walmsley C.M., Churchwell E., Terzian Y., 1981, *A&A* 96, 278

Walsh A.J., Burton M.G., Hyland A.R., Robinson G., 1998, *MNRAS* 301, 640

Watarai H., Matsuhara H., Takahashi H., Matsumoto T., 1998, *ApJ* 507, 263

Waters L.B.F.M., Beintema D.A., Zijlstra A.A., et al., 1998, *A&A* 331, L61
Watson A.M., Coil A.L., Shepherd D.S., Hofner P., Churchwell E., 1997, *ApJ* 487, 818
Watson A.M., Hanson M.M., 1997, *ApJ Lett.* 490, L165
Weaver R., McCray R., Castor J., Shapiro P., Moore R., 1977, *ApJ* 218, 377
Williams P.M., 1997, *Ap&SS* 251, 321
Williams P.M., 1999, In: *IAU Symp. 193: Wolf-Rayet Phenomena in Massive Stars and Starburst Galaxies*, 267
Williams P.M., van der Hucht K.A., Thé P.S., 1987, *A&A* 182, 91
Williams R.M., Leone S.R., 1995, *ApJ* 443, 675
Witteborn F.C., Sandford S.A., Bregman J.D., et al., 1989, *ApJ* 341, 270
Wolfire M.G., Cassinelli J.P., 1987, *ApJ* 319, 850
Wolfire M.G., Tielens A.G.G.M., Hollenbach D., 1990, *ApJ* 358, 116
Wood D.O.S., Churchwell E., 1989, *ApJS* 69, 831
Wood D.O.S., Churchwell E., 1991, *ApJ* 372, 199
Wooden D.H., Rank D.M., Bregman J.D., et al., 1993, *ApJS* 88, 477
Wouterloot J.G.A., Brand J., 1989, *A&AS* 80, 149
Yang J., Epstein S., 1983, *Geochim. Cosmochim. Acta* 47, 2199
Yorke H.W., 1986, *ARA&A* 24, 49
Yudin B., Balega Y., Blöcker T., et al., 2001, *A&A* 379, 229
Zavagno A., Cox P., Baluteau J.P., 1992, *A&A* 259, 241
Zhang Q., O'Brien S., Heath J., et al., 1986, *J. Phys. Chem.* 90, 525
Zijlstra A., Pottasch S., Bignell C., 1990, *A&AS* 82, 273
Zinner E., 1997, In: *Astrophysical Implications of the Laboratory Study of Presolar Materials*, 3
Zuckermann B., Palmer P., Morris M., et al., 1977, *ApJ Lett.* 211, L97

Published papers

Refereed journal articles

A mid-IR spatial study of the compact H II regions IRAS 18434-0242 and IRAS 21190+5140
Peeters E., Tielens A. G. G. M., Cami J., Boogert A. C. A., Hayward T. L., 2002, A&A, submitted

The profiles of the 3 to 12 μm PAH features
van Diedenhoven B., Peeters E., Van Kerckhoven C., Hony S., Tielens A. G. G. M., Allamandola L. J., Hudgins D. M., 2002, A&A, submitted

Deuterated PAHs
Peeters E., Allamandola L. J., Bauschlicher C. W., Hudgins D. M., Sandford, S. A., Tielens A. G. G. M., 2002, Nature, submitted

The infrared emission features in the spectrum of the Wolf-Rayet star WR48a
Chiar J. E., Peeters E., Tielens A. G. G. M., 2002, ApJL, 579

The rich 6 to 9 μm spectrum of interstellar PAHs
Peeters E., Hony S., Van Kerckhoven C., Tielens A. G. G. M., Allamandola L. J., Hudgins D. M., Bauschlicher C. W., 2002, A&A, 390, 1089

The stellar content, metallicity and ionization structure of H II regions
Martín-Hernández N. L., Vermeij R., Tielens A. G. G. M., van der Hulst J. M., Peeters E., 2002, A&A, 389, 286

A photoionization model of the compact H II region G29.96-0.02
Morisset C., Schaerer D., Martín-Hernández N. L., Peeters E., Damour F., Baluteau, J.-P., Cox, P., Roelfsema, P., 2002, A&A, 386, 558

The PAH emission spectra of Large Magellanic Cloud H II regions
Vermeij R., Peeters E., Tielens A. G. G. M., van der Hulst J. M., A&A, 382, 1042

ISO spectroscopy of compact H II regions in the Galaxy. I. The catalogue
Peeters E., Martín-Hernández N. L., Damour F., Cox P., Roelfsema P. R., Baluteau J.-P., Tielens A. G. G. M., Churchwell E., Kessler M. F., Mathis J. S., Morisset C., Schaerer D., 2002, A&A, 381, 571

ISO spectroscopy of compact H II regions in the Galaxy. II. Ionization and elemental abundances
Martín-Hernández N. L., Peeters E., Morisset C., Tielens A. G. G. M., Cox P., Roelfsema P. R., Baluteau J.-P., Schaerer D., Mathis J. S., Damour F., Churchwell E., Kessler M. F., 2002, A&A, 381, 606

The CH out-of-plane bending modes of PAH molecules in astrophysical environments
Hony S., Van Kerckhoven C., Peeters E., Tielens A. G. G. M., Hudgins D. M., Allamandola L. J., 2001, A&A, 370, 1030

The C-C-C bending modes of PAHs: a new emission plateau from 15 to 20 μm
Van Kerckhoven C., Hony S., Peeters E., Tielens A. G. G. M., Allamandola L. J., Hudgins D. M., Cox P., Roelfsema P. R., Voors R. H. M., Waelkens C., Waters L. B. F. M., Wesselius P. R., 2000, A&A, 357, 1013

Selection of a sample of bright southern Slowly Pulsating B Stars for long-term photometric and spectroscopic monitoring
Aerts C., De Cat P., Peeters E., Decin L., De Ridder J., Kolenberg K., Meeus G., Van Winckel H., Cuypers J., Waelkens C., 1999, A&A, 343, 872

Published proceedings

Circumstellar carbonaceous material associated with late-type dusty WC Wolf-Rayet stars
Chiar J. E., Tielens A. G. G. M., Peeters E., 2003, ESA SP-511, in press

ISO spectroscopy of ultracompact H II regions
Martín-Hernández L., Tielens A. G. G. M., Peeters E., Roelfsema P. R., Morisset C., Baluteau J. -P., Damour F., Cox P., Shearer D., Mathis J., Churchwell E., Kessler M. F., 2002, ASP Conference Series, 267, 391

ISO spectroscopy of PAH features
Peeters E., Tielens A. G. G. M., Van Kerckhoven C., Hony S., Allamandola L. J., Hudgins D. M., Bauschlicher C. W., 2002, ASP Conference Series, 267, 403

The heating of the ISM
Tielens A. G. G. M., Peeters E., 2002, EAS Publication Series, 4, 43

Photoionization model for G29.96-0.02
Morisset C., Baluteau J.-P., Cox P., Martín-Hernández N. L., Peeters E., Roelfsema P., Schaerer D., 2002, RMxAC (Serie de Conferencias), 12 , 29

ISO spectroscopy of ultracompact H II regions: Element abundance gradient in the galaxy
Martín-Hernández N. L., Peeters E., Damour F., Cox P., Roelfsema P. R., Baluteau J.-P., Tielens A. G. G. M., Churchwell E., Jones A. P., Kessler M. F., Mathis J. S., Morisset C., Schaerer D., 2002, RMxAC (Serie de Conferencias), 12 , 41

The CH out-of-plane bending modes of polycyclic aromatic hydrocarbon molecules in an astrophysical context
Hony S., Van Kerckhoven C., Peeters E., Tielens A. G. G. M., Hudgins D. M., Allamandola L. J., 2000, ESA SP-456, 63

ISO spectroscopy of compact H II regions in our galaxy
Martín-Hernández N. L., Peeters E., Damour F., Cox P., Roelfsema P. R., Tielens A. G. G. M., Baluteau J.-P., Churchwell E., Jones A. P., Mathis J. S., Morisset C., Schaerer D., Kessler M. F., 2000, ESA SP-456, 135

The C-C-C bending modes of PAHs: A new emission plateau from 15 to 20 μm
Van Kerckhoven C., Hony S., Peeters E., Tielens A. G. G. M., Allamandola L. J., Hudgins D. M., 2000, ESA SP-456, 223

Interstellar and Circumstellar PAHs
Tielens A. G. G. M., Van Kerckhoven C., Peeters E., Hony S., 2000, IAUS 197, 349

Galactic abundance gradients determined from ISO observations of compact H II regions
Roelfsema P. R., Cox P., Baluteau J.-P., Peeters E., 1999, in *The Physics and Chemistry of the Interstellar Medium, Proceedings of the 3rd Cologne-Zermatt Symposium*, 116

Interstellar and Circumstellar PAHs
Tielens A. G. G. M., Hony S., Van Kerckhoven C., Peeters E., 1999, ESA SP-427, 579

ISO spectroscopy of dense regions
Cox P., Roelfsema P. R., Baluteau J. P., Peeters E., Martín-Hernández L., Tielens A. G. G. M., Swinyard B. M., Lim T., Kessler M. F., 1999, ESA SP-427, 631

PAHs in compact HII regions
Peeters E., Tielens A. G. G. M., Roelfsema P. R., Cox P., 1999, ESA SP-427, 739

Thanks

Vele mensen hebben op een of andere manier bijgedragen tot dit proefschrift. Ik wil hen hier dan ook graag bedanken.

Xander, de manier waarop jij met je studenten omgaat is buitengewoon. Als ik de weg kwijt was of leek te verdrinken in de details, was jij de reddende engel; je kan me dan ook keer op keer verbazen met je gigantisch goede kennis van de literatuur en je magische pen waaruit alles als vanzelf lijkt te komen. Ik kon altijd terecht bij jou voor een luisterend oor. Ik ben echt met mijn gat in de boter gevallen!

Dit proefschrift was er niet zonder Pjotr en Pierre. Het was snel duidelijk dat de spectra verkregen met jullie ISO proposal gedomineerd worden door PAHs, voldoende stof voor een tweede student. Pjotr en Adwin introduceerden mij in de geheimen van de SWS reductie. Dankzij Pjotr moest ik mij ook nooit zorgen maken om de financiële aspecten.

Ik wil graag SRON, NWO en LKBF bedanken voor de financiële steun die mij toeliet deel te nemen aan een hele resem conferenties, zomerscholen en consortium meetings. Dit onderzoek is financiëel gesponsord door SRON, NWO (beurs 783-70-000). Dankzij SRON en een tikkeltje geluk, kon ik de lancering van XMM in Kourou bijwonen. Het was een overweldigende belevenis!

I would also like to thank the members of the reading committee. François, Lou and Thijs, I appreciate your carefull reading of this manuscript a lot.

Lou and Doug gave me a very warm welcome when visiting Ames. We have had and will surely continue to have a fruitful collaboration. Thanks also to Bas, Charlie, Jean, Thijs, Tom and Ronald, it was a pleasure to work with you!

Being part of the H II consortium was a unique experience. Anthony, Christophe, Daniel, Ed, Frédérique, Jean-Paul, John, Pierre, Pjotr and Xander, I enjoyed our very informal meetings.

I also had many profits of the hard work from the people of DIDAC and the SWS instrument team. Russ, Freddy, Do, Pjotr, Bart, Douwe and Leen, I always felt welcome to knock on your doors (or send an e-mail) with all the questions and problems I had concerning the SWS reduction and you immediately took the time to help and sort out things.

The Dutch-Flamish SWS community came together regularly before ISO retired. I appreciated these meetings particularly for the social contacts with other SWS-fellows. It was always great fun when we met at these meetings or at conferences.

Een woordje van dank gaat zeker ook naar onze systeembeheerders, in het bijzonder Wim, Eite en Kor voor het oplossen van alle simpele en minder simpele computerproblemen

van een leek als ik. Mede dankzij jullie hebben hackers geen kans gekregen om deze thesis uit te stellen. Verder wil ik ook de administratieve staf en in het bijzonder Engelien, Petra, Loes en Jacquie, bedanken voor hulp allerhande. Ook de gezellige babbels met George wist ik te appreciëren.

Leti, I owe you a lot (besides several dinners and an ice-cream). Our PhD-life went along the same tracks at the same time, allowing us to share the ups and downs of it; finishing together meant I could enjoy your company during the lonely hours in the institute. I always liked observing how you deal with things in your own funny way. Thanks for your friendship and don't forget the postcards!

De samenwerking met Sacha & Caroline was bijzonder aangenaam. Jullie waren immer en altijd bereid tot het beantwoorden van mijn vragen, discussies en uitwisselen van data en programma's. Jullie bezoekjes aan Groningen stonden garant voor gezellige avonden, waarin jullie beider kookkunsten uitgebreid aan bod kwamen, doorspekt met leuke discussies en pogingen om Sacha wat Vlaamse tact bij te brengen. Ik keek er telkens naar uit.

De vele discussies, al dan niet met gesloten deur, met mijn bureaugenoten Diah en Henrik, alsook de aangename verassing om een kinder surprise ei of een hele fles chocomelk 's morgens tussen mijn paperassen te vinden, hebben dikwijls mijn dag gemaakt!

Adwin, bij jou kon ik terecht met al mijn vragen over IR waarnemingen. Maar bovenal wil ik je bedanken voor je vriendschap, onze reis naar Teton and Yellowstone was gewoon fantastisch! Mercedes, even though I don't drink coffee, I will always remember the coffee breaks in your office as my afternoon-escapes. Jacquie, it's time to pick up again our joint dinners and relaxing evenings : I'll see you soon! Jero, it's been a pleasure to be your personal Dutch/English translator; I especially enjoyed the meals and company I got in return! Carlos, I really enjoyed your company, our joint holidays were fantastic and your food is wonderful! Íñigo, I appreciate your friendship very much; you also introduced me to indoor climbing, which I fancy a lot. Emilio, I really enjoyed the long talks we used to have! Isa & Lourdes, I appreciate a lot our joint visits to the swimming pool. Jorge, often I dropped by your office – as a stop-over on my way to or back from Xander – to have a nice chat. César, I really like your sympathetic character. Annette, your enthousiasm for the gym is very contagious. Jelte, dank voor de loop-sessies en de aangename maaltijden in de aclo. Willem and Hans, thanks for the enjoyable breaks. Miguel, it was very agreeable to come home (in this last month) knowing somebody is there. Arjan, mijn bezoekjes aan Amsterdam werden mede opgefleurd door jou! Bjorn, Edo, Eline, Enzo, Filippo, Hanadi, Jean-Philippe, Jocelyn, Ilse, Laura, Marco, Michiel, Nissim, Nasser, Ole, Peter, Rense, Rob, Roelof, Stéphanie, Scott, Ole, Wilfried, you all made life in Holland more colourful bringing your own traditions, meals and culture.

Leren duiken had een grote impact op mijn verblijf in Nederland. Niet alleen is de stille, wonderlijke onderwaterwereld de ideale omgeving om je voor 200 % te ontspannen, in de duikers gemeenschap van De Tuimelaar is gezelligheid troef. Met veel plezier kwam ik dan ook regelmatig over de vloer bij De Tuimelaar voor een gezellige babbel, een leuke duik of om te "divemasteren". Een speciaal woordje is hier ook zeker op zijn plaats voor de CMC & CWC leden, in het bijzonder Marck & Queenie, Bart, Alexander en Nanne, jullie zijn een hoopje zotten bij elkaar, altijd in voor een grap. Het was een plezier bij jullie te zijn! Marck, een groot dank-je-wel speciaal voor jou, ik kon immer en altijd op je rekenen.

Dichter bij huis, maakt(e) ons madam van ’t schoon leven ook mijn leven heel wat schoner door het delen van alle labo – *en ander* – lief en leed. Dank voor je vriendschap, Mich! Kathleen & Natalie, de frequenties van de bezoekjes was door mijn verblijf in Groningen minimaal zodat we te pas en te onpas verjaardagsfeestjes hadden (zelfs voor- én afterparty’s). Kor, Annick & Pol, Veerle & Steven, het is altijd weer een feest om jullie terug te zien!

Ma en va, bedankt voor jullie goede zorgen en onwankelbare liefde. Mijn kleine broertje, ik kijk altijd uit naar onze gesprekken bij mijn thuiskomst!

Jan, van op afstand ben je erin geslaagd om de laatste loodjes voor mij een pak lichter te maken, je maakte ook heel veel tijd voor de mij zo broodnodige telefoontjes. Ik wil je hier echter vooral bedanken dat je met mij je leven wilt delen, voor je oneindige geduld en de talloze pogingen mij bepaalde dingen te verduidelijken. Je bent mijn steun en toeverlaat!